CONDITION MONITORING OF INDUCTION MOTORS:

The Detection of Broken Rotor Bars in Variable Speed Induction Motor Drives

by Andrew Gary Innes, B.E. (Hons.)

Submitted in fulfilment of the requirements for the degree of Doctor of Philosophy.

University of Tasmania

June 1999

Statement of Originality

This thesis contains no material which has been accepted for a degree or diploma by the University or any other institution, except by way of background information and duly acknowledged in the Thesis, and to the best of my knowledge and belief no material previously published or written by another person except where due acknowledgement is made in the text of the Thesis.

A. Innes. June 1999

Andrew Innes.

Authority of Access

This thesis may be made available for loan and limited copying in accordance with the Copyright Act 1968.

A. Innes.

Andrew Innes. June 1999

Abstract

The squirrel cage induction motor is the most common means of converting electrical energy to mechanical energy. As such they form a very important part of modern industrial plants. Adverse service conditions may cause faults to develop within a motor that eventually result in the motor failing. If warning of an impending failure can be obtained, the motor can be scheduled for repair or replacement before catastrophic failure occurs, thus avoiding costly excess down-time of plant.

A fault which occurs in cage induction motors, is where a fracture occurs between the end ring and a rotor bar, or in an end-ring segment. These faults may be detected by examining the frequency spectrum of the stator current, while the motor is operating under loaded conditions, for the presence of characteristic frequency components. The basic theory is reasonably well known, however little work has been done on detecting faults when the motor is controlled by a variable-frequency drive, which causes extra frequency components to appear in the stator current spectrum.

A variable speed drive controls the speed of an induction motor by changing the frequency of the supply voltage. Thus the problem of detecting faults becomes one of analysing a non-stationary signal. One approach to solve this problem is to synchronously sample the stator current waveform, such that the sampling process tracks any change in frequency, producing a useful frequency spectrum. A hardware system based on a phase locked loop circuit is developed in order to implement such a process.

In order to determine which frequencies are produced by a pulse-width modulated (PWM) drive, a theoretical analysis of various PWM methods is carried out, with

particular reference to fault frequency components. The change in frequency component amplitudes between mains operation and VSD operation and also with change in load is also examined experimentally. The uncertainty in amplitude due to the signal processing techniques employed, is also determined by experiment. The effects of changes in frequency component amplitudes on the detection of faults is discussed.

A full-transient model for the induction motor is developed as an assembly of inductively coupled coils using a model that can represent the effects of individual rotor bars. The effect of a broken rotor bar on the frequencies that are introduced into the supply current can then be predicted.

Finally, the possible application of time-frequency and continuous wavelet transform analysis to the problem of a non-stationary signal is examined. Various types of transform are compared to find the most suitable for tracking frequency components as they change.

Acknowledgements

Firstly I would like to thank my supervisor Mr Richard Langman for his guidance and support in conducting this research. I would also like to acknowledge my associate supervisor Mr Peter Watt for initiating this project and for providing some initial impetus in the practicalities of data acquisition and signal processing.

I would like to thank Mr Graeme Vertigan and Pasminco EZ Pty. Ltd., for their permission to take measurements around their factory and for tolerating the subsequent disruption to their production.

Also I would like to thank Dr Michael Robinson and Pope Electric Motors Australia Pty. Ltd. for providing extra rotors and proprietary information on our laboratory motor, and the illuminating technical discussions on induction motor design.

This research was partially funded by a grant from the Electricity Supply Association of Australia Limited.

My thanks must go to all the academic staff in the Department of Electrical and Electronic Engineering at the University of Tasmania, in particular Dr Richard Lane (now with the University of Canterbury), Dr David Lewis, Dr John Arneaud (now with the Hydro Electric Commission Tasmania), Mr Gregory Thé, Dr Habib Talhami, Mr John Brodie, and Professor Thong Nguyen, for the many and varied discussions we have had. I would also like to acknowledge all the technical staff, in particular Mr Glenn Mayhew for his help with electronic design work and solving electromagnetic interference problems, Mr Steven Avery for the design and fabrication of various mechanical devices, and Mr Russell Twining and Mr David Craig for their help with computing.

Many thanks must go to my fellow students, John McCulloch, Quang Ha, Bonnie Law, Alan Liew, and Mike O'Day for their help and friendship. In particular I would like to thank Jason Pieloor, Marc Stoksik, David McLaren and Andrew Bainbridge-Smith who have been there since the start. I would also like to thank Sarah Booker for some proof reading.

I would like to thank Joanna Foulkes for her support and encouragement, and proof reading of the manuscript.

Finally, I would like to thank my parents for the many years which they have supported and encouraged me.

Contents

Figures

Symbols and Abbreviations

The following symbols are used in this thesis:

a_k, b_k	Fourier coefficients of order k.
α_i	Angular span of coil i.
$\boldsymbol{F}$	Fourier transform.
Φ	Magnetic flux.
φ	Angular position around stator bore from some reference.
φ_{in}	Phase of input signal.
φ_{out}	Phase of output signal.
F	Magnetomotive force.
f	Frequency (Hz).
f_r	*F*requency of rotor current (Hz).
f_c	PWM carrier frequency.
f_m	PWM modulating frequency.
f_1	Supply frequency (Hz).
f_{bb}	Broken rotor bar fault frequencies (Hz).
f_s	Sampling frequency (Hz).
g	Air gap length.
g^{-1}	Inverse gap function.
I	Current.
I_{bb}	Broken bar current.
I_N	Normal bar current.
i	Current.
J	Moment of inertia.
$J_n(x)$	Bessel function of the first kind, order n.
K	Viscous friction.

K_{VCO} VCO gain.

K_{PC} Phase comparator gain.

K_p Pitch factor.

K_{pi} Pitch factor for *ith* harmonic.

K_d Distribution factor.

K_{di} Distribution factor for *ith* harmonic.

λ Magnetic flux linkage.

Λ Permeance.

L Inductance.

L_{ls} Stator leakage inductance.

L_{lr} Rotor leakage inductance.

L_m Magnetising inductance.

l Length of rotor.

M Mutual inductance.

N Number of turns in a coil.

N_b Number of rotor bars.

N_{st} Number of turns in stator winding.

N_r Number of rotor slots.

N_s Number of stator slots.

N_i Winding function of coil i.

p Number of pole pairs.

R Resistance and Reluctance.

R_c Inter-bar reistance per unit core length.

R_{bb} Rotor bar resistance.

r Average air gap radius.

s Per unit slip.

θ Angular displacement.

θ_m Mechanical angular displacement of rotor with respect to a stator reference.

T Period.

T_e Eectromagnetic torque developed by the motor.

T_L Load torque.

t	Time.
V	Voltage.
v_c	Control voltage.
v_{in}	Input voltage.
v_{PC}	Phase comparator voltage.
ω_s	Synchronous angular frequency (rad/s).
ω_1	Fundamental supply angular frequency (rad/s).
ω_{in}	Input signal angular frequency (rad/s).
ω_r	Angular frequency of rotor current (rad/s).
ω_{out}	Output signal angular frequency (rad/s).
ω_0	PLL free running angular frequency (rad/s).
X_b	Rotor bar leakage reactance.
Z_b	Rotor bar leakage impedance.
z_i	Number of turns in coil i.

The following subscripts may be applied to the symbols above:

d_e	Dynamic eccentricity.
i_s	Sator harmonic orders.
i_r	Rotor harmonic orders.
j_s	Sator harmonic orders.
j_r	Rotor harmonic orders.
l_s	Stator harmonic orders.
l_r	Rotor harmonic orders.
m_s	Stator harmonic orders.
m_r	Rotor harmonic orders.
r	Rotor.
rt	Rotor.
s	Stator.
st	Stator.
sa	Saturation.
se	Static eccentricity.

The following abbreviations are used in the text:

ASD	Adjustable speed drive.
A/D	Analogue to digital.
CSI	Current source inverter.
hp	Horsepower.
PLL	Phase locked loop.
PWM	Pulse width modulation.
TEFC	Totally enclose, fan cooled.
VSD	Variable speed drive.
VSI	Voltage source inverter.

Preface

This project originated in 1989 with a local zinc company, Pasminco EZ Ltd., who were having problems with some critical induction motors. These motors were driving two large cooling tower fans via reduction gearboxes. If one of these fans were to become inoperative during the summer months, it would shut down the entire plant. The company estimates that this would cost around one million dollars per day. The motors are in an awkward position high above the ground, requiring a large crane to be brought onsite in order to effect replacement. Hence the company were interested in any warning of impending failure that could be obtained. Due to a lack of local commercial expertise, they called the University, whereupon Peter Watt, Richard Langman and Dr David Lewis began an investigation and took some initial measurements.

Two years later this project was continued as a PhD topic by the author. After some initial work assembling a suitable data acquisition system, and examining the literature in the field, it was noticed that the number of variable speed drives in industry was increasing, yet no work had been done on fault detection in the motors controlled by these drives. Hence it was decided to concentrate on fault detection in induction motors controlled by variable speed drives.

As there are no drive manufacturers in Australia, it was not feasible to develop an integrated condition monitoring system. Bearing in mind the existing large installed base of variable speed drives and the necessity to make non-invasive, non-destructive measurements in industrial situations, it was decided to concentrate on condition monitoring methods which depend only on measurements made external to the drive. Due to the lack of internal, often proprietry information concerning the drive and the motor the methods developed must also be independent of any such information.

Supporting Publications

In the course of this work the following papers were published:

Innes A.G., Watt P.A., and Langman R.A., "Condition monitoring of large induction motors", *Proceedings of the Australasian Instrumentation and Measurement Conference*, pp265-271, Auckland, New Zealand, 24-27 November 1992.

Innes A.G., "The use of Prony's method for modelling induction motor current waveforms under fault conditions", *Proceedings of the 2nd International Conference on Modelling and Simulation*, Vol. 1, pp297-303, Melbourne, Australia, 12-14 July 1993.

Innes A.G., Langman R.A., and Mayhew G.R., "Condition monitoring of variable speed induction motor drives", *Proceedings of the International Conference on Electrical Machines in Australia*, Vol. 1, pp158-163, Adelaide, Australia, 14-16 September 1993.

Innes A.G. and Langman R.A., "The effects of variation in the supply frequency on the detection of broken rotor bars in variable speed induction motor drives", *Proceedings of the 29th Universities Power Engineering Conference*, Vol. 2, pp581-584, Galway, Ireland, 14-16 September 1994.

Innes A.G. and Langman R.A., "The detection of broken rotor bars in variable-speed induction motor drives", *Proceedings of the International Conference on Electrical Machines*, Vol. 2, pp294-298, Paris, France, 5-8 September 1994.

Ho S.Y.S., Innes A.G., and Langman R.A., "Stator current frequency analysis for condition monitoring of induction motors. Part II: Variable supply frequency", *Journal of Electrical and Electronics Engineering Australia*, Vol. 17, No. 1, pp 57-69, March 1997.

The following reports were also produced:

Innes A.G., Langman R.A., *Report on tests conducted at Pasminco EZ Pty. Ltd.*, December 1991.

Innes A.G., Langman, R.A., Watt P.A., *Final Report to ESAA - Condition Monitoring of Induction Motors*, November 1994.

CHAPTER 1

Introduction

Electrical machines are very important to the modern way of life, indeed we have become very dependent upon them in our daily lives. Machines generate the electricity that we use and they also convert that electrical energy into mechanical energy to perform useful work. Hence it can be very important that these machines do not fail unexpectedly.

1.1 Maintenance and Condition Monitoring

There are three means of maintaining a plant [1]:

(i) run to breakdown,

(ii) fixed-interval maintenance,

(iii) condition-based maintenance.

The first option, run to breakdown, simply operates the system until a part breaks. The part is then replaced and the system operation resumed. This method has the

advantage of being extremely simple to implement, and also uses the component to the end of its useful life. Of course, the major disadvantage is that the time at which system breakdown occurs tends to be random. This may result in unexpected, and hence often costly, system outages.

The second, and probably most familiar, option is fixed-interval maintenance, where parts of the system are replaced at pre-determined time intervals. The choice of time interval is dictated by two requirements, maximum utilisation of component lifetime to minimise waste, and minimisation of unexpected failures. A compromise between these two factors is generally established by experience and testing. However, system failures will still occur, and maximum lifetime of components will not generally be used before they are replaced, leading to wastage.

Condition-based maintenance is a method where component replacement is scheduled according to an estimate of the remaining life of the part. Condition monitoring of the system is required in order to provide knowledge of the system condition and of the rate at which deterioration is occurring. A condition-based maintenance program provides the best of both worlds; maximum lifetime of equipment is ensured and unscheduled outages are minimised. However, all of this comes at the cost of actually implementing such a program, in terms of both labour and capital costs. Condition monitoring of a system relies on measuring one or more parameters of that system in order to determine any deterioration that is occurring. Such measurements may require expensive instrumentation, a significant labour commitment to record the data, and expert knowledge to interpret the results.

Condition monitoring is only financially feasible where either the replacement cost of the equipment being monitored is high, or where unscheduled outages have a high cost in terms of lost production time. Since induction motors are relatively cheap items, it is plant outages caused by motor failure which incur the high costs that can justify a condition monitoring programme.

1.2 Types of Electric Motors

There are many different types of electric motor for converting electrical energy into mechanical energy. The three main types used in industry are DC motors, synchronous motors, and induction motors. A DC motor needs a source of DC power to supply a stationary field winding, and, via a commutator and brushes, a rotating armature winding. This complexity of construction means that the DC motor is the most expensive to build and maintain of the three types. The advantage that DC motors have is the ease of speed control, which until recently, has seen them dominate variable speed drive applications.

The synchronous motor uses a source of DC power to excite a rotating field winding and an AC source to excite the stator winding. The synchronous motor rotates at a synchronous speed set by the frequency of the AC supply. This machine is used where a constant speed is required, regardless of load. The cost of a synchronous machine is more than for a similarly rated induction motor although it is still less than a DC machine. The main applications of synchronous machines is in very high power applications.

The polyphase induction motor is the cheapest to produce and run of the three types. It only requires a source of polyphase AC voltage to be applied to the stator winding in order to operate, no connection need be made to the rotor. The voltage applied to the stator produces a magnetic flux wave which rotates around the stator at synchronous speed. With the rotor rotating at a slower speed, currents are induced in the rotor winding which produce a magnetic flux which couples with the stator flux to produce torque. The rotor accelerates until the torque produced balances the load torque. The difference between this speed and the synchronous speed is known as the slip, usually expressed in per unit terms by dividing by synchronous speed.

There are two different types of rotor windings which may be used to construct an induction motor. Both have a laminated iron core with slots for the windings. One is known as a wound rotor and has a full three-phase winding of copper wire, similar to the stator. The ends of each phase winding are brought out via slip rings

and brushes to allow external connection of resistors to improve starting torque [2].

The second type of winding is called the squirrel cage, and consists of rotor bars which run axially through the rotor laminations, and are joined at the ends by end-rings, to form a cylindrical cage. The cage may be constructed by fabricating copper bars and end-rings, or by casting aluminium into the previously prepared rotor iron. The latter technique is mainly used in the smaller sizes of induction motor (<50kW), as the probability of producing a good casting decreases with increasing size. The squirrel cage winding is by far the most common of the two. It also contributes to the simplicity and high reliability of the induction motor, making the induction motor the most commonly used electric motor.

1.3 Failure Modes of the Induction Motor

In order to monitor the condition of an induction motor, or indeed any system, it is necessary to know the manner in which failure can occur and the relevant parameters to measure in order to detect impending failure. The failure modes of induction motors may be divided into four main groups: bearing faults, stator faults, rotor faults, and other faults. There have been a few surveys performed in order to quantify the relative incidence of these failure modes.

The IEEE Industry Applications Society has carried out two industrial reliability surveys, one in 1973 [3] and another in 1982 [4]. The EPRI performed its own survey in 1982 [5]. Recently Thorsen and Dalva [6] also performed a survey. The results obtained by these surveys are illustrated in Figure 1.1.

The four surveys are not directly comparable as they all survey different target groups, nevertheless they do provide useful information on the relative incidence of fault types in induction motors. The 1973 IEEE report [3] is a very broad survey of many types of electrical equipment, such as transformers, generators, transmission lines, etc., as well as motors.

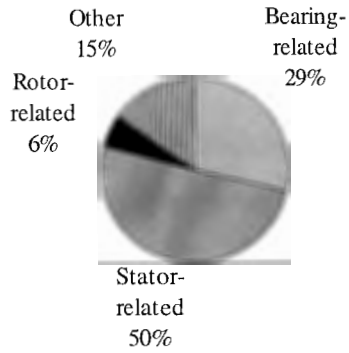

(a) 1973 IEEE Survey [3].

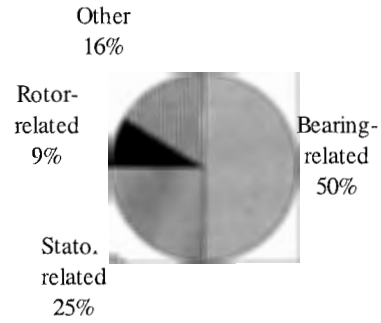

(b) 1982 IEEE Survey [4].

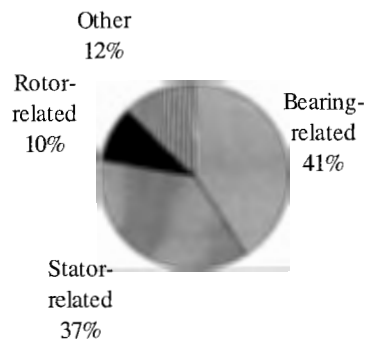

(c) EPRI Survey [5].

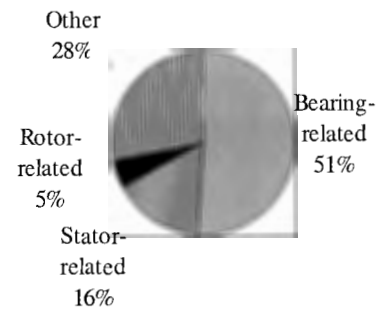

(d) Thorsen and Dalva Survey [6].

Figure 1.1: Incidence of fault types in induction motors.

It is clear that the predominant fault type is bearing-related with stator related faults second. Rotor-related faults account for around 5-10% of induction motor failures, which is quite small, but still a significant number.

The 1973 IEEE report [3] surveyed 17 companies with motors, covering 10 different industries. It is not very clear on the exact split up of failure types nor does it give any indication of the proportion of wound rotor induction motors included in the survey. This is probably because it was a very broad survey of many types of electrical equipment, such as transformers, generators, transmission lines, etc., as well as motors. It is likely that the motors were, on average, quite old

and this is why the distribution of faults is somewhat different to the other surveys.

The 1982 IEEE report [4] surveyed 75 plants from 33 companies across a number of different industries. It concentrates on motors only, and specifically, motors no older than 15 years, and greater than 200hp rated output. A total of 294 induction motor failures were reported, all of which were presumably cage rotor machines, as there is a separate category listed for wound rotor motors. Again bearing faults predominate (50%) with stator faults second (24.7%) as the leading causes of failure. Rotor related faults account for 9% of failure, however, on closer inspection the rotor cage and core account for only 3% of failures.

The 1982 EPRI report [5] surveyed only electric utility companies. There were 4797 motors surveyed, of which 97% were cage rotor induction motors. 872 of these motors were found to have failed. Bearing related faults accounted for 41% of failures and stator faults 37%. Rotor faults caused 105 failures with cage faults accounting for 5% of all failures.

The more recent (1994) survey of Thorsen and Dalva [6], surveyed only squirrel cage induction motors in the offshore oil industry, petrochemical industry, gas terminals, and oil refineries. Most of the 2596 motors surveyed were offshore. There were a total of eight companies surveyed with eleven plants. The number of failures reported was 1637.

From the details of the four reports, it would appear that the greatest number of faults are due to bearings (50%). Stator faults account for around 20% of faults. Actual cage faults, as a subset of rotor-related faults, account for around 5% of failures. Although small, this is still a significantly large number to warrant detailed study, as the major cost involved with induction motor failures is not the motor itself, but the cost of downtime.

1.4 Condition Monitoring of Induction Motors

The previous section described the various failure modes of the induction motor. This section describes the techniques which have been developed to detect the various types of fault. Bearing damage is probably the fault which is best understood, and the easiest to detect [1]. The technology developed for the detection of bearing faults in other industrial machines, principally by vibration measurements, is directly applicable to induction motors. Damage to stator windings can be detected by various means. Partial discharge tests can detect actual damage that has occurred [7]. Negative-sequence components can give an indication of stator damage [8]. Chow and Fei [9] used the bispectrum for detecting asymmetrical faults, including supply unbalance and stator winding faults. Chen et al. [10] described a novel system for measuring the temperature inside an induction motor which used the power supply leads as a data transmission link to a variable speed drive. Natarajan [11] detected failures by sensing unbalanced stator currents.

Rotor faults are much more difficult to deal with, mainly because the rotor is rotating quite quickly making it very difficult to attach transducers directly to the rotor body. Hence, indirect measurement techniques are required to detect rotor damage. There are a number of different faults which are classified as rotor-related. The rotor may not be supported such that it is centred in the stator bore, which is termed static eccentricity, and the air gap length varies only with position around the bore and is independent of movement. Dynamic eccentricity occurs when the rotor shaft is bent, or the rotor and shaft are not concentric. This causes the length of the air gap to vary with both bore position and rotor movement. Both types of eccentricity cause an unbalanced magnetic pull on the rotor [12], which may result in the rotor and stator rubbing which can quickly cause serious damage.

Other rotor-related faults which can occur include rotor balancing weights becoming dislodged from the rotor and being jammed between rotor and stator. Wound rotor machines may have winding insulation breakdown.

The last type of rotor-related fault, which only occurs in cage rotor machines, is broken rotor bars. A cage rotor is constructed either by fabricating copper bars, or by casting aluminium, to create a structure similar to that shown in Figure 1.2. The iron laminations are first prepared by punching holes for the shaft and bars, and then stacking them together to form the core. For a fabricated rotor, copper bars are then driven through each slot to give a tight fit. The end rings are formed by welding on a copper ring, or sometimes in smaller machines, the bars are made longer and bent over and brazed to form the end ring. A cast rotor is formed by placing the iron stack in a sand casting mould and filling the mould with molten aluminium. This forms the bars and the end rings in one operation. This method is only used on the smaller sizes of motor (<50kW) because it is difficult to keep the core hot enough for the aluminium to flow through the core in larger machines. The casting method can cause difficulties in that voids can form due to air bubbles and also due to aluminium cooling prematurely in the slots. It has the advantage that it is possible to construct rotors with more complex bar shapes than with fabricated copper cages.

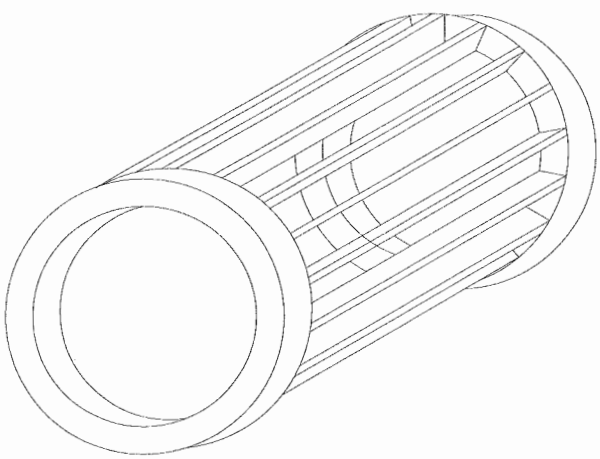

Figure 1.2: Squirrel cage rotor (iron core not shown).

With fabricated rotors, breaks can occur between where the rotor bars and end rings are joined, due to movement of the bars in the slots. The centrifugal and

magnetic forces on the rotor bars are high, especially during starting, and when combined with forces due to thermal expansion, can cause rotor bars to move slightly in the slots. This may cause fatigue cracking to occur between the rotor bars and end rings, resulting in a high-resistance joint. The heating caused by this can cause further damage to the bars and end rings, as well as the iron laminations. Squirrel cage rotors can also suffer from fatigue cracking, although there is not the welded joint there is in fabricated rotors. Small voids in the casting can also cause stress concentrations and localised heating effects which may ultimately lead to failure.

1.5 Detection of Broken Rotor Bars

There has been a large amount of work done on the detection of broken rotor bars in induction motors. It has been noted that broken rotor bars cause a pulsation at twice the slip frequency in the stator current [13] [14]. Others have used this as a means of detecting broken bars in an induction motor [7] [15-27].

In addition to the current, axial flux may be monitored in order to detect faults [28] [29]. Axial flux is difficult to measure as modern motors are designed to limit this flux as much as possible. Therefore, it is hard to detect. Vibration can also be used to detect rotor faults [28], although the amplitude of vibrations caused by a damaged rotor is small relative to that caused by damaged bearings.

Another technique which has been applied to the detection of broken rotor bars, and condition monitoring in general, is parameter estimation [30] [31]. A model is assumed for the motor, and an algorithm is used to calculate the model parameters based on measurements of current and voltage. When the parameter being measured changes too much an alarm is raised. Du et al. [32] used such a method to calculate the rotor resistance and rotor temperature on-line. These methods are dependent on the correct model being chosen, and are also vulnerable to noise and normal parameter variation, as they generally involve numerical integration.

Legowski and Trzynadlowski [33] have recently suggested that the instantaneous stator power could be more useful than current analysis for the detection of faults.

However, their method is more difficult to use than just current analysis as it requires the voltage to be measured as well. The advantage that it has is that the fundamental component of the spectrum of the instantaneous power is twice the frequency of the voltage and the current. Hence fault frequency components are further removed from the fundamental in the spectrum which makes them easier to resolve.

1.6 Condition Monitoring of Induction Motors fed by Variable Speed Drives

As noted in the previous section, a large amount of research work has been done on detecting induction motor faults, but in the main, this has concerned only mains supplied induction motors. Very little has been performed on motors supplied by variable speed drives. As the use of variable speed drives is increasing it would seem pertinent to further explore the subject. The first publication on condition monitoring of variable speed drives was by Thomson [34] which gave a general overview of the possibilities. Cardoso and Saraiva [35] were the first to describe a practical application of condition monitoring to a variable speed drive fed induction motor. They used a current-source inverter to control their induction motor, and calculated the two-phase Park's vector for the supply current and voltage. By displaying the locus of this vector on a CRO, they showed that faults could be detected through changes in the patterns displayed.

Thian [36] published a PhD thesis on the topic of methods of condition monitoring variable speed drive fed induction motors, although he does not appear to have published any papers. In this work, he considers some of the fault frequencies and the interactions of these with the extra supply harmonics caused by the variable speed drive. He also considers monitoring of current, vibration and axial flux for the detection of stator and rotor faults. Some experimental work was done on the change in amplitude of various frequency components, but these changes do not appear to have been calculated relative to the supply frequency component magnitude.

Sethuraman and Sarvanan [37] examined some of the harmonics produced by pulse-width modulated voltage waveforms and the impact these had on their test motor and drive.

1.7 Contribution of this Thesis

To date no-one has examined the detection of rotor damage in an induction motor controlled by a variable speed drive, *when the drive output frequency varies*. This thesis examines the implications that variable speed drives have for the detection of rotor damage and the impact of fault frequencies.

One way of coping with varying frequency signals is synchronous sampling of the signal. A circuit based on a phase locked loop was constructed in order to achieve synchronous sampling. The circuit was found to work very well with mains supplied induction motors. However, it was affected by the frequency jitter of some variable speed output waveforms, which resulted in it not working on some drives.

A transient model of the induction motor was developed so that pulse width modulated voltage waveforms could be simulated. The effects of simulating a broken rotor bar in the model were also examined.

Time-frequency and wavelet analysis are very new techniques which are particularly suited to the analysis of waveforms where the frequency components vary with time. This thesis applies such methods to the problem of detecting fault frequencies in stator current waveforms, as the supply frequency varies.

1.8 Organisation of the Thesis

The next chapter of this thesis examines the theoretical air gap flux distribution for a symmetrical induction motor, and from this information predicts the frequency components that should be present in the stator current waveform. The effect of a broken bar in the rotor is then considered and the effect on the stator current waveform predicted.

Chapter 3 examines the Fourier Transform and the effects of synchronous and non-synchronous sampling of signals. The use of window functions and their effect on the calculation of frequency spectra is investigated. The theory of a parametric spectrum estimation technique, Prony's method, is developed, and the results of applying the method to measured data is reported.

Chapter 4 develops the theory of phase locked loops and the design of a circuit based on a phase locked loop which ensures that a signal is synchronously sampled. The circuit is used to sample the stator current waveform of a mains supplied induction motor and also with a variable speed drive. The benefits and difficulties encountered with synchronous sampling for condition monitoring are described.

Chapter 5 describes the theory of operation of variable speed drives for the speed control of induction motors. The various types of pulse width modulated output waveforms from these drives are analysed to obtain the frequency content. The implications that the extra frequency components have for condition monitoring are examined. The impact that operating induction motors at different supply frequencies has on the detection of fault frequencies, and the variation due to different load levels is experimentally assessed.

Chapter 6 develops and implements a mathematical model for the induction motor with a broken rotor bar. Each rotor bar is modelled individually, as is each coil of the stator winding. Transient loads are also accounted for. These factors make the model suitable for simulating variable speed drive supplied induction motors. Some results using the model are also presented.

Chapter 7 reflects upon the correspondence between the theoretical studies and the practical applications. Some more industrial case studies are also presented.

Chapter 8 examines the application of time-frequency and wavelet analysis to the stator current waveform of an induction motor with a broken rotor bar. It is shown that such an analysis is helpful in detecting fault frequency components, especially

in variable speed drives when the drive frequency varies during the time that the data is recorded.

The last chapter of this thesis provides a summary of the work done and gives some suggestions for future work on the topic.

CHAPTER 2

The Air Gap Flux Density of the Induction Motor

2.1 Introduction

In order to monitor the condition of an induction motor, it is necessary to know what to monitor in order to detect damage. For an operating induction motor it is possible to measure the stator current, stator voltage, leakage flux, speed, torque, temperature, and vibration. The stator temperature is commonly measured with a thermistor inserted into the stator windings when the machine is manufactured. The stator temperature can be very different to the rotor temperature because of the insulating effects of the air gap. Hence temperature measurement by the thermistor is not very useful for detecting high rotor temperatures. The external frame temperature will reflect any internal rise, but at a much reduced magnitude due to external cooling. Speed and torque sensors are not usually attached to motors in industrial situations, so these cannot be directly measured. Vibration is

routinely measured, especially in large motors, by attaching transducers at strategic locations on the motor frame. These measurements can be very helpful in detecting bearing faults [1] [38].

The axial leakage flux can be measured by using a search coil consisting of a number of turns of wire, placed near either end of the motor. Any flux which couples with the coil induces a voltage in it which may be measured [39]. However, modern induction motors are designed so that leakage flux is minimised, which makes it rather difficult to measure.

Voltage and current are the easiest quantities to measure as there is generally a control cabinet where connections to the motor are made. The voltage can be measured here by connecting a sensor to the motor supply terminals. Current is measured by clamping a current transformer or Hall effect transducer around the motor supply cable.

Rotor faults may be detected by the presence of particular frequency components in the spectrum of the stator current [13]. An analytical expression for the flux pattern in the air gap of the induction motor, is required to predict the frequency components in the spectrum of the stator current which result from stator and rotor winding slots. This is then extended to deal with the asymmetry caused by a broken rotor bar. This chapter develops such an analysis.

2.2 Air Gap Flux Analysis

2.2.1 Torque Production in the Induction Motor

Torque is produced by an induction motor as a result of the interaction of the air gap flux produced by the stator windings and the flux produced by the rotor windings. The stator windings are constructed in such a way so that a three phase voltage applied to the windings sets up a rotating three-phase magnetic field. This process has been described by many authors [40-45]. This magnetic field rotates around the stator bore at synchronous speed, ω_s rad/s:

$$\omega_s = \frac{2\pi f_1}{p} \tag{2.1}$$

where f_1 is the frequency of the supply voltage, and p is the number of pole pairs.

The magnetomotive force, F, produced by the field sets up a magnetic flux $\Phi = F/R$, in the air gap and the rotor core (where R is the reluctance of the magnetic path). This magnetic flux links with the rotor windings and induces a voltage in them, which in turn causes a current to flow [45]. Since the rotor winding is in a magnetic field there is a force exerted on it given by Ampere's law [45]. The tangential force is converted to torque and the rotor will turn.

Since this thesis deals only with three phase induction motors, the mathematical theory will only be derived for three phase stator windings. If required, all results can be extended to an arbitrary number of phases.

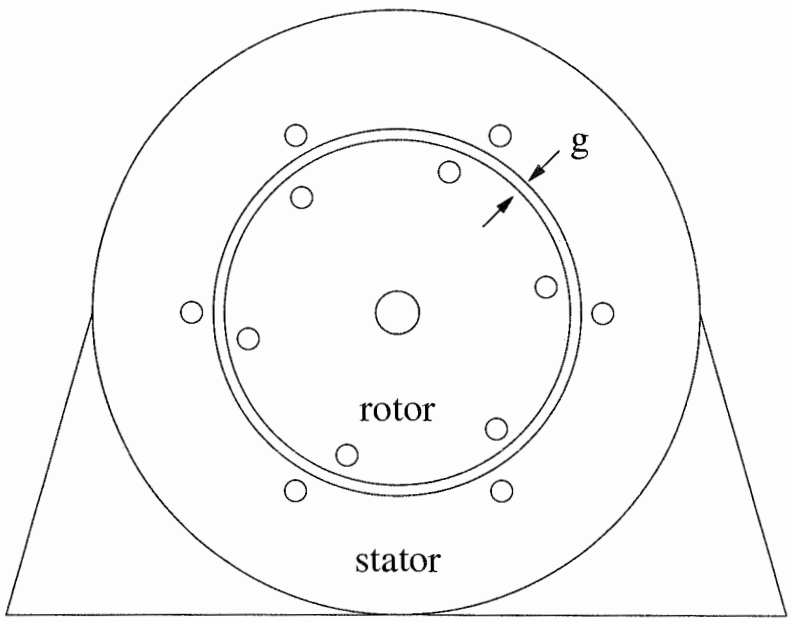

Figure 2.1: Induction motor cross-section.

2.2.2 Induction Motor Model

As a first approximation, an induction motor can be considered to consist of two smooth, coaxial ferromagnetic cylinders separated by an air gap of radial length g. Several conductors are distributed around the surface of each cylinder and

connected in a certain pattern. A cross-section of such a motor, with six stator and six rotor conductors, is shown in Figure 2.1. The following analysis assumes that the stator windings are symmetrical, and that the stator voltage is balanced and sinusoidal.

2.2.3 Magnetomotive Force of an AC Winding

A mathematical expression for the magnetomotive force of the stator winding can be developed by recognising that the stator winding consists of a number of coils connected together. In order to build up the complete magnetomotive force pattern in the machine, it is best to start by examining a single turn of wire in the stator.

2.2.3.1 Magnetomotive Force of a Single Turn

First consider a single, full-pitched stator coil carrying a current *i*. A developed diagram of this coil is shown in Figure 2.2.

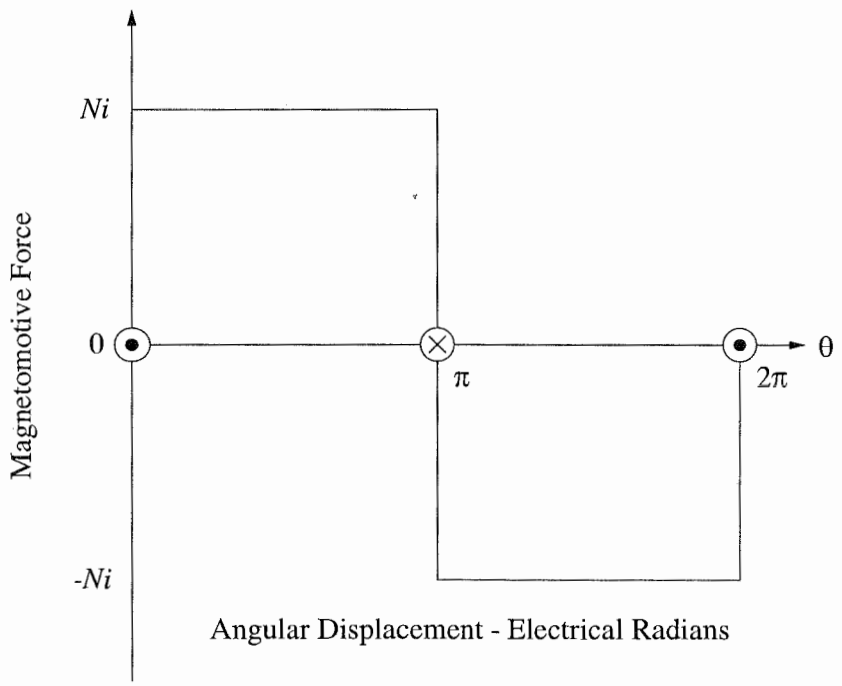

Figure 2.2: Magnetomotive force distribution of a single full-pitched coil.

For the current directions shown and a coil of N turns, the magnetomotive force, F, has a value of Ni from zero to π radians, and $-Ni$ from π to 2π. That is, it is a square wave and may be expressed as a Fourier series [41]:

$$F = \frac{4Ni}{\pi}\left(\sin\theta + \frac{\sin 2\theta}{2} + \frac{\sin 3\theta}{3} + \ldots\right) \tag{2.2}$$

If the current is then assumed to be sinusoidal, $i = I\cos\omega_1 t$, then:

$$F = \frac{4NI}{\pi}\cos\omega_1 t \sum_{\nu=1}^{\infty}\frac{1}{\nu}\sin\theta \tag{2.3}$$

2.2.3.2 Magnetomotive Force for the Whole Stator Winding

In order to construct the stator winding, a number of coils are connected in series to form a group, which makes up one magnetic pole of the stator winding. Each phase winding is formed by connecting an appropriate number of groups in a series or parallel combination. The complete three-phase stator winding consists of three of the phase windings. This situation is illustrated in Figure 2.3 for a four-pole machine.

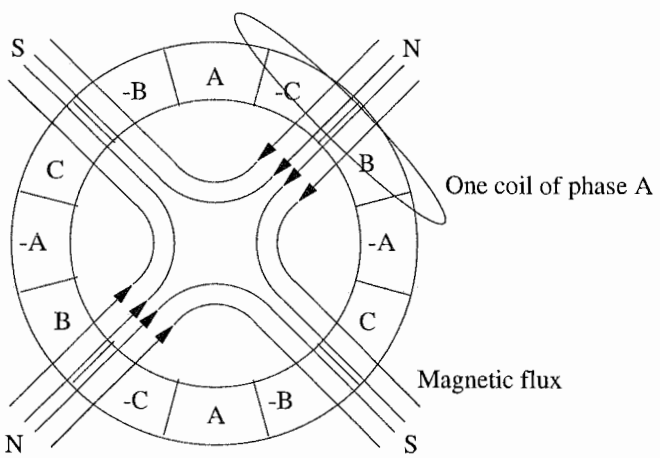

Figure 2.3: Stator winding and flux pattern.

The flux pattern for phase A at the instant the current in phase A is at a maximum is shown. The actual connection of coils to form a group is shown in Figure 6.4 for a 36 slot, concentric coil, stator winding, with three coils per group.

The angle around the stator bore can either be measured in mechanical angle or electrical angle. If, in Figure 2.3, the flux density is followed around the stator bore, it proceeds from a maximum at a North pole to a minimum at a South pole, maximum, and then a minimum again. That is, it goes through two complete cycles or 4π electrical radians, but only 2π mechanical radians. Calculating quantities in electrical angles makes them independent of the number of pole pairs.

If the coils do not span the complete pole, that is, the span is less than π electrical radians, then the voltage induced in the coil is slightly less than that for the equivalent full-pitch coil. The proportion by which it is lower is known as the pitch factor K_p [45], and each harmonic has a different value. The coils which make up the group are usually distributed over an angle of 60°. Thus the voltages in each coil are slightly out of phase. When the voltages are added vectorially, the resultant is slightly less than if they were all in phase. The reduction in the voltage is given by the distribution factor K_d [45], and again each harmonic has a different value. This chapter is only concerned with the frequency components that are present, not the amplitudes, thus both the pitch and distribution factors will be ignored.

By adding together the magnetomotive forces of all the coils which comprise the stator, and adjusting the currents appropriately for each phase, the complete magnetomotive force for the stator winding can be found [45]:

$$\begin{aligned} F = \frac{6N_{st}\sqrt{2}I_1}{\pi p}\Big[& K_{p1}K_{d1}\sin(\theta-\omega_1 t)+\tfrac{1}{5}K_{p5}K_{d5}\sin(5\theta+\omega_1 t) \\ & +\tfrac{1}{7}K_{p7}K_{d7}\sin(7\theta-\omega_1 t)+\tfrac{1}{11}K_{p11}K_{d11}\sin(11\theta+\omega_1 t) \\ & +\tfrac{1}{13}K_{p13}K_{d13}\sin(13\theta-\omega_1 t)+\tfrac{1}{17}K_{p17}K_{d17}\sin(17\theta+\omega_1 t)+\ldots\Big] \end{aligned} \tag{2.4}$$

It should be noted that there are no harmonics in this equation that are even, or a multiple of three (triplen). This is because the three phase winding causes these harmonics to be cancelled when the magnetomotive forces are summed together. This is only the case for a balanced three phase winding, and a balanced three

phase supply voltage. If one or both of these conditions is false then all harmonics will be contained in the magnetomotive force.

The above expression assumes an integral number of stator slots per pole. It is also possible to calculate an expression for a fractional slot winding, where the number of stator slots per pole is not an integer. In this case the expression contains all of the harmonics, resulting in [46]:

$$F_s(\theta,t)=\sum_{l_s=1}^{\infty}\sum_{m_s=-\infty}^{\infty}F_{l_s m_s}\cos\left[l_s p\theta - m_s\omega_1 t\right] \tag{2.5}$$

In practice, most useful induction motor designs can be considered to be equivalent to a full-pitch winding [47].

2.2.3.3 Rotor Magnetomotive Force

The magnetomotive force for the rotor winding, referred to the stator, may be found in a similar manner to the stator, resulting in:

$$F_r(\theta,t)=\sum_{l_r=1}^{\infty}\sum_{m_r=-\infty}^{\infty}F_{l_r m_r}\cos\left[l_r p\theta-(m_r s\omega_1+l_r p\omega_r)t\right] \tag{2.6}$$

The order of the harmonics, l_s, m_s, l_r, m_r, and the corresponding magnitudes, F_{lm}, in Equations (2.5) and (2.6) are dependent on the construction details of the machine such as the number and shape of slots, number of phases, and the winding connections.

The total magnetomotive force in the air gap is simply the sum of the stator and rotor equations, giving:

$$\begin{aligned}F_{total}(\theta,t)=&\sum_{l_s=1}^{\infty}\sum_{m_s=-\infty}^{\infty}F_{l_s m_s}\cos\left[l_s p\theta - m_s\omega_1 t\right]\\&+\sum_{l_r=1}^{\infty}\sum_{m_r=-\infty}^{\infty}F_{l_r m_r}\cos\left[l_r p\theta-(m_r s\omega_1+l_r p\omega_r)t\right]\end{aligned} \tag{2.7}$$

2.2.4 Air gap Magnetic Permeance [46]

The magnetic flux distribution in the air gap may be calculated by multiplying the magnetomotive force distribution of the windings by the permeance of the air gap. The initial assumption that the air gap is smooth is not true, as both the rotor and stator iron laminations contain slots in which the windings are contained. This will have an effect on the air gap permeance, as the permeance of the winding material is different to that of iron.

In practical machines, due to the presence of stator slotting, rotor slotting and saturation effects, the air gap permeance varies continuously when the rotor is in motion. The permeance of an air gap bounded by a slotted stator and a smooth rotor is given by [46]:

$$\Lambda_{st}(\theta) = \sum_{n_{st}=0}^{\infty} \Lambda_{n_{st}} \cos n_{st} N_{st} \theta \tag{2.8}$$

where N_{st} is the number of stator slots, n_{st} is the harmonic order.

The permeance of an air gap bounded by a slotted rotor and a smooth stator is given by [46]:

$$\Lambda_{rt}(\theta) = \sum_{n_{rt}=0}^{\infty} \Lambda_{n_{rt}} \cos\left[n_{rt} N_{rt} (\theta - \omega_r t)\right] \tag{2.9}$$

where N_{rt} is the number of rotor slots, ω_r is the angular speed of the rotor, n_{rt} is the harmonic order.

The combination of these two permeance effects is given approximately as [46]:

$$\Lambda_{st,rt} \approx k \Lambda_{st} \Lambda_{rt} \tag{2.10}$$

where k is a constant. Hence the combination of the stator and rotor slotting permeances is approximately:

$$\Lambda_{st,rt}(\theta, t) = \sum_{n_{st}=0}^{\infty} \sum_{n_{rt}=0}^{\infty} \Lambda_{n_{st} n_{rt}} \cos\left[(n_{rt} N_r \pm n_{st} N_s)\theta - n_{rt} N_r \omega_r t\right] \tag{2.11}$$

The air gap permeance wave due to static rotor eccentricity can be expressed as:

$$\Lambda_{se}(\theta) = \sum_{n_{se}=0}^{\infty} \Lambda_{n_{se}} \cos n_{se}\theta \tag{2.12}$$

Similarly, the air gap permeance wave due to dynamic rotor eccentricity is given by:

$$\Lambda_{de}(\theta,t) = \sum_{n_{de}=0}^{\infty} \Lambda_{n_{de}} \cos\left[n_{de}(\theta-\omega_r t)\right] \tag{2.13}$$

Saturation of the iron core can be represented by an air gap which varies in both space and time. The apparent air gap becomes larger in regions of maximum flux density and has twice the number of pole pairs and twice the frequency of the fundamental wave [47]. The permeance is thus:

$$\Lambda_{sa}(\theta) = \sum_{n_{sa}=0}^{\infty} \Lambda_{n_{sa}} \cos\left[n_{sa}(2p\theta-2\omega_1 t)\right] \tag{2.14}$$

where n_{sa} is an integer, p is the number of pole pairs, and ω_1 is the fundamental angular frequency.

Assuming that the permeances from the gap centre to the stator is equal to that from the gap centre to the rotor, then the total air gap permeance, Λ_{total}, can be obtained by combining Equations (2.11) to (2.14) [48]:

$$\begin{aligned}\Lambda_{total}(\theta,t) = \sum_{n_{st}=0}^{\infty}\sum_{n_{rt}=0}^{\infty}\sum_{n_{se}=0}^{\infty}\sum_{n_{de}=0}^{\infty}\sum_{n_{sa}=0}^{\infty} \Lambda_{n_{st},n_{rt},n_{se},n_{de},n_{sa}} \\ \times\cos\left\{\left[n_{st}N_s \pm n_{rt}N_r \pm n_{se} \pm n_{de} \pm 2n_{sa}p\right]\theta \right. \\ \left. -\left[(n_{rt}N_r \pm n_{de})(1-s)/\,p \pm 2n_{sa}\right]\omega_1 t\right\}\end{aligned} \tag{2.15}$$

where $\Lambda_{n_{st},n_{rt},n_{se},n_{de},n_{sa}}$ is the coefficient resulting from the appropriate combinations of the individual permeance amplitude coefficients.

2.2.5 Air gap Flux Density Distribution

The flux density in the air gap of an induction motor is given by the product of the magnetomotive force and the permeance as:

$$B(\theta,t)=\sum_{i_s}\sum_{j_s}B_{i_sj_s}\cos(i_s\theta-j_st)+\sum_{i_r}\sum_{j_r}B_{i_rj_r}\cos(i_r\theta-j_rt) \tag{2.16}$$

where

$$i_s=n_rN_r\pm n_sN_s\pm n_{se}\pm n_{de}\pm 2n_{sa}p\pm l_sp \tag{2.17}$$

$$j_s=(n_rN_r\pm n_{de})\omega_r\pm 2n_{sa}\omega_1\pm m_s\omega_1 \tag{2.18}$$

$$i_r=n_rN_r\pm n_sN_s\pm n_{se}\pm n_{de}\pm 2n_{sa}p\pm l_rp \tag{2.19}$$

$$j_r=(n_rN_r\pm n_{de}\pm m_rp)\omega_r\pm 2n_{sa}\omega_1\pm m_rs\omega_1 \tag{2.20}$$

It can be seen that the flux density distribution varies in both space (*i* coefficients), and time (*j* coefficients). It is the time components that affect the frequency components of the flux, and, since these fluxes are moving relative to the stator winding, the harmonics are induced in the stator current. Hence frequency analysis of the stator current should reveal these frequencies.

Obviously there is a vast number of frequency components which result from the above equation. In order to simplify matters somewhat, consider just the frequencies caused by stator and rotor slotting, and neglect eccentricity and saturation effects. That is, $n_{se}=0$, $n_{de}=0$, $n_{sa}=0$, while n_s and n_r vary from 0 to ∞, l_s and l_r vary from 1 to ∞, and m_s and m_r vary from $-\infty$ to $+\infty$. Some of the lower frequency components caused by slotting effects are listed in Table 2.1. The amplitude of the harmonic components decreases with increasing frequency, hence the higher order frequencies are not usually significant, or even measurable above the background noise level.

From Table 2.1 it can be seen that the rotor slotting will cause frequency components to appear in the stator current spectrum at $N_r\omega_r$ and $N_r\omega_r\pm\omega_1$. These components can be used to obtain an estimate for the speed of the motor if the number of rotor slots is known.

n_r	m_s	m_r	l_r	j_s	j_r
1	0	0	0	$N_r\omega_r$	$N_r\omega_r$
1	1	0	0	$N_r\omega_r \pm \omega_1$	$N_r\omega_r$
1	0	1	0	$N_r\omega_r$	$N_r\omega_r \pm s\omega_1$
1	0	0	1	$N_r\omega_r$	$(N_r \pm p)\omega_r$

Table 2.1: Stator current frequency components caused by rotor slotting.

2.3 Effect of Broken Rotor Bars

The derivations above considered a perfectly symmetrical rotor cage. The frequency spectrum of the stator current with a broken rotor bar can then be considered as the sum of the effects of the symmetrical case, and a disturbance caused by the broken bar. Deleroi [49] [50] modelled a broken rotor bar by replacing it with a current source exactly opposite to the current that would normally flow in the bar.

This current sets up a magnetic field which is superimposed on the symmetrical rotor magnetic field. If the stator magnetic field is considered to consist of only a single frequency component, f_1, then the currents induced in the rotor bars are also sinusoidal and have a frequency of sf_1 (slip frequency). This current creates two magnetic fields which rotate with respect to the rotor, one which rotates in the same direction as the rotor and another which rotates in the opposite direction. When this is referred to the stator reference frame, the fields are rotating at synchronous speed and synchronous speed minus twice slip frequency, respectively.

The disturbance current introduced to model the broken bar, flows equally to the adjacent bars via the end-rings. This is the cause of the two magnetic fields

travelling in opposite directions. In fact, there are more than just two frequencies because the magnetic field has a shape similar to Figure 2.2. Hence a Fourier series contains many harmonics. When these harmonics are referred back to the stator reference frame, and then to the stator current, the frequency components found in the current are given by [49]:

$$f_{bb} = f_1\left[\frac{k}{2p}(1-s) \mp s\right] \tag{2.21}$$

where p is the number of pole pairs. Most common winding designs cancel the triplen harmonics, hence $k/2p$ = 1,5,7,11,13, ...

Thus the stator current frequency components caused by a broken rotor bar are as stated in Table 2.2. The first component ($k/2p$ = 1) has the largest magnitude, because the magnitudes decrease with increasing order, and this is the frequency component which is most often used for detecting broken rotor bars [13].

$k/2p$	f_{bb1}	f_{bb2}
1	$f_1(1\text{-}2s)$	f_1
5	$f_1(5\text{-}6s)$	$f_1(5\text{-}4s)$
7	$f_1(7\text{-}8s)$	$f_1(7\text{-}6s)$
11	$f_1(11\text{-}12s)$	$f_1(11\text{-}10s)$
13	$f_1(13\text{-}14s)$	$f_1(13\text{-}12s)$

Table 2.2: Stator current frequency components due to a broken rotor bar.

2.4 The Effect of Inter-Bar Currents

The core of the rotor is constructed from a stack of pre-punched circular iron laminations which are separated by an insulating layer. As described in Chapter 1,

the squirrel cage is constructed by either driving copper bars through the laminations, or casting molten aluminium into the slots. There is no insulating material between the bars and the laminations in either case. This gives rise to a low contact resistance between bar and core, which is a function of temperature and current [51]. The low resistance will allow inter-bar currents to flow through the laminations [47]. If there is a broken rotor bar, these currents can become quite large, and the assumption that no current flows in a broken bar, is false.

Kerszenbaum and Landy [52] studied the existence of inter-bar currents in an induction motor with a damaged rotor. They developed an approximation for the current entering a bar from the opposite end to which it is broken. As a proportion of the normal, unbroken bar, current, it is:

$$\frac{I_{bb}}{I_N} \approx 1 - \frac{1}{\cosh \lambda l} \tag{2.22}$$

where:

$$\lambda = \sqrt{3\left|\frac{Z_b}{R_c}\right|} \tag{2.23}$$

and Z_b is the bar impedance ($R_b + jX_b$), R_c is the inter-bar resistance per unit core length, and l is the core length.

Thus the current in the broken bar is dependent on the slip because the bar leakage reactance, X_b, is dependent on the slip-frequency, sf_1, of the rotor current.

In their experimental work, Kerszenbaum and Landy measured rotor bar currents by placing Rogowski coils around the bars, close to the end rings. One of the bars was broken by detaching it from the end ring at one end. They found that the current entering the non-broken end of the bar was as large or larger than the normal bar current for most frequencies. They also found that the current in the adjacent bars at the broken end was up to twice the normal bar current, and that the results from Equation (2.22) were found to fit the measured data reasonably well, especially if the end-ring impedance was taken into account.

The inter-bar currents can cause burning of the rotor core laminations due to the heating caused by the contact resistance. This can provide a visual clue to the location of rotor bar damage, when the machine is disassembled, as it is often difficult to find cage faults due to the bars being located in closed slots.

Since inter-bar currents have the effect of increasing the current which flows in a broken bar, it would appear that the unbalance in the magnetic field would be lessened. Hence the amplitudes of fault frequencies in the stator current would also decrease. Walliser and Landy [53] examined the effect that inter-bar currents have on the detection of these fault frequencies.

Their experimental studies confirmed this theory. The amplitude of the lower twice slip-frequency sideband in the frequency spectrum of the stator current of their test motor, was found to be about 4dB less when the broken bar was not insulated from the laminations. They also discovered that there was not a significant change in the sideband amplitude between the non-broken bar cage and the uninsulated broken bar case. The sideband appearance for the non-broken cage was attributed to imbalances resulting from the construction of the test motor. The test motor was an inverted motor, that is, the rotor cage is stationary while the stator rotates inside it. These findings imply that inter-bar currents may make the detection of broken rotor bars (by stator current analysis), more problematic.

The effect of inter-bar currents will generally be ignored, except where stated, in this thesis.

2.5 Summary

This chapter has examined how the induction motor operates. Theoretical expressions for the magnetic field harmonics in the air gap of the machine are developed which account for the effects of slotting. The effect of a broken rotor bar on the magnetic field in the air gap is determined qualitatively and an expression for the fault frequency components, which appear in the stator current spectrum, developed. The main fault frequencies for broken rotor bar detection are

known as twice slip-frequency sidebands, as they result from the modulation of the supply frequency, $f_{bb} = f_1(1 \pm 2s)$.

The result of considering a slotted stator is that frequency components could appear in the stator current spectrum, with a principal frequency of $N_r\omega_r - \omega_1$.

Finally, the effect of inter-bar currents are discussed. It is shown that their presence will tend to lessen the effect that a broken bar will have on the production of distinct frequencies in the stator current.

CHAPTER 3

Signal Processing

3.1 Introduction

As described in Chapter 2, induction motor faults can cause various frequency components to appear in the stator current spectrum. There are several useful signal processing techniques that can be implemented in software to analyse sampled data records of the stator current waveform. The first, and most common method, is the Fourier transform, usually implemented as the Fast Fourier Transform (FFT) for sampled data. Less well known are the parametric methods of signal analysis [54] [55], such as Prony's method and Auto-Regressive Moving Average (ARMA) techniques. These methods use a mathematical model to approximate the signal, and the algorithm then finds values for the parameters of the model which give the best fit to the data. From the parameters, the frequency spectrum can be determined.

This chapter covers basic Fourier Transform theory and the use of window functions to reduce the effects of leakage. The effect of the different window

functions on a typical stator current spectrum are examined. The theoretical basis of Prony's method is described and the application of the technique to the detection of broken rotor bars in induction motors is explained.

3.2 The Fourier Transform

The Fourier Series represents a periodic signal as a sum of sinusoids. For a signal $x(t)$ which is a periodic time function, integrable over its period, then the Fourier Series is defined as [56]:

$$x(t) = \frac{a_0}{2} + \sum_{n=1}^{\infty}\left[a_n \cos\frac{2\pi nt}{T} + b_n \sin\frac{2\pi nt}{T}\right] \tag{3.1}$$

where T is the period of the signal and:

$$a_k = \frac{2}{T}\int_{-T/2}^{T/2} x(t)\cos\frac{2\pi kt}{T}\,dt \tag{3.2}$$

$$b_k = \frac{2}{T}\int_{-T/2}^{T/2} x(t)\sin\frac{2\pi kt}{T}\,dt \tag{3.3}$$

The series may be expressed in a complex exponential form as [57]:

$$x(t) = \sum_{k=-\infty}^{\infty} X(k)e^{j\frac{2\pi kt}{T}} \tag{3.4}$$

where

$$X(k) = \frac{1}{T}\int_{-T/2}^{T/2} x(t)e^{-j\frac{2\pi kt}{T}}\,dt \tag{3.5}$$

The Fourier Transform of $x(t)$ is defined as

$$X(f) = \int_{-\infty}^{\infty} x(t)e^{-j2\pi ft}\,dt \tag{3.6}$$

$X(f)$ is known as the spectrum of $x(t)$ and may be a real or complex valued function. The signal $x(t)$ may be recovered from its spectrum via the inverse Fourier transform:

$$x(t) = \int_{-\infty}^{\infty} X(f) e^{j2\pi ft} df \tag{3.7}$$

The symbol $\boldsymbol{F}$ is used to denote the Fourier transform Equation (3.6), that is $X(f) = \boldsymbol{F}\{x(t)\}$.

3.2.1 The Discrete Fourier Transform

When working with sampled data, the signal is only known for a finite set of discrete times. Thus a discrete version of Equation (3.6), known as the Discrete Fourier Transform (DFT), is required:

$$X(k) = \frac{1}{N} \sum_{n=0}^{N-1} x(n) e^{-j\frac{2\pi kn}{N}} \qquad k = 0,1,2,\ldots,N-1 \tag{3.8}$$

where N is the number of samples of $x(t)$.

The sampled data $x(n)$, which is the discrete-time version of $x(t)$, is transformed to give a discrete spectrum $X(k)$. The integer values, k, are known as frequency bin numbers.

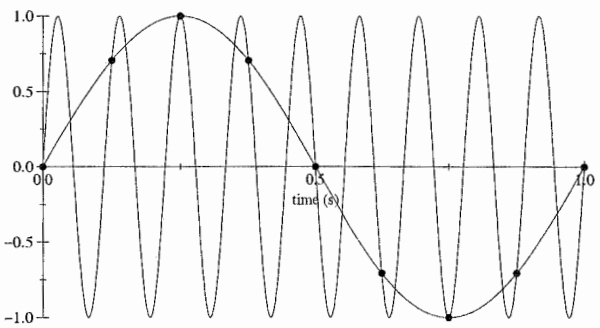

Figure 3.1: Aliasing of sampled waveforms.

If a signal is sampled at a frequency f_s Hz, where $f_s = 1/T$ and T is the sampling interval, then the signal has a spectrum that repeats at intervals of f_s. This is because a sinusoid with frequency f_0 Hz, sampled at f_s Hz has the same sampled waveform as a sinusoid with frequency (f_0+mf_s) Hz, sampled at f_s Hz where m is an integer. This gives rise to the phenomenon known as aliasing, which is illustrated in Figure 3.1. A 1 Hz sine wave and a 9 Hz sine wave are sampled at

0.125 second intervals. It can be seen that the sampled values obtained are the same for each wave, hence it is not possible to distinguish the frequency of the wave from the sampled values.

Shannon's theorem [58] states that aliasing only occurs when the sampling frequency is less than twice the highest frequency in the sampled signal. In sampled data systems the input signal must be filtered so that the input bandwidth is less than half the sampling frequency (the Nyquist frequency). Typically this is done by low-pass filtering the input signal before sampling. The cutoff frequency of this filter is usually made significantly less than half of the sampling frequency to allow sufficient margin for the filter response to roll off.

The DFT is actually periodic in N, since:

$$e^{\frac{-j2\pi n(k+mN)}{N}} = e^{\frac{-j2\pi kn}{N}} e^{-j2\pi mn} = e^{\frac{-j2\pi kn}{N}} \tag{3.9}$$

Thus, from Equation (3.9):

$$X(k+mN) = \frac{1}{N}\sum_{n=0}^{N-1} x(n) e^{\frac{-j2\pi(k+mN)n}{N}} = X(k) \tag{3.10}$$

In addition to this property, the inverse DFT:

$$x(n) = \sum_{k=0}^{N-1} X(k) e^{j\frac{2\pi kn}{N}} \tag{3.11}$$

implies that the input data sample is also periodic, with a period of N, that is:

$$x(n+mN) = \sum_{k=0}^{N-1} X(k) e^{j\frac{2\pi k(n+mN)}{N}} = x(n) \tag{3.12}$$

Hence when the DFT is applied to any sampled data, it is implicitly assumed that the data is repeated outside the sampled interval in a periodic fashion as illustrated in Figure 3.2. This is often referred to as the data being periodically extended, and can cause an apparent discontinuity in the signal.

If the input data are real, then the Fourier coefficients are symmetrical about $f_s/2$:

$$X(N-k)=\frac{1}{N}\sum_{n=0}^{N-1}x(n)e^{-j\frac{2\pi(N-k)n}{N}}=\left[\frac{1}{N}\sum_{n=0}^{N-1}x(n)e^{-j\frac{2\pi kn}{N}}\right]^{*}=X^{*}(k) \quad (3.13)$$

where * indicates the complex conjugate.

For real data $X(k) = X^*(N-k)$, so to examine the frequency spectrum of a signal we only need to look at the first $N/2$ Fourier coefficients. This gives the positive half of the spectrum from zero frequency up to the Nyquist frequency.

3.2.2 The Fast Fourier Transform (FFT)

The DFT may be calculated directly using Equation (3.8), but this is a process that takes a time proportional to the square of the number of points (N^2), hence the time taken to compute the transform can rapidly become intractable for large values of N. However an alternative exists, discovered by Cooley and Tukey [59], which computes the DFT in a time proportional to the logarithm of the number of points multiplied by the number of points ($N \log N$). This algorithm is known as the Fast Fourier Transform (FFT) and has become a commonly used engineering tool with the advent of the digital computer. The general algorithm has been described by many authors [59-64].

One limitation of the FFT algorithm is that it requires the number of input data samples to be a power of two. In general it requires a special effort to ensure that the number of data points sampled is a power of two. If it is not convenient to sample a number of points which is a power of two, there are more complicated algorithms, known as Prime Factor Algorithms (PFA) [65], which can still calculate the Fourier transform quickly. These methods can compute the DFT efficiently when the prime factors of the number of input samples are small in magnitude. However, as the prime factors of N grow larger, these algorithms reduce to the direct implementation of the DFT, Equation (3.8). Practically, these algorithms are useful only when all prime factors of the number of samples are less than about 30, although this depends on the speed of the computer which is performing the computation, and upon the requirements of the application. In general, it is easier to sample a number of points which is a power of two.

3.3 Windowing and Window Functions

Since the Fourier Transform assumes that the input data is periodic, Equation (3.12), there can appear to be a jump discontinuity in the periodic extension of the input signal if it is not sampled such that a whole number of cycles are captured, that is, if it is not synchronously sampled. This is illustrated in Figure 3.2. Figure 3.2(a) shows the original time-domain signal (5Hz sine wave), 3.2(b) illustrates synchronous sampling, while 3.2(c) shows the effects of asynchronous sampling and the jump discontinuities which result.

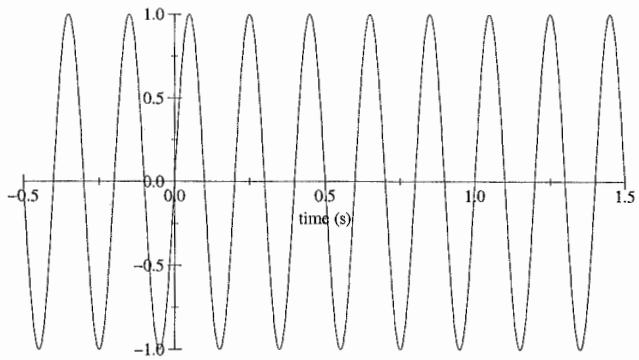

Figure 3.2(a): Original time signal.

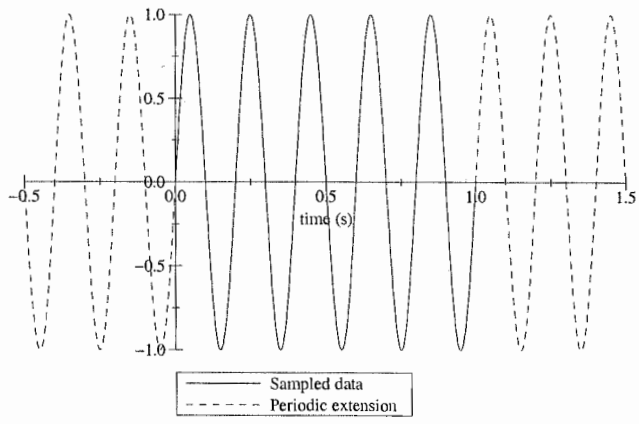

Figure 3.2(b): Synchronously sampled signal.

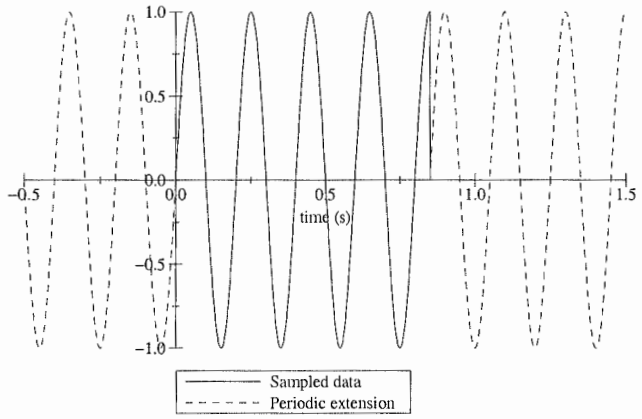

Figure 3.2(c): Asynchronously sampled signal.

The frequency spectra of the signals in Figure 2 are shown below:

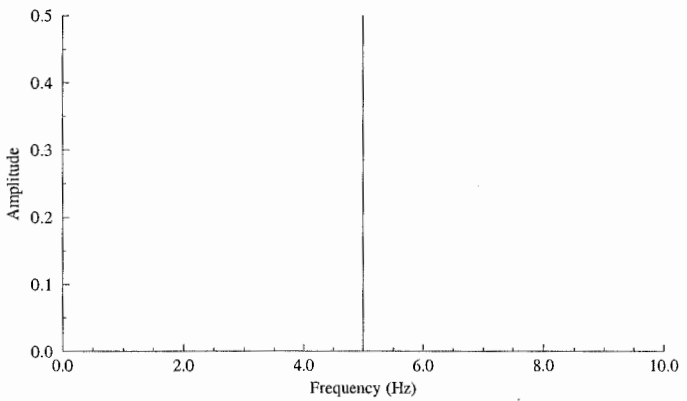

Figure 3.3(a): Frequency spectrum of Figure 3.2(a).

It can be seen that the discontinuity in the asynchronous sampling of Figure 3.2(c) causes spreading of the peak in the frequency domain in Figure 3.3(c). This is known as leakage. The DFT maps the continuous frequency spectrum onto a discrete set of basis functions, which are the complex exponentials of Equation (3.8). Only frequencies which map exactly onto one of the basis functions will be represented by a single component in the frequency spectrum, as shown in Figure 3.3(b). Frequencies which do not map exactly will map onto all of the basis functions, causing the leakage observed in Figure 3.3(c).

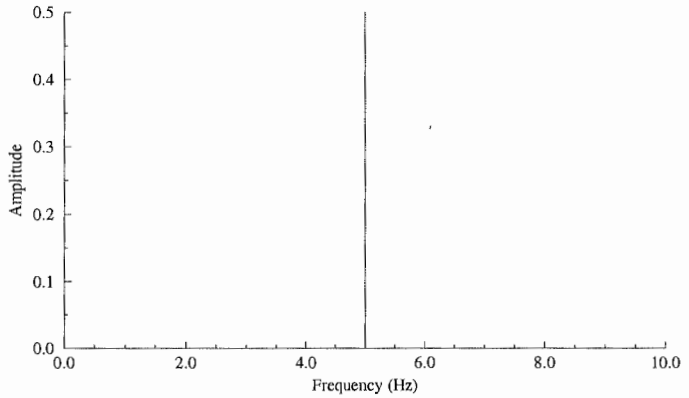

Figure 3.3(b): Frequency spectrum of Figure 3.2(b).

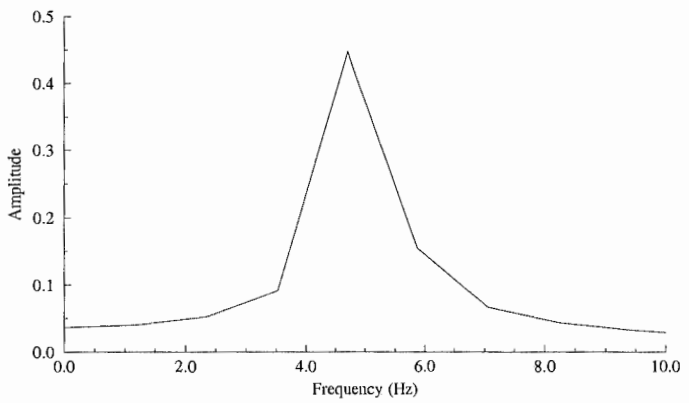

Figure 3.3(c): Frequency spectrum of Figure 3.2(c).

The effects of leakage can be reduced by windowing, which is also known as weighting [66]. The process of weighting data consists of multiplying it by a window function which is chosen so that it reduces the discontinuities at the ends of the sampled data. Usually this is achieved by a window function which smoothly brings the data to zero at the boundaries, as illustrated in Figure 3.4. The windowing process can also be viewed in the frequency domain. The frequency domain window function is designed so that when it is multiplied by the set of basis functions, the effect of a frequency component is limited to the basis functions closest to that frequency. The windowing process is sometimes referred to as weighting in the time domain and windowing in the frequency domain.

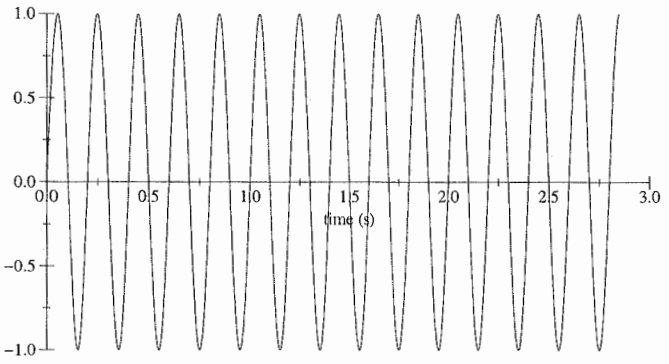

Figure 3.4(a): Sampled data.

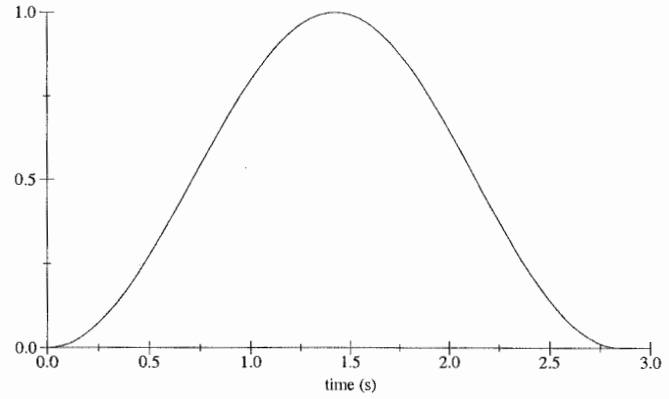

Figure 3.4(b): Window function (Hanning window).

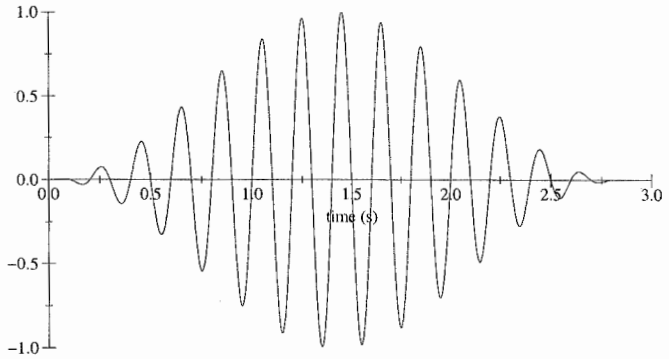

Figure 3.4(c): Windowed data.

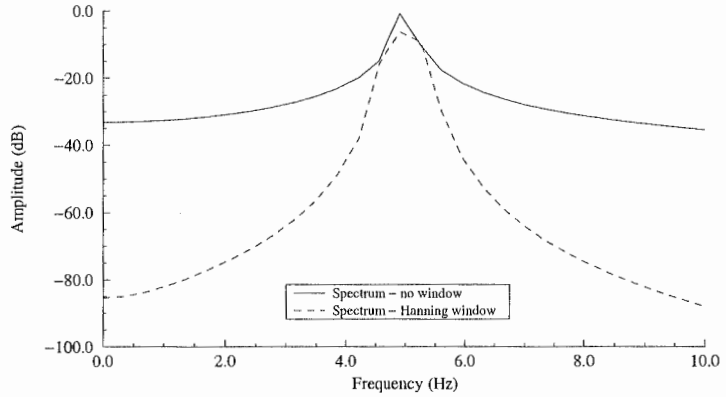

Figure 3.4(d): Frequency spectrum of windowed and non-windowed data.

3.3.1 Figures of Merit for Window Functions

Harris [66] describes several figures of merit by which the performance of window functions may be judged. He calculates these figures for many different windows. The minimum resolution bandwidth of a window is the minimum spacing between two frequency components of equal amplitude, if they are to be resolved. This is given as a number of bins, where a bin is the fundamental frequency resolution f_s/N. For one frequency component to have the minimum effect on another due to leakage, it is best if the rate at which sidelobes decrease is as large as possible. This is usually quoted in dB/octave. For detecting small amplitude frequency components in the presence of those of larger amplitude, it is important that the sidelobes adjacent to the mainlobe be as low as possible.

Since a window reduces the amplitude of the data at either end of the sampled data record, it appears to the DFT that the signal changes in amplitude. The effect that this has on the amplitudes of the components of the frequency spectrum is known as processing loss [66]. If a frequency component lies half-way between two DFT frequency bins, then the power will be spread equally between the two bins, neither of which will have an amplitude as great as the single component alone would have. This is known as scalloping loss [66]. Processing loss and scalloping loss can be combined to give the worst case processing loss for a particular window. Harris [66] noted that this was always between 3.0dB and 4.3dB for the

windows which he examined. This means that a frequency component of a signal may have its amplitude reduced by an amount up to the worst case processing loss, when the DFT is calculated, depending on where it lies with respect to the frequency bins. Hence, several different records of the same signal may exhibit different spectra, due to slight changes in the frequency sampled, and the sampling process itself. This is explored further in Section 3.3.4.

3.3.2 Window Functions

There are many useful window functions available. Harris [66] and Nuttall [67] provide a good overview and evaluation of the performance of each window according to certain metrics. There are a few of particular relevance to this thesis, namely the rectangular, Hanning, Hamming, and Blackman windows. The following sections detail the time and frequency responses of these windows, and shows the results of applying the windows to a typical stator current spectrum.

3.3.2.1 Rectangle Window

The rectangle window has a value of one over the observation interval and zero elsewhere. It is automatically applied by the process of sampling a signal. It is defined as:

$$w(n) = 1 \qquad n = 0,1,2,\ldots,N-1 \tag{3.14}$$

The normalised frequency spectrum for the rectangle window is:

$$D(\theta) = \exp\left(-j\frac{N-1}{2}\theta\right)\frac{\sin\left(\frac{N\theta}{2}\right)}{\sin\left(\frac{\theta}{2}\right)} \tag{3.15}$$

This function is known as the Dirichlet kernel [66]. This has a first sidelobe level of about -13dB and the sidelobes fall off at a rate of 6dB per octave. The 6dB bandwidth is 1.21 bins, which is the minimum possible for any window, and the worst case processing loss is 3.92dB.

The frequency response of the rectangle window is shown in the following diagrams where $N = 40$:

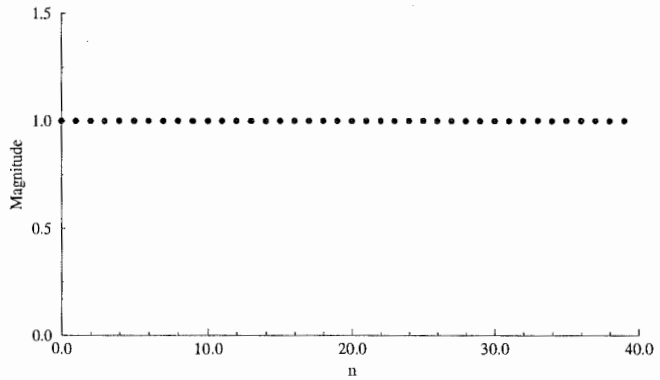

Figure 3.5(a): Rectangle window.

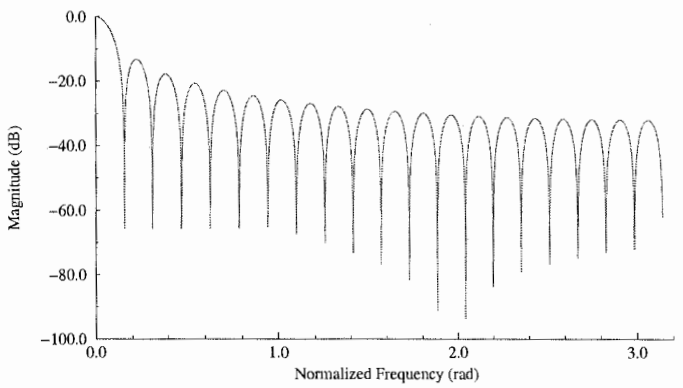

Figure 3.5(b): Normalised frequency response of rectangle window.

3.3.2.2 Hanning Window

The Hanning window belongs to a general class of window functions of the form $\cos^{\alpha}$. The special case of the Hanning window has $\alpha = 2$:

$$w(n) = \cos^2 n\pi/N = 0.5\left[1 - \cos(2n\pi/N)\right] \tag{3.16}$$

The normalised frequency spectrum of is:

$$W(\theta) = 0.5D(\theta) + 0.25\left[D(\theta - 2\pi/N) + D(\theta - 2\pi/N)\right] \tag{3.17}$$

where $D(\theta)$ is defined by Equation (3.15). That is, the frequency response is the sum of three Dirichlet kernels. The highest sidelobe level is -32dB and the 6dB bandwidth is 2.00 bins. Sidelobes fall off at 18dB/octave, and the worst case processing loss is 3.18dB.

The window and normalised frequency spectrum are as follows for $N = 40$:

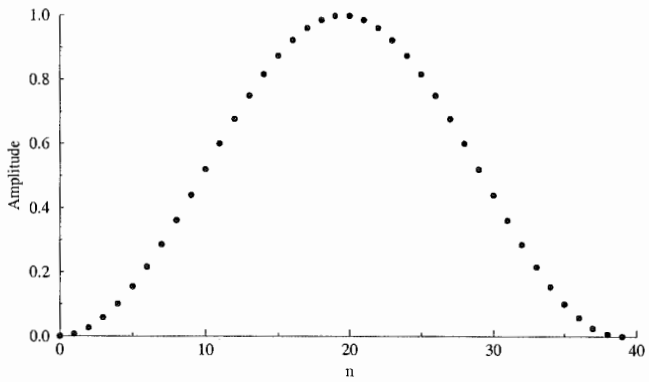

Figure 3.6(a): Hanning window.

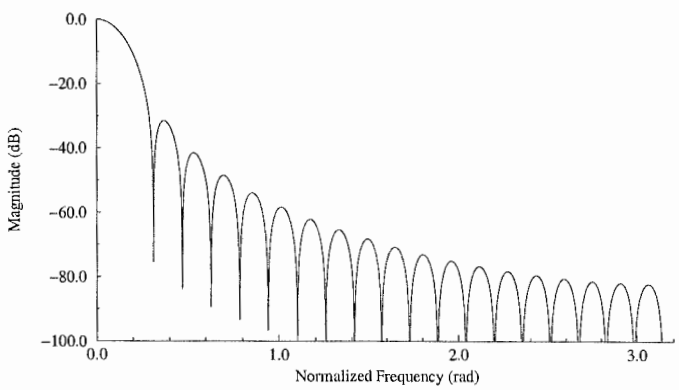

Figure 3.6(b): Normalised frequency response of Hanning window.

3.3.2.3 Hamming Window

The Hamming window is constructed by modifying the form of the Hanning window resulting in:

$$w(n) = 0.54 - 0.46\cos(2\pi n/N) \qquad n = 0,1,2,\ldots,N-1. \qquad (3.18)$$

The normalised frequency spectrum of Equation (3.18) is:

$$W(\theta) = 0.54D(\theta) + 0.23\left[D(\theta - 2\pi/N) + D(\theta + 2\pi/N)\right] \tag{3.19}$$

where $D(\theta)$ is defined by Equation (3.15).

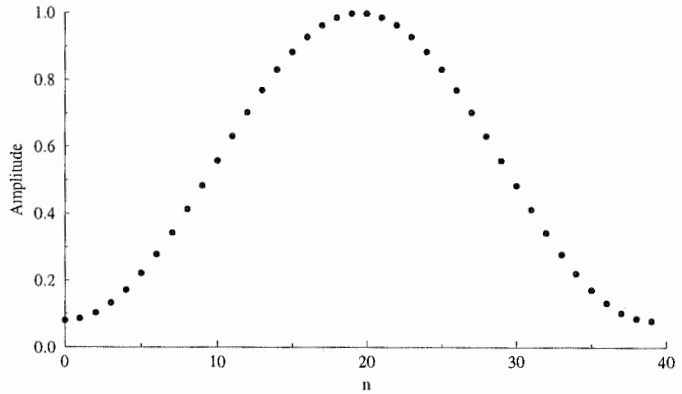

Figure 3.7(a): Hamming window.

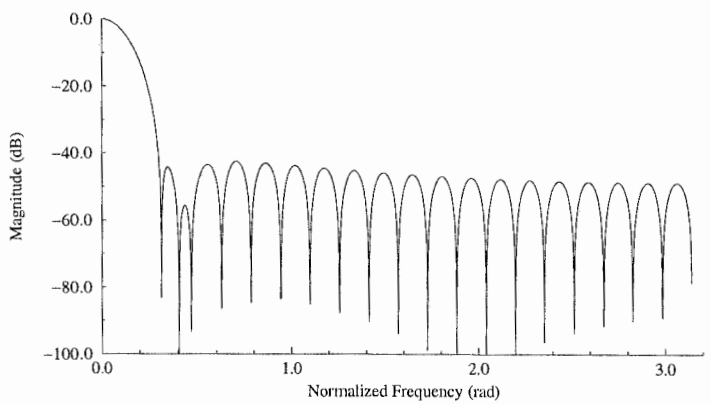

Figure 3.7(b): Normalised frequency response of the Hamming window.

This choice approximately cancels the first sidelobe of the Hanning response, giving high attenuation around the main lobe, with a highest sidelobe level of -43dB. However the discontinuity at the boundaries causes the remaining sidelobes to fall of at only 6dB per octave, which is much slower than the Hanning window. The 6dB bandwidth is 1.81 bins, and the worst case processing loss 3.10dB.

3.3.2.4 Blackman Window

The Blackman window is similar to the Hamming window in that it is also a constructed window. It is a member of the more general class of windows of the form:

$$w(n) = \sum_{m=0}^{N/2} (-1)^m a_m \cos(2\pi mn/N) \qquad n = 0,1,2,\ldots,N-1 \qquad (3.20)$$

where $\sum_{m=0}^{N/2} a_m = 1$.

This general form also includes the Hanning and Hamming windows where only a_0 and a_1 are non-zero in Equation (3.20). The Blackman window is generated using $a_0 = 0.42$, $a_1 = 0.50$, $a_2 = 0.08$, giving:

$$w(n) = 0.42 - 0.50\cos(2\pi n/N) + 0.08\cos(4\pi n/N) \qquad n = 0,1,2,\ldots,N-1 \quad (3.21)$$

The normalised frequency spectrum is then:

$$\begin{aligned} W(\theta) = {} & 0.42D(\theta) - 0.25\left[D\left(\theta - \frac{2\pi}{N}\right) + D\left(\theta + \frac{2\pi}{N}\right)\right] \\ & + 0.04\left[D\left(\theta - \frac{4\pi}{N}\right) + D\left(\theta + \frac{4\pi}{N}\right)\right] \end{aligned} \qquad (3.22)$$

The window and spectrum are shown in Figure 3.8.

This construction cancels the third and the fourth sidelobes of the Dirichlet kernel, whilst eliminating boundary discontinuities, giving sidelobes which fall off at a rate of 18dB per octave. The first sidelobe level is -53dB and the 6dB bandwidth is 2.13 bins, the worst case processing loss is 3.47dB. This makes it particularly suitable for detecting low magnitude frequency components in the presence of larger components.

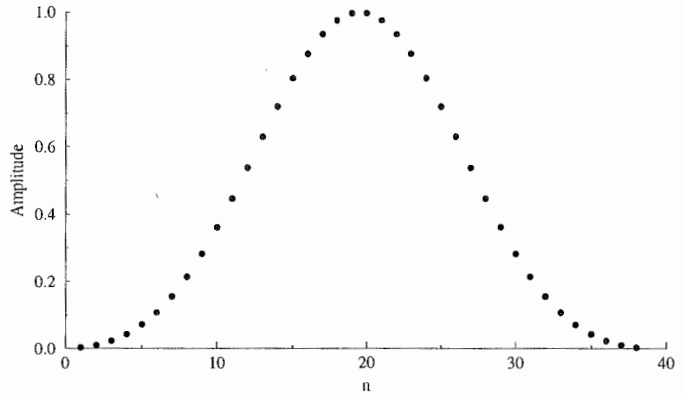

Figure 3.8(a): Blackman window.

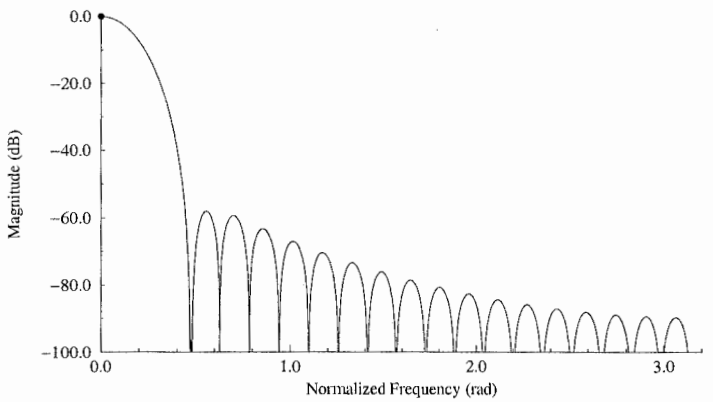

Figure 3.8(b): Normalised frequency spectrum of the Blackman window.

3.3.3 Effect of Window Functions on a Typical Stator Current Spectrum

In order to demonstrate the effect that each of the above window functions has on a typical stator current spectrum, each of one of them is applied in turn to the same data set. The motor used was the Pope motor (Appendix A) with a broken rotor bar. It was supplied from the mains and the speed was measured with an optical tachometer as 1464 rpm. Hence the twice slip-frequency sidebands should appear at (50±2.4)Hz. Data was sampled at a rate of 10kHz, and 32768 data points were collected, giving a basic frequency resolution (see Section 3.4.1) of 0.3052Hz. The results are shown in Figure 3.9.

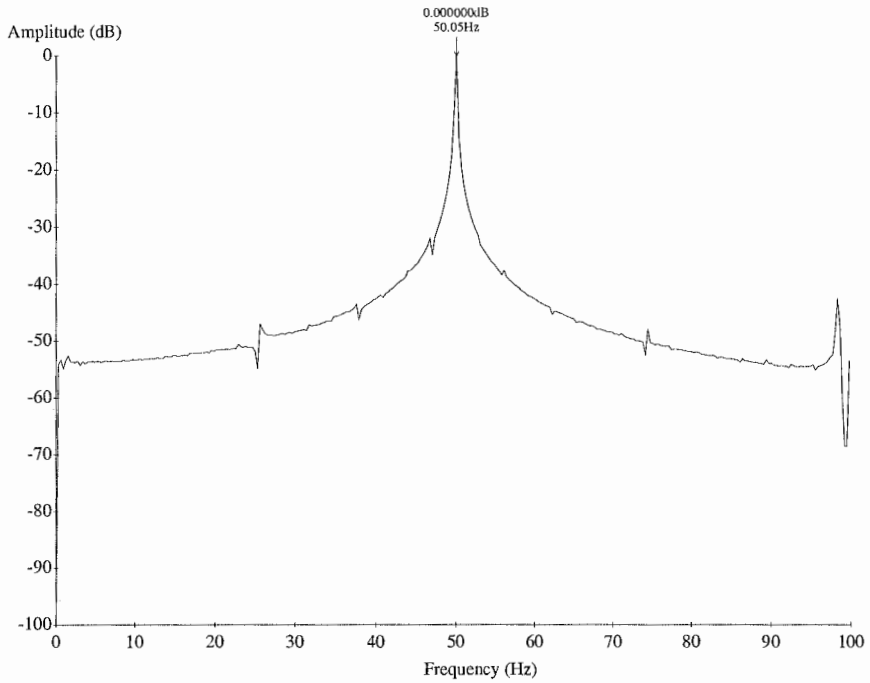

Figure 3.9(a): Stator current frequency spectrum - rectangle window.

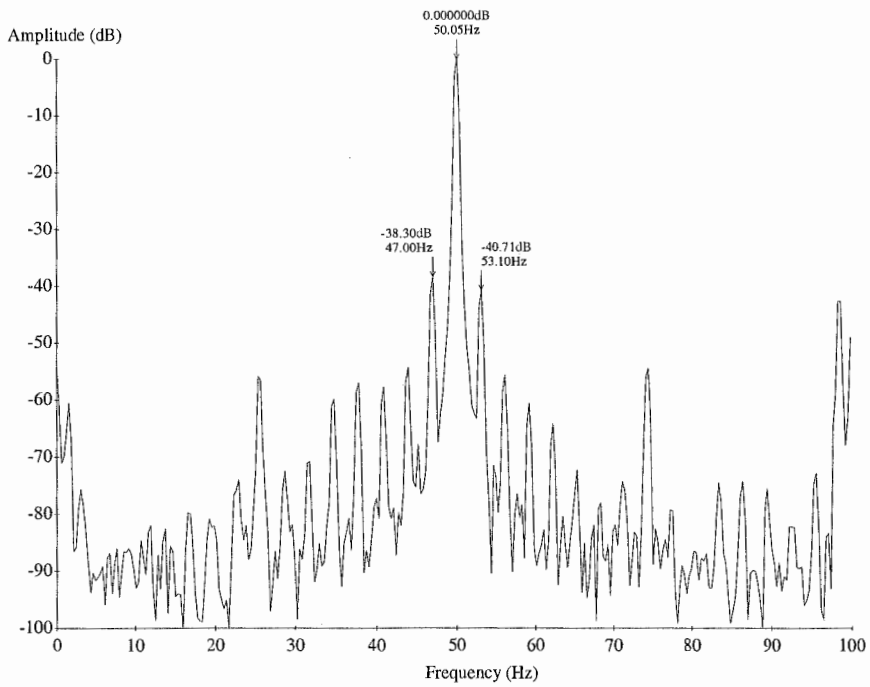

Figure 3.9(b): Stator current frequency spectrum - Hanning window.

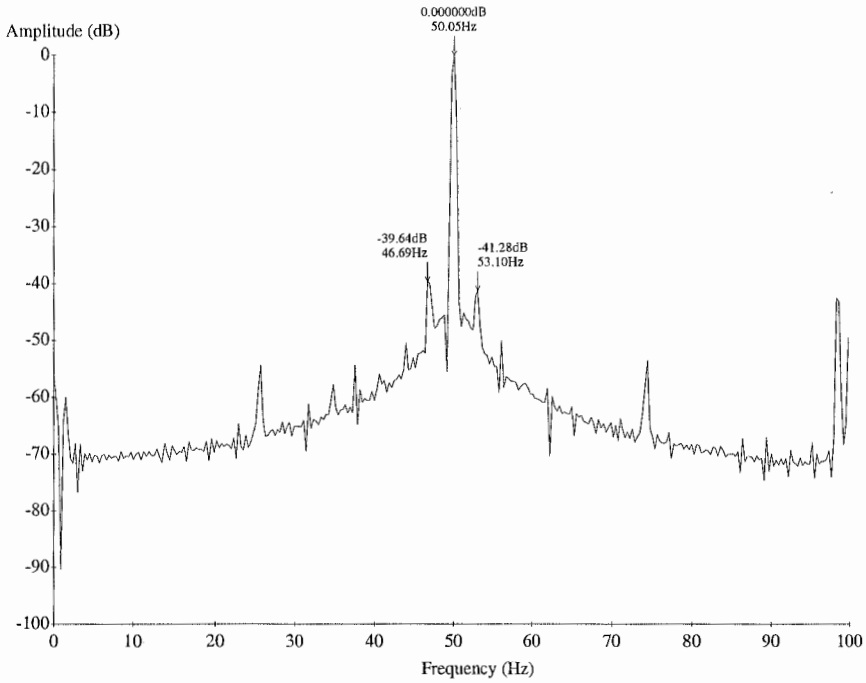

Figure 3.9(c): Stator current frequency spectrum - Hamming window.

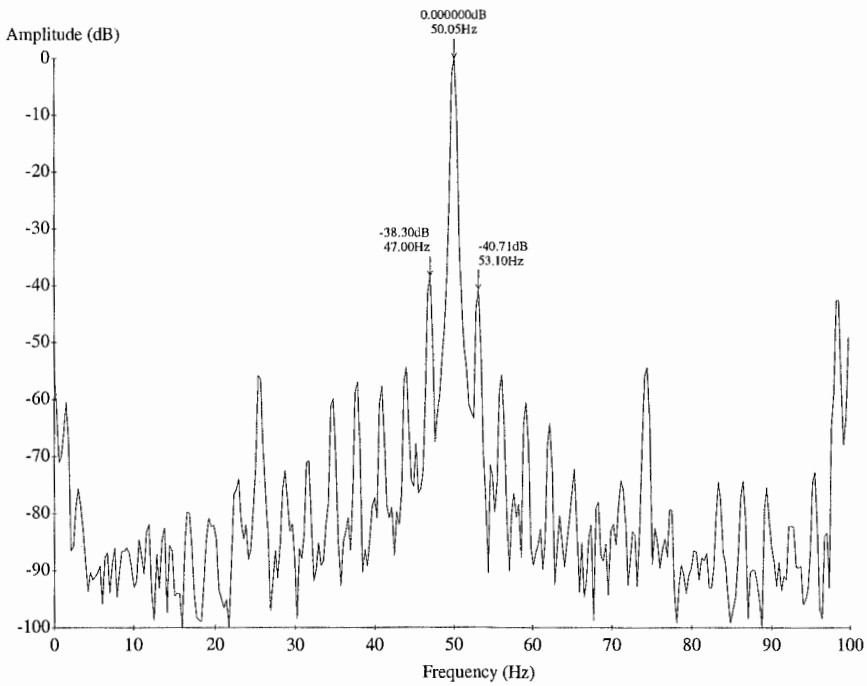

Figure 3.9(d): Stator current frequency spectrum - Blackman window.

The difference in the rate at which the sidelobes fall off for different windows is evident when Figures 3.9(a) and (c) are compared with 3.9(b) and (d). The former have sidelobes which fall off at 6.0dB/octave, whilst the latter fall off at 18.0dB/octave. It is also interesting to note the difference in the amplitudes of the twice slip-frequency sidebands caused by the window functions. The sidebands cannot even be seen when the rectangle window is used, which shows how useful the window functions are.

3.3.4 Statistical Analysis of Variation in Sideband Amplitudes

In order to determine the variation in amplitude which could be encountered in a practical application of the sampling process, an experiment was performed. The Pope motor (see Appendix A), with a broken rotor, was supplied from the mains and loaded to rated load by a DC generator and resistor bank. After waiting a while for the system to reach a steady state, one hundred records of the stator current waveform were consecutively sampled. The signal was sampled at a rate of 3.2kHz with an 800Hz low-pass filter for anti-aliasing. 32 768 data points were sampled for each record and the FFT, with a Blackman window, used to compute the spectrum. The amplitudes of the twice slip-frequency sidebands were then extracted and the following statistics computed:

Statistic	Lower Sideband	Upper sideband
Mean Amplitude (dB)	-36.05	-35.79
Standard Deviation	1.11	1.12
Range (dB)	5.13	5.65

Table 3.1: Statistics for sampling under constant conditions.

It can be seen that, even though the load and input voltages were not changed, there was some variation in the amplitudes of the sidebands. The standard deviation was about 1.1 for both sidebands whilst the range of values was about

5dB. That is, there was a 5dB variation between the maximum and minimum values of the sidebands. Figure 3.10 plots the variation in sideband amplitude with the data record number. This is effectively a plot against time as the current was sampled at approximately regular intervals. The total time taken to collect all of the data records was about 30 minutes. From the graph it would appear that the amplitude fluctuations are random over this time, with no trend being apparent. This would indicate that the machine system had reached a steady-state before sampling was begun.

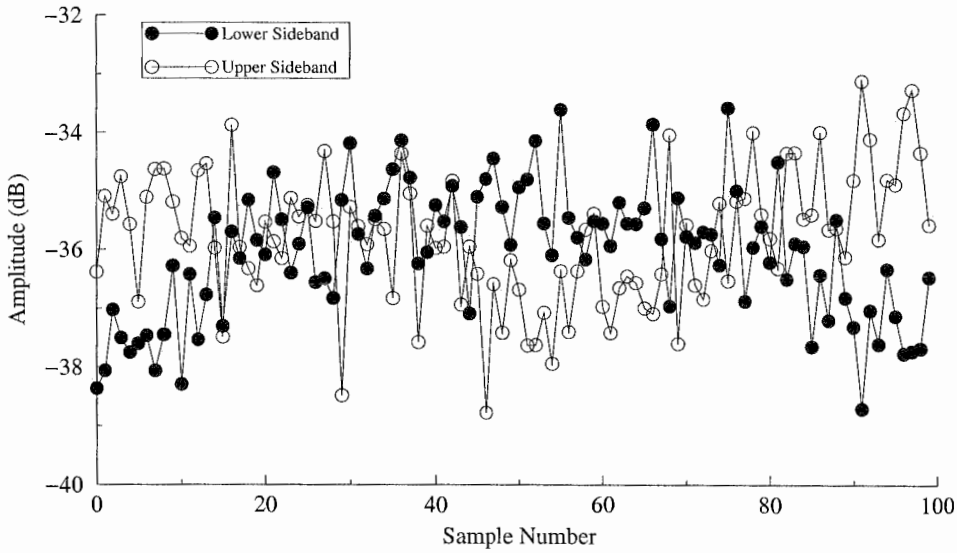

Figure 3.10: Variation in sideband amplitude with data record number.

3.4 Parametric Models for Spectral Estimation

The Fourier transform uses a fixed set of basis functions as a model for the signal being analysed. The functions are a discrete set of sinusoids as given in Equation (3.8), the frequency of which are fixed by the sampling frequency, and the number of data points. Parametric methods also assume that the time domain signal can be described by a mathematical model, but not necessarily a sum of sinusoids. The parameters of that model are then calculated using the sampled data, from which the frequency spectrum of the signal may be obtained.

Parametric models can produce better spectral estimates than Fourier transform methods, particularly with regard to spectral resolution, because the basis functions of the model are not restricted in the way that those of the Fourier transform are. The Fourier methods assume that the signal outside the sampling interval window is zero, that is, it is implicitly windowed by a rectangular window function. This is not a realistic assumption. By constructing a time-domain model we can make a more realistic estimate of the signal outside the window. Thus the need for window functions, and the adverse effects they can have on the spectral estimate, is eliminated. However, improvement in the estimation of the spectrum is highly dependent upon how well the model approximates the signal in question.

The assumption that the signal is stationary is particularly troublesome when dealing with variable speed drives, since the speed control is achieved by varying the fundamental frequency. If this happens whilst sampling data, then a Fourier transform of the data will not generally yield useful results. Since a parametric model requires far less data to produce a spectral estimate, the data is sampled for a much shorter time, reducing the likelihood of the frequency changing during sampling.

The particular parametric technique examined here is Prony's method, as it offers better results than other techniques.

3.4.1 Frequency Resolution of Spectrum Estimates

The basic resolution of the DFT is f_s/N, that is, it is governed by the sampling rate and the number of points sampled. To increase the resolution, either the number of points sampled must be increased, or the sampling frequency decreased. The highest frequency in the resulting spectrum is $f_s/2$, so the sampling frequency cannot be reduced indefinitely, especially when it is considered that an anti-aliasing filter limits the highest frequency to be less than this. Increasing the number of points sampled causes the sampling time to increase as well. This implies that the signal sampled must remain stationary for longer, which can be a problem with industrial drives. As a guide, if the sampling frequency is 5kHz, and the anti-aliasing filter cutoff is 2kHz, 16 384 points sampled gives a basic

frequency resolution, f_s/N, of only 0.3052Hz. If the twice slip-frequency sidebands are at ±1Hz, then there are only three bins separating them from the supply frequency peak. The total sampling time to collect the data, is 3.2768 seconds.

Parametric methods only require a few data samples in order to form a spectral estimate. If the model has n parameters, then only n points are required in order to solve for those parameters. Generally, parametric methods use a system of over-determined equations so that a least-squares fit may be performed to determine the parameters, which lessens the effect of any noise. In this case a number of points required is greater than n. For example, a model consisting of 20 sinusoids, would have 60 parameters, amplitude, frequency and phase of each sinusoid, and the number of samples required to solve for these parameters would be greater then 60, dependent on the algorithm used. Hence the signal is required to be stationary for a much shorter time than a Fourier spectrum of equivalent resolution.

3.4.2 Prony's Method

Prony's method is not a spectral estimation technique in the usual sense, rather it is a way of modelling data by fitting damped exponential functions. However it can be extended to provide a spectral estimate.

In 1795 Gaspard Riche, Baron de Prony [54] [55], proposed that the laws governing the expansion of gases could be modelled by the sum of damped exponentials. His original model had two parameters for each exponential function, A_n and α_n. Hence for a model of order p, $2p$ data points are required in order to solve the set of simultaneous equations. If x_i is the datum recorded at time t_i, then the set of equations that must be solved is given by:

$$x_i = \sum_{n=1}^{p} A_n \exp(\alpha_n t_i) \tag{3.23}$$

for $1 \leq i \leq 2p$.

Fitting a set of parameters by exactly the same number of equations always yields an exact solution. However, the process is sensitive to noise which can lead to parameters which are wildly inaccurate when used to model the system. This problem is usually overcome by using an over-determined set of equations, that is, where the number of data samples is larger than the number of parameters to be calculated. This has the effect of averaging out the effect of any noise, and thus provides a more robust estimate of the parameters.

From a signal processing point of view, complex exponential functions are more useful than real exponential functions. This leads to the development of the extended Prony method [54] [55] which models a set of N data points, x_i, by the sum of p damped complex exponentials with arbitrary frequency f_m, phase θ_m, amplitude A_m, and damping factor α_m. The model produces approximations to the data, $\hat{x}_i$, given by:

$$\hat{x}_n = \sum_{m=1}^{p} b_m z_m^{n-1}, \qquad \text{for } n = 0,\ldots,N-1 \tag{3.24}$$

where b_m and z_m may be complex and

$$\begin{aligned} b_m &= A_m \exp(j\theta_m) \\ z_m &= \exp[(\alpha_m + j2\pi f_m)\Delta t] \end{aligned} \tag{3.25}$$

and Δt is the sample interval.

Where a real data sequence may be modelled by p real, undamped ($\alpha_m = 0$) sinusoids, a special case of Equation (3.24) may be developed. The model may be refined to

$$\hat{x}_n = \sum_{m=1}^{p}\left[b_m z_m^{n-1} + b_m^*\left(z_m^*\right)^{n-1}\right] = \sum_{m=1}^{p} 2A_m \cos\left(2\pi f_m (n-1)\Delta t + \theta_m\right) \tag{3.26}$$

where $b_m = A_m \exp(j\theta_m)$ and $z_m = \exp(j2\pi f_m \Delta t)$. Note that the z_m are roots of unit modulus with arbitrary frequencies and occur in complex conjugate pairs as long as $f_m \neq 0$ or $1/2\Delta t$.

Finding the set of A_m, θ_m, f_m, and p that minimise:

$$\varepsilon = \sum_{n=0}^{N-1} \left| x_n - \hat{x}_n \right|^2 \tag{3.27}$$

is a difficult non-linear problem, which may be solved iteratively. Another method is Prony's technique, which solves two sets of linear equations leaving the non linearity in a polynomial rooting procedure.

In order to do this one must solve for the roots, which are the z_m above, of the polynomial:

$$\Psi(z) = \prod_{i=1}^{2p} (z - z_i) = \sum_{k=0}^{2p} a_k z^{2p-k} = 0 \tag{3.28}$$

with $a_0 = 1$ and the a_i being real coefficients. It is obvious that coefficient a_{2p} is given by:

$$a_{2p} = \prod_{i=1}^{2p} z_i \,. \tag{3.29}$$

Due to each z_i having unit modulus, $z_k^{-1} = z_k^*$, and $\left| a_{2p} \right| = 1$, it can be shown that the polynomial below has the same roots as (3.28)

$$a_{2p} z^{2p} \Psi^*(z) = \sum_{k=0}^{2p} a_{2p} a_{2p-k}^* z^{2p-k} \tag{3.30}$$

Since the roots are of unit modulus and occur in complex conjugate pairs, then we must have $a_k = a_{2p} a_{2p-k}^*$ for $k = 0,\ldots,2p$. A linear difference equation with (3.28) as its solution may be written [54]:

$$a_p x_{n-p} + \sum_{k=1}^{p} \left(a_{p-k} x_{n-p+k} + a_{p+k} x_{n-p-k} \right) = 0 \qquad \text{for} \quad 2p+1 \le n \le N \,. \tag{3.31}$$

This equation may be divided through by a_p to provide a more convenient form:

$$x_{n-p} + \sum_{k=1}^{p} \left(g_k x_{n-p+k} + g_k^* x_{n-p-k} \right) = 0 \tag{3.32}$$

where $g_k = a_{p-k}/a_p$. From this equation the conjugate linear smoothing error can be defined as:

$$e_n^s = x_n + \sum_{k=1}^{p}\left(g_k x_{n+k} + g_k^* x_{n-k}\right) \text{ for } p+1 \le n \le N-p \tag{3.33}$$

which minimises the squared smoothing error:

$$\rho^s = \sum_{n=p+1}^{M-p}\left|e_n^s\right|^2 \tag{3.34}$$

Setting the partial derivatives of ρ^s with respect to g_1 through to g_p to zero gives the following equations expressed in matrix form.

$$\mathbf{R}_{2p}\mathbf{g}_{2p} = \begin{bmatrix} \mathbf{0}_p \\ 2\rho^s \\ \mathbf{0}_p \end{bmatrix} \tag{3.35}$$

where

$$\mathbf{R}_{2p} = \begin{bmatrix} r_{0,0} & \cdots & r_{0,2p} \\ \vdots & & \vdots \\ r_{2p,0} & \cdots & r_{2p,2p} \end{bmatrix}, \quad \mathbf{g}_{2p} = \begin{bmatrix} g_p \\ \vdots \\ g_1 \\ 1 \\ g_1^* \\ \vdots \\ g_p^* \end{bmatrix} \quad \text{and} \; r_{j,k} = \sum_{n=2p+1}^{N}\left(x_{n-j}^* x_{n-k} + x_{n-p+j} x_{n-p+k}^*\right).$$

Solving this set of equations gives the set of polynomial coefficients a_k, which satisfy the least squares criteria. Once these have been determined, the roots of the polynomial (3.28) may be found using a polynomial rooting procedure. Once the roots have been found, the problem becomes linear in the remaining parameters, $b_1,\ldots,b_p$. The set of linear equations which must be solved using a least squares procedure is:

$$\mathbf{Z}^H\mathbf{Z}\,\mathbf{b} = \mathbf{Z}^H\mathbf{x} \tag{3.36}$$

where

$$\mathbf{Z}=\begin{bmatrix} 1 & 1 & \cdots & 1 \\ z_1 & z_2 & \cdots & z_p \\ \vdots & \vdots & & \vdots \\ z_1^{N-1} & z_2^{N-1} & \cdots & z_p^{N-1} \end{bmatrix}, \quad \mathbf{b}=\begin{bmatrix} b_1 \\ b_2 \\ \vdots \\ b_p \end{bmatrix}, \quad \mathbf{x}=\begin{bmatrix} x_1 \\ x_2 \\ \vdots \\ x_N \end{bmatrix}. \tag{3.37}$$

$\mathbf{Z}^H\mathbf{Z}$ may be shown to be Hermitian, so a Cholesky decomposition procedure may be used to solve Equation (3.36). Once this has been done all of the b_i and z_i have been determined and it is a simple matter to calculate A_i, θ_i, f_i:

$$\begin{aligned} A_i &= |b_i| \\ \theta_i &= \tan^{-1}\left[\mathrm{Im}(b_i)/\mathrm{Re}(b_i)\right] \\ f_i &= \frac{\tan^{-1}\left[\mathrm{Im}(z_i)/\mathrm{Re}(z_i)\right]}{2\pi\Delta t}. \end{aligned} \tag{3.38}$$

3.4.3 Results

A modified Prony's method, for real undamped sinusoids, was implemented using the technique of Marple [54], and used to model the stator current waveform of an induction motor with a broken rotor bar. The motor was somewhat over-loaded, using a DC machine, with a slip of about 0.12. This results in the twice slip-frequency sidebands appearing at about 38Hz and 62Hz.

Table 3.2 shows the frequencies and amplitudes calculated using Prony's method compared to the corresponding values found using the FFT. Only the major frequency components have been included. After examining the frequency spectrum calculated using the FFT, the order for Prony's method was selected to be 20 as there were about this number of large peaks in the FFT spectrum. This means that the algorithm will attempt to fit the stator current waveform data using 20 sinusoidal components. Model order selection is a very difficult problem and is the Achilles heel of parametric modelling techniques [54] [58]. There has been much research performed on the selection of the model order [58], and various techniques have been developed. In this case the model order was selected by trial and error, in order to give the best results. If an automatic condition monitoring system were to be designed, model order selection techniques would have to be examined more closely.

The same set of sampled stator current data was used for both sets of results. The stator current was sampled at 3200 Hz, to gather 32 768 samples. The FFT used all of these data points to obtain a reasonable frequency resolution, whilst the Prony results were generated using only 200 sample points. It can be seen that the Prony method generates comparable results to the FFT method while using two orders of magnitude less data points.

Prony Frequency (Hz)	FFT Frequency (Hz)	Prony Amplitude (dB)	FFT Amplitude (dB)
49.98	50.03	0.00	0.00
38.36	38.01	-22.47	-20.20
13.22	13.88	-20.43	-35.21
63.31	62.05	-38.81	-40.29
76.15	74.07	-39.12	-48.30
85.42	86.19	-35.75	-49.57
97.60	98.21	-38.70	-51.36
149.81	150.09	-34.57	-34.73
250.84	250.16	-34.61	-31.93
211.93	214.00	-37.62	-39.01
314.55	314.06	-36.17	-37.79
351.12	350.22	-42.71	-40.31

Table 3.2: Comparison of Prony analysis and FFT results

Prony's method makes the problem of peak detection much easier than with the FFT. Any leakage in the spectrum causes a single frequency component to be spread over a number of frequency bins, making detection of the single frequency component much more difficult. Since Prony's method models the signal by single frequency components, no such difficulties are encountered.

Unfortunately Prony's method is not all that useful, when applied in the manner above, as it is not all that good at modelling signals where there are two frequency components close together, but with a large difference in amplitude. In this case the smaller signal tends to be overlooked. This is why such a large slip value was used in the experimental work, as it was found that if the slip was much smaller then the sidebands became undetectable. An attempt was made to remove the mains frequency using a highly tuned notch filter, unfortunately it was not possible to make the notch selective enough so that it did not affect the sidebands of interest.

3.5 Summary

Chapter 2 showed that faults in induction motors could be detected by examining the frequency spectrum of the stator current waveform. This chapter has examined the theoretical basis of the signal processing techniques used in order to calculate the frequency spectrum. The Fourier transform is the basic tool for calculating frequency spectra, and it is often misunderstood and misused. The consequences of aliasing and the implicit periodicity of the Discrete Fourier Transform were examined. The use of window functions for reducing the effects of leakage due to the periodic nature of the DFT was also examined. Various common window functions and their properties were discussed and their effect on frequency spectra calculated was illustrated using a typical stator current spectrum.

Since the twice slip-frequency sidebands are so important for the detection of rotor damage, a statistical analysis of the variation in sideband amplitude due to slight variations in sampling and motor operation, was performed. One hundred records of the stator current were sampled with the motor and load operating in a steady state. The sideband amplitudes were calculated and their variation analysed and plotted. It was found that the standard deviation was about 1dB for an average value of about -36dB, whilst the amplitudes had a range of about 5dB. Thus for any particular frequency spectrum there may be an uncertainty in the sideband amplitudes of up to ±3dB. It is important to take this variation into account when trying to detect broken rotor bars.

Finally, a parametric spectrum estimation technique, Prony's method was examined. Parametric techniques model the signal using a limited number of frequency components, and require only a small number of data points in order to solve for the model parameters. The Prony method examined here uses a model order of 20, which required 200 data points to be sampled. In contrast, the Fourier transform required 32 768 data points in order to generate a spectrum with reasonable frequency resolution. This illustrates the great advantage of parametric techniques. However, the disadvantage is that they are not good at modelling signals with components that are close together in frequency, but of greatly different amplitude.

CHAPTER 4

Phase Locked Loops and Synchronous Sampling

4.1 Introduction

In Chapter 2 it was shown that broken rotor bars in an induction machine cause modulation sidebands of twice slip-frequency ($\pm 2sf_1$) to appear around the supply frequency (f_1 Hz) component in the frequency spectrum of the stator current, when the machine is running with a per-unit slip of s. These peaks may be quite close to the supply frequency peak if the slip is small, especially for large induction motors which often have a slip at rated load of around 0.01. If there is any leakage (as described in Chapter 3) of the supply frequency peak, then these sidebands may be obscured. One possible solution is windowing, as outlined previously; however if the basic frequency resolution is low, this may still be insufficient to distinguish the sidebands.

A more elegant solution is to ensure that the current waveform is synchronously sampled, which causes the supply frequency peak to occupy only a single frequency bin in the resulting spectrum. Thus the sideband peaks will not be obscured so long as the frequency bin width is narrow enough to resolve them from the supply peak. A hardware solution, in the form of a phase locked loop, can be utilised in order to ensure that synchronous sampling occurs. In variable speed drive applications it also has the benefit of tracking any change in the supply frequency, and thus produce a useful spectrum.

This chapter outlines the principles of operation of phase locked loops and the development of a circuit to control the sampling process. Results are presented for motors on both fixed (mains) and variable frequency supplies.

4.2 The Phase Locked Loop

The phase locked loop (PLL) is a circuit which produces an output signal which has a frequency the same as, or a constant multiple of, the frequency of the input signal. The output frequency of the circuit can track changes in the input frequency over a limited range, called the tracking range. When the signal is first applied to the circuit, the PLL will only lock if the input frequency is within the capture range of the circuit. The tracking range is normally greater than the capture range. To ensure that a signal is synchronously sampled, an integer number of cycles of the fundamental must be sampled. The easiest way to do this is to sample a fixed number of points per cycle. A frequency multiplying PLL multiplies the frequency of the input signal by an integer. If the resulting frequency is used to control the sampling device, then a fixed number, dependent on the frequency multiplier, of samples per cycle will be sampled. Thus, a frequency multiplying PLL can ensure that a signal is synchronously sampled.

4.2.1 The Basic PLL Circuit

The basic configuration of a PLL circuit consists of a phase comparator, a low-pass filter (loop filter), and a voltage controlled oscillator (VCO). The phase comparator produces a voltage which is proportional to the phase difference

between the input and output waveforms. This voltage is then low-pass filtered to obtain the DC component, which is then applied to the VCO. The VCO produces a periodic output waveform at a frequency which is controlled by the input DC voltage. This configuration is illustrated in Figure 4.1.

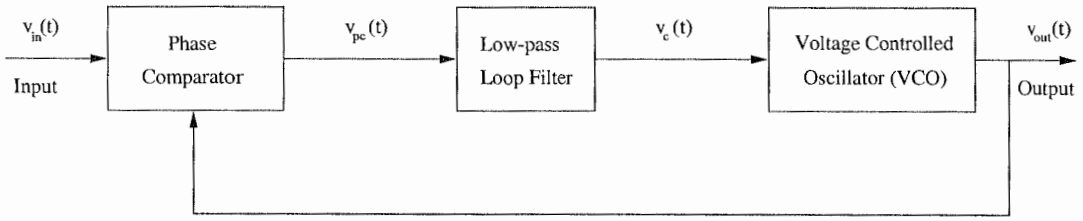

Figure 4.1: Basic PLL block diagram.

The principle of operation of the circuit is quite simple. The frequency of the output signal of the VCO, $\omega_{out}(t)$, is proportional to the input control voltage:

$$\omega_{out}(t) = \omega_0 + K_{VCO} v_c(t) \tag{4.1}$$

where ω_0 is the free-running frequency (zero control voltage) of the VCO, K_{VCO} is the gain of the VCO, and $v_c(t)$ is the control voltage.

The phase comparator compares the phases of the input and output waveforms, and produces a voltage, $v_{pc}(t)$, proportional to the difference:

$$v_{pc}(t) = K_{pc}\left(\phi_{in}(t) - \phi_{out}(t)\right) \tag{4.2}$$

where K_{pc} is the gain of the phase comparator, $\phi_{in}(t)$ is the phase of the input signal, and $\phi_{out}(t)$ is the phase of the output signal. $v_{pc}(t)$ will usually have an AC component which is undesirable, hence a low-pass filter is used to obtain the DC component which is used to control the VCO.

When the circuit is operating in the locked state, $\omega_{out} = \omega_{in}$. The VCO control voltage is then:

$$v_c = \left(\omega_{out} - \omega_0\right) / K_{VCO} \tag{4.3}$$

This must also be the average value of the phase comparator output voltage. In general this means that there must be a constant phase difference between the input and output waveforms, if ω_{in} is constant. If the input frequency changes, then the phase comparator output voltage will also change, causing the VCO output frequency to change. Eventually the output frequency becomes the same as the input frequency and the PLL is locked. The time taken for this to occur is known as the settling time of the PLL.

4.2.2 Frequency Multiplying PLL Circuit

There are several types of phase comparator circuit which may be used to implement a PLL. Conceptually, the simplest is an analog multiplier. If the input and output signals are sinusoids of frequency ω, then the output of such a phase comparator is:

$$\begin{aligned} v_{pc}(t) &= K_{pc} v_{in}(t) v_{out}(t) \\ &= V_{in} \sin(\omega t + \phi_{in}) V_{out} \sin(\omega t + \phi_{out}) \\ &= \frac{K_{pc} V_{in} V_{out}}{2} \left[\sin(\phi_{in} - \phi_{out}) + \sin(2\omega t + \phi_{in} + \phi_{out}) \right] \end{aligned} \tag{4.4}$$

where V_{in} and V_{out} are the amplitudes, and ϕ_{in} and ϕ_{out} are the phases, of the input and output signals respectively.

Equation (4.4) shows that the phase comparator output voltage has a DC component proportional to the phase difference of the input and output waveforms, and an AC component at twice the input frequency. The loop filter removes the unwanted AC component.

Usually [69] PLL circuits are used to produce square wave output and need a square wave input signal. In this case a digital logic circuit can be used to perform the function of a phase detector. Such circuits are termed digital phase locked loops (DPLLs), although most of the circuit is still analog. This is the type of PLL which is designed here, as a logic level output signal is required to drive the A/D converters.

It is also possible [69] to construct all-digital phase locked loops (sometimes termed ADPLLs) which may be implemented in hardware or software. Since an ADPLL is digital in nature, the output frequency can only change in discrete steps. This causes the output frequency to suffer from frequency jitter because the required output frequency is most likely *not* to be one of the possible discrete output frequencies. The number of output frequency possibilities is dependent on the clock frequency of the digital circuit, and hence the magnitude of the jitter is also dependent on the clock frequency. A significant amount of jitter in the output frequency will prevent synchronous sampling from being achieved, hence the jitter must be minimised by using a high clock frequency. A preliminary design for a hardware ADPLL required a clock frequency of several gigahertz, in order to keep the predicted frequency jitter to an acceptable level. This frequency requirement makes implementation of an ADPLL impractical as it would require a custom fabricated chip in GaAs technology.

For the remainder of this thesis the term PLL is used to broadly refer to DPLLs as well.

A frequency divider may be added into the feedback loop of a DPLL as shown in Figure 4.2. The PLL then produces an output signal at a frequency N times the input signal frequency, where N is the frequency divisor.

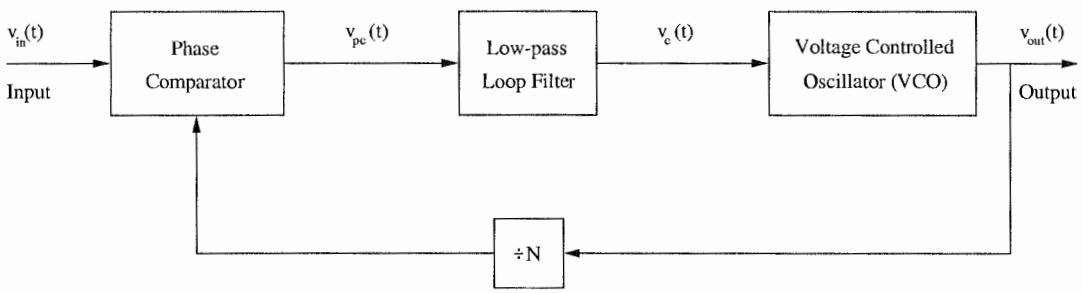

Figure 4.2: Frequency multiplying digital phase locked loop block diagram.

The theory of operation of such a PLL is covered in great detail by Best [69], and Encinas [70].

4.3 Synchronous Sampling and the PLL

As shown in Chapter 3, synchronously sampling a sinusoidal signal causes the resulting spectrum to consist of a single line. A multi-component signal composed of one large sinusoid plus many smaller components can be sampled in synchronism with the main component. This component and any multiples of it will then appear as single lines in the frequency spectrum. Other, asynchronous components will appear as peaks which are spread over several frequency bins, as illustrated in Chapter 3. Since the largest component will appear as a single line, it will not mask smaller components allowing them to be more easily detected.

In order to synchronously sample a signal it is necessary to capture an integral number of cycles of the waveform. In order to perform an FFT on the resulting data it is preferable to have a number of samples that is a power of two. Taking into account the aforementioned constraints, and the fact that the frequency multiplication factor for the PLL must be an integer, it is best to take a number of samples per cycle that is a power of two. That is, the frequency multiplication factor should be a power of two.

Thus synchronous sampling can be achieved by using a digital phase locked loop, with a frequency multiplying factor that is a power of two, to drive the sampling control of an A/D converter. The complete system block diagram for acquiring current waveforms in this manner is shown in Figure 4.3.

There are three signals which could be used as the input signal for the PLL in a VSD system. One is the supply voltage, another is the modulating signal, and the third is the drive carrier frequency. VSDs generally only have the first signal available at externally accessible terminals, hence for an independent condition monitoring system, this is the only useful signal. Hence the PLL circuit is designed to lock only to this signal. Should the other two signals be available, then it might be possible to use either of them, however detailed knowledge of the drive is required. The modulating signal is essentially the same as the voltage output signal as far as the PLL is concerned, but should provide a cleaner frequency signal. The carrier frequency may not be useful since it is not

necessarily related to the actual drive output frequency. This is completely dependent on the drive system, however if the carrier frequency is, in fact, related to the output frequency then it may prove to be quite useful in that it could eliminate some of the frequency multiplication necessary in the PLL resulting in a more stable system.

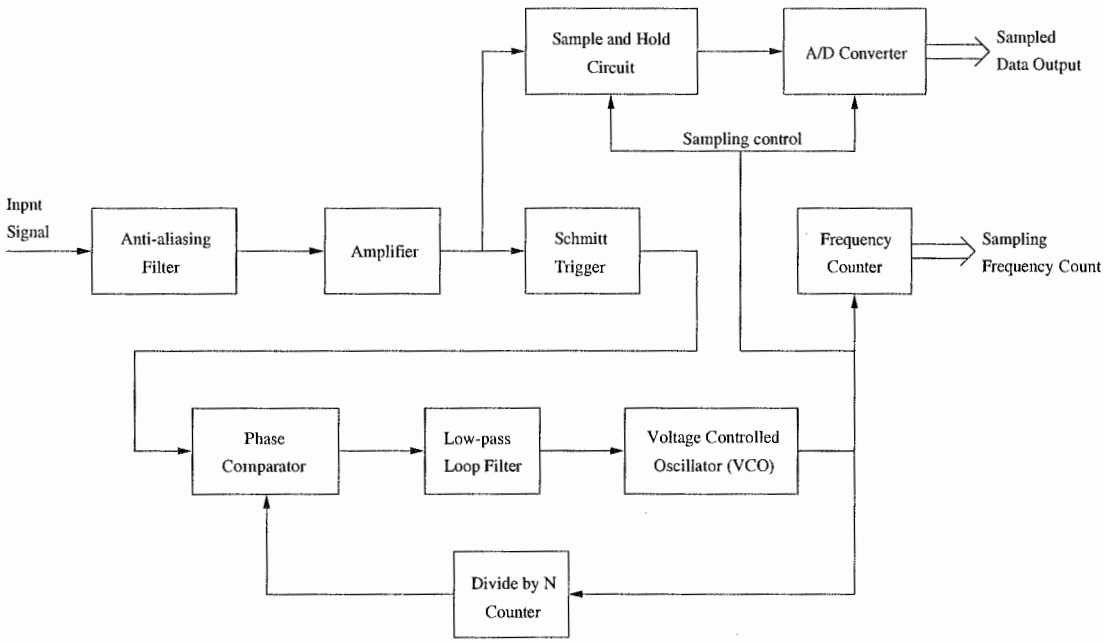

Figure 4.3: Block diagram of the synchronous sampling system.

4.4 PLL Circuit Implementation

A circuit to implement the system of Figure 4.3 was designed and built and is shown in Figure 4.4. The circuit is based around the CD4046B Micropower Phase-Locked Loop chip [71] made by National Semiconductor Corporation. A similar circuit was developed by Ferrero and Ottoboni [72], for power systems applications. Another similar circuit for condition monitoring use was recently granted a patent by Linehan et al. [73]. The circuit described in the patent is essentially the same as that in Figure 4.4, and previously reported in [74].

The 4046 PLL chip has two phase comparators, a source follower, VCO, and a zener diode. The zener diode is supplied for power supply regulation purposes and was not used in the circuit. Phase comparator one is an exclusive OR gate which

maintains 90° phase shift between input and output signals at the VCO free-running frequency, the phase shift varies from 0° to 180° over the tracking range of the PLL. The second phase comparator is an edge-controlled digital memory network that gives 0° phase shift between the input and output signals whenever the circuit is locked. The frequency range of the output signal of the wide-range linear VCO is determined by external components. Equations for calculating the value of these components may be found in [75]. Phase comparator one was chosen to be used in this application as it has a much greater immunity to noise [71] than the alternative.

The amplitude of the input wave is not critical, however it should be greater than about 0.5 Vrms. The input enters the circuit at terminals P1 and P2, and a comparator based on a TL071 operational amplifier, detects the zero crossings to produce a square wave at the same frequency. This is used as the input to the 4046 digital phase locked loop, the output of which is divided by a 4020 digital counter and passed back to the phase detector input to form the feedback loop. The fundamental frequency is multiplied by a factor of either 16, 32, 64, 128 or 256, which is manually set by SW1, to generate the output clock signal. The resulting clock waveform is passed through a 4049 inverter to provide buffering for external sampling circuitry.

A 74LS393 binary counter chain is used to accurately count the frequency of the clock signal output. The counter may either be gated externally, or internally by a 4538 monostable, which provides a gating pulse of 0.6 seconds. A 4011 provides logic to control the source of the gating pulse.

The circuit is tuned for a 50Hz centre frequency and a tracking range of 32-68Hz, which gives a capture range of 45-55Hz. This is because the mains frequency is 50Hz, so the circuit may also be used on mains supplied motors as well as VSDs operating in the 45-55Hz range.

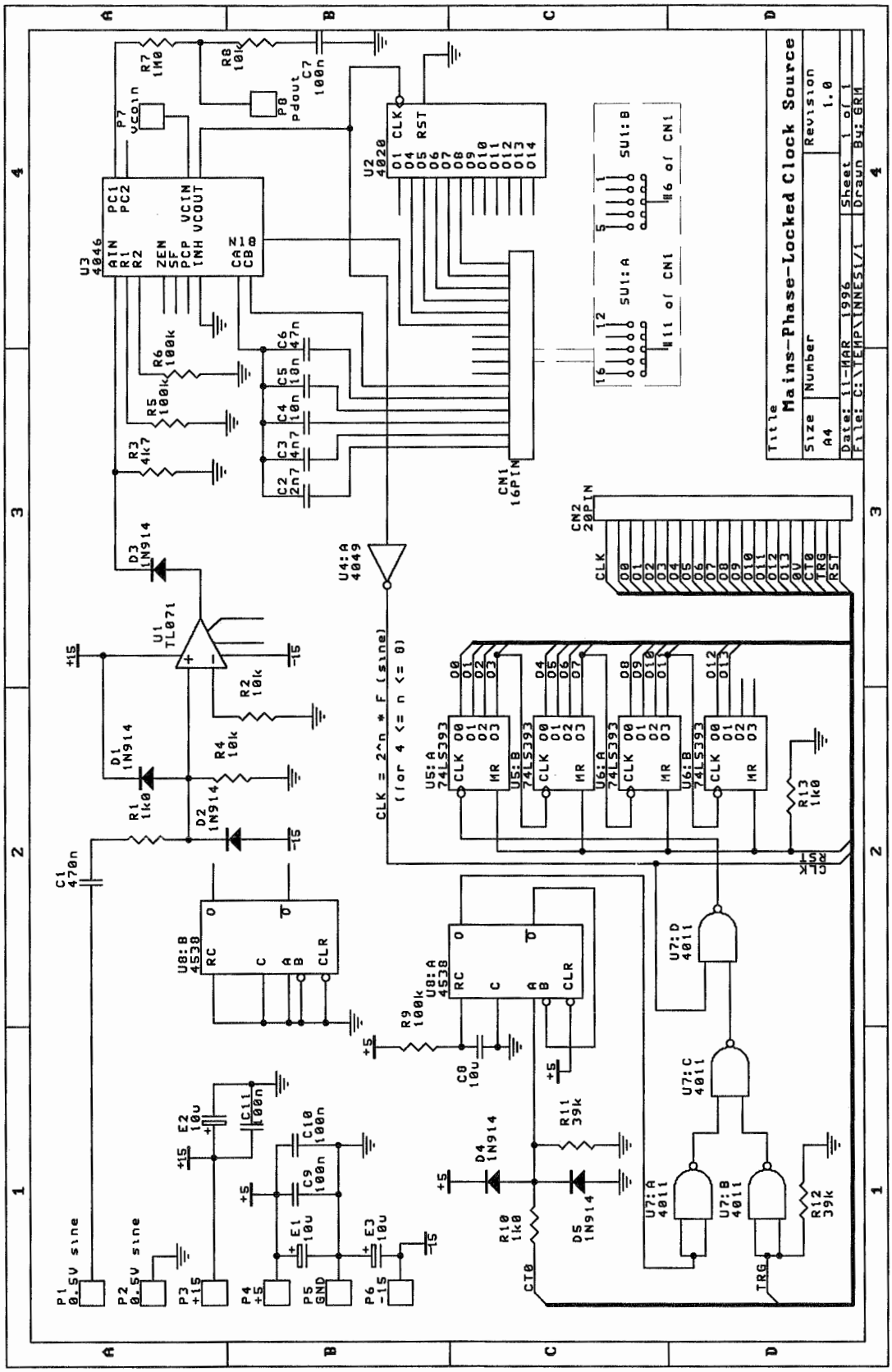

Figure 4.4: Circuit for implementation of phase locked loop.

4.5 Circuit Performance with Mains Supplied Induction Motors

The mains supply voltage is a more or less smooth sinsusoid at a fixed frequency (50Hz in Australia), which produces a sinusoidal stator current waveform at the same frequency in the induction motor. The frequency may vary due to changes in the total load on the whole power system, but in general any deviation from the nominal frequency is quite small and occurs reasonably slowly. In Tasmania, the deviation is usually less than ±0.1Hz, although it may occasionally be more due to extreme changes in system load [76]. These are the conditions for which the PLL circuit (Figure 4.4) was designed.

The results obtained were very good as can be seen by comparing a windowed non-synchronously sampled spectrum (Figure 4.5) with a PLL sampled spectrum (Figure 4.6). The mains supply frequency peak reduces to a single line in the spectrum, allowing the twice slip frequency sidebands, at 47.64Hz and 52.33Hz, to stand out much more clearly. The two sets of data were sampled at slightly different load levels, which is why the sidebands are at slightly different frequencies in the two spectra. There were 16 384 points sampled for each data record, at a rate of 3.2kHz

Any change in the mains frequency, that occurs during sampling, tends to expand the width of the peak at that frequency in Figure 4.5. The PLL synchronous sampling circuit causes the sampling frequency to change in sympathy with any change in the mains frequency, so no spreading occurs.

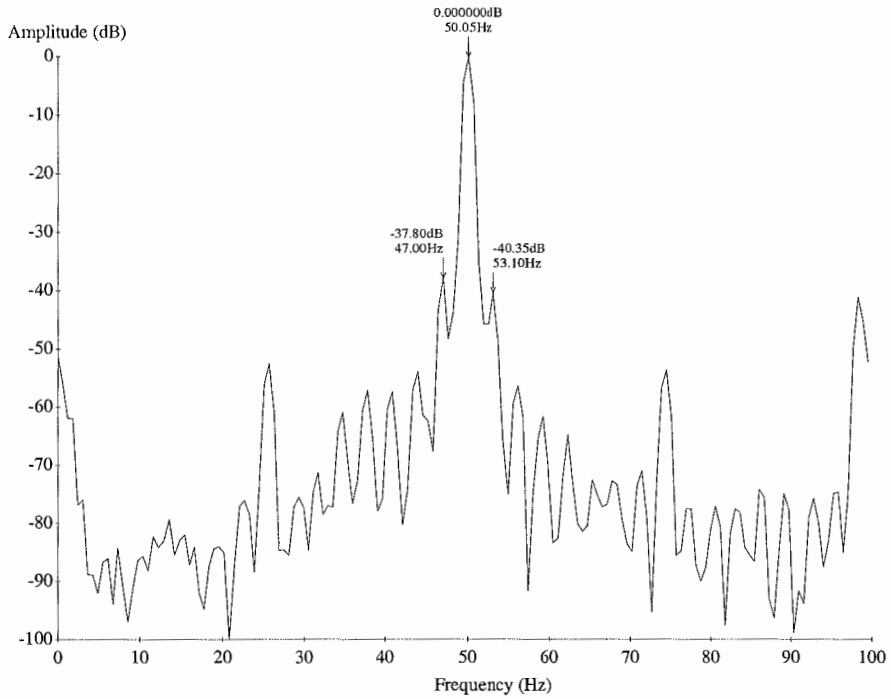

Figure 4.5: Non-synchronously sampled spectrum.

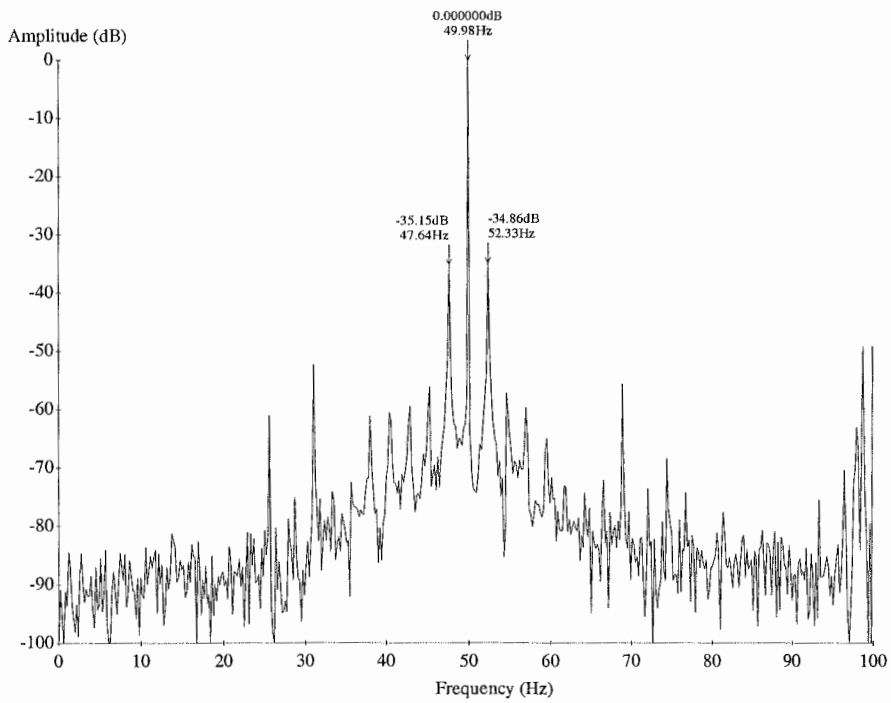

Figure 4.6: Synchronously sampled spectrum.

4.6 Application to Variable Speed Drives

A variable speed drive (VSD) changes the speed of an induction motor by changing the frequency of the voltage supplied to the stator windings. This makes the detection of sidebands caused by broken rotor bars much more difficult, as these too will move as the supply frequency changes. If fixed-rate sampling is used to acquire data, and the supply frequency changes during the acquisition period, then the spectrum calculated is similar to that shown in Figure 4.7. Obviously there is no useful information visible in this spectrum.

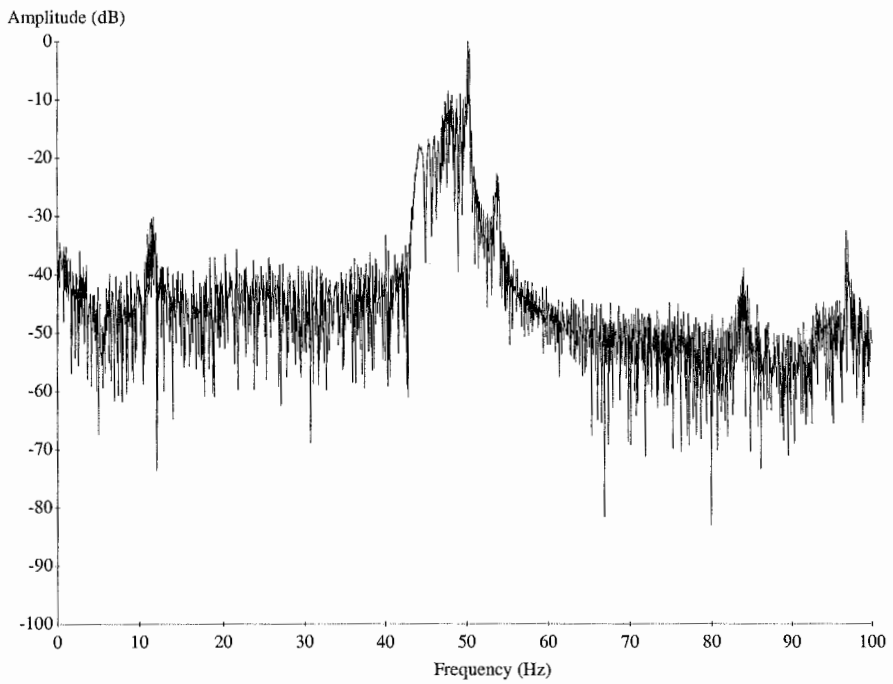

Figure 4.7: Stator current spectrum for fixed frequency sampling with varying supply voltage frequency.

Using the PLL to control the sampling process causes the sampling frequency to track any change that occurs in the supply frequency. This allows a clean spectrum to be produced as shown in Figure 4.8. The sidebands and supply frequency can be seen quite clearly in comparison to Figure 4.7. There is some spreading of the sideband peaks which is due to the change in supply frequency and the change in the slip, and hence of the sideband frequency relative to the supply frequency.

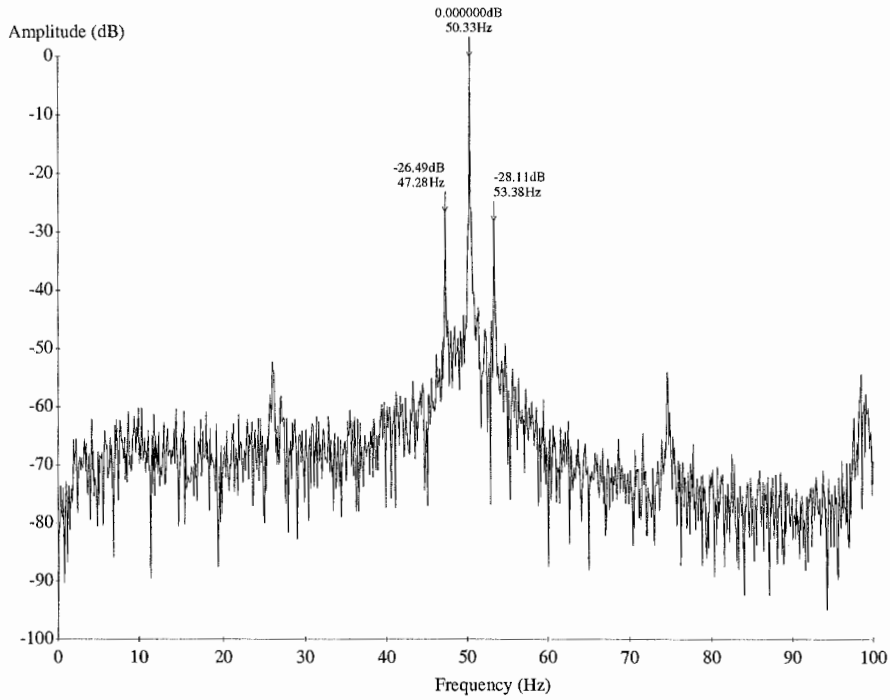

Figure 4.8: Spectrum of stator current with PLL controlled sampling and varying supply voltage frequency.

Since the sampling frequency changes over the time of data acquisition the frequencies assigned to the bins of the FFT are rather arbitrary. The values actually assigned in Figure 4.8 are based on the average sampling frequency over the 0.65536 seconds immediately prior to the start of the sampled data record. This value is obtained using the counter circuit described in Section 4.4, and external gating controlled by software.

4.6.1 Circuit Performance with Variable Speed Drives

The PLL sampling circuit was tried on a number of VSD - induction motor combinations, both in the field and the laboratory. It was found to perform reasonably well in some circumstances and rather badly in others. One difficulty was found to lie with the limited tracking range of the phase locked loop. It is quite difficult to design a PLL with a wide tracking range and a good step response at such low frequencies. Thus the operation of the device is constrained

by the limited tracking range of approximately 36Hz, centred about 50Hz. It is possible to increase the tracking range of the PLL at the expense of step response time, which may be a viable solution in some circumstances.

Another solution which would be applicable if the frequency variation of the drive system did not exceed the tracking range but was centred at a different frequency, would be to have a bank of PLL circuits, each with a different centre frequency. These circuits would have overlapping tracking ranges, so an initial fixed-frequency sampling of the signal could occur to determine the best PLL circuit to use. In practice this would be somewhat cumbersome, and it would probably be better to simply custom design a PLL to suit a particular drive system, if such a design is possible.

A second, more serious, problem was discovered in the course of laboratory tests. One VSD in the laboratory, an ABB SAMI GS (Appendix A), was found to have a very high frequency jitter on the output waveform, even when operating at a "constant" output frequency. This jitter was occasionally of large enough magnitude to cause the PLL circuit to lose lock, causing non-synchronous sampling to occur until it regained lock. This produced spectra of the form shown in Figure 4.9, with broadening of the supply frequency peak apparent when compared to Figure 4.8.

In order to quantify the magnitude of the frequency jitter, the stator current waveform was observed on a digital CRO. The CRO was triggered on the rising zero crossing of the waveform, and the timebase adjusted to display about one cycle across the display at the nominal drive frequency. The next rising zero crossing after the trigger was then observed to vary in position by up to 5% from one cycle to the next. This is an extremely fast rate of change, and it would be impossible to design a PLL circuit which could track frequency changes this rapid.

In order to combat the effects of the jitter and the noise spikes, an attempt was made to filter the signal before applying it to the input of the PLL. To do this a commercial Kron-Hite double-gang variable filter (see Appendix A) was used. A low pass Butterworth response was chosen and the two filters cascaded with a

cutoff frequency of 80Hz selected. However, this appeared to make no noticeable difference to the results obtained. Varying the cutoff frequency of the filters also made no discernable difference to the resulting frequency spectra, until the supply frequency was filtered out of course.

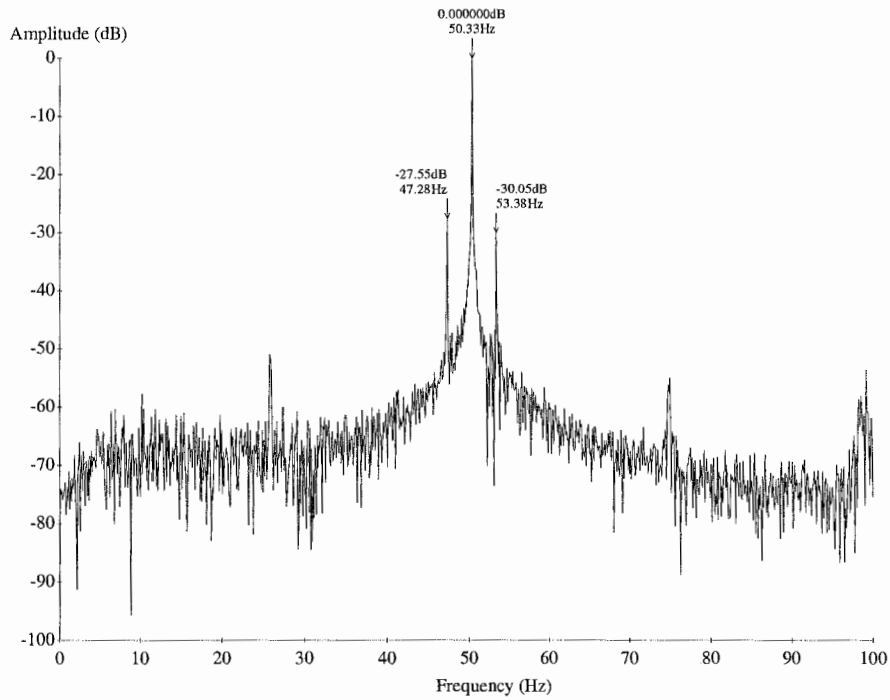

Figure 4.9: Broadening of supply frequency peak due to PLL losing lock.

It is thought that the jitter may be due to the variation in turn-on and turn-off time of the semiconductor switches in the drive, as a result of varying amounts of current being switched [77]. It is likely that all drives may suffer this to greater or lesser degrees. Hence, the PLL method may not be that useful. However, if the circuit could be integrated as part of the drive, then the PLL could be driven from the power electronics control signals. This would solve the problem as these signals should not suffer from frequency jitter.

4.7 Summary

A frequency multiplying phase locked loop can be used to ensure that the stator current waveform is synchronously sampled. This has the benefit of reducing the

supply frequency peak to a single line in the frequency spectrum, eliminating the need for windowing, and allowing the broken rotor bar sidebands to be very well defined and easy to identify. It also has the major advantage that any change in the supply frequency is tracked and synchronous sampling maintained.

This chapter develops a design for a PLL circuit, based on the 4046B integrated circuit, which generates a clock waveform at a constant multiple of the frequency of the signal being sampled. When used to control the sampling hardware, this circuit ensures that a signal is synchronously sampled. The circuit was designed for a centre frequency of 50Hz, and tuned to have a capture range of 45-55Hz, and a tracking range of 32-68Hz. This design makes it particularly suitable for mains supply operation.

The frequency tracking behaviour of the PLL sampling method naturally leads to application of the system to motors supplied by variable speed drives. In this case the supply frequency can vary quite widely. It was found that the circuit performance was unsatisfactory in some cases, depending on the drive used and the frequency variation that occurred. The main problem was found to be rapid jitter of the output frequency of the drive, which caused the PLL to lose lock. However, this problem could be overcome if the PLL sampling technique was integrated as part of the variable speed drive itself, as jitter-free control signals would be accessible.

CHAPTER 5

Variable Speed Drives

5.1 Introduction

The great disadvantage of the induction motor in industrial applications, is that it is very difficult to control the speed, because it is dependent on the supply frequency and the load torque. Before the advent of semiconductor switching devices, speed control of the induction motor could only be done by manipulating the rotor currents on wound rotor machines, or by using a pole changing stator winding. These methods have now become obsolete due to the invention of the variable speed drive (VSD), which changes the frequency of the supply to the motor, hence controlling the speed.

The VSD produces a variable frequency output waveform by rectifying the AC mains supply to produce a DC source, which is then switched on and off by the semiconductor switches in order to produce a pulsed output waveform. By controlling the fundamental frequency of these pulses, the motor supply frequency, and hence speed, is controlled. Since the output waveforms are

essentially a string of square pulses, the frequency spectrum contains many more harmonics than does the mains frequency spectrum.

This chapter describes the various classifications of variable speed drives, and examines the frequency spectra of the switching strategies that are used. The implications that the extra harmonic frequency components have for the detection of fault frequencies in the supply current for condition monitoring, are examined. An experimental study of the impact of the motor supply frequency on the relative amplitudes of fault frequency components of the stator current waveform is also reported. As is the influence of different load power levels on the twice slip-frequency sideband amplitudes.

5.2 Induction Motor Speed Control

In the past, when only a fixed frequency mains supply was available, there were three methods of speed control [42]. The first method works only if the motor is loaded, and it is based on the observation that the slip is dependent on the rotor resistance and the rotor current. By changing the rotor resistance, via variable resistors connected to the rotor windings by slip rings, the speed can be controlled. This method has the disadvantage that a significant amount of power is dissipated in the rotor circuit, decreasing the efficiency, approximately in proportion to the decrease in speed.

The second technique uses a special stator winding that allows the number of poles of the motor to be varied. Motors wound in this way are known as pole-changing motors. Of course, this only allows step changes in speed and requires a specially constructed motor. It may be combined with the aforementioned method, to give a wider speed range.

The third method requires the use of one or more other machines to impress a voltage on the rotor winding which controls the actual rotor currents. By controlling the impressed voltage so that it adds or subtracts to the rotor voltage, the slip and hence the speed may be controlled. Particular drives of this type are the Scherbius drive and the Krämer system [41].

The first and third methods of speed control require a wound rotor induction motor rather than the more robust cage rotor, and even so it is difficult to control the speed accurately. A better alternative, which works for both cage and wound rotor induction motors, is to control the frequency of the supply voltage. This may be done by controlling the generation of the supply voltage. Prior to the invention of power semiconductor switching devices, this had to be done by controlling the generating machine itself. Power semiconductor switching devices have made it possible to control the switching of large currents at high frequencies, by small control signals. It is now possible to build rectifiers which produce a DC voltage from the AC mains, and inverters which switch this voltage suitably to produce an AC voltage at a different frequency. This voltage can then be used to control the speed of an induction motor. The complete device, consisting of a rectifier, a DC link, and an inverter (as shown in Figure 5.1), is known variously as a variable speed drive (VSD), variable frequency drive (VFD), and an adjustable speed drive (ASD). This thesis uses the term variable speed drive, or simply, drive.

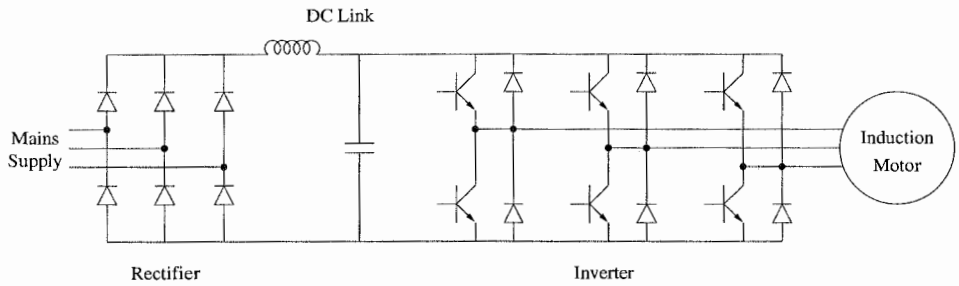

Figure 5.1: Circuit diagram of a variable speed drive.

The object of a VSD is to produce a three phase voltage with a fundamental component which is as large as possible because induction motors are usually designed to suit a single frequency supply voltage. It is also desirable to reduce harmonics in the audible range as these may be detrimental to people working in the vicinity of the motor or drive. Harmonics also contribute to heating [78] [79] [51], by increased core loss, and torques at non-synchronous speeds. The heating is detrimental to motor longevity as it causes insulation degradation, and also mechanical stresses due to thermal expansion and contraction.

There are three broad classifications of frequency converters used for AC motors [80]. They are the voltage-source inverter (VSI), the current-source inverter (CSI), and the cycloconverter. The VSI uses a DC voltage link from the mains supply rectifier to the inverter. The CSI uses a DC current link as the input to the inverter, which produces a switched current output waveform. Cycloconverters are direct AC to AC frequency converters and are only used in very high power applications where the output frequency is generally less than the input frequency. This thesis examines only the VSI as it is by far the most common type of frequency converter in all but the highest power applications [81].

The AC output voltage of the drive may take various forms, all of which have the common property that they are switched waveforms. The output voltage is switched to a number of discrete levels, with the object being to produce a fundamental component that is as large as possible in comparison to any harmonics that are produced. Obviously the simplest example of such a switching strategy is simply a square wave, however this has many large amplitude harmonics. A better approach is to have more than two output levels, for example, a six-step method [82]. However, as the number of output levels increases, the complexity of the switching circuits increases. Another way to reduce harmonics is to change the duration of the output pulses rather than the amplitude. This process is known as pulse-width modulation (PWM) and is currently the most popular form of drive output.

5.3 Pulse-width Modulation

Pulse-width modulation (PWM) is a technique derived from communications theory [83], where a pulse train has the width of each pulse varied by an instantaneous sample of a modulating signal. In VSD applications the modulating signal is usually a sinusoid, which produces an inverter output voltage that has a fundamental component at the frequency of the modulating signal. A typical, three-level, PWM waveform and the corresponding fundamental frequency component is shown in Figure 5.2.

There are several different modulation strategies that can be used to produce a PWM output. The most widely used PWM techniques are carrier-based, that is, there is a basic underlying switching signal, called the carrier, which is compared to a modulating signal in order to determine the switching times of the inverter. There are several different ways of making this comparison, resulting in PWM methods known as natural sampled, symmetric and asymmetric regular sampled, optimised, random, and space vector.

There are two definitions which are relevant to PWM waveforms. First there is the frequency ratio, R, which is the ratio between the carrier frequency, f_c, and the modulating frequency, f_m:

$$R = \frac{f_c}{f_m} \tag{5.1}$$

When R is an integer, the modulation process is called synchronous PWM. Asynchronous PWM, where R is not an integer, causes subharmonics of the fundamental frequency to appear in the output which is undesirable in most applications [81].

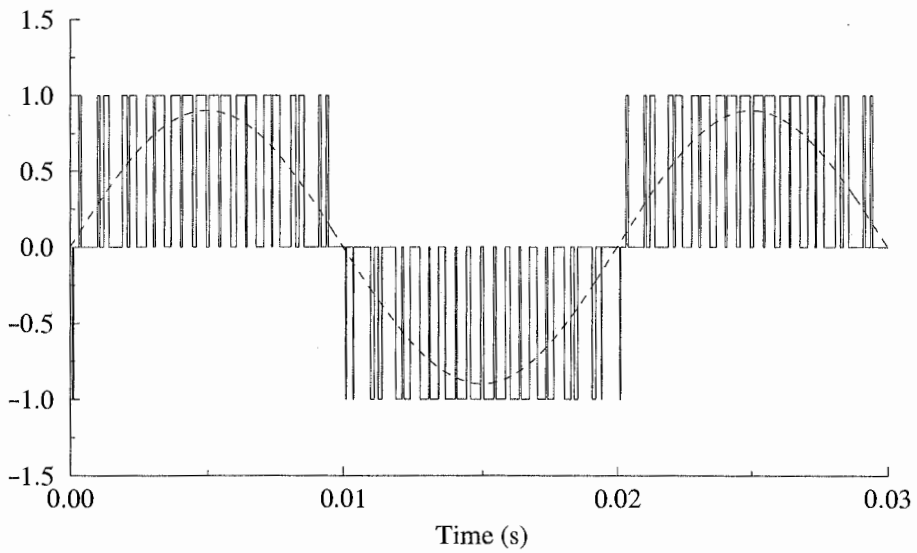

Figure 5.2: Three-level PWM waveform, $R = 21$, $M = 0.9$, with 50Hz fundamental.

The other definition is the modulation depth, M, which is the ratio between the amplitude of the modulating signal, A_m, and the amplitude of the carrier signal, A_c:

$$M = \frac{A_m}{A_c} \tag{5.2}$$

When M is greater than one the process is said to be overmodulated. Overmodulation can cause the output to contain many more harmonics than when M is less than one. As M is increased the inverter output waveform degenerates to a square wave.

5.3.1 Natural Sampled PWM

In natural sampled PWM [83] [84] the switching times are defined by the intersection points of the carrier and modulating signals, as illustrated in Figure 5.3. Generally, the carrier signal is a triangular waveform and the modulating signal is a sinusoid. This method is the simplest to implement in analog electronics and has been the favoured option for such drives.

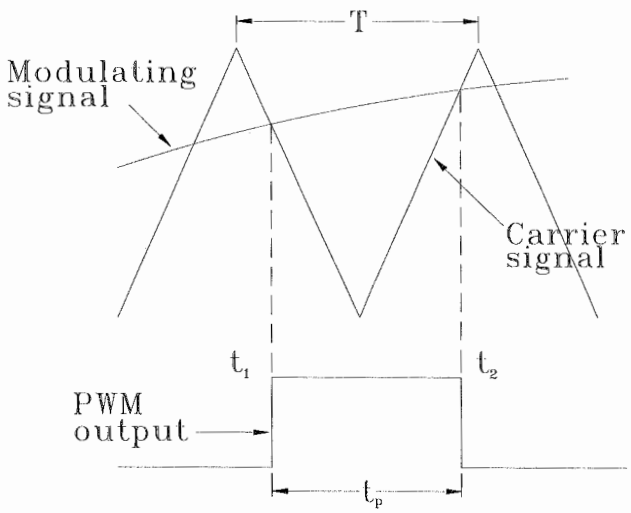

Figure 5.3: Natural sampled PWM.

It can be seen that the width of the output pulses is proportional to the amplitude of the modulating wave at the switching instants. To find the pulse widths

analytically, it is necessary to solve for the intersections of the two waveforms. This results [84] [85] in a transcendental equation for the pulse width:

$$t_p = \frac{T}{2}\left[1 + \frac{M}{2}\left(\sin \omega_m t_1 + \sin \omega_m t_2\right)\right] \tag{5.3}$$

A theoretical expression for the frequency spectrum (Appendix B) was derived by Bowes [85], and is illustrated in Figure 5.4.

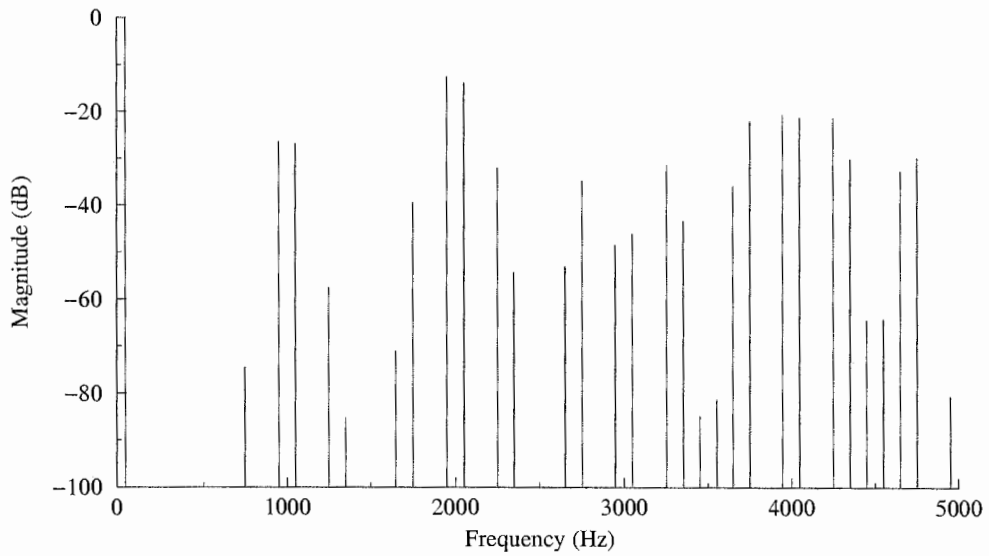

Figure 5.4: Frequency spectrum of natural sampled PWM, $R = 20$, $M = 0.9$, $f_m = 50$.

5.3.2 Symmetric Regular Sampled PWM

Symmetric regular sampled PWM uses a sample-and-hold circuit to sample the modulating signal at the same frequency as the carrier, as shown in Figure 5.5. This sampled version of the modulating signal is compared to the carrier signal to generate the switching points from the intersections. This results in pulsewidths given by [86]:

$$t_p = \frac{T}{2}\left[1 + M \sin(\omega_m t_1)\right] \tag{5.4}$$

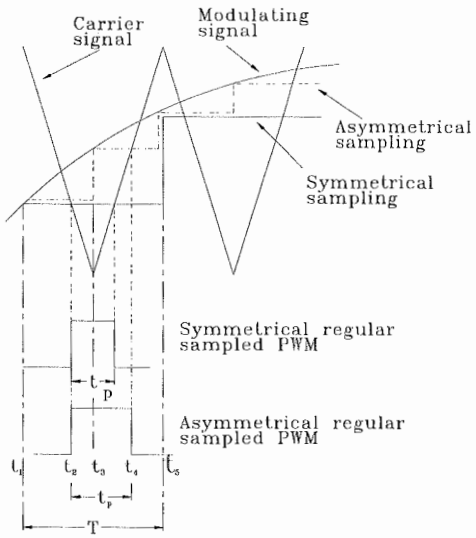

Figure 5.5: Regular Sampling.

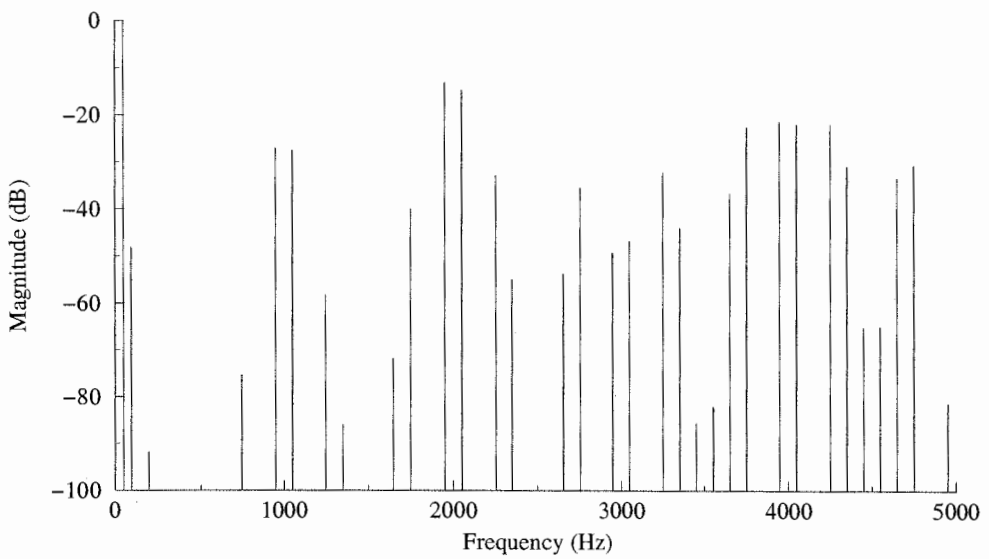

Figure 5.6: Frequency spectrum of regular sampled PWM, $R = 20$, $M = 0.9$, $f_m = 50$Hz.

Thus, the pulse widths are proportional to the amplitude of the modulating signal at the instants at which it is sampled. Both the width and positions of the pulses are predictable due to the regular sampling of the modulating signal. An expression for the frequency spectrum was derived by Franzó et al [87] (Appendix

B) and is illustrated in Figure 5.6. The amount of second and third harmonic of the modulating signal is rather large in Figure 5.6. A practical design would use parameters which minimise these harmonics.

5.3.3 Asymmetric Regular Sampled PWM

Asymmetric regular sampled PWM also uses a sample-and-hold circuit to sample the modulating signal, but at a frequency twice that of the carrier, as shown in Figure 5.3. In this case the leading and trailing edges of the pulse are modulated by different amounts, hence the modulation is asymmetric. The pulse widths are given by [86]:

$$t_p = \frac{T}{2}\left[1+\frac{M}{2}\left\{\sin(\omega_m t_1)+\sin(\omega_m t_3)\right\}\right] \tag{5.5}$$

Franzó et al [87] derived an expression for the frequency spectrum (Appendix B) and results in the spectrum of Figure 5.7.

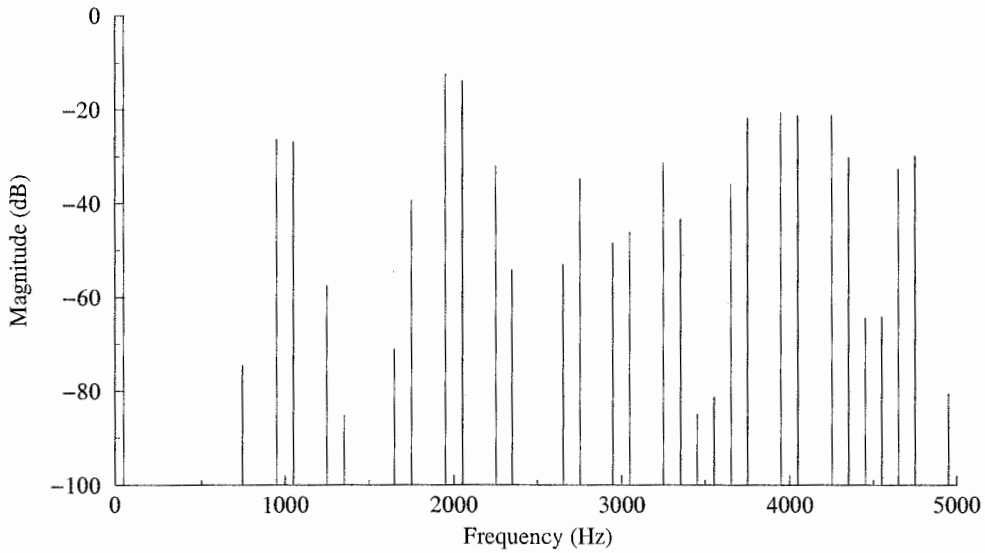

Figure 5.7: Frequency spectrum of asymmetric regular sampled PWM, $R = 20$, $M = 0.9, f_m = 50\text{Hz}$.

5.3.4 Optimised PWM

It is possible to optimise the PWM waveform with respect to some performance criteria, for example, elimination of particular harmonics, or limiting peak current. From these criteria a set of equations in terms of the switching angles of the inverter can be found. These equations may be solved numerically to find the switching angles, which can then be programmed into the controller. Optimised PWM methods are not strictly carrier based since the number of switching angles during an output cycle is usually fixed and thus it is these values which are optimised. Usually optimised PWM can only be implemented in digital microprocessor based drives. Naturally there are many possible optimisation schemes [86] [88-92] which all have different spectra, which will not be quoted here. In general, these methods have frequency spectra which are similar to the spectra of the natural or regular sampled methods described above, except that some harmonics may be eliminated.

5.3.5 Random PWM

Random PWM (RPWM) is a technique which randomises the pulse positions of the PWM output waveform [93]. It is usually implemented by randomly adjusting the frequency of the carrier wave and using a regular sampling technique to generate the switching angles. RPWM causes part of the harmonic power to be transferred to the continuous spectrum as noise, which contrasts with the PWM methods discussed previously (Sections 5.2.1-4), which all have a discrete frequency spectrum. The harmonics in these spectra can cause harmful effects in the induction motor [94], so by reducing the amplitudes of these harmonics and spreading the power out as noise, RPWM can reduce these undesirable effects.

The frequency spectrum of RPWM depends on the exact algorithm used to generate the waveform [95] [96]. However, most have in common that there is a large fundamental component present, a low number and level of harmonics, and a high background noise level in the spectrum [97]. This can only be good for condition monitoring purposes as it means that the number and level of harmonics

resulting from the drive are quite small, hence frequency components relevant to fault detection are not masked.

5.3.6 Space Vector PWM

Space vector PWM represents the required three-phase output voltage on a phasor diagram by Park's transform [98]. This vector is then approximated by the closest vector that the inverter is capable of producing [99]. This determines the switching angles of the inverter. Depending on the algorithm used, the output can be equivalent to regular sampled asymmetric PWM [98], or it can be optimised [99]. Thus the frequency spectrum of space vector PWM is similar to the regular and optimised spectra. Boys and Handley [100] have derived a theoretical expression for the spectrum (Appendix B) and a typical example is shown in Figure 5.8.

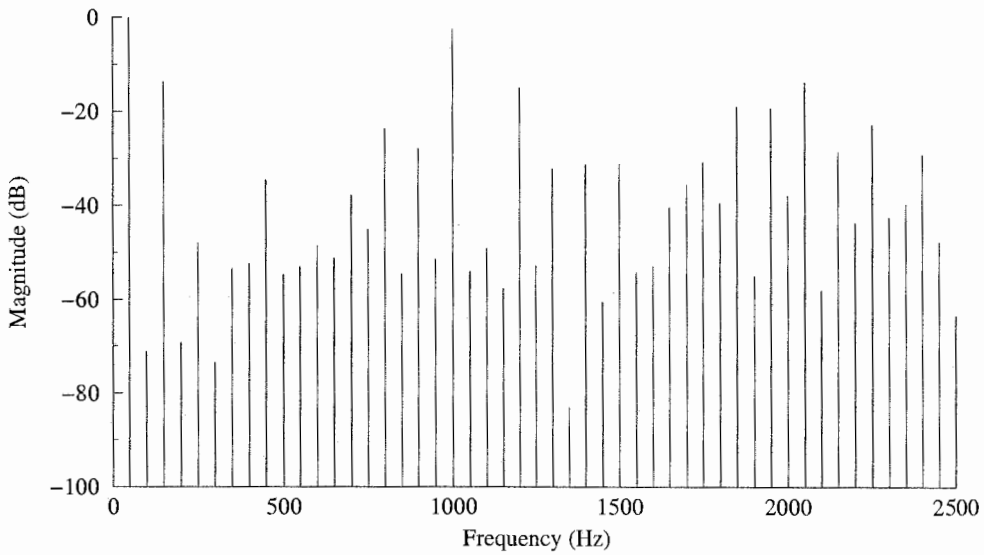

Figure 5.8: Frequency spectrum of space vector PWM waveform, $R = 20$, $M = 0.9, f_m = 50\text{Hz}$.

5.4 Effects of PWM Voltage Waveforms on Detection of Fault Frequencies

The mains supply voltage should, theoretically, consist of a single frequency sinusoid. The analysis of Chapter 2 was based on such an assumption. In practice the mains will also contain odd harmonics of the fundamental frequency. These components will cause currents at these frequencies in the stator windings, which will cause currents to flow in the rotor at frequencies suitably modified by the slip. This implies that if there is a rotor bar fault, fault frequency components will also be generated at frequencies other than those in Table 2.2.

Since PWM voltage waveforms are essentially sinusoids with severe harmonic distortion, this same argument also holds for stator current frequencies generated by rotor faults. From the analysis of the preceding section it can be seen that the spectrum of PWM waveforms generally have components at $m\omega_c \pm n\omega_m$, and the main output frequency ω_m. There may also be multiples of ω_m and ω_c present, depending on the type of modulation used. In addition to these components, there may be subharmonics of the modulating frequency present if the frequency ratio, R, is not an integer.

These frequency components must be taken into account for condition monitoring purposes. Most of the components are quite high in the frequency range, so would not pose a problem for fault frequency detection, however, this is dependent on the exact parameters used to implement the PWM. If the frequency ratio is low, then it is quite possible that products of the modulation process may interfere with the detection of fault frequency components. The components listed above appear in the voltage waveform. When these enter the motor, extra currents are induced in the stator and rotor. Hence the stator current spectrum will contain all of the above frequency components, plus any modulation products that result from the interaction of the various frequency components within the machine.

The frequency components may mask the rotor slotting frequencies, as these are usually quite high, and could well be in the range of drive harmonics. This makes the task of speed detection rather difficult. Ideally the drive and condition

monitoring system would be integrated, so that the drive would use an optimised modulation strategy that eliminated harmonics that could mask fault frequency components.

5.5 Effect of Supply Frequency on Rotor Fault Frequency Amplitudes in the Stator Current Spectrum

Changing the supply frequency of an induction motor will also change the values of reactances within the motor. Naturally, this will have an effect on the amplitudes of the stator current frequency spectrum, which has implications for the detection of faults, as faults are detected by relative amplitudes of frequency components. This problem is too difficult to solve theoretically for all frequency components, so an experimental approach was taken. In order to determine the effects of change in drive output frequency on the relative amplitudes of frequency components, the Pope motor (Appendix A) with a damaged rotor was run at different frequencies by the ABB drive (Appendix A). The induction motor was loaded by a DC generator and resistor bank combination.

In order to evaluate the change in twice-slip frequency sideband amplitudes, twenty records of the current were measured at drive output frequencies between 20Hz and 62Hz. The motor was loaded by a DC machine such that the slip was held constant at 0.04p.u. for each drive frequency tested. A FFT was then performed on each record to obtain the frequency spectrum, a Blackman window was used to weight the data to avoid end-effects. A typical spectrum is shown in Figure 5.9. The average values, over the twenty records, for the lower sideband and the upper sideband were then plotted against frequency (Figure 5.10). The average of these sideband amplitudes was also plotted on the same axes.

It can be seen that the amplitude of the lower sideband increases with frequency, whilst that of the upper sideband decreases with frequency. However the change in the sideband frequencies is such that the average of the two amplitudes remains relatively constant at about -40dB. The standard deviation of the sideband amplitudes is acceptably small when compared to the magnitude of the average. It

is somewhat larger than that calculated in Table 3.1, however the sample population for each point in Figure 5.11, is only 20% of that used to generate the results in the table.

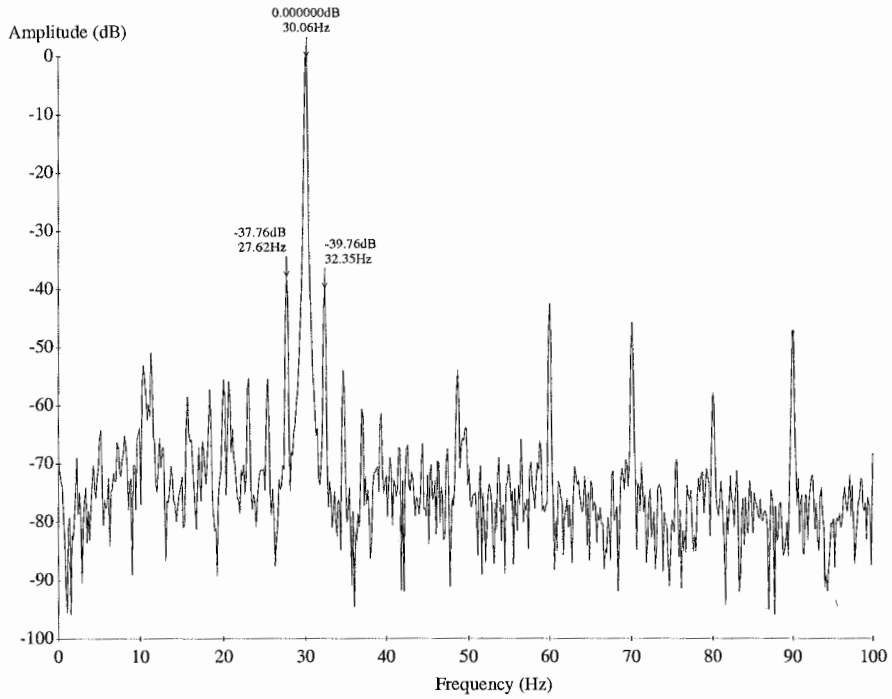

Figure 5.9: Typical stator current frequency spectrum.

The upper sideband results from the third harmonic of the drive frequency [101], and speed oscillations. Figure 5.11 shows that the relative amplitude of the third harmonic decreases as the frequency increases, and hence the amplitude of the upper sideband also decreases. This is not unexpected since the impedance of the motor to third harmonic increases with frequency, as does the influence of the skin effect in the rotor bars [41]. Hence the third harmonic current decreases with increasing frequency. This may be the cause of the decrease in the relative amplitude of the upper sideband.

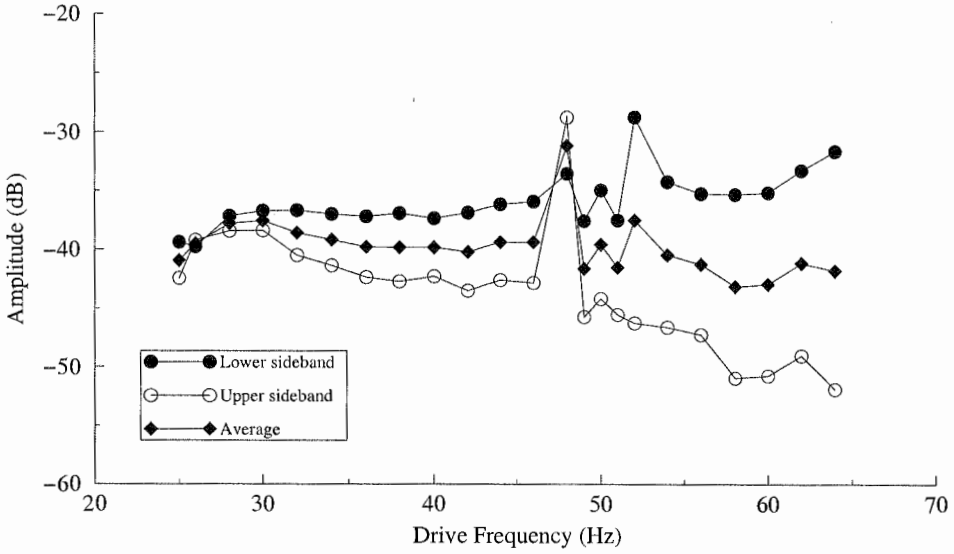

Figure 5.10: Average sideband amplitude - constant slip (0.04 p.u.).

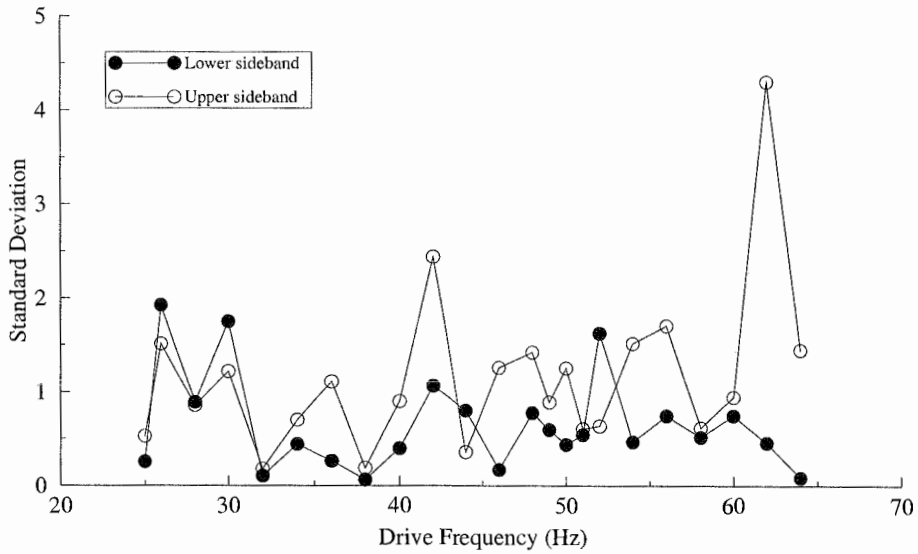

Figure 5.11: Standard deviation of average sideband amplitude - constant slip (0.04 p.u.).

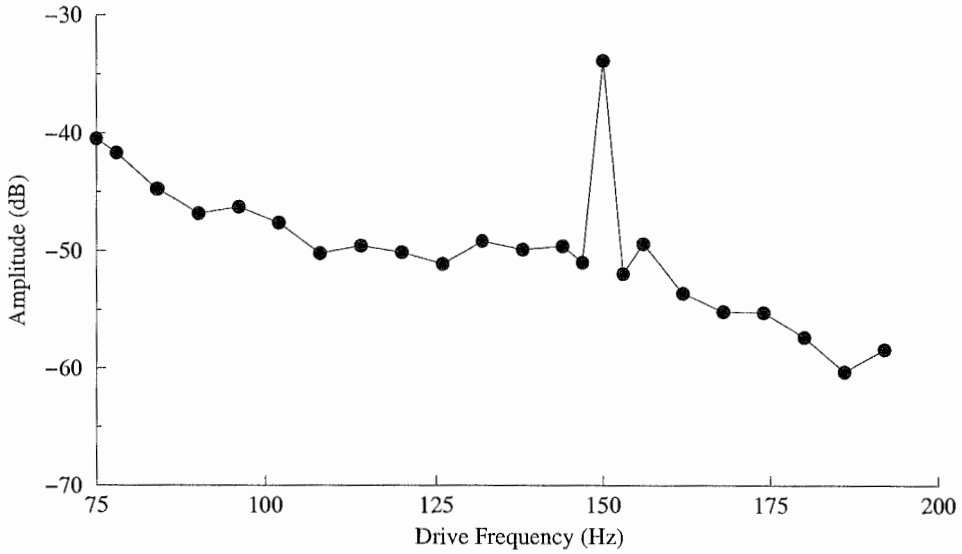

Figure 5.12: Amplitude of third harmonic of drive frequency.

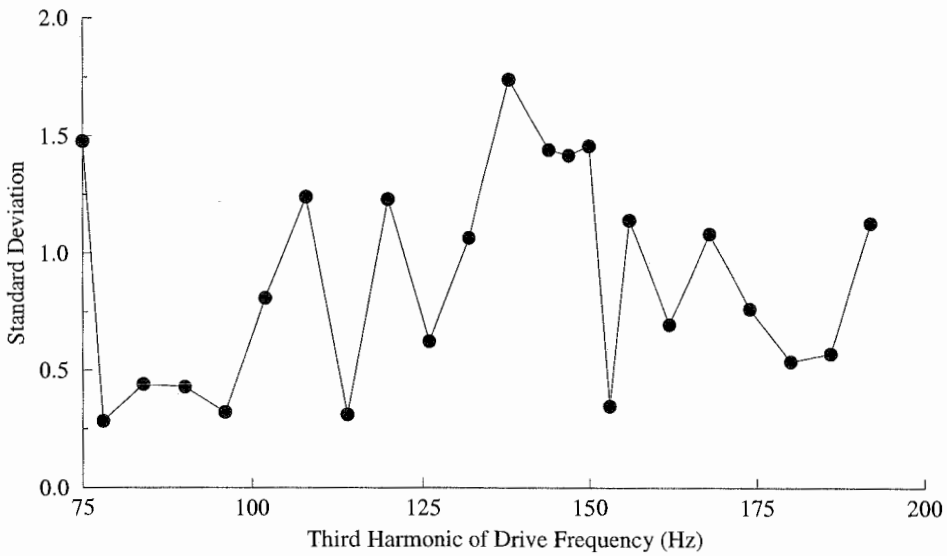

Figure 5.13: Standard deviation of amplitude of third harmonic of drive frequency.

Upon close examination of the spectra of the recorded data, it was noticed that each spectrum had a frequency component at (100 - f_d)Hz, where f_d is the drive output frequency. This component is henceforth termed the *reflected frequency*.

The amplitude variation of the reflected frequency is shown in Figure 5.14, and the corresponding standard deviation is shown in Figure 5.15. The standard deviation of the reflected frequency component at a drive frequencey of 50Hz and the amplitude are both zero since the reflected frequency is the same as the drive frequency and all amplitudes are normalised to the amplitude of this frequency component. It can be seen that the average amplitude of the reflected frequency component increases with increasing drive output frequency. The reflected frequency is an interesting phenomenon, especially if it is present for all drives, because it can potentially coincide with one of the sideband peaks. This could make it appear as though a fault were present when there is actually none.

The origin of the reflected frequency is unclear. Empirically it appears at a frequency of $(100 - f_d)$Hz, suggesting that it could be a product of the mains supply which was 50Hz, and 100 is twice this value. One possibility is that the rectification of the mains to produce the DC link voltage, creates a ripple which, when passed through the modulation process, becomes the reflected frequency component. In order to examine this theory, the ripple on the DC link was measured using a CRO and coupling capacitor network. A screen dump of the waveform captured is shown in Figure 5.16. The amplitude of the ripple is about 10V and the frequency is about 150Hz. The output voltage waveform for a drive frequency of 45Hz is shown in Figure 5.17 and its spectrum in Figure 5.18. The amplitude of the DC link voltage is about 590V, although the axis in Figure 5.17 is not calibrated. It can be seen that there is a significant amount of ripple on the output voltage. This may be the source of the reflected frequency, however, attempts to simulate this situation failed to produce the reflected frequency component. The reflected frequency can be seen in the spectrum of the voltage waveform at about 55Hz. Figure 5.19 shows the spectrum of the voltage from 0-5000Hz. Major peaks resulting from the PWM process can be seen around 3.2kHz, and at multiples and sub-multiples of this. No relationship between the reflected frequency component and any of these frequency peaks was found.

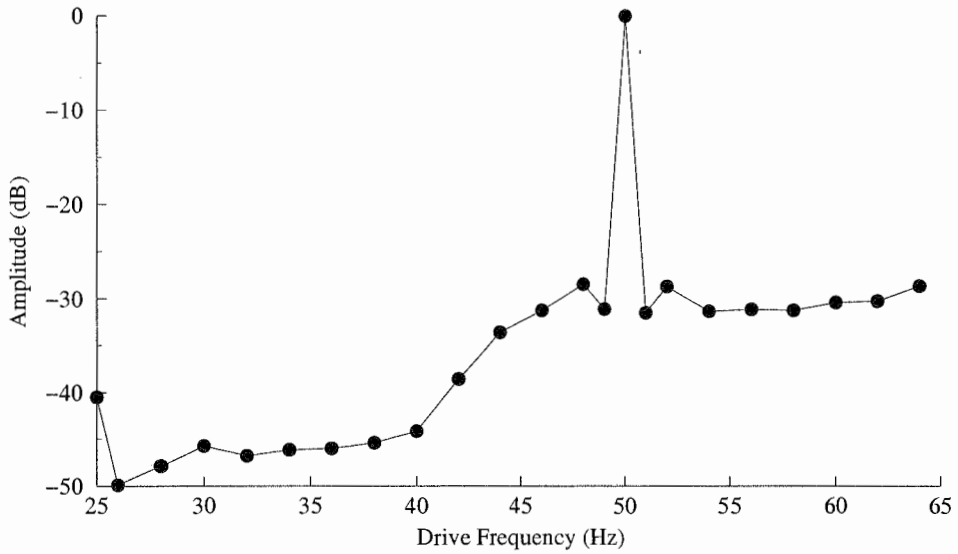

Figure 5.14: Amplitude of reflected frequency component relative to drive frequency amplitude.

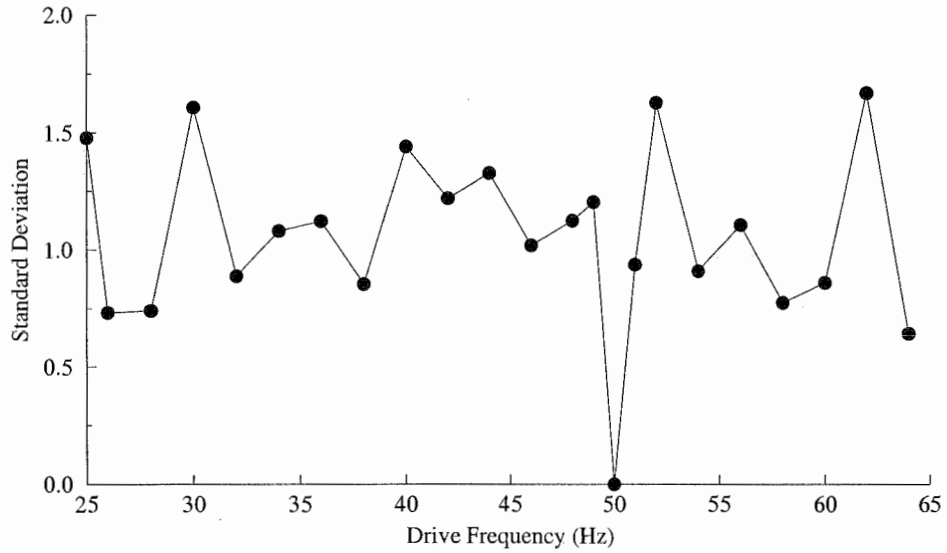

Figure 5.15: Standard deviation of amplitude of reflected frequency component.

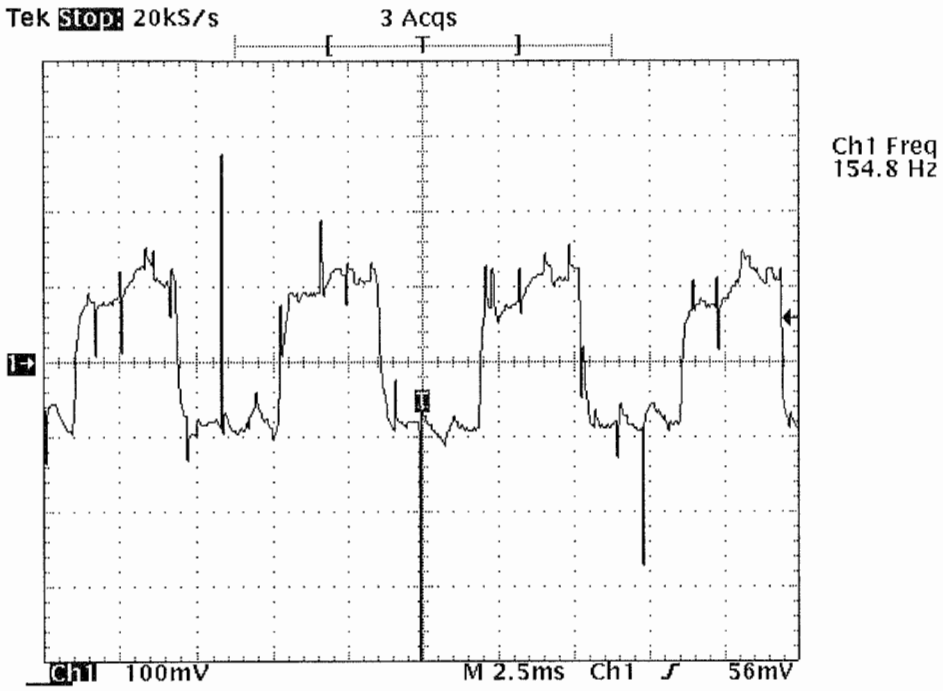

Figure 5.16: Ripple on the DC link voltage.

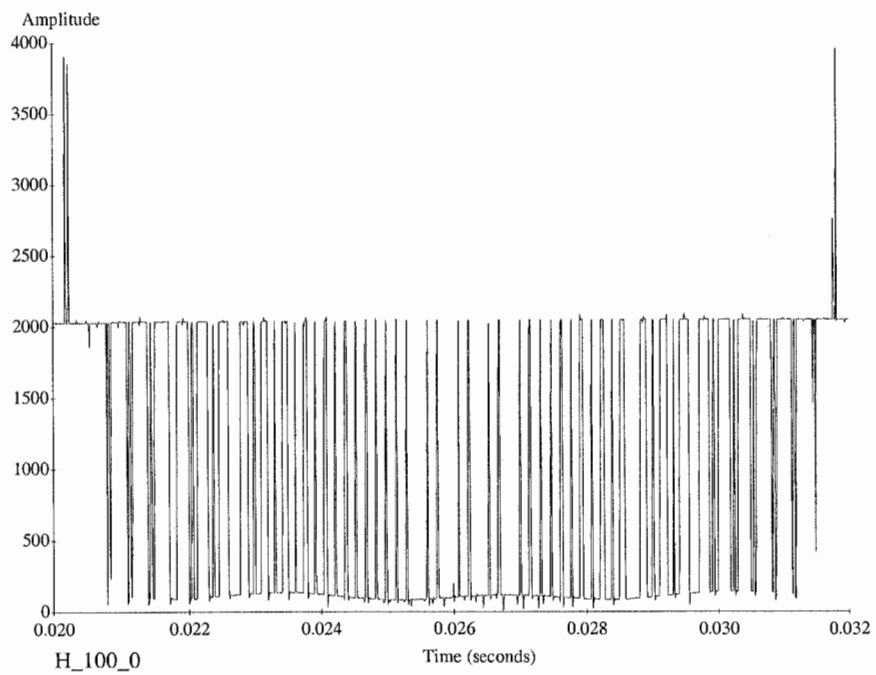

Figure 5.17: Measured drive voltage output waveform - f_d = 45Hz. Vertical axis is not calibrated.

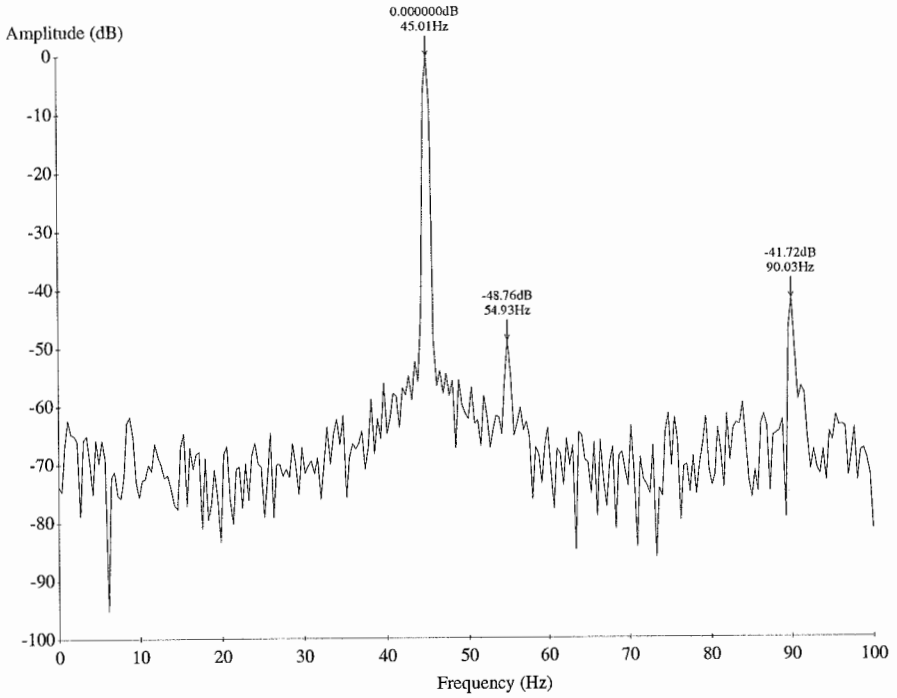

Figure 5.18: Frequency spectrum of PWM voltage waveform 0-100Hz.

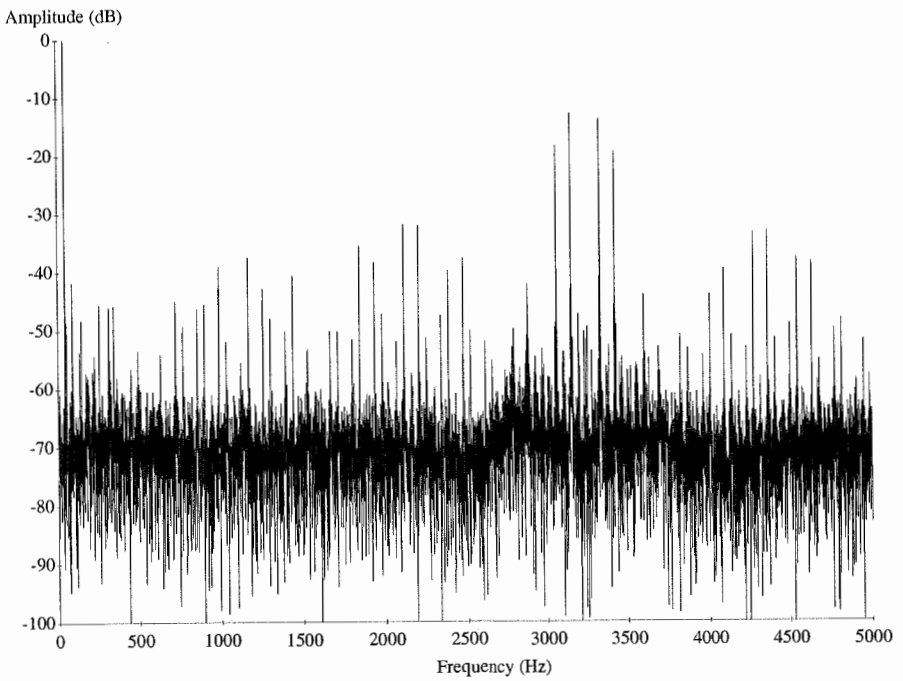

Figure 5.19: Frequency spectrum of PWM voltage waveform 0-5000Hz.

The variation of sideband amplitude with load was also examined. The results are plotted in Figures 5.20-5.25 together with the standard deviation. It can be seen that the amplitude of the upper sideband decreased with increasing load and the amplitude of the lower sideband increases with load. Thus, it is necessary to take into account the load level when examining the amplitude of sidebands for condition monitoring.

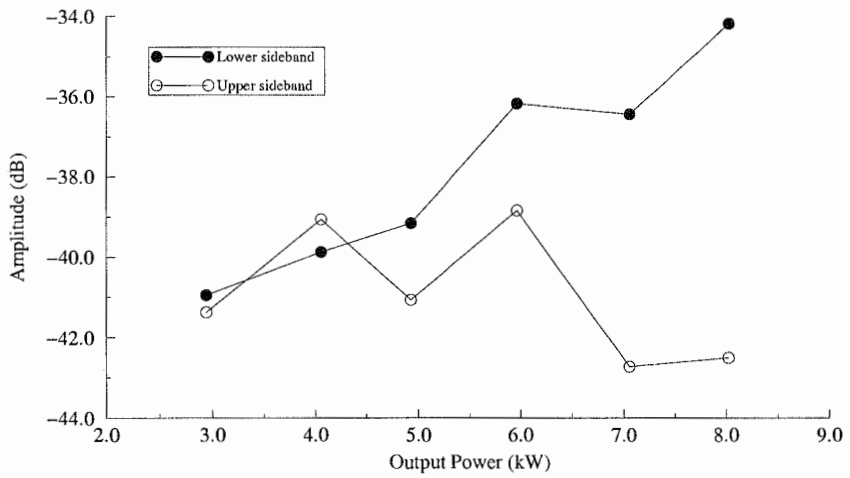

Figure 5.20: Variation of sideband amplitude with load (50Hz).

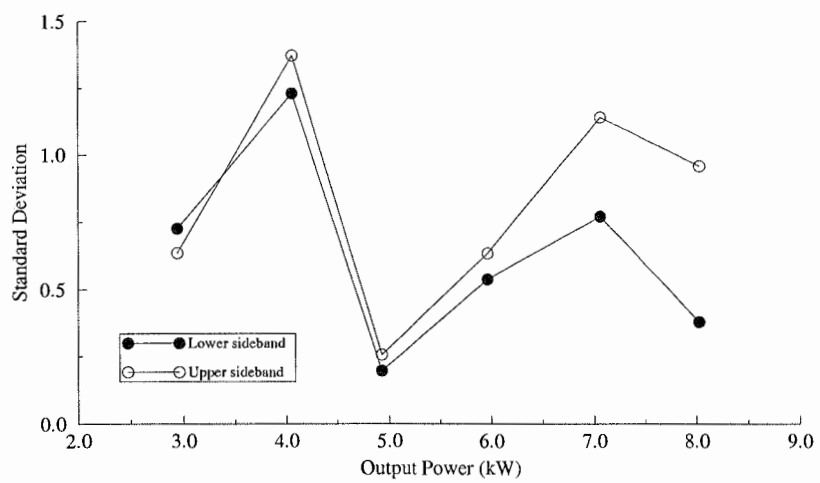

Figure 5.21: Standard deviation of sideband amplitude with load (50Hz).

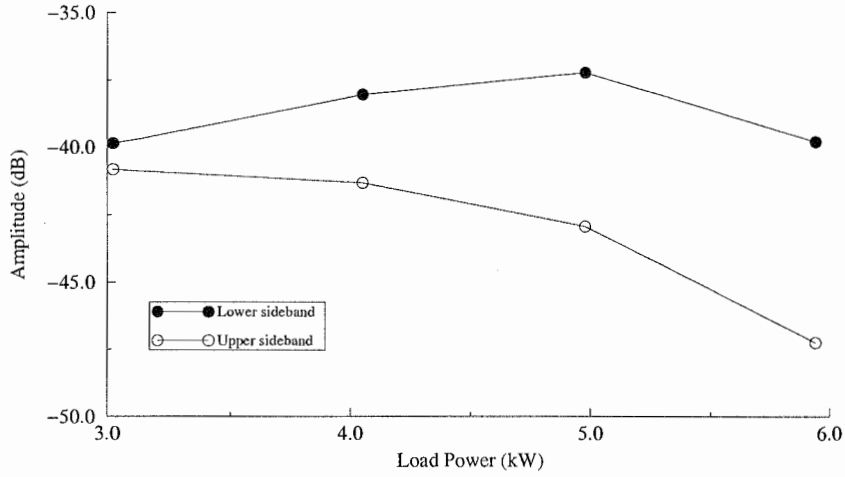

Figure 5.22: Variation of sideband amplitude with load (45Hz).

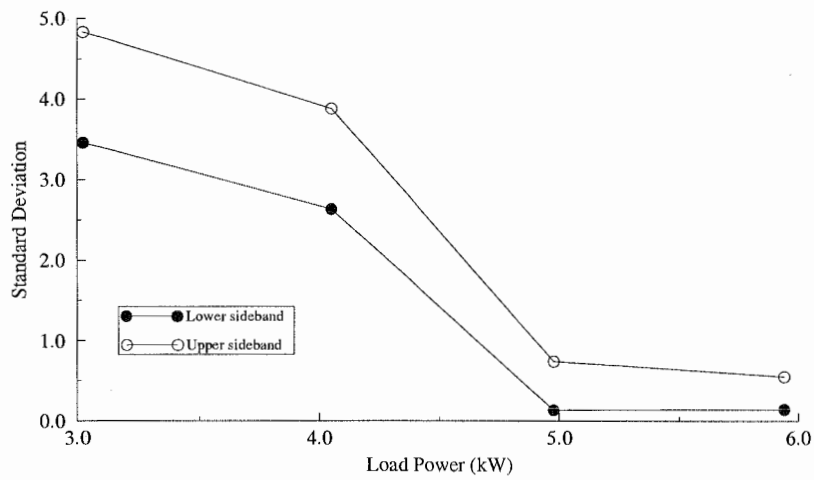

Figure 5.23: Standard deviation of sideband amplitude with load (45Hz).

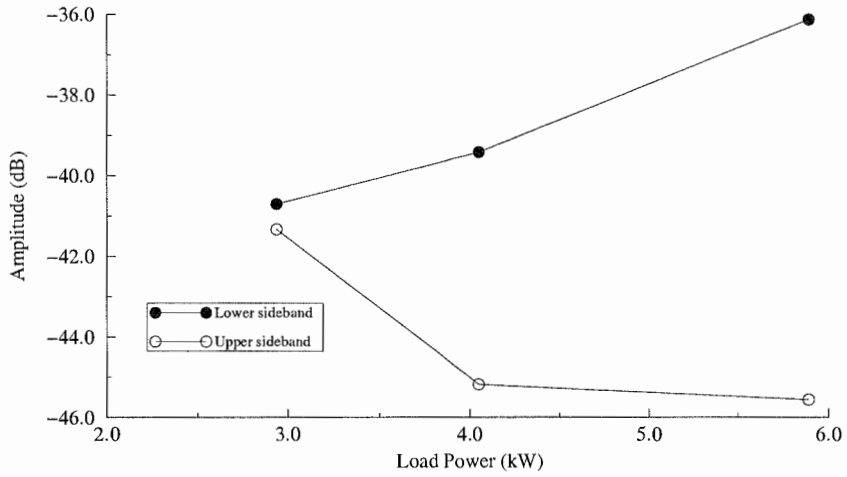

Figure 5.24: Variation of sideband amplitude with load (40Hz).

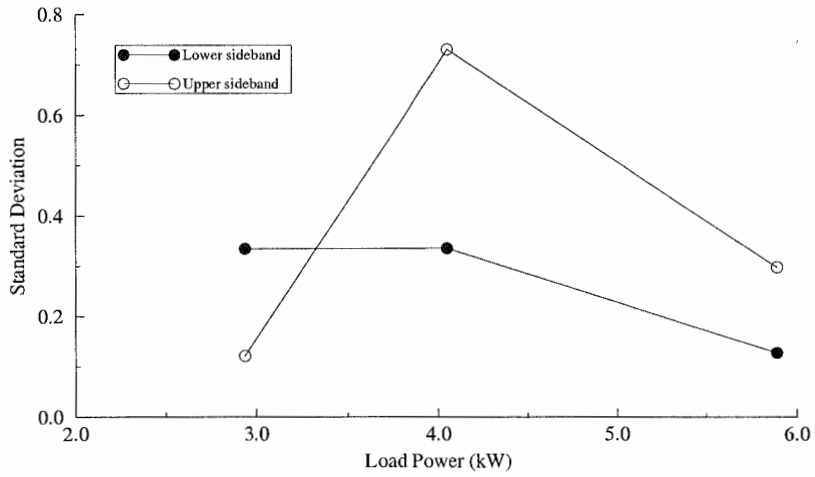

Figure 5.25: Variance of sideband amplitude with load (40Hz).

5.6 Summary

The advent of the semiconductor switch has led to the development of inverters which can produce an output waveform of controllable frequency. This chapter has examined various pulse-width modulation strategies which are used by inverters in order to produce the desired output voltage waveform. The strategies examined include natural-sampled, symmetric and asymmetric sampled,

optimised, random, and space vector. The frequency spectra of these strategies have been examined, as has the implications that they have for condition monitoring.

It was found that PWM strategies generally produce output harmonics at a number of discrete frequencies including the modulating frequency and harmonics, the carrier frequency and harmonics, and modulation products which combine the carrier and modulating frequencies. These frequency components are only a problem if they mask any fault frequency components. Most of the components are quite high in the frequency range, but this is dependent on the parameters used to implement the PWM waveform. They may mask the rotor slotting frequencies, which could be a problem for condition monitoring systems which depend on these to find the speed of the motor. The effect of drive harmonics could be completely disregarded if the drive and condition monitoring systems were integrated. The drive could then use an optimised PWM technique to eliminate any frequency components that may mask fault frequency components.

This chapter also considered the effect of the drive frequency on the amplitudes of the twice slip-frequency sidebands. The amplitude of the upper sideband was found to decrease with increasing drive frequency, whilst that of the lower sideband increased. The average of the two appeared to remain about constant. Hence it may be better to consider using the average of the upper and lower sideband amplitudes as an indicator of rotor damage rather than either in isolation.

The effect of load level on the amplitude of the sidebands was also examined by varying the load at constant supply frequencies. It was found that the amplitude of the lower sideband increased with increasing load, whilst that of the upper sideband decreased. Again it is necessary to consider both sidebands to gain a better indication of damage.

Finally an interesting phenomenon, which was termed the reflected frequency, was noted when examining the spectra collected at different drive frequencies. The reflected frequency appeared at (100 - f_d)Hz, where f_d is the drive frequency, in the spectrum of the stator current. This component can mask the sideband frequencies,

so it must be taken into account when examining the sideband amplitudes. The origin of the reflected frequency is unknown, though it is thought it could be a product of the rectification of the mains to produce the DC link voltage. A drive output waveform was observed to contain a large ripple component and its spectrum contained the reflected frequency. However attempts to simulate this were unsuccessful.

CHAPTER 6

Numerical Modelling of Induction Motors with Broken Rotor Bars

6.1 Introduction

A mathematical model of a system can be used to simulate the behaviour of a real system and aid in its study. If a set of mathematical equations can be obtained which describe the behaviour of the system, then numerical methods can be used to solve those equations to simulate the behaviour of the system.

In general, there are two distinct methods of simulating induction motors, finite element analysis and coupled circuit analysis. Finite element analysis effectively breaks the machine up into very small regions and then solves magnetic field equations subject to constraints at the boundaries of each of these regions [102]. A

complete flux pattern in the machine can thus be built up. Finite element analysis of a motor with an undamaged rotor has been shown to be successful, for dynamic modelling of VSD supplied motors [103], and for the calculation of torque pulsations [104]. Williamson et al [105] have described a time-stepping, transient finite element model of the induction motor. A steady-state finite element model, with broken rotor bars, was developed by Elkasabgy et al. [22]. A finite element model of the flux due to inter-bar currents in a motor with broken rotor bars is described by Muller and Landy [106]. A full transient, three-dimensional, finite element model of an induction motor with a broken rotor bar, has not yet been reported in the literature, probably because of the huge amount of computer processing time it would require to solve. Finite element analysis is not used in this thesis for this reason.

The alternative to finite element analysis is to view the induction motor as a set of coupled coils. An equivalent circuit for the motor can then be built up using the theory of coupled coils. Any voltages and currents of interest can then be calculated by solving the equivalent circuit equations. There are many equivalent circuit models for the induction motor ranging from the familiar per-phase equivalent circuit, to generalised machine theory models, and to models which specifically use the construction details of the motor to simulate individual stator and rotor windings.

This chapter examines the development of induction motor models in order to obtain a suitably detailed form for transient analysis. The model is then adapted for the modelling of an induction motor with a broken rotor bar, supplied by a pulse width modulated, voltage source inverter, variable speed drive (see Chapter 5). Some simulation results for this model are reported.

6.2 The Theory of Coupled Coils

Consider a system of n magnetically coupled circuits. Assuming that the circuits can be represented by concentrated coils where all fluxes in a coil link every turn of that coil, then there are three magnetic fluxes that must be considered. These are termed the magnetising flux, the leakage flux and the mutual flux.

The total flux linking any one of the coils is the superposition of the self flux and (n-1) components of mutual flux, as shown in Figure 6.1. For a coil, k, the self flux consists of two components, the magnetising flux, Φ_{mk}, which links all the other coils, and the leakage flux, Φ_{lk}, which links only the one coil. Thus the total flux is:

$$\Phi_k = \Phi_{lk} + \Phi_{mk} + \sum_{\substack{j=1 \\ j \neq k}}^{n} \Phi_{kj} \tag{6.1}$$

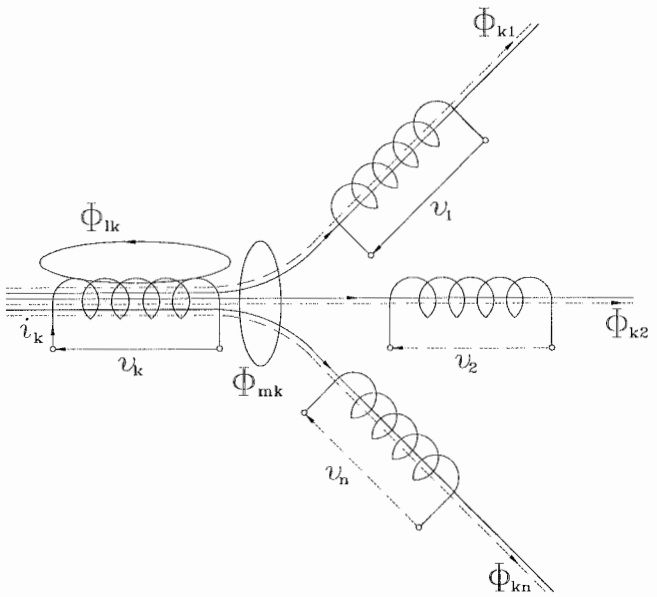

Figure 6.1: The total flux linking coil k is the sum of self and mutual fluxes.

The flux linkages are:

$$\lambda_k = N_k \Phi_k = \lambda_{lk} + \lambda_{mk} + \sum_{\substack{j=1 \\ j \neq k}}^{n} \lambda_{kj} \tag{6.2}$$

where N_k is the number of turns of coil k.

Since $\Phi = \Lambda N i$, these components may be written in terms of the magnetic permeance, Λ, of one turn as:

$$\begin{aligned}\lambda_{lk} &= N_k \Phi_{lk} = \Lambda_{lk} N_k^2 i_k \\ \lambda_{mk} &= N_k \Phi_{mk} = \Lambda_{nk} N_k^2 i_k \\ \lambda_{kj} &= N_k \Phi_{kj} = \Lambda_{kj} N_k N_j i_j\end{aligned} \tag{6.3}$$

where i_k is the current flowing in coil k.

Hence the following inductances may be defined:

Leakage inductance:

$$L_{lk} = \Lambda_{lk} N_k^2 = \frac{N_k \Phi_{lk}}{i_k} \tag{6.4}$$

Magnetising inductance:

$$L_{mk} = \Lambda_{mk} N_k^2 = \frac{N_k \Phi_{mk}}{i_k} \tag{6.5}$$

Self inductance:

$$L_k = L_{lk} + L_{mk} = (\Lambda_{lk} + \Lambda_{mk}) N_k^2 = \frac{N_k \Phi_{kk}}{i_k} \tag{6.6}$$

Mutual inductance between coil k and coil j:

$$M_{kj} = \Lambda_{kj} N_k N_j = \frac{N_k \Phi_{kj}}{i_j} \tag{6.7}$$

The permeances $\Lambda_{kj} = \Lambda_{jk}$, hence $M_{kj} = M_{jk}$.

The total flux linkage for each of the n coils can be expressed in matrix form using Equations (6.3)-(6.7)as:

$$\begin{bmatrix} \lambda_1 \\ \lambda_2 \\ \lambda_3 \\ \vdots \\ \lambda_n \end{bmatrix} = \begin{bmatrix} L_1 & M_{12} & M_{13} & \cdots & M_{1n} \\ M_{21} & L_2 & M_{23} & \cdots & M_{2n} \\ M_{31} & M_{32} & L_3 & \cdots & M_{3n} \\ \vdots & \vdots & \vdots & \ddots & \vdots \\ M_{n1} & M_{n2} & M_{n3} & \cdots & L_n \end{bmatrix} \begin{bmatrix} i_1 \\ i_1 \\ i_1 \\ \vdots \\ i_1 \end{bmatrix} \tag{6.8}$$

Which may be written:

$$\lambda = \mathbf{L}\mathbf{i} \tag{6.9}$$

The instantaneous voltage applied to coil k is:

$$v_k = i_k R_k + \frac{d\lambda_k}{dt} \tag{6.10}$$

Which is written in matrix form for all coils as:

$$\mathbf{v} = \mathbf{R}\mathbf{i} + \frac{d\lambda}{dt} \tag{6.11}$$

If the inductance matrix, **L**, is constant then (6.11) may be written:

$$\mathbf{v} = \mathbf{R}\mathbf{i} + \mathbf{L}\frac{d\mathbf{i}}{dt} \tag{6.12}$$

otherwise:

$$\mathbf{v} = \mathbf{R}\mathbf{i} + \mathbf{i}\frac{d\mathbf{L}}{dt} + \mathbf{L}\frac{d\mathbf{i}}{dt} \tag{6.13}$$

The induction motor can be modelled using this theory since the stator and rotor windings can be considered to consist of concentrated coils, linked by magnetic flux. Models can either use Equation (6.13) directly, or Equations (6.9) and (6.11) can be used simultaneously.

6.3 Simple Coupled Coil Models of the Induction Motor

Coupled circuit models view the induction motor as a set of concentrated windings, which move relative to each other, coupled by mutual magnetic fluxes. The simplest such model is the familiar per-phase equivalent circuit [41] as shown in Figure 6.2.

This model is only suited to the analysis of an induction motor under balanced, steady-state conditions. Using Kron's generalised machine theory [107]. and reference-frame theory [40], a two-phase equivalent circuit model can be derived [108], which can be used for a rotor with unbalanced impedances [40].

The models which are most useful for modelling broken rotor bars explicitly model each rotor bar. It is also useful if the model can account for transient effects in order to account for the effects of PWM voltage waveforms. A truly general model also includes the separate effects of each coil of the stator winding.

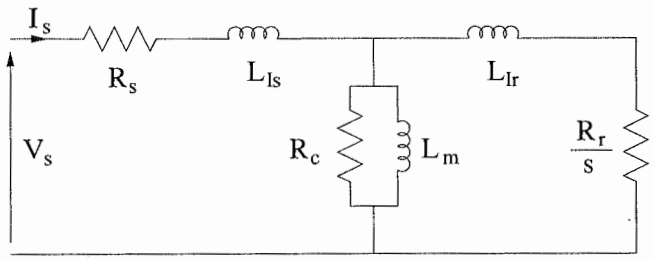

Figure 6.2: The per-phase equivalent circuit of the induction motor.

The simplest models for damaged rotors are based on the assumption that the rotor can be represented by an unbalanced three-phase winding. This is obviously more realistic in the case of wound-rotor induction machines that for squirrel-cage rotor machines.

One of the first models proposed was by Barton [109] which modelled the machine as a combination of positive and negative-sequence equivalent circuits. The basis of the model is that a balanced, positive-sequence, three-phase voltage system applied to the symmetrical stator winding of an induction motor, produces a magnetic field in the air gap, which rotates forward at synchronous speed ω_s. This field also rotates forward with respect to the rotor windings at a speed $s\omega_s$ (where s is the slip) and induces in these windings a voltage at this frequency (sf_s) which causes positive-sequence currents to flow in these windings.

If the rotor windings are asymmetrical, then the positive-sequence currents generate negative-sequence voltages. These cause a negative-sequence magnetic field to be produced in the air gap, which rotates backward relative to the rotor at a speed of $s\omega_s$ and backward relative to the stator at a speed of $(2s - 1)\omega_s$. The negative-sequence current induced in the stator windings thus has a frequency of $(2s - 1)f_s$.

This model is very simple and easy to implement. However it is not a comprehensive model of the machine and only allows for two components of the stator current, namely the mains frequency (f_s) and mains minus twice slip frequency ($f_s(1 - 2s)$). This is insufficient for a detailed analysis of a machine. The effect of individual bars must be incorporated into the model for a more comprehensive treatment.

Vas and Vas [110] extend this model to wound-rotor slip-ring machines, and transient operation. Vas [111] also presented some numerical results from this model. Models of wound rotor machines are not considered any further here because of the rarity of these machines today.

6.4 Coupled Coil Models of the Induction Motor with Individual Rotor Bars Modelled

A coupled coil model of the induction motor may be formed by considering both the stator and the rotor to consist of sets of concentrated coils. In order to form such a model successfully, it is necessary to know the detailed construction details of both the stator and the rotor. For the stator, the number of coils, number of turns per coil, and the physical arrangement and connection of the coils, must be known. For the rotor model, the number of rotor bars, and the physical dimensions needs to be known.

6.4.1 Rotor Model

A diagram of the squirrel cage rotor winding is shown in Figure 1.2. An electric circuit model of the cage can be formed by considering two adjacent rotor bars, and the end ring segments joining the two, as a mesh. If this is done for all of the N_b rotor bars, a model consisting of interconnected meshes is formed. A portion of such a model is developed in Figure 6.3.

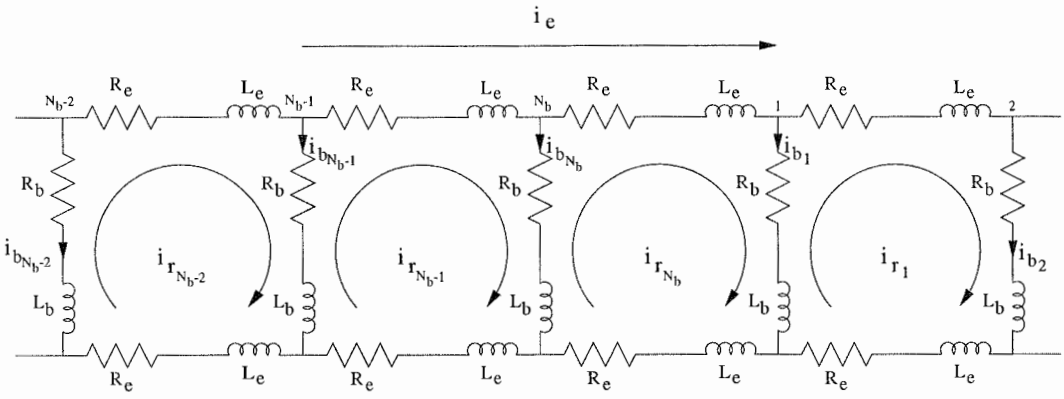

Figure 6.3: Equivalent circuit of rotor loops.

The rotor is modelled as N_b individual loops each with a loop current of i_{r_k} as shown above. R_b is the resistance of each rotor bar, R_e is the resistance of the section of end ring between adjacent bars, L_b is the rotor bar leakage inductance, and L_e is the end ring leakage inductance. The actual bar currents, i_{b_k}, may be found as the difference of adjacent mesh currents:

$$i_{b_k} = i_{r_{k-1}} - i_{r_k} \tag{6.14}$$

Thus writing Equations (6.9) and (6.1) for the rotor we have the following equations:

$$\mathbf{V}_r = \mathbf{R}_r \mathbf{I}_r + \frac{d\lambda_r}{dt} \tag{6.15}$$

$$\lambda_r = \mathbf{L}_{sr}^T \mathbf{I}_s + \mathbf{L}_{rr} \mathbf{I}_r \tag{6.16}$$

where

$$\begin{aligned}
\mathbf{V}_r &= \begin{bmatrix} v_{r_1} & v_{r_2} & \dots & v_{r_n} & v_e \end{bmatrix}^T = [\mathbf{0}] \\
\mathbf{I}_r &= \begin{bmatrix} i_{r_1} & i_{r_2} & \dots & i_{r_n} & i_e \end{bmatrix}^T \\
\mathbf{I}_s &= \begin{bmatrix} i_{s_1} & i_{s_2} & \dots & i_{s_n} \end{bmatrix}^T \\
\lambda_r &= \begin{bmatrix} \lambda_{r_1} & \lambda_{r_2} & \dots & \lambda_{r_n} & \lambda_e \end{bmatrix}^T
\end{aligned} \tag{6.17}$$

$$\mathbf{R}_r = \begin{bmatrix} 2(R_b+R_e) & -R_b & 0 & \cdots & 0 & R_e \\ -R_b & 2(R_b+R_e) & -R_b & \cdots & 0 & R_e \\ 0 & -R_b & 2(R_b+R_e) & \cdots & 0 & R_e \\ \vdots & \vdots & \vdots & \ddots & \vdots & R_e \\ -R_b & 0 & 0 & \cdots & 2(R_b+R_e) & \vdots \\ R_e & R_e & R_e & \cdots & R_e & N_b R_e \end{bmatrix} \tag{6.18}$$

$$\mathbf{L}_{rr} = \begin{bmatrix} L_{r_1}+2(L_b+L_e) & L_{r_1r_2}-L_b & \cdots & L_{r_1r_n}-L_b & L_e \\ L_{r_2r_1}-L_b & L_{r_2}+2(L_b+L_e) & \cdots & L_{r_2r_n} & L_e \\ L_{r_3r_1} & L_{r_3r_2}-L_b & \cdots & L_{r_3r_n} & L_e \\ \vdots & \vdots & \ddots & \vdots & \vdots \\ L_{r_nr_1}-L_b & L_{r_nr_2} & \cdots & L_{r_n}+2(L_b+L_e) & L_e \\ L_e & L_e & \cdots & L_e & N_b L_e \end{bmatrix} \tag{6.19}$$

There is no coupling between the magnetic field created by the end ring current and the stator magnetic field, hence the mutual inductance terms are zero:

$$\mathbf{L}_{sr} = \begin{bmatrix} L_{s_1r_1} & L_{s_1r_2} & \cdots & L_{s_1r_n} & 0 \\ L_{s_2r_1} & L_{s_2r_2} & \cdots & L_{s_2r_n} & 0 \\ \vdots & \vdots & \ddots & \vdots & \vdots \\ L_{s_mr_1} & L_{s_mr_2} & \cdots & L_{s_mr_n} & 0 \end{bmatrix} \tag{6.20}$$

The end ring current, i_e, is zero except when one end ring is broken. For simplicity, the remaining analysis will ignore i_e.

6.4.2 Stator Model

For a stator which consists of m coils, the following equations can be formed in a similar manner to the rotor, from Equations (6.9) and (6.11):

$$\mathbf{V}_s = \mathbf{R}_s\mathbf{I}_s + \frac{d\lambda_s}{dt} \tag{6.21}$$

$$\lambda_s = \mathbf{L}_{ss}\mathbf{I}_s + \mathbf{L}_{sr}\mathbf{I}_r \tag{6.22}$$

where

$$\begin{aligned}\mathbf{V}_s &= \begin{bmatrix} v_{s_1} & v_{s_2} & \dots & v_{s_m} \end{bmatrix}^T \\ \lambda_s &= \begin{bmatrix} \lambda_{s_1} & \lambda_{s_2} & \dots & \lambda_{s_n} \end{bmatrix}^T \end{aligned} \tag{6.23}$$

$$\mathbf{L}_{ss} = \begin{bmatrix} L_{s_1} & L_{s_1 s_2} & \cdots & L_{s_1 s_m} \\ L_{s_2 s_1} & L_{s_2} & \cdots & L_{s_2 s_m} \\ \vdots & \vdots & \ddots & \vdots \\ L_{s_m s_1} & L_{s_m s_2} & \cdots & L_{s_m} \end{bmatrix} \tag{6.24}$$

$$\mathbf{R}_s = \begin{bmatrix} R_{s_1} & 0 & \cdots & 0 \\ 0 & R_{s_2} & \cdots & 0 \\ \vdots & \vdots & \ddots & \vdots \\ 0 & 0 & \cdots & R_{s_m} \end{bmatrix} \tag{6.25}$$

Equations (6.15), (6.16), (6.21), and (6.22) form the general coupled circuit model for an induction motor with m stator coils and n rotor bars. In order to determine the parameters of this model and solve it, several different approaches have been taken. These differ in the assumptions made about the machine.

Williamson and Smith [105] developed a steady-state model which assumes that the speed is constant, and that the stator winding is a symmetrical three-phase winding supplied by a balanced three-phase voltage source. Since the stator is symmetrical and the speed is constant, the stator can be represented by a single phase with all quantities being phasors as all frequencies are fixed. Only two frequency components, mains frequency and a twice slip frequency component, are modelled in the stator current. The rotor loops have only slip-frequency loop currents flowing. This model is good for modelling mains supplied induction motors, however it is not a transient model as the speed is assumed constant.

Equations (6.15), (6.16), (6.21), and (6.22) may be combined to eliminate the flux linkage terms to obtain:

$$\mathbf{V}_r = \mathbf{R}_r \mathbf{I}_r + \frac{d\mathbf{L}_{sr}^T \mathbf{I}_s}{dt} + \frac{d\mathbf{L}_{rr} \mathbf{I}_r}{dt} \tag{6.26}$$

$$\mathbf{V}_s = \mathbf{R}_s \mathbf{I}_s + \frac{d\mathbf{L}_{sr} \mathbf{I}_r}{dt} + \frac{d\mathbf{L}_{ss} \mathbf{I}_s}{dt} \tag{6.27}$$

Now $\mathbf{L}_{rr}$ and $\mathbf{L}_{ss}$ are constant, hence:

$$\mathbf{V}_r = \mathbf{R}_r\mathbf{I}_r + \frac{d\mathbf{L}_{sr}^T}{dt}\mathbf{I}_s + \mathbf{L}_{sr}^T\frac{d\mathbf{I}_s}{dt} + \mathbf{L}_{rr}\frac{d\mathbf{I}_r}{dt} \tag{6.28}$$

$$\mathbf{V}_s = \mathbf{R}_s\mathbf{I}_s + \frac{d\mathbf{L}_{sr}}{dt}\mathbf{I}_r + \mathbf{L}_{sr}\frac{d\mathbf{I}_r}{dt} + \mathbf{L}_{ss}\frac{d\mathbf{I}_s}{dt} \tag{6.29}$$

Now
$$\frac{d\mathbf{L}_{sr}}{dt} = \frac{d\mathbf{L}_{sr}}{d\theta_m}\frac{d\theta_m}{dt} = \frac{d\mathbf{L}_{sr}}{d\theta_m}\omega_m \tag{6.30}$$

where θ_m is the angular displacement, and ω_m is the angular velocity.

Hence,

$$\mathbf{V}_r = \mathbf{R}_r\mathbf{I}_r + \omega_m\frac{d\mathbf{L}_{sr}^T}{d\theta_m}\mathbf{I}_s + \mathbf{L}_{sr}^T\frac{d\mathbf{I}_s}{dt} + \mathbf{L}_{rr}\frac{d\mathbf{I}_r}{dt} \tag{6.31}$$

$$\mathbf{V}_s = \mathbf{R}_s\mathbf{I}_s + \omega_m\frac{d\mathbf{L}_{sr}}{d\theta_m}\mathbf{I}_r + \mathbf{L}_{sr}\frac{d\mathbf{I}_r}{dt} + \mathbf{L}_{ss}\frac{d\mathbf{I}_s}{dt} \tag{6.32}$$

The quantities $\omega_m\, d\mathbf{L}_{sr}^T/d\theta_m\, \mathbf{I}_s$, and $\omega_m\, d\mathbf{L}_{sr}/d\theta_m\, \mathbf{I}_r$, are commonly referred to as rotational voltages as they arise due to the relative motion of the rotor coils with respect to stator coils.

In order to form a transient model, the mechanical equations governing the system must be considered. They are usually framed as:

$$\omega_m = \frac{d\theta_m}{dt} \tag{6.33}$$

$$\frac{d\omega_m}{dt} = \frac{1}{J}\left(T_e - T_L - K\omega_m\right) \tag{6.34}$$

$$T_e = \mathbf{I}_s^T\frac{d\mathbf{L}_{sr}}{d\theta_m}\mathbf{I}_r \tag{6.35}$$

where J = moment of inertia of rotor and load, T_e = electromagnetic torque developed by the motor, T_L = load torque on motor, and K = viscous friction.

6.5 Previous Work

Vas [112] combined Equations (6.31) and (6.32) into one matrix equation, and transformed the equations into the rotor reference frame in order to simplify solution of the equations. His model represented the stator windings as a symmetrical two-phase d-q model, with sinusoidal air gap magnetic flux density. He also considered the mechanical equations creating a full transient model.

Lipowski and Duggal [113] used a similar formulations to Vas, but failed to notice that a transformation in to the rotor reference frame greatly simplifies the solution. They examined only harmonics of the supply frequency in the stator current and defined a "distortion factor" which is a measurement of the harmonic distortion. The behaviour of the distortion factor with change in relative position of broken rotor bars was examined. It would appear that the distortion factor is not very useful as there was only a very small change in the value as the number of broken bars increased.

Ritchie et al. [114] also used Equations (6.31) and (6.32) combined into one set of equations, though in this case, they considered the stator and rotor variables in their respective reference frames. The stator winding was modelled as an ideal, sinusoidally distributed winding, excited from a balanced, three phase voltage source. The air gap length was regarded as constant and the rotor and stator surfaces smooth. They calculated a stator current waveform and compared it to a measured waveform. To simulate a broken bar, they assumed that the current in it was zero. This gave them a result which did not match the measured results very closely. Instead of modelling the broken bar by an open circuit, they adjusted the bar resistance until the simulated results matched those measured. This was found to occur when the broken bar resistance was about eleven times the normal bar resistance. They did not calculate the frequency spectrum of the stator current, nor did they use a metric to compare their simulated and measured waveforms, presumably making the comparison by eye.

Deng and Ritchie [101] also modelled the motor using flux linkages, that is Equations (6.15), (6.16), (6.21), and (6.22), again combined into one system of

equations, They discuss the stator magnetomotive force harmonics, but do not model them. Again, they use an ideal stator winding, but no mechanical equations. As a result, the stator current spectrum that is calculated, contains only the supply frequency and $(1\text{-}2s)f_1$ components.

6.6 Models Including the Stator Windings Explicitly

The first attempt at modelling the induction motor to explicitly include the effects of all magnetomotive force harmonics was that of Fudeh and Ong [115] [116]. They considered a general m coil stator winding, and n coil rotor winding, machine. However the stator windings were restricted to be identical, symmetrical and uniformly distributed, while the rotor had n uniformly distributed windings. They developed equations which transformed all the variables into the two phase α-β-0 form. They then used the equations developed to numerically model the torque-speed characteristics of induction motors [117].

Toliyat et al. [118] [119] took a different approach and modelled arbitrary stator windings by considering them to be concentrated coils. The magnetomotive force generated by each coil was assumed to be rectangular, as in Figure 2.2. The inductances were calculated using winding function analysis [119]. The model was then used to analyse a five phase induction machine for variable speed drive applications.

Toliyat and Lipo [120] and Luo et al. [121] considered the effect of broken rotor bars and end rings on this model. However, Luo only considered mains supply and current source inverter operation, while Toliyat considered mains supply and a six-step voltage source inverter. Toliyat and Lipo gave a stator current spectrum for a broken bar case, however it is difficult to interpret their results as their graphs are inadequately labelled. It would appear that their simulation produced only the $(1\text{-}2s)f_1$ sideband and did not produce the upper sideband. This is odd as their model includes the mechanical equations, and the upper sideband is a result of speed variation caused by the broken rotor bar. Luo et al. neglected the end ring current in their model, which calls into question the technique they use to model a

broken end ring. They model the broken end ring by forcing the relevant loop current to zero, however there should be a voltage across the intact end ring segment of the loop, which would cause a current to flow [105]. This should then affect the other loop currents; however this does *not* appear to have been taken into account.

The remainder of this chapter develops the equations to model an induction motor driven by a PWM-VSI variable speed drive. The effect of broken rotor bars on the frequency spectrum of the stator current is examined.

6.6.1 Phase Model [121]

Luo et al [121] use the model as defined by Equations (6.15), (6.16), (6.21), (6.22) , (6.33), and (6.34), although they neglect any friction coefficient *K*. Restating these equations, but neglecting the end ring current as broken end rings are not modelled:

$$\mathbf{V}_s = \mathbf{R}_s\mathbf{I}_s + \frac{d\lambda_s}{dt} \tag{6.36}$$

$$\mathbf{V}_r = \mathbf{R}_r\mathbf{I}_r + \frac{d\lambda_r}{dt} \tag{6.37}$$

$$\lambda_s = \mathbf{L}_{ss}\mathbf{I}_s + \mathbf{L}_{sr}\mathbf{I}_r \tag{6.38}$$

$$\lambda_r = \mathbf{L}_{sr}^T\mathbf{I}_s + \mathbf{L}_{rr}\mathbf{I}_r \tag{6.39}$$

$$\mathbf{T}_e = \mathbf{I}_s^T\frac{d\mathbf{L}_{sr}}{d\theta_m}\mathbf{I}_r \tag{6.40}$$

$$\frac{d\omega_m}{dt} = \frac{T_e - T_L}{J} \tag{6.41}$$

$$\frac{d\theta_m}{dt} = \omega_m \tag{6.42}$$

The machine inductances are calculated by the use of winding functions [119], which can model any arrangement of concentrated coils within the machine. Assuming that the permeance of iron is infinite, the mutual inductance between any two windings, *i* and *j*, in a machine is given by [119]:

$$L_{ij}(\theta_m) = \mu_0 lr \int_0^{2\pi} g^{-1}(\theta_m, \varphi) N_i(\theta_m, \varphi) N_j(\theta_m, \varphi) d\varphi \tag{6.43}$$

where θ_m is the angular position of the rotor with respect to a stator reference, φ is an angular position around the stator surface, $g^{-1}(\theta_m, \varphi)$ is the inverse gap function and is $1/g$ if the air gap is assumed to be uniform, l is the length of the rotor, and r is the average air gap radius. $N_i(\theta_m, \varphi)$ is the winding function of coil i, and represents the magnetomotive force distribution along the air gap for a unit current in coil i. The self-inductance for a coil can be calculated by setting $i = j$.

The winding function $N_i(\theta_m, \varphi)$ for a coil is similar to the magnetomotive force diagram in Figure 2.2, except that the span of the loop is not π, resulting in:

$$N_i(\theta_m, \phi) = \begin{cases} z_i\left(1 - \dfrac{\alpha_i}{2\pi}\right) & \theta_{i1} \le \theta \le \theta_{i2}; \\ -z_i \dfrac{\alpha_i}{2\pi} & \text{otherwise.} \end{cases} \tag{6.44}$$

where α_i is the angular span of the coil, which extends from θ_{i1} to θ_{i2}, z_i is the number of turns in the coil. For a squirrel cage rotor, each coil is considered to consist of just one turn, that is $z_i = 1$.

6.6.2 Line-to-line Model [121]

The model described by Equations (6.15), (6.16), (6.21), (6.22), (6.33), and (6.34) is unsuitable for simulating most motors, which have delta connected windings or a star point which is not readily accessible, as Equation (6.21) uses the stator phase voltages. These are not readily measured, but the line-to-line voltages are. If the voltages are balanced and the motor is symmetrical, then it is easy to calculate the phase voltages, however this is not useful for a general simulation which allows unbalanced conditions. A model can be developed from the equations which uses the line-to-line voltage rather than the phase voltage [121].

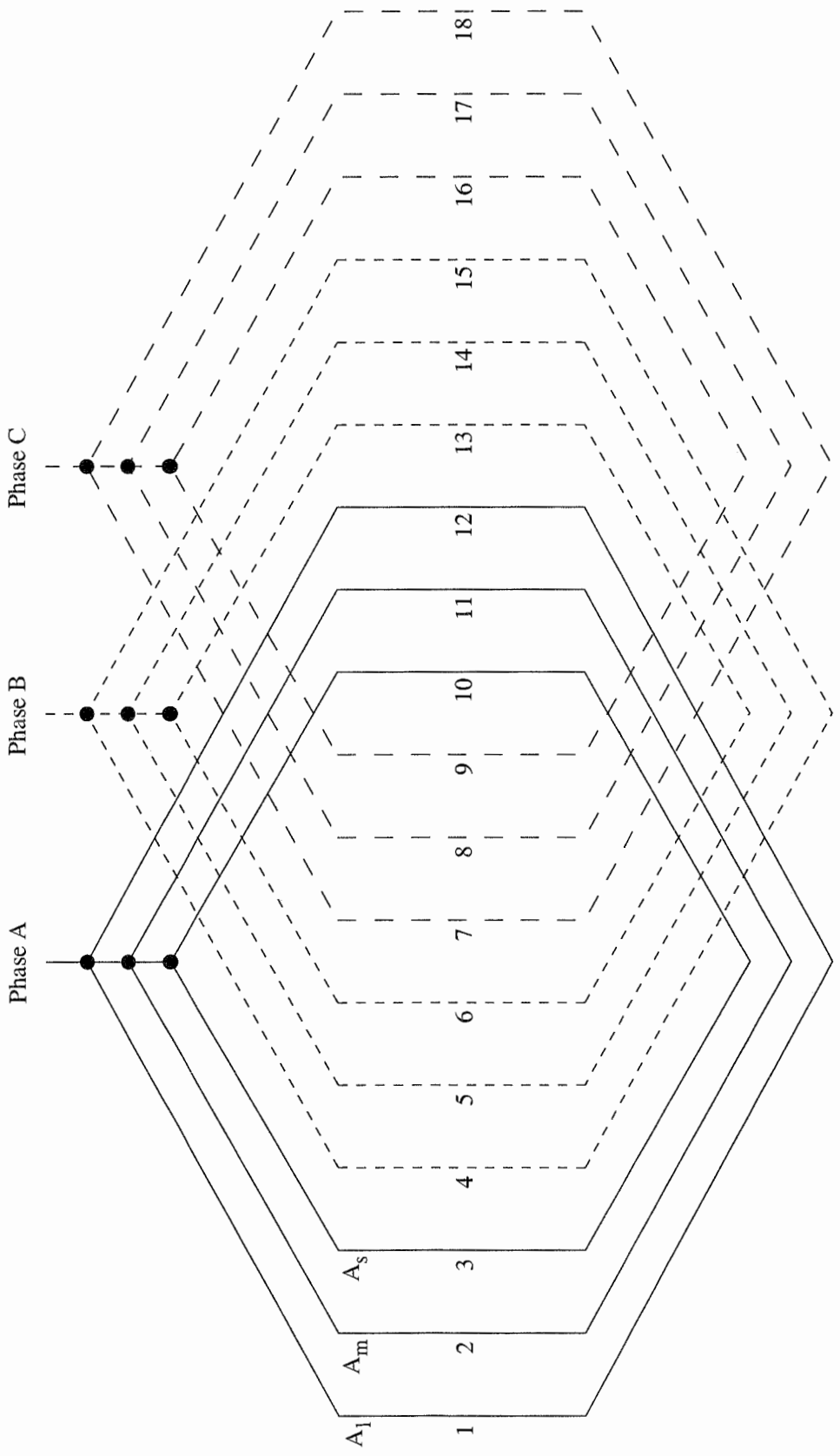

Figure 6.4: Developed diagram of the connections of half the stator windings in a concentrically wound stator with 36 slots and 3 coils per group.

In particular, for a three phase machine depicted in Figure 6.4, the stator equations are:

$$\begin{bmatrix} V_a \\ V_b \\ V_c \end{bmatrix} = \begin{bmatrix} R_a & 0 & 0 \\ 0 & R_b & 0 \\ 0 & 0 & R_c \end{bmatrix} \begin{bmatrix} I_a \\ I_b \\ I_c \end{bmatrix} + \begin{bmatrix} \frac{d\lambda_a}{dt} \\ \frac{d\lambda_b}{dt} \\ \frac{d\lambda_c}{dt} \end{bmatrix} \tag{6.45}$$

$$\begin{bmatrix} \lambda_a \\ \lambda_b \\ \lambda_c \end{bmatrix} = \begin{bmatrix} L_{aa} & L_{ab} & L_{ac} \\ L_{ba} & L_{bb} & L_{bc} \\ L_{ca} & L_{cb} & L_{cc} \end{bmatrix} \begin{bmatrix} I_a \\ I_b \\ I_c \end{bmatrix} + \begin{bmatrix} \mathbf{L}_{ar} \\ \mathbf{L}_{br} \\ \mathbf{L}_{cr} \end{bmatrix} \begin{bmatrix} I_{r_1} \\ I_{r_2} \\ \vdots \\ I_{r_n} \end{bmatrix} \tag{6.46}$$

where $\mathbf{L}_{ar}$, $\mathbf{L}_{br}$, and $\mathbf{L}_{cr}$ are 1 by n vectors of stator-rotor mutual inductances.

Subtracting from rows in both Equations (6.45) and (6.46) results in a model in terms of line-to-line voltages:

$$\begin{bmatrix} V_a - V_b \\ V_b - V_c \\ V_c - V_a \end{bmatrix} = \begin{bmatrix} R_a & -R_b & 0 \\ 0 & R_b & -R_c \\ -R_a & 0 & R_c \end{bmatrix} \begin{bmatrix} I_a \\ I_b \\ I_c \end{bmatrix} + \begin{bmatrix} \frac{d\lambda_a}{dt} - \frac{d\lambda_b}{dt} \\ \frac{d\lambda_b}{dt} - \frac{d\lambda_c}{dt} \\ \frac{d\lambda_c}{dt} - \frac{d\lambda_a}{dt} \end{bmatrix} \tag{6.47))}$$

that is,

$$\mathbf{V}_{sll} = \mathbf{R}_{sll}\mathbf{I}_s + \frac{d\lambda_{sll}}{dt} \tag{6.48}$$

$$\begin{bmatrix} \lambda_a - \lambda_b \\ \lambda_b - \lambda_c \\ \lambda_c - \lambda_a \end{bmatrix} = \begin{bmatrix} L_{aa} - L_{ba} & L_{ab} - L_{bb} & L_{ac} - L_{bc} \\ L_{ba} - L_{ca} & L_{bb} - L_{cb} & L_{bc} - L_{cc} \\ L_{ca} - L_{aa} & L_{cb} - L_{ab} & L_{cc} - L_{ac} \end{bmatrix} \begin{bmatrix} I_a \\ I_b \\ I_c \end{bmatrix} + \begin{bmatrix} \mathbf{L}_{ar} - \mathbf{L}_{br} \\ \mathbf{L}_{br} - \mathbf{L}_{cr} \\ \mathbf{L}_{cr} - \mathbf{L}_{ar} \end{bmatrix} \begin{bmatrix} I_{r_1} \\ I_{r_2} \\ \vdots \\ I_{r_n} \end{bmatrix} \tag{6.49}$$

If the stator of the machine is symmetrical and balanced then $L_{aa} = L_{bb} = L_{cc} = L_{self}$ and $L_{ab} = L_{ba} = L_{ac} = L_{ca} = L_{bc} = L_{cb} = L_{mutual}$, and the stator inductance matrix in Equation (6.49) is of the form:

$$\begin{bmatrix} L & -L & 0 \\ 0 & L & -L \\ -L & 0 & L \end{bmatrix} \tag{6.50}$$

where $L = L_{self} - L_{mutual}$. This matrix is singular and hence does not have an inverse, which makes numerical solution of the model, as described later, impossible. However, if there is no neutral connection to the machine the stator currents must sum to zero, hence the last equation of (6.49) may be replaced by an equation involving only the stator currents to obtain:

$$\begin{bmatrix} \lambda_a - \lambda_b \\ \lambda_b - \lambda_c \\ 0 \end{bmatrix} = \begin{bmatrix} L_{aa} - L_{ba} & L_{ab} - L_{bb} & L_{ac} - L_{bc} \\ L_{ba} - L_{ca} & L_{bb} - L_{cb} & L_{bc} - L_{cc} \\ 1 & 1 & 1 \end{bmatrix} \begin{bmatrix} I_a \\ I_b \\ I_c \end{bmatrix} + \begin{bmatrix} \mathbf{L}_{ar} - \mathbf{L}_{br} \\ \mathbf{L}_{br} - \mathbf{L}_{cr} \\ 0 \end{bmatrix} \begin{bmatrix} I_{r_1} \\ I_{r_2} \\ \vdots \\ I_{r_n} \end{bmatrix} \tag{6.51}$$

or:

$$\lambda_{sll} = \mathbf{L}_{sll}\mathbf{I}_s + \mathbf{L}_{srll}\mathbf{I}_r \tag{6.52}$$

Equations (6.48) and (6.52) together with the rotor equations (6.37) and(6.39) and the mechanical equations (6.41) and (6.42) form a complete line-to-line model of the induction machine.

6.7 Modelling a Broken Rotor Bar

A broken rotor bar can be modelled by simply removing one bar from the above model, and adjusting the matrices accordingly. For example, if the last rotor bar is broken (bar number N_b), then the rotor equivalent circuit has this bar removed and a double-width loop instead, as shown in Figure 6.5.

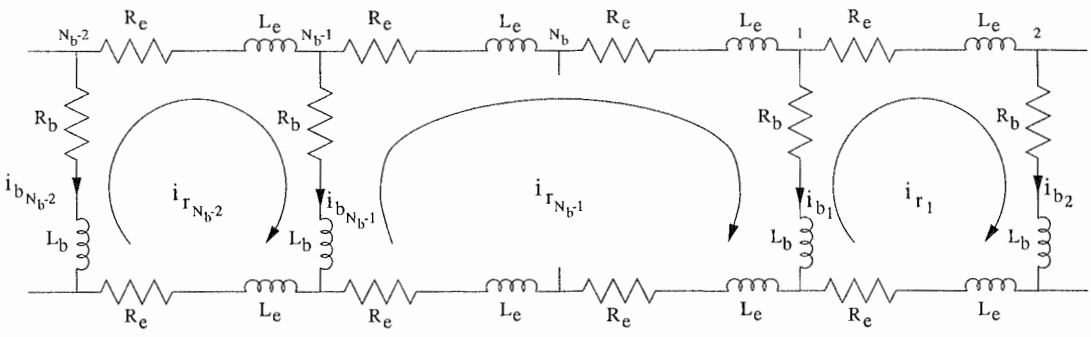

Figure 6.5: Equivalent circuit with rotor bar N_b broken.

This reduces the number of loop currents by one. The parameters for the new, double-width, loop are changed slightly from the non-broken case. The mutual inductance, L_{mrb}, between rotor loops increases, the self inductance, L_{rrb}, also changes, and the leakage for the new loop has two extra L_e components. That is, only the last row and column are different. The new rotor self-inductance matrix is then:

$$\mathbf{L}_{rr} = \begin{bmatrix} L_{rr}+2(L_b+L_e) & L_{mr}-L_b & \cdots & L_{mrb}-L_b \\ L_{mr}-L_b & L_{rr}+2(L_b+L_e) & \cdots & L_{mrb} \\ L_{mr} & L_{mr}-L_b & \cdots & L_{mrb} \\ \vdots & \vdots & \ddots & \vdots \\ L_{mrb}-L_b & L_{mrb} & \cdots & L_{rrb}+2L_b+4L_e \end{bmatrix} \tag{6.53}$$

Only the last element of the rotor resistance matrix changes, as no change occurs to the mutual resistances between rotor loops, hence:

$$\mathbf{R}_r = \begin{bmatrix} 2(R_b+R_e) & -R_b & 0 & \cdots & 0 \\ -R_b & 2(R_b+R_e) & -R_b & \cdots & 0 \\ 0 & -R_b & 2(R_b+R_e) & \cdots & 0 \\ \vdots & \vdots & \vdots & \ddots & \vdots \\ -R_b & 0 & 0 & \cdots & 2R_b+4R_e \end{bmatrix} \tag{6.54}$$

The stator-rotor inductance matrix also changes because one of the rotor loops is now a double-width loop, hence the winding function for the loop $N_i(\theta_m,\phi)$ changes since it is dependent on the span of the loop. Therefore any mutual inductances involving this loop must also change.

6.8 Solving the Model

The set of differential equations which form the model can be solved numerically to produce a time domain simulation of the behaviour of the motor. A model was constructed based on the 4 pole Pope motor (see Appendix A). This motor has 36 stator slots, with three coils per group, and a 32 slot rotor.

6.8.1 Calculation of Inductances

In order to calculate the inductances, the construction details of the machine must be known. The matrices $\mathbf{L}_{ss}$, $\mathbf{L}_{sll}$, $\mathbf{L}_{sr}$, $d\mathbf{L}_{sr}/d\theta_m$, and $\mathbf{L}_{rr}$, can then be calculated using Equation (6.43). Since the stator is symmetrical, it is sufficient to calculate inductances for $0 \leq \theta_m \leq \pi$ as the patterns repeat for the other half of the bore.

6.8.2 Calculation of Flux Linkages

The flux linkage vectors, λ_{sll} and λ_r, can be found by integrating Equations (6.36) and (6.37). Once the flux linkages and the inductance matrices are calculated, the stator and rotor current vectors can be found.

6.8.3 Calculation of Currents

In order to solve the model it is necessary to find expressions for $\mathbf{I}_r$ and $\mathbf{I}_s$, which may be found by solving Equations (6.38), (6.39), (6.48), and (6.52) simultaneously to give:

$$\mathbf{I}_r = \left(\mathbf{L}_{rr} - \mathbf{L}_{sr}^T \mathbf{L}_{sll}^{-1} \mathbf{L}_{srll}\right)^{-1} \left(\lambda_r - \mathbf{L}_{sr}^T \mathbf{L}_{sll}^{-1} \lambda_{sll}\right) \tag{6.55}$$

$$\mathbf{I}_s = \mathbf{L}_{sll}^{-1} \lambda_{sll} - \mathbf{L}_{sll}^{-1} \mathbf{L}_{srll} \left(\mathbf{L}_{rr} - \mathbf{L}_{sr}^T \mathbf{L}_{sll}^{-1} \mathbf{L}_{srll}\right)^{-1} \left(\lambda_r - \mathbf{L}_{sr}^T \mathbf{L}_{sll}^{-1} \lambda_{sll}\right) \tag{6.56}$$

6.8.4 Calculation of Speed and Angular Displacement

The torque generated by the motor can be calculated from Equation (6.40), then this can be used in Equation (6.41) which is integrated to find ω_m. This is then integrated (6.42) to obtain θ_m.

6.9 Numerical Solution of Ordinary Differential Equations

An ordinary differential equation (ODE) can always be written as a set of first-order differential equations of the form:

$$\frac{dy}{dt} = f\left(t, y(t)\right) \tag{6.57}$$

This is usually expressed as an initial value problem, that is, an initial value $y(a) = y_0$ is given and it is required to find a function $y(t)$ defined over an interval $[a,b]$ which satisfies Equation (6.57). Thus an initial value is required, as well as the differential equation.

There are a number of techniques for numerically solving initial value problems. The simplest, and easiest to understand, are one-step methods. Given the initial value problem above, we seek an approximation to the solution $y(t)$. The general one-step method is an iteration of the form:

$$y_{i+1} = y_i + h\phi\left(x_i, y_i; h\right), \qquad i = 0,1,\ldots,n-1. \tag{6.58}$$

The function $\phi(x_i,y_i;h)$ is called the increment function, and provides a means of obtaining y_{i+1} from y_i. The step size, h, may be changed when proceeding from a to b to estimate $y(t)$ if an error analysis indicates a need to do so. The two one-step methods which will be considered here are Euler's method and the Runge-Kutta method.

6.9.1 Euler's Method

Euler's method is the simplest one-step method. Given that we know $y(a) = y_0$ and that we also know the gradient of the curve, $y' = f(t,y)$, at that point, then it seems reasonable that the next point on the curve could be found by proceeding along a line of this gradient. So $y(a+h)$ can be approximated by:

$$y(a+h) \approx y(a) + hy'(a) = y_0 + hf\left(a, y_0\right) \tag{6.59}$$

In general, the estimated value of $y(a+h)$ will not be on the solution curve $y(t)$, but for well-behaved functions and sufficiently small step size a satisfactory

approximation should result. Continuing the process of (6.59) gives the general Euler's method iteration:

$$y_{i+1} = y_i + hf(x_i, y_i) \qquad i = 0,1,\ldots,n-1 \tag{6.60}$$

where the step size $h = (b-a)/n$.

6.9.2 Runge-Kutta Methods

The inaccuracy of Euler's method stems from the method used to find the amount, $h\phi(x_i,y_i;h)$, by which the solution $y(t)$ changes over the step h. It is assumed that the value of the gradient remains constant over the whole step, which is not generally true. A better estimate could be gained by examining the gradient at various points close to $(x_i,y(x_i))$, in order to get a better idea of the behaviour of the gradient. In doing this the following is obtained:

$$\phi(x_i, y_i; h) = w_1 f(p_1, q_1) + w_2 f(p_2, q_2) + \cdots + w_m f(p_m, q_m) \tag{6.61}$$

That is, $\phi(x_i,y_i;h)$ is a weighted average of the gradients near $(x_i,y(x_i))$. Euler's method is the case where $m = 1$ and $w_1 = 1$, and only one term is used. The weights w_k and the sample points (p_k, q_k) in (6.61) must be chosen carefully for best results. The Runge-Kutta methods are one scheme for choosing these values [62]. A very popular Runge-Kutta method is the 4th order with weights selected so that:

$$y_{i+1} = y_i + \frac{h}{6}[K_1 + 2K_2 + 2K_3 + K_4] \tag{6.62}$$

where

$$K_1 = f(x_i, y_i)$$
$$K_2 = f\left(x_i + \frac{h}{2}, y_i + \frac{h}{2}K_1\right)$$
$$K_3 = f\left(x_i + \frac{h}{2}, y_i + \frac{h}{2}K_2\right)$$
$$K_4 = f(x_i + h, y_i + hK_3)$$

It is popular because it is easy to implement, and virtually always succeeds in giving a good approximation. The drawbacks are that it is computationally inefficient and errors are harder to control than other methods. The Runge-Kutta can also be modified so that the step size, h, is not constant, but changes in response to an estimation of the error in the approximation. These are generally referred to as variable-step Runge-Kutta methods or Runge-Kutta-Fehlberg methods.

6.9.3 Other Methods of Solving ODEs

Other alternative methods of solving ODEs exist [60] such as Richardson extrapolation, also known as Burlisch-Stoer methods, and predictor-corrector methods. Both of these methods are more complex to implement than the Runge-Kutta and also less likely to converge. However they are potentially more accurate and faster to compute.

6.10 Numerical Solution of the Induction Motor Model

Equations (6.36) and (6.37) can be written in the form of (6.57) by the substitution of (6.53) and (6.54). Hence these equations can be solved using a Runge-Kutta method to find the flux linkages, λ_{sll} and λ_r. This is not the case for the mechanical equations (6.41) and (6.42), which cannot easily be written in the form $y' = f(t,y)$. Hence a Runge-Kutta method cannot be used to find the solution. Instead a Euler method was chosen to perform the integration.

In order to solve the system of equations it is necessary to calculate the various coefficient matrices. Some of the matrices are constant, whereas others are dependent on the angular displacement of the rotor and must be calculated for every iteration. Those which are constant involve either the stator or the rotor only, and these need only be calculated once. These matrices are $\mathbf{R}_s$, $\mathbf{L}_{ss}$, $\mathbf{R}_r$, $\mathbf{L}_{rr}$, $\mathbf{R}_{sll}$, and $\mathbf{L}_{sll}$. The stator-rotor inductance matrices, $\mathbf{L}_{sr}$, $\mathbf{L}_{srll}$, and $d\mathbf{L}_{sr}/d\theta_m$, are dependent on the exact position of the rotor at each iteration, hence these matrices must be re-calculated at every step. This is not difficult as the mutual inductance

curves are piecewise linear functions, which may be implemented using a fast, table-lookup function.

6.10.1 Stator-Rotor Mutual Inductance

The stator-rotor mutual inductance curves were calculated using Equation (6.44), and the stator winding layout shown in Figure 6.4. The resulting curves for both a normal rotor loop, and a broken bar (double width) loop are shown, as are the derivatives of these two curves.

Unfortunately it was found that the model was numerically unstable with the derivative of inductance curves as shown in Figure 6.6. The step changes in the derivative curves caused the torque calculation to become unstable. In order to circumvent this problem, it was noted that a real winding coil in an induction motor is not infinitely narrow. In fact, the winding occupies the width of one whole slot, hence instead of there being a step change in the derivative of inductance curve, as in Figure 6.6, there should be a gradual change over the slot width. For simplicity the winding function was modelled as a linear change over the slot width, for both the stator and the rotor windings. When this type of change is taken into account the resulting derivative of the mutual inductance curves is modelled as shown in Figure 6.7. Using these curves stabilised the model.

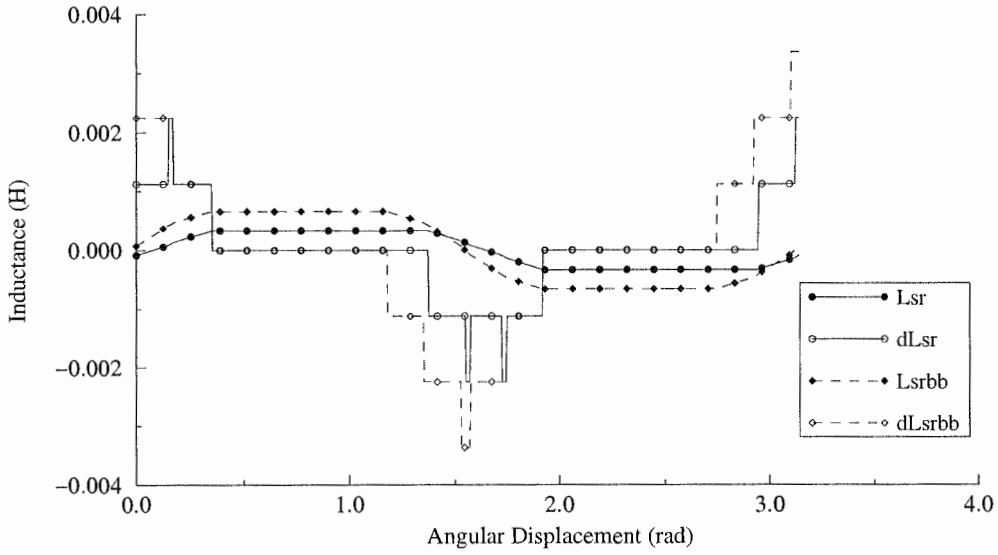

Figure 6.6: Inductance and derivative curves calculated for the Pope motor.

Also considered was the effect of modelling the inductance curves as pure sinusoids, which is the basis of most models which consider "ideal" stator windings. The stator-rotor mutual inductance curves which result from this assumption are shown in Figure 6.8.

The speed and torque curves calculated for a no-load run-up test, using the sinusoidal form of the inductance curves is shown in Figure 6.9. The corresponding curves for the inductances shown in Figure 6.7 (referred to as piecewise-linear inductance curves), is shown in Figure 6.10. It can be seen that the torque curve in the piecewise-linear case are much more jagged. This is a result of the discontinuities in the derivative of inductance curves.

6.10.2 Tuning Stator Inductance Value

It was found, through trial and error, that the torque output of the modelled motor was highly dependent on the value used for the sum of the magnitudes of the stator self and mutual inductances, L in Equation (6.50). Changing this value only slightly had a large effect on the torque and speed calculated. In order to obtain a useful model this value was tuned until the motor performance was similar to that

measured from the test motor. In order to do this the value of L was adjusted to give best results in terms of torque, speed and current, and also to match the run-up time of the test motor. The other model parameters were adjusted slightly to examine the effects on the simulation, however none exhibited such strong influence as the stator inductances.

6.10.3 Computer Implementation Issues

The model was implemented using a program written in the 'C' language, using the Meschach [122] matrix library to implement the matrix functions. Matrix inverses were calculated using a singular value decomposition (SVD) routine. The program was run on a variety of computers, but the principal platform was a Sun Microsystems SPARC 10, Model 402, with dual 40MHz processors. The amount of RAM required was minimal (less than 1 megabyte).

For simulating 50Hz sinusoidal mains voltages, a step size of 78.125 micro-seconds was used, as this effectively synchronously sampled the current waveforms. The maximum step size for satisfactory simulation of PWM voltage waveforms was found to be about 10 micro-seconds. Simulating the Pope machine with PWM voltage waveforms required about 34 hours of CPU time in order to produce one second of simulated time data! It is quite possible that the program could be optimised somewhat in various areas, as no serious effort was expended, however it would still be a *very* CPU intensive task. It may also be possible to make some performance gains by using an alternative to the fourth order Runge-Kutta algorithm for integration, but the problem remains that both the PWM voltage and the derivative of the stator-rotor mutual inductance contain step changes. This can be troublesome for most integration algorithms, which is why the Runge-Kutta was chosen as it converges under most circumstances.

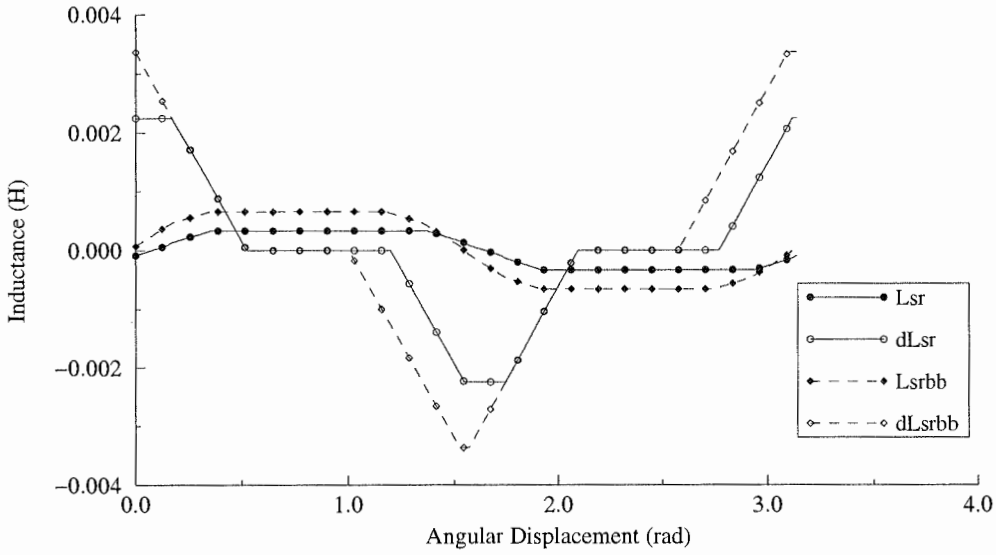

Figure 6.7: Modified stator-rotor mutual inductance curves.

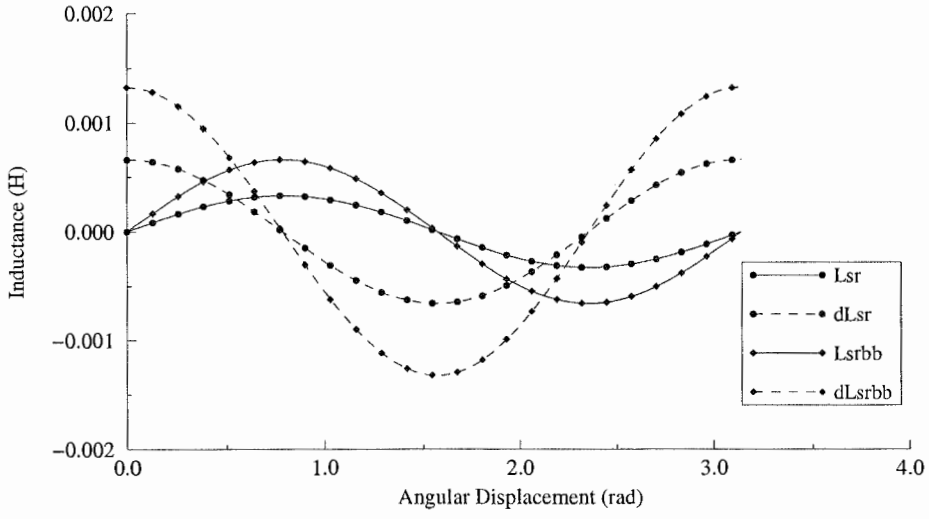

Figure 6.8: Sinusoidal stator-rotor mutual inductance curves.

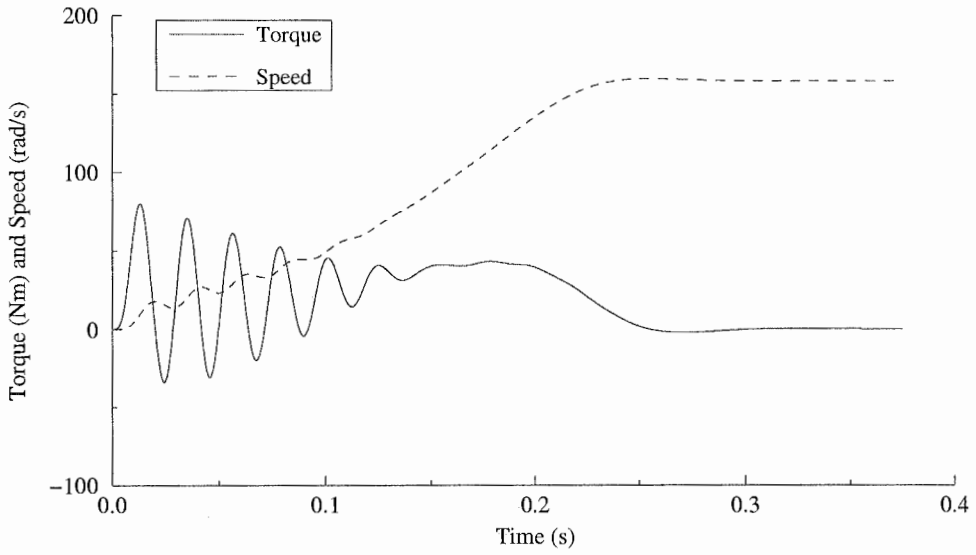

Figure 6.9: Speed and torque for simulated start up with sinusoidal stator voltage and sinusoidal inductance curves.

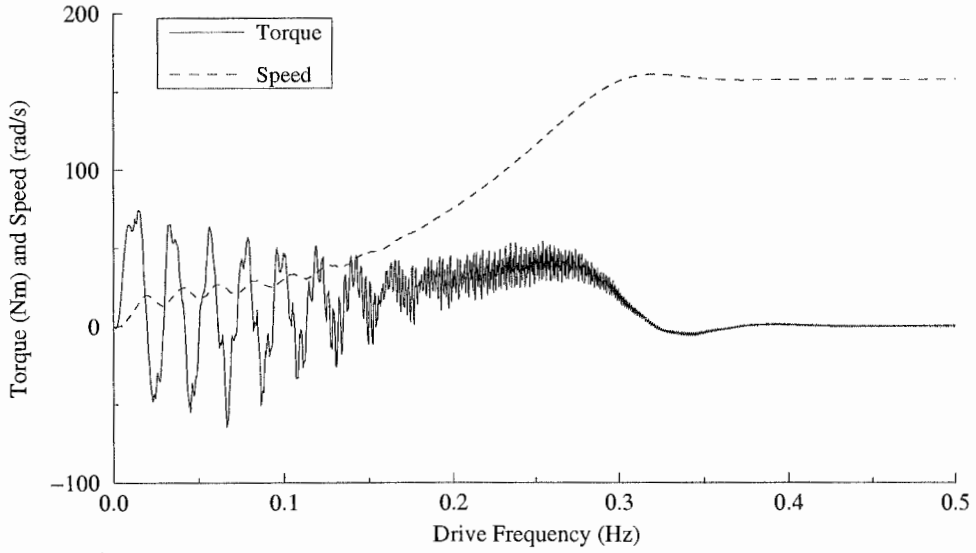

Figure 6.10: Speed and torque for simulated start up with sinusoidal stator voltage and piecewise linear inductance curves.

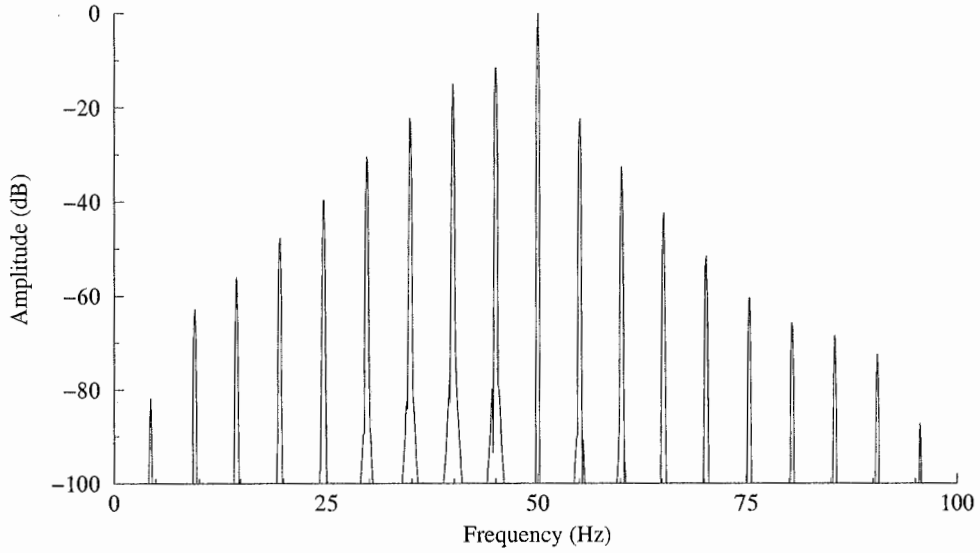

Figure 6.11: Spectrum of simulated stator current using a sinusoidal voltage supply and sinusoidal inductance curves, with a broken rotor bar.

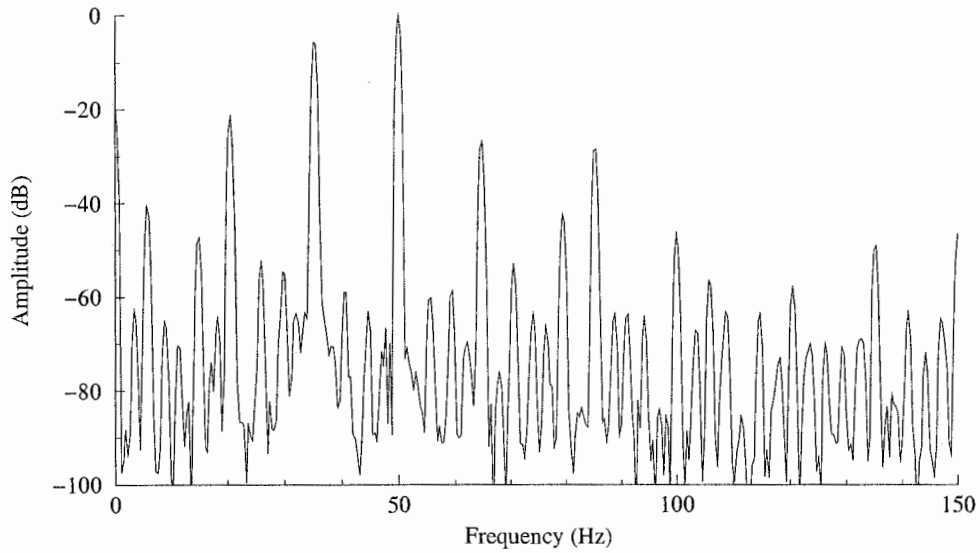

Figure 6.12: Spectrum of simulated stator current using a 50Hz PWM voltage supply and piecewise linear inductance curves, with a broken rotor bar.

6.10.4 Simulation of Broken Rotor Bars

The spectrum of the stator current for a motor with broken rotor bars is shown in Figure 6.11, for sinusoidal voltage and sinusoidal inductance curves. The slip is about 0.060 which gives a twice slip-frequency of 6.0Hz. The twice slip-frequency sidebands and their multiples, are the only components of the spectrum other then the 50Hz supply frequency. The lower twice slip-frequency sideband has an amplitude of about -12dB relative to the fundamental, whilst the upper sideband has an amplitude of about -22dB. Multiples of these sidebands decrease in amplitude in an approximately linear fashion.

Figure 6.12 is the frequency spectrum of the stator current for a motor with a broken rotor bar, supplied by a PWM voltage and using the piecewise-linear inductance curves. The slip is 0.149, thus twice slip-frequency is 14.9Hz. Sidebands around the 50Hz supply frequency peak can be noticed at these frequencies. The amplitudes of the lower sidebands are even greater than those in the sinusoidal case. The lower sideband has an amplitude of about -6dB, whilst the upper sideband has an amplitude of about -26dB.

6.11 Summary

This chapter has outlined the development of a model for the cage rotor induction motor, which takes into account the physical arrangement of the stator windings and rotor bars. It is a model that incorporates mechanical equations so that full transient simulation can be performed. The model has the basic theory of magnetically coupled coils as its foundation, and models the interaction of the stator and rotor magnetic fields as the rotor rotates. The model is modified so that the effects of broken rotor bars may be incorporated.

A computer implementation of the model was used to simulate the operation of a laboratory motor, both with and without a broken rotor bar. Simulations for both mains and PWM voltage operation were performed, and the resulting stator current spectrum analysed. The expected $(1\text{-}2s)f_1$ frequency component was observed to be present when a broken bar was simulated. In addition to this, the

upper sideband $(1+2s)f_1$ was also observed due to the full transient nature of the model, which allowed the speed and torque to oscillate.

The amplitude of the sidebands was rather higher than those measured from the test motor. This was probably due to inter-bar currents in the test motor, which would tend to reduce the amplitude of the magnetic disturbance, and hence, the amplitude of the sidebands that were measured. Inter-bar currents were not accounted for in the model, which assumed that the bars were insulated from the iron core, whereas in practice they are not. It would be possible to account for the effects of inter-bar currents using the model of Walliser and Landy [53], or that of Heller [47]. However, these models would add extra components to the matrices used in the differential equations. Given that the model already required 34 hours per second of simulated time to run, this would make the model intractable at the present time.

CHAPTER 7

Experimental Studies

7.1 Introduction

This thesis has examined methods of detecting rotor faults in induction motors driven by variable speed drives and developed a numerical model to simulate such a motor. Some work has been done previously on detecting rotor damage in induction motors operating from the mains supply, however very little interest has been shown in induction motors supplied by variable speed drives. Given the large installed base of variable speed drives, and that a large number of new drive installations in industrial situations tend to be variable speed drives, this topic is of growing importance.

Several methods of detecting rotor damage have been examined in this thesis. The basic theory of detecting damage in a motor with a variable speed drive is the same as that with the motor driven from the mains supply. However, there are a number of complicating factors which make the detection of broken rotor bars with a variable speed drive difficult; the major problem is, of course, that the

output frequency of the variable speed drive can vary, whereas the frequency of the mains is constant for all practical purposes. This makes the detection of fault frequency components quite difficult, as the components must be detected relative to a changing fundamental supply frequency.

In addition to this, the drive itself introduces various frequency components due to the modulation techniques used to control the drive output frequency. These frequencies may mask or interfere with fault frequency components, and must be taken into account.

A numerical model of the induction motor was developed in order to simulate the effects of a broken rotor bar.

This chapter starts by examining the differences in the current spectra between the motor with an undamaged rotor and one with a damaged rotor when that motor is supplied by the mains or a VSD. This shows the effect of rotor damage on the spectra and also the difference when a VSD supply is used instead of the mains supply.

An example of using the PLL circuit developed in Chapter 4 to confirm the diagnosis of rotor damage in a motor supplied by a VSD driving a pump in an industrial plant is also described. This motor was initially diagnosed by a commercial vibration condition monitoring company as having rotor damage, the plant operating company wanted confirmation of this diagnosis by electrical monitoring methods before proceeding with any remedial action. Fortunately the electrical testing performed confirmed the results of the vibration testing.

7.2 Differences Between the Detection of Broken Rotor Bars in Mains-supplied and VSD-supplied Induction Motors

It has already been established that broken rotor bars in mains-supplied induction motors can be detected by examining the frequency spectrum of the stator current for the presence and amplitude of sidebands around the supply frequency at twice the slip frequency. It stands to reason that such sidebands should be present when

the motor is supplied by a variable speed drive. The differences in the frequency spectra between the two situations needs to be examined.

It would be very difficult, if not impossible, to fully describe the difference between frequency spectra theoretically, hence an experimental approach is taken. In order to make a valid comparison, one motor is used with two rotors, one of which is deliberately damaged. This motor is then operated from either the mains supply or a VSD, with either rotor in order that the resulting spectra may be compared.

7.2.1 Experimental Arrangements

A motor was bought specifically for conducting laboratory tests. It is the previously mentioned 7.5kW Pope induction motor, the specifications of which are given in Appendix A. Two rotors were purchased for this machine in order to have one which could be intentionally damaged and one which could remain undamaged for comparison purposes. The alternative to this would be to construct a machine which would allow a rotor bar to be "broken" as has been described by several authors [7, 29]. The former approach was taken in preference to building a laboratory motor for two reasons; one was that it was a commercially designed and manufactured motor exactly as would be used in industry hence could be expected to perform as such, whereas a constructed laboratory machine may have different performance characteristics. The other reason was that budgetary constraints would not allow a major project to construct a machine to be undertaken.

A commercially produced VSD (a SAMI GS drive manufactured by ABB) was also purchased in order to drive the motor. The drive selected was rated at 20kVA in order to allow the motor to be moderately overloaded without tripping the drive overload protection, should the need arise.

This motor was coupled to a DC generator and resistor load board in order to provide a variable load on the motor. The DC generator specifications are included in Appendix A. A photograph of this arrangement is included as Figure

7.1. The load resistor bank can be seen to the right, next to the loading DC generator, the test motor is under the table, and the data acquisition computer and VSD are on top of the table. Figure 7.2 gives another view of the data acquisiton equipment setup. The FCC current clamp can be seen resting on top of the sample-and-hold hardware, which is next to the acquisition computer. The VSD unit can be seen at the top-left corner of the picture.

Figure 7.1: Arrangement of motor and loading generator.

Figure 7.2: Arrangement of data acquisition system.

7.2.2 Undamaged Rotor Measurements

In order to make a comparison between damaged and undamaged rotors some baseline measurements were made with the undamaged rotor in the machine. The motor was loaded by a DC generator connected to a resistor load bank. The load was adjusted by changing the field voltage of the DC machine until the power measured going into the resistor load bank was approximately 7.5kW as this is the rated output power of the motor. The mains frequency is 50Hz, hence the VSD output frequency was also adjusted to 50Hz so that a valid comparison between the spectra could be made.

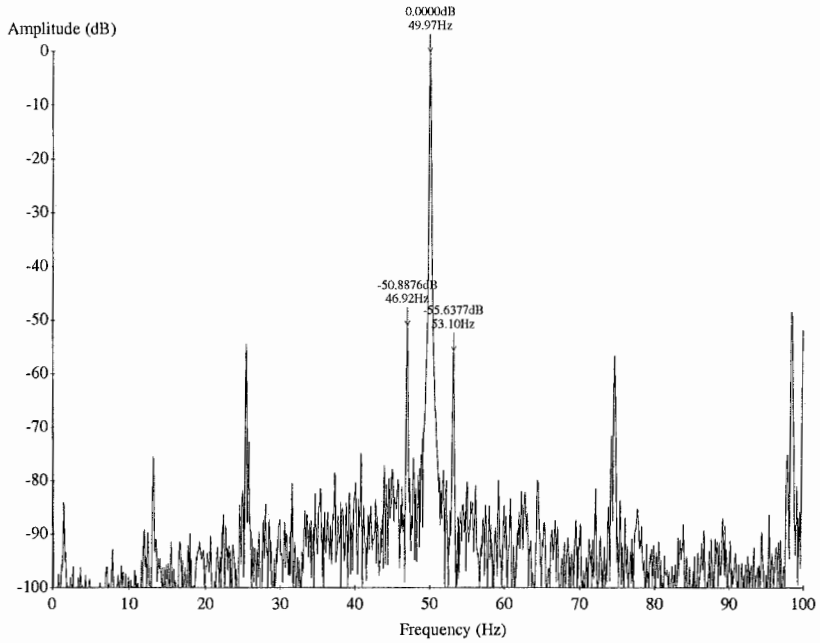

Figure 7.3: Stator current spectrum with undamaged rotor and mains supply.

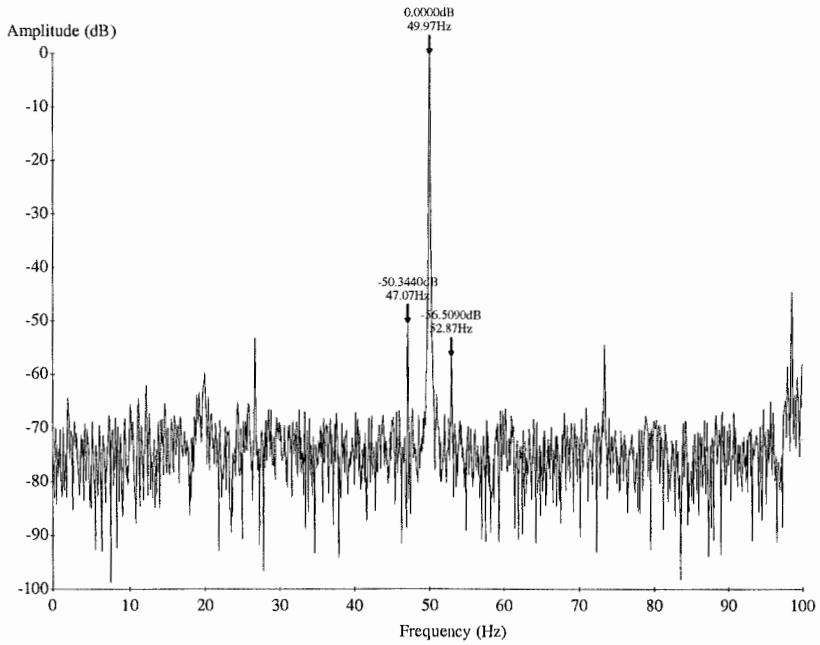

Figure 7.4: Stator current spectrum with undamaged rotor and VSD supply.

7.2.3 Damaged Rotor Measurements

The same measurements as were made in the previous section were repeated after the rotor had been deliberately damaged in order to simulate a real fault. This was achieved by milling through the end-ring to separate one end-ring and a rotor bar. A photograph of the rotor after this operation this is shown in Figure 7.5. This rotor was then replaced in the machine and the measurements performed again, resulting in the current spectra shown in Figures 7.6 and 7.7.

Figure 7.5: Damage to rotor of test motor.

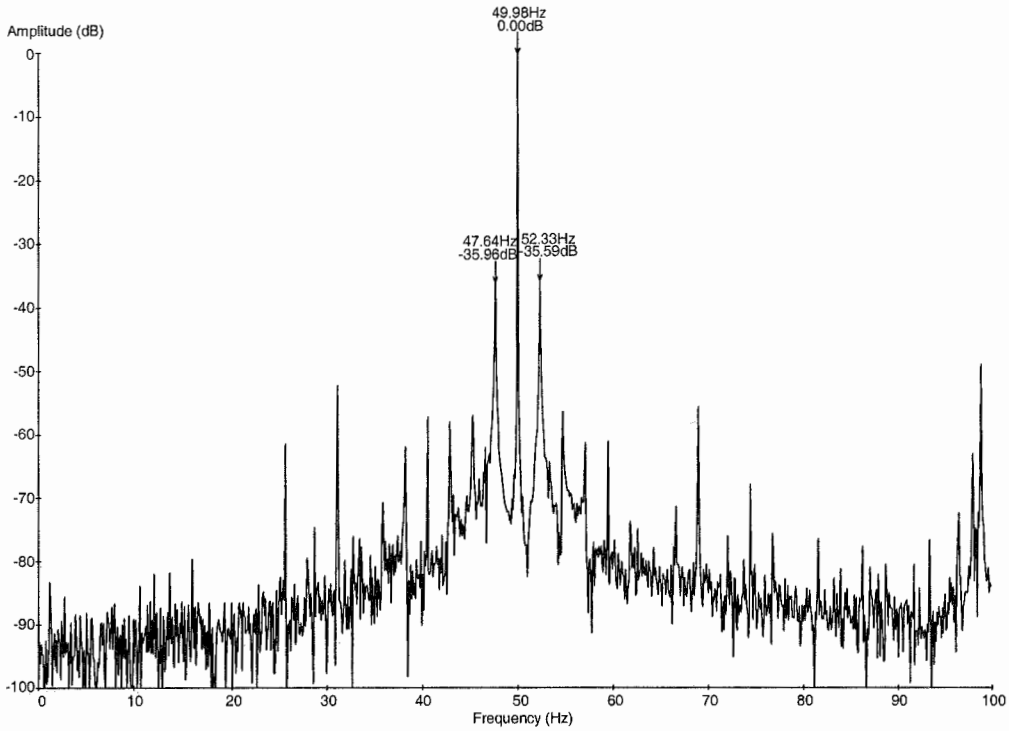

Figure 7.6: Stator current spectrum with damaged rotor and mains supply.

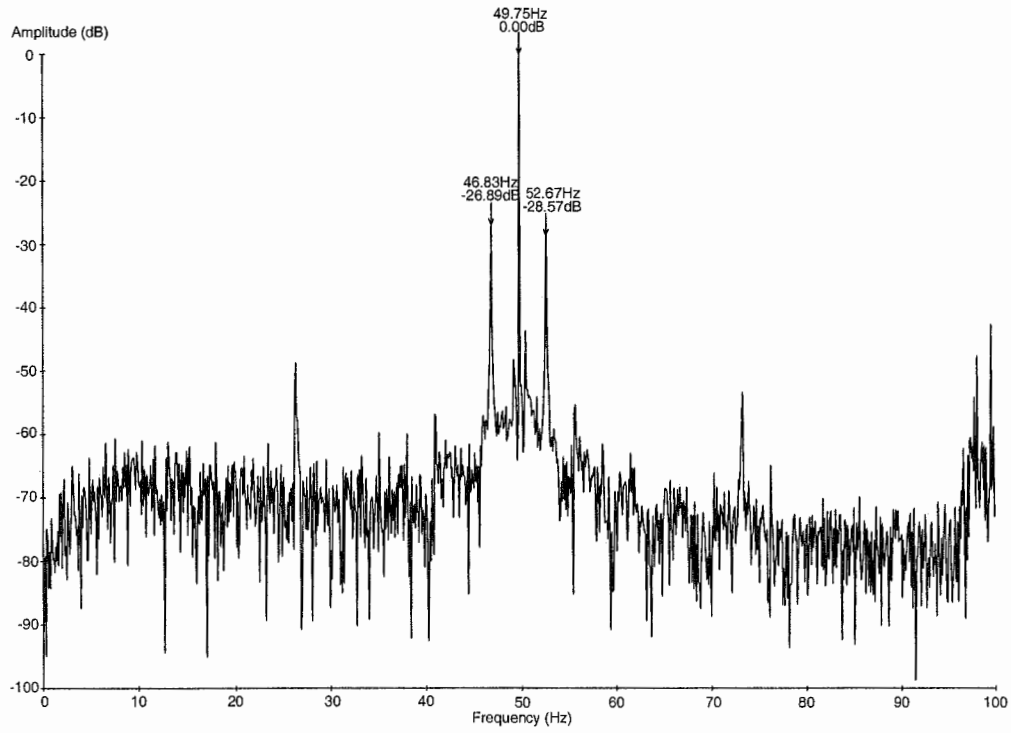

Figure 7.7: Stator current spectrum with damaged rotor and VSD supply.

7.2.4 Comparison of Reference Spectra

It can be seen that by comparing Figure 7.3 and Figure 7.6 the spectrum with the motor supplied by the mains develops large sidebands at twice the slip frequency around the supply frequency peak.

When comparing Figure 7.4 and Figure 7.7 it can be seen that there is a similar difference between the two spectra as was seen in the prior case. Again there are significant sidebands at twice the slip frequency around the supply frequency peak.

Figure 7.6 and Figure 7.7 are the stator current spectra for the same motor under approximately the same loading conditions, with practically the same supply frequency, yet the amplitudes of the sideband peaks are markedly different. The sideband amplitudes are about 8dB higher with a VSD supply than with the mains supply. This is quite a significant difference and is a factor which must be taken into account when examining the current spectra of induction motors for condition monitoring purposes. The difference in the amplitudes is probably due to larger amplitudes of the supply frequency harmonics contributing to the larger sideband amplitudes.

7.3 Detection of Rotor Damage in an Industrial Plant using the PLL

In addition to the tests performed with the PLL described in Chapter 4 several tests were made on the circuit at an industrial plant. Some of these tests are detailed in the following passages.

A pump motor at an industrial plant had been diagnosed by a vibration condition monitoring company as having rotor damage. The plant operator requested that this diagnosis be checked by electrical methods. The motor was supplied by a VSD hence this was a prime opportunity to test the PLL circuit.

Very little was known about the drive, motor and pump combination, however the following details were noted. The motor was a Pope TEFC induction motor rated

at 90kW, 1480 rpm, 415V, 50Hz. The drive was manufactured by PDL, model ASD330, and the motor was directly coupled to a centrifugal pump.

The data acquisition set up was the same as usual. A portable computer with a PCL-818 A/D card, anti-aliasing filters, sample and hold circuitry. An isolation transformer was used to supply the computer from the mains in order to avoid any earth loops which could potentially trigger any drive protection systems. The Fluke current probe was clamped around one of the motor supply cables in order to sense the stator current.

Data was sampled at a rate of 32 times the fundamental supply frequency which is approximately 1600Hz in this case. During sampling the supply voltage frequency varied between 48Hz and 50Hz. The resulting frequency spectrum of the stator current is shown in Figure 7.8.

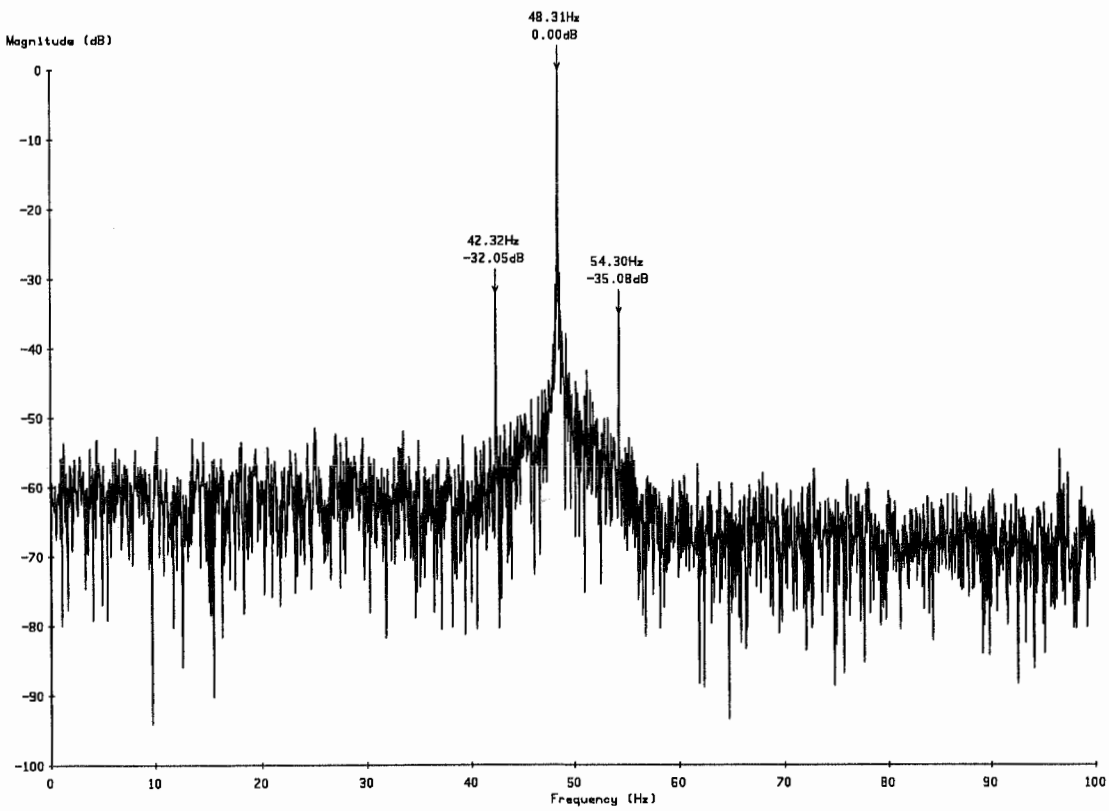

Figure 7.8: Stator current spectrum of pump motor, 48.3Hz supply frequency.

It is quite obvious that there are significant sidebands at about ±5.5Hz around the supply frequency peak. It was not possible to measure the speed of the motor due

to the inaccessible location. The sidebands are at a rather high frequency offset from the supply frequency, which means that either the motor was heavily overloaded and running at a much slower speed than the rated speed, or that the sidebands are not twice slip-frequency sidebands. A third alternative is that the peaks are not due to rotor damage at all, but are instead due to varying load torque. The last scenario is fairly unlikely as the mechanical setup was a direct coupled centrifugal pump. Since the pump was direct coupled, there was no gearing to influence the torque, so this cannot cause any variation in load torque. A centrifugal pump should be balanced, so the pump itself should also not cause any variation in load torque. Thus the conclusion is that the sidebands are most likely due to rotor damage and that they are either twice slip-frequncy or a multiple.

The conclusion of rotor damage is also consistent with the findings of the vibration analysis which was performed. Unfortunately the vibration analysis results cannot be presented here as permission was not granted for the proprietry information to be published.

The motor was later taken out of service, dismantled and examined by the technical staff of the company. Some evidence of rotor damage was found, confirming the prognosis determined from processing the data obtained using the PLL sampling circuit.

An interesting side-effect of using the PLL circuit for data acquisition when a VSD is involved is illustrated in Figure 7.9. Here the PLL has locked on to the upper sideband frequency since the supply frequency was outside the capture range of the PLL. This causes the sideband to appear as a single line, whilst the supply freqeuncy appears as a spread peak. This redistribution of the spectral energy affects the relative amplitude of the peaks, leading to values which are not comparable with those shown in Figure 7.8. This situation must be detected so that misleading results are not reported when using the PLL sampling method.

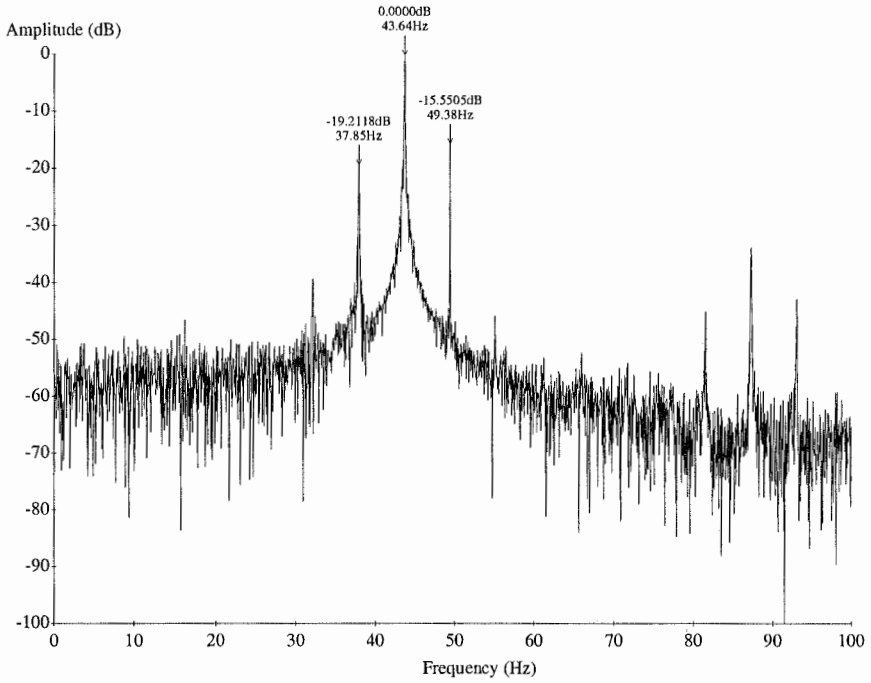

Figure 7.9: Stator current spectrum of pump motor, 43.6Hz drive frequency.

7.4 Software Methods

The PLL sampling method works reasonably well, but it does have a number of problems. There is an extra circuit board which must be included somewhere, it was contained in an external box attached to the sampling system for the protable equipment setup used in the previous section. However the most important constraint is the lock range of the PLL circuit design itself. The lock range is quite limited for acceptable response time for the low frequencies encountered in power systems, this in turn limits the range over which the frequency of a VSD can vary yet good data still be obtained.

In order to overcome these limitations, a software approach was sought that could use a standard data acquisition system and obtain useful spectral estimates. Prony's method was selected after reviewing the literature as offerring the most promise of the parametric spectral estimate methods [55]. This is because Prony's method models the spectrum as a set of individual frequency components, which

is the expected behaviour of the motor system, rather than as a continuous spectral envelope.

The result of applying Prony's method to an induction motor system was reported in Table 3.2. Whilst these results seem reasonable, it was found by experimentation that Prony's method had difficulty resolving two components of similar frequency, but differing magnitude. This behaviour is due to the number of frequency components which exist in the current spectrum of an induction motor which result from harmonics of the supply frequency and are of comparable amplitude to the slip-frequency sidebands. When the least-squares algorithm solves for the minimum error, the desired frequencies are often lost amongst all of the others. Note that all of the spectra shown in this thesis display the amplitude on a logarithmic scale, whereas Prony's method solves for the amplitudes linearly, hence the apparent difference in amplitude is not so pronounced. An attempt was made to use a notch filter to remove the fundamental frequency component in order to reduce this effect. However the notch filter also had the effect of removing the adjacent sidebands, resulting in no net improvement.

7.5 Simulation Methods

Since the simulation methods rely on calculation of machine parameters which require intimate design details of the motor, it is generally only possible to simulate laboratory machines. The construction details of commercially available motors are not generally made available by the motor design companies because this represents their investment in intellectual property. Hence it is quite difficult to obtain the required data in order to calculate the values of the circuit elements in the simulation model. However, simulation can be a useful tool when trying to understand the behaviour of an induction machine, thus it is worth the effort of trying to develop a usable model.

Chapter 6 describes the development of a simulation model based upon a circuit model of the induction motor which allows for the effects of individual rotor bars to be modelled. Due to the generosity of Pope Electric Motors Australia Pty. Ltd., it was possible to obtain some of the design blueprints of the laboratory motor.

This allowed the calculation of the values of circuit components, and thus actually solve the model to produce the results shown in Chapter 6.

The difficulty with the circuit model of the induction motor is that calculation of the circuit parameters is a very approximate task at best. In order to tune these parameters, small deviations were made in the parameters on a trial and error basis, and the effect that this had on the speed and torque curves for a simulated run up was observed. The curves were compared to those obtained from the real motor start up and the set of parameters which gave the best match were selected to form the model.

When a VSD supplied motor was simulated, it was found that the model parameters needed to be re-tuned. This is to be expected as the VSD ouput contains a much richer variety of harmonic frequency than does the mains supply. Due to saturation effects, the circuit parameters do not behave in a linear fashion with change in frequency, hence the net effect of the circuit components can be expected to vary with harmonic content. This is one of the major draw backs of the circuit modelling technique.

The simulation results of Figures 6.11 and 6.12 were the best that could be obtained after tuning the model parameters for mains and VSD operation of the motor. As can be seen, these exhibit similar behaviour to the physical system in that the relevant frequency components are present. However, the amplitude and frequency of these components do not match the experimental system very well. In order to obtain a better match, the circuit model may need to be modified to include frequency dependent component values but this would require more computing power than was available.

7.6 Conclusion

This chapter has expanded upon some of the experimental work described in the previous chapters. Results were presented for the laboratory motor with both a damaged and undamaged rotor running from either a mains or a VSD supply. This shows the emergence of the twice-slip frequency sidebands and how the amplitude

An industrial case study describing the successful application of the PLL sampling was elaborated upon, showing the usefulness of the device in a VSD application.

Parametric spectral modelling using Prony's method was also expanded upon and compared to the Fourier transform current spectrum on the laboratory motor. Unfortunately it was found that the fundamental supply frequency masked the sideband frequency components too much to be detected by Prony's method.

Simulation of the laboratory motor using a circuit based model was also discussed in reference to the measured spectra. Although the model exhibited the same general behaviour as the physical system, the resulting absolute values were not in good agreement with reality. This is probably due to the non-linear nature of the physical system being modelled by a linear circuit. The model could possibly be improved by introducing frequency-dependent parameters, however this would exponentially increase the computation time.

CHAPTER 8

Time-Frequency and Wavelet Analysis

8.1 Introduction

The problem of detecting broken rotor bars in an induction motor controlled by a variable speed drive is really one of determining the frequency spectrum of a non-stationary signal. The basic problem with Fourier analysis is that the Fourier transform assumes that the signal is stationary over the period of the analysis, as explained in Chapter 3. The purpose of a variable speed drive is to vary the supply frequency in order to control the speed of the motor. If a change in the supply frequency occurs during the time that the current waveform is sampled, then the signal is *not* stationary. This may also occur with a mains supplied induction motor, because if the load torque varies during the sampling period, then the slip changes, and hence any frequency components dependent on the slip also change. This is not as serious a problem as the VSD case since the supply frequency is

always the dominant component in the frequency spectrum of the stator current, which doesn't change significantly with a mains supplied motor.

Given that the signal that is sampled is non-stationary, what techniques can be used to overcome the problem? One technique is to discover how the frequency components change with time, that is, analyse the signal in a two-dimensional time-frequency space. Such methods try to determine the instantaneous frequency components of the signal at an instant of time. Of course it is impossible to achieve such an aim, due to the uncertainty principle, so the time-frequency plane is broken up into regions, and the time and frequency components of these regions is estimated.

There are two distinct types of analysis in current use. The first is time-frequency analysis, and the second wavelet analysis. The basic difference between the two methods is that time-frequency methods have constant resolution in both the time and frequency axes, whereas in wavelet analysis the time and frequency resolutions are inter-dependent.

Time-frequency and wavelet methods have only recently been applied to condition monitoring and fault detection problems. Newland [123] [124] applied wavelets to the analysis of vibration signals in buildings in order to learn more about ground-transmitted vibration. Tansel et al. [125] used wavelet based encoding and neural networks to detect tool damage in microdrilling operations. Forrester [126] used the STFT and Wigner-Ville distribution to find faults in the gears of helicopter transmission systems. Loughlin et al. [127] used time-frequency analysis to examine drilling and grinding operations in order to detect tool wear. Williams et al. [128] also apply time-frequency analysis to the detection of bearing failure from vibration measurements. McFadden [129] use the wavelet transform to analyse vibration signals from a helicopter gearbox in order to detect damage to a gear caused by fatigue cracking.

There has been very little application of time-frequency and wavelet methods to VSDs and condition monitoring of induction motors. Salvatore and Stasi [130] used the Wigner-Ville distribution and their own time-frequency representation to

examine the voltage and current signals of a VSD in order to monitor the instantaneous complex power, but only with a constant drive output frequency. The most interesting work to date has been that of Burnett et al. [131] [132], who use a time-frequency method to examine the stator current during the run up of a mains supplied induction motor with broken rotor bars. The 50Hz mains frequency and the twice slip-frequency sidebands are removed using a notch filter, and the resulting waveform digitised. By tracking the variation over time of what they term "Deleroi" frequency components, they claim to be able to predict the location of broken rotor bars. The change in slip over time is found from the time-frequency representation of the lower twice slip-frequency sideband. From this information, the change in speed over time can be found and, by integration, the angular displacement. By working backwards from the time-frequency plot, the location of the rotor damage with respect to the reference point, can be found.

This chapter develops the theory of time-frequency analysis and wavelet analysis techniques, and applies them to some sampled stator current waveforms.

8.2 Time-Frequency Analysis

The application of time-frequency analysis is a recent development in the signal processing field, partially due to the amount of computing power required to calculate time-frequency distributions in a reasonable time. One of the first to examine signals in the time-frequency domain was Gabor [133], who developed the technique now known as the Short-Time Fourier Transform (STFT), and also known as the spectrogram or Gabor transform.

The STFT is perhaps the easiest time-frequency distribution to comprehend, as the STFT calculates the Fourier Transform of the input signal by applying a short window function centred at a particular time, and then taking the Fourier transform of the result. The window is then moved along to a new time and the process repeated. Effectively the STFT assumes that the signal remains stationary over the length of the window.

If the time at which the window is centred is t, the input signal is $s(\tau)$, and the window is $h(\tau)$, then the windowed signal is:

$$s_w(\tau - t) = s(\tau)h(\tau - t) \tag{8.1}$$

Now, if the time variable is considered to be τ, the Fourier transform of the windowed signal is:

$$S(t,f) = \int_{-\infty}^{\infty} e^{-j2\pi f\tau} s(\tau)h(\tau - t)d\tau \tag{8.2}$$

and the power spectrum is:

$$\rho_s(t,f) = \left|S(t,f)\right|^2 \tag{8.3}$$

Performing this at a multiplicity of times, t, forms the complete STFT distribution

Most popular time-frequency representations can be expressed in terms of the general bilinear time-frequency distribution proposed by Cohen [138]:

$$\rho_z(t,f) = \iiint e^{j2\pi v(u-t)} g(v,\tau)z(u+\tau/2)z^*(u-\tau/2)e^{-j2\pi f\tau} dvdud\tau \tag{8.4}$$

Here z is an analytic signal, that is, it contains no negative frequencies. The function $g(v,\tau)$ determines the characteristics of the time-frequency distribution, and is known as the *kernel*. If the integration with respect to v is performed, we have:

$$\rho_z(t,f) = \iint G(t,\tau)z(u+\tau/2)z^*(u-\tau/2)e^{-j2\pi f\tau} dud\tau \tag{8.5}$$

The discrete time implementation of this is:

$$\rho_z(n,k) = \sum_{m=-M}^{M} \sum_{p=-M}^{M} G(p,m)z(n+p+m)z^*(n+p-m)e^{-j4\pi mk/N} \tag{8.6}$$

This is equivalent to the following:

$$\rho_z(n,k) = F\left[G(n,m) * K_z(n,m)\right] \tag{8.7}$$

where F is the discrete Fourier transform operator, * is discrete time convolution, and $K_z(n,m) = z(n+m)z^*(n-m)$ is the bilinear kernel function. The time-frequency distribution may be calculated from this form, given any determining function $G(n,m)$.

8.2.1 Short Time Fourier Transform (STFT)

As explained previously, the STFT may simply be viewed as the process of sliding a window along the data and calculating the Fourier transform of each windowed data segment. This gives the frequency components at times corresponding to the centres of the windows. The kernel function for the STFT is:

$$g(v,\tau) = \int h^*(u-\tfrac{1}{2}\tau)e^{-j2\pi vu}h(u+\tfrac{1}{2}\tau)du \tag{8.8}$$

and the determining function for a rectangular window is:

$$G(n,m) = \begin{cases} \dfrac{1}{P}, & |m+n| \le \dfrac{(P-1)}{2}; \\ 0, & \text{otherwise.} \end{cases} \tag{8.9}$$

The results obtained from the STFT are highly dependent on the function which is used to window the data. The window used may be any suitable function as discussed in Chapter 3.

The STFT does have some disadvantages. If a signal has two distinctly different components which are combined together, then two different window functions may be needed to give the best results for each component. In this case a compromise window may have to be chosen, which may not give satisfactory results for either component. The STFT also has difficulties when analysing rapidly varying signals, because if the window is made short enough to resolve the rapid changes, then the frequency resolution is very low and may not resolve the frequency components of the signal. However, this is true for most time-frequency distributions, although it is possible to design distributions which are optimal for particular types of signals.

8.2.2 Wigner-Ville Distribution (WVD)

The Wigner-Ville distribution was developed as an alternative to the STFT to overcome its shortcomings with respect to time and frequency resolution of rapidly varying signals. It is particularly optimal for a chirp [134], which is a signal that has a frequency which increases quadratically with time.

The kernel function of the WVD is:

$$g(\nu,\tau)=1 \tag{8.10}$$

or expressed as the determining function:

$$G(n,m)=\begin{cases}\delta(n), & \frac{-(M-1)}{2}\le m\le\frac{(M-1)}{2};\\ 0, & \text{otherwise.}\end{cases} \tag{8.11}$$

Unfortunately, the WVD suffers from a phenomenon known as cross terms. If a signal, $x(t)$, consists of two sinusoids of frequencies f_1 and f_2, and amplitudes A_1 and A_2 respectively:

$$x(t)=A_1e^{j2\pi f_1t}+A_2e^{j2\pi f_2t} \tag{8.12}$$

then the Wigner-Ville distribution is:

$$\begin{aligned}\rho(t,f)&=A_1^2\delta(f-f_1)+A_2^2\delta(f-f_2)\\&\quad+2A_1A_2\delta\left(f-\frac{f_1+f_2}{2}\right)\cos\{2\pi(f_2-f_1)t\}\end{aligned} \tag{8.13}$$

The first two terms are the two sinusoids, whilst the third term is a component at a frequency of $(f_1+f_2)/2$ which has an amplitude that varies sinusoidally in time. This is the cross term and results from the interaction of the two sinusoids. If there are more than two sinusoidal components, in the signal, then there will be cross terms present which result from all combinations of the frequencies. The cross terms can make interpretation of the distribution difficult, hence other distributions have been introduced which suppress these terms.

8.2.3 Choi-Williams Distribution (CWD)

The Choi-Williams distribution (CWD) [135], also known as the exponential distribution (ED), has a kernel which is an exponential function. This distribution overcomes some of the disadvantages of both the STFT and the WVD, providing good resolution with reduced interference effects [136]. The kernel of the CWD is:

$$g(\nu,\tau) = e^{-\nu^2\tau^2/\sigma} \tag{8.14}$$

and the corresponding determining function is:

$$G(n,m) = \frac{\sqrt{\sigma/\pi}}{2m} e^{-\sigma n^2/4m^2} \tag{8.15}$$

where σ is a smoothing parameter. As σ becomes very large, Equation (8.14) approaches one and the distribution becomes equivalent to the WVD. Varying σ trades off cross term suppression and resolution; the larger σ is the better the frequency resolution becomes, but the cross terms become larger. Choi and Williams [135] experimented with the value of σ , and decided that a value of one was optimal for their purposes. In applying the method to stator current waveforms, it was decided that better frequency resolution was called for than Choi and Williams required. After examining their results, a value of 10 was chosen for σ.

8.2.4 Zhao-Atlas-Marks Distribution (ZAM)

The Zhao-Atlas-Marks (ZAM) distribution has a kernel [137]:

$$g(\nu,\tau) = g_1(\tau)\frac{\sin(2\pi\nu|\tau|/a)}{\pi\nu} \tag{8.16}$$

where $g_1(\tau)$ is a window function, and parameter a is greater than or equal to 2 in order to satisfy theoretical requirements [138].

The determining function is:

$$G(n,m) = \begin{cases} e^{-2\alpha n^2} & |n| \le m/a \\ 0 & \text{otherwise} \end{cases} \tag{8.17}$$

where $\alpha = \ln(100)/(2M^2)$ and M is the window length. This kernel enhances the time and frequency resolutions while suppressing cross terms [138]. Most work has taken g_1 to be one and a to have a value of 2. The distribution has been applied to speech [139], with good results, especially for signals that are rich in harmonics. For this reason it was chosen to be applied to the stator current waveform.

8.3 Wavelet Analysis

Any time-frequency analysis of signals would be incomplete without an investigation of the use of the continuous wavelet transform (CWT). This section therefore uses the CWT to analyse current waveforms of induction motors (both fixed and variable speed drives) with undamaged and broken rotor bars. We begin with an introduction to the CWT before presenting the results of this analysis.

8.3.1 The Continuous Wavelet Transform

The CWT provides an alternative time-frequency representation by trading time and frequency resolution. This is particularly appropriate for signals composed of high frequency components of short duration plus low frequency components of long duration [140] which are often characteristic of the type of current waveforms produced by an induction motor with a damaged rotor bar.

One way of interpreting the CWT is to compare it to the Short Time Fourier Transform (STFT) (see Section 8.2.1). Figure 8.1 shows the division of the frequency domain for (a) the STFT with uniform coverage and (b) for the wavelet transform with logarithmic coverage.

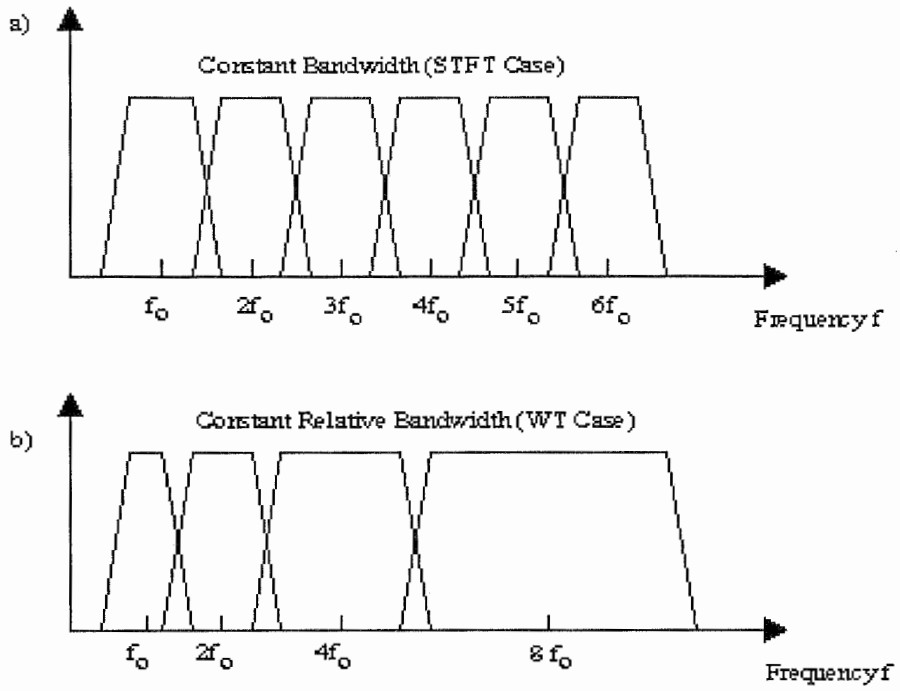

Figure 8.1: Division of the frequency domain (a) for the STFT (uniform coverage) and (b) for the wavelet transform (logarithmic coverage) [140].

When the wavelet analysis is viewed from a filter bank point of view we can see, from Figure 8.1 that the analysis filter is no longer spread evenly over the frequency axis (as for the STFT case), but regularly spread in a logarithmic scale. In other words the time resolution increases with the central frequency of the analysis filters, and the change in frequency, Δf, must be proportional to f. Accordingly, Δf and therefore Δt, change with the centre frequency of the analysis filter, with the only limitation imposed by the uncertainty principle (otherwise known as Heisenberg's inequality),

$$\Delta f \, \Delta t \geq \frac{1}{4\pi}. \tag{8.18}$$

As a result the time resolution becomes arbitrarily good at high frequencies, while the frequency resolution becomes arbitrarily good at low frequencies. For example, two closely located impulsive events can be distinguished in the analysis by going up to higher frequencies in order to increase time resolution, or two very

close peaks in the frequency spectrum can be eventually separated by going down to lower analysis frequencies in order to increase the frequency resolution [140].

The CWT implements the above ideas by using filter banks with impulse responses defined as scaled (that is dilated or compressed) versions of the same mother wavelet, or analysing wavelet [141]:

$$\psi_a(t) = \frac{1}{\sqrt{|a|}}\psi\left(\frac{t}{a}\right) \tag{8.19}$$

where a is a scale factor and $1/\sqrt{|a|}$ is used for energy normalisation. The CWT of a function $x(t)$ is then defined as,

$$\mathrm{CWT}_x(a,\tau) = \frac{1}{\sqrt{|a|}}\int x(t)\psi^*\left(\frac{t-\tau}{a}\right)dt \tag{8.20}$$

where * denotes the complex conjugate and τ is a shift parameter [140]. From Equation (8.20) we see that the transform domain consists of a time-scale plane (or time frequency-plane as scale and frequency are inversely related) similar to those resulting from the STFT.

There are many known wavelets. Strictly speaking, only functions that are bandpass in nature, have some degree of regularity and satisfy an admissibility function can be classed as wavelets. The admissibilty condition is given by [142]:

$$\int \frac{|\hat{\psi}(w)|}{|w|}dw < \infty \tag{8.21}$$

where $\hat{\psi}(w)$ is the Fourier transform of $\psi(x)$.

Finding functions that satisfy this condition is not always easy. In many cases this condition is relaxed slightly so that all that is required is that the wavelet have a DC value of zero, that is.,

$$\int \psi(x)dx = 0. \tag{8.22}$$

In this section the current waveforms are analysed using the mother wavelet

$$\psi(t) = e^{jct} e^{-\frac{t}{2}} \tag{8.23}$$

which is called the Morlet wavelet [143] [144]. The Morlet wavelet is not, strictly speaking, an admissible wavelet basis since $\hat{\psi}(0) \neq 0$. For certain values of c, however, ($c \geq 5.0$) this wavelet becomes very close to admissible and, due to its mathematically tractable closed form expression, its implementation is relatively straightforward. The shape of the Morlet wavelet is illustrated in Figure 8.2.

Following Heneghan et al. [145] we approximate a sampled version of the CWT by:

$$\begin{aligned} CWT_x[a,b] &= \sum_{m=-\infty}^{+\infty} x[m]\psi_a^*[b-m] \\ &= \sum_{m=-\infty}^{+\infty} x[b-m]\psi_a^*[m] \end{aligned} \tag{8.24}$$

where $\psi_a^*[m]$ represents a sampled version of the continuous function.

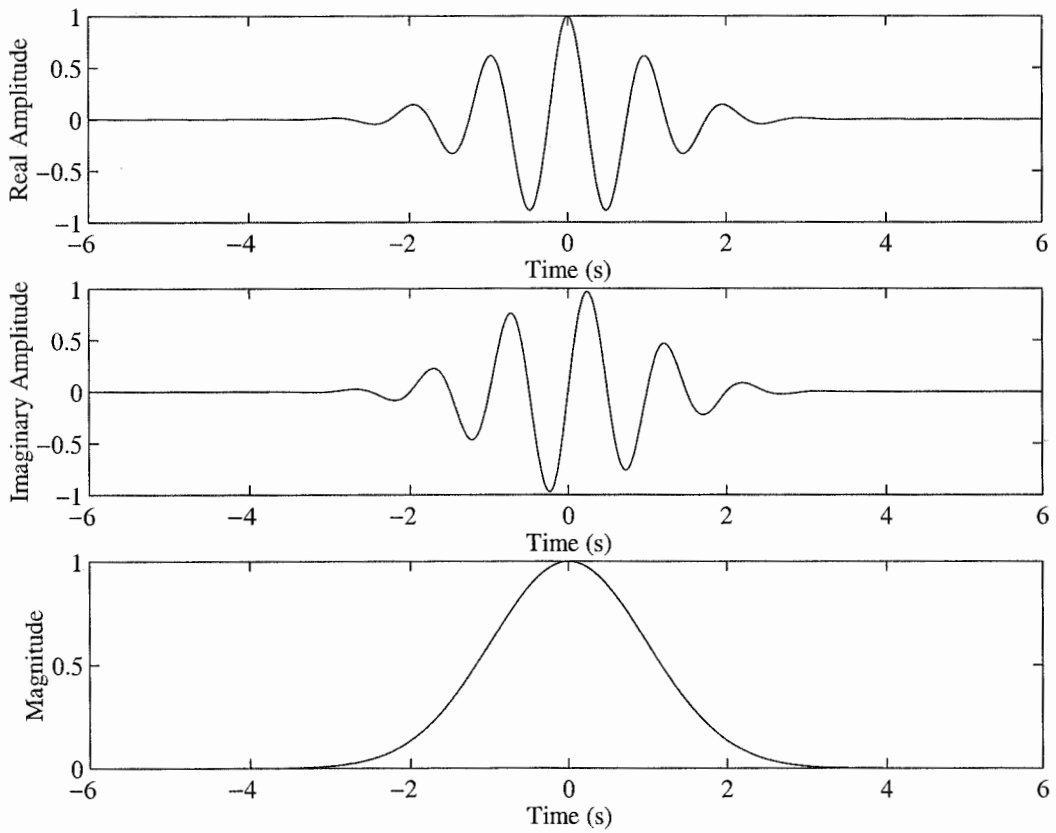

Figure 8.2: The Morlet wavelet.

8.4 Analysis of Stator Current Waveforms

In order to compare the time-frequency and wavelet analysis techniques, the methods were applied to two measured stator current waveforms. Both waveforms were taken from the Pope motor (Appendix A), with a damaged rotor and loaded by a DC machine. The first is the current waveform for mains supply, and the second is the current waveform for a VSD ramping the drive frequency from 30Hz to 50Hz, and is shown in Figure 8.3.

The STFT and wavelet transforms were applied to a mains frequency current waveform, in which the signal is stationary, and the results are shown in Figure 8.5 and Figure 8.6, respectively.

8.4.1 Time-Frequency Analysis of Current Waveforms

Time-frequency distributions were calculated using the TFSA 4.0 package [146] and MATLAB® [147]. They are displayed as greyscale images where white indicates the highest amplitude and black the lowest. The amplitudes are plotted on a logarithmic scale. Unless otherwise stated the window length used is 1024 points. Filtering of the current waveform was achieved using the signal processing toolbox of MATLAB®.

The results of applying the STFT to the mains frequency current waveform is shown in Figure 8.5, and the spectrum calculated using the whole data record is in Figure 8.4. It can be seen that, in this case, the STFT does not have sufficient frequency resolution to resolve the twice slip-frequency sidebands. The frequency resolution can be increased by lengthening the window used to include more data points. Naturally this decreases the time resolution, and in the limit, the time-frequency distribution collapses to the spectrum of Figure 8.4. It can still be displayed as a time-frequency distribution because when the window function falls outside the data length it is simply zero-padded. The zero padding is the cause of the fringing patterns that can be seen at times less than 0.1 seconds, and greater than 0.9 seconds in Figure 8.5. However, some useful information can still be gained from the time-frequency distribution. If the data is high-pass filtered by a

filter with a cutoff frequency of 400Hz, the result is the STFT shown in Figure 8.7. The rotor slotting frequency at about 800Hz can be seen quite clearly. This frequency component provides valuable information about the speed of the motor. There is still a residual mains frequency component as the filter employed only attenuated frequencies in the stop band by 70dB.

Figure 8.9 shows the STFT of the current waveform when the drive frequency ramps up from 30Hz to 50Hz. The fundamental drive frequency is visible at the bottom of the image and can be seen to increase slightly over time, as would be expected. The twice slip-frequency sidebands are not at all visible. The effect of different window lengths on the STFT, is illustrated in Figures 8.10-8.12. These figures are the STFT of the stator current waveform as the drive frequency ramped up from 30Hz to 50Hz, with a 400Hz high-pass filter. Figure 8.10 has a window length of 512 samples giving a frequency resolution of 4.88Hz. Figure 8.11 has a window length of 1024 samples giving a frequency resolution of 2.44Hz, and Figure 8.12 has a window length of 2048 samples, giving a frequency resolution of 1.22Hz. It can be seen that the long window length gave the narrowest lines when the frequency was constant, yet had the largest amount of blur as the frequency ramped up. Conversely, the shortest window had the widest frequency lines, but tracked the change in frequency the best.

The other frequency components in the time-frequency plane are the result of the modulation process. The two components below 1000Hz decrease in frequency, while the two above increase. This behaviour is consistent with that described in Chapter 5, where the drive output frequency components include multiples of the carrier plus and minus multiples of the carrier frequency. Hence as the modulating (drive) frequency increases, the sidebands will move away from the multiples of the carrier frequency. This is what occurs in Figures 8.10-8.12 up until about 0.8 seconds. At this point in time it would appear that the drive modulation process changes, causing the jump in frequencies. The new frequencies are present until about 1 second, at which point the spectrum returns to a similar situation to the start, except that it would appear that the carrier frequency has increased, and thus all components have increased in frequency.

Figures 8.13-8.18 show the time-frequency distributions which result from application of the various distributions described above to the stator current waveform as the drive ramped up in frequency from 30Hz to 50Hz. Time-frequency distributions for both 400Hz high-pass filtered and unfiltered data are calculated.

The Wigner-Ville distribution of the stator current is shown in Figure 8.13. The drive frequency can be seen at the lower edge of the image. It then shows what can only be cross terms around 500Hz. The Wigner-Ville distribution of the filtered waveform, Figure 8.14, looks much more like the STFT result, except that there are many more lines present, most of which are also cross terms. This serves to illustrate the problems that cross terms are for the Wigner-Ville distribution. It would appear that the Wigner-Ville distribution is not particularly useful for condition monitoring purposes.

Figure 8.15 shows the Choi-Williams distribution for the unfiltered current waveform. Not many frequency components are evident in this image, due to the large amplitude fundamental. The Choi-Williams distribution of the filtered current waveform, Figure 8.16, shows the same frequency components as the STFT in Figure 8.11, except that the regions of changing frequency are more clearly defined than with the STFT.

The Zhao-Atlas Marks distribution is shown in Figures 8.17 and 8.18 for the unfiltered and filtered stator current waveforms, respectively. The first image is again dominated by the drive frequency, and little else is apparent. The second figure is similar to that obtained from the Choi-Williams distribution. The rotor slotting frequency can be seen, as can the drive harmonics. However, there are a lot more cross terms in between these components.

8.4.2 Wavelet Analysis of Current Waveforms

The wavelet transforms were all calculated using the Uvi_Wave toolbox for MATLAB® from the Universidad de Vigo in Spain.

The wavelet transform of the mains supply current waveform is shown in Figure 8.6 for scale values form 1 to 40. The mains frequency component causes the broad band centred at a scale of about 17. Frequency and scale have an inverse relationship, thus low frequencies have high scales, and high frequencies, low scales. The wavelet transform of the filtered current waveform is shown in Figure 8.8. There is a component at a scale of about 10 which is probably the rotor slotting frequency, but little else is evident.

The wavelet transform of the ramped frequency current waveform is shown in Figure 8.19. The broad sweep of the frequency as it ramps up dominates the image to the exclusion of all else. Little useful information is provided.

8.5 Summary

Time-frequency and wavelet transform analysis can provide a picture of how the frequency components of a multiple component signal change in time. The resolution is limited by the uncertainty theorem, as the frequency resolution is increased, the time resolution decreases.

The application of these methods to the analysis of stator current waveforms was not very successful. It would appear that the frequency resolution would never be good enough to distinguish the twice slip-frequency sidebands from the supply frequency. It would appear that this is a general problem of detecting low-level signals in the presence of larger signals.

More success was obtained when the current waveform was high-pass filtered to eliminate the supply frequency component. The short-time Fourier transform displayed the rotor slotting harmonics and drive modulation products. The Choi-Williams distribution did an even better job of this for sections of the signal where the frequency components were changing. The Wigner-Ville suffered severely from cross terms which cluttered up the image and obscured the real signal components. The Zhao-Atlas-Marks distribution provided no information at all, and is clearly the wrong distribution to be using for these purposes.

Thus it can be concluded that time-frequency and wavelet methods are not useful for detecting twice slip-frequency sidebands. However, they do serve a purpose in that the rotor slotting frequency and drive modulation frequency components can be observed after high-pass filtering the signal. This could be useful for condition monitoring because it allows the speed variation to be calculated if the number of rotor slots are known. Also it can identify sections of the sampled data where the supply frequency is constant, which may allow other techniques to concentrate their analysis on this section. There is a huge disadvantage to these methods in that they require a lot of computer processing time to calculate and also require a large amount of computer memory due to the three-dimensional nature of the result.

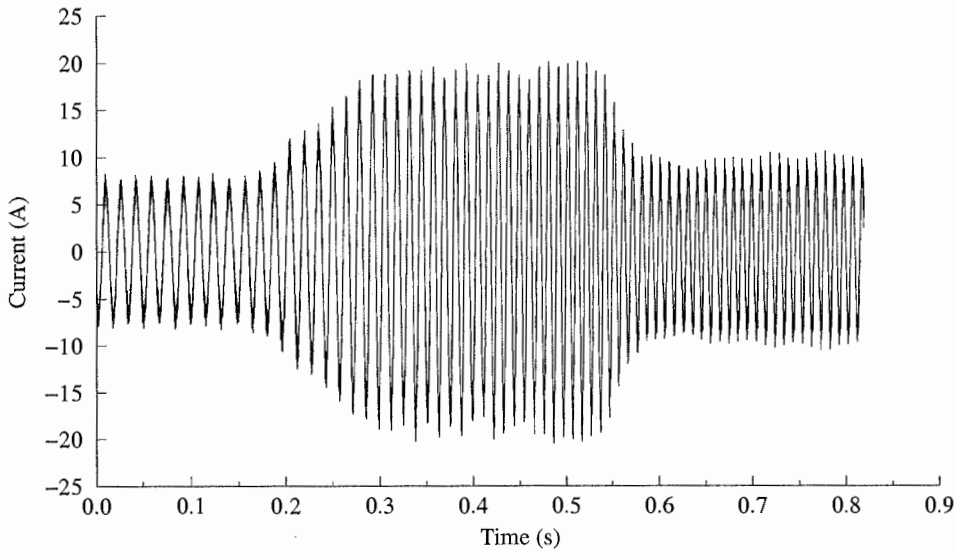

Figure 8.3: Stator current waveform for drive frequency ramping from 30Hz to 50Hz.

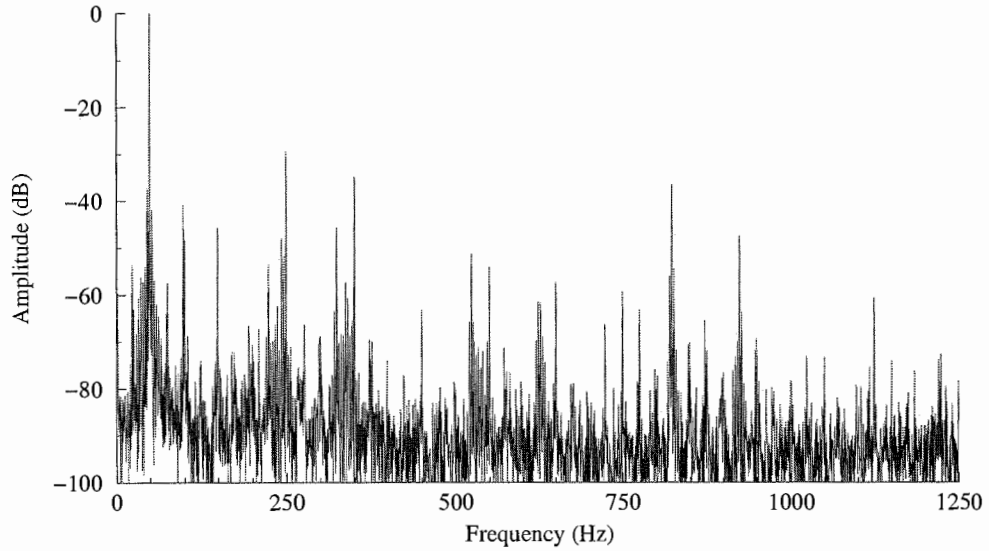

Figure 8.4: Spectrum of mains supply current waveform.

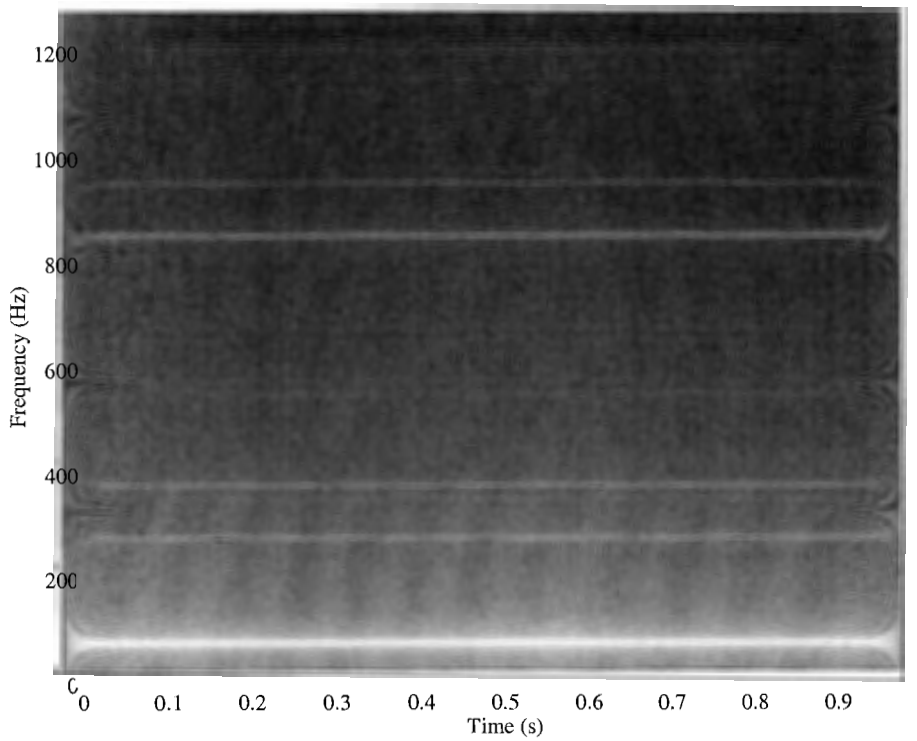

Figure 8.5: STFT of mains supply current waveform.

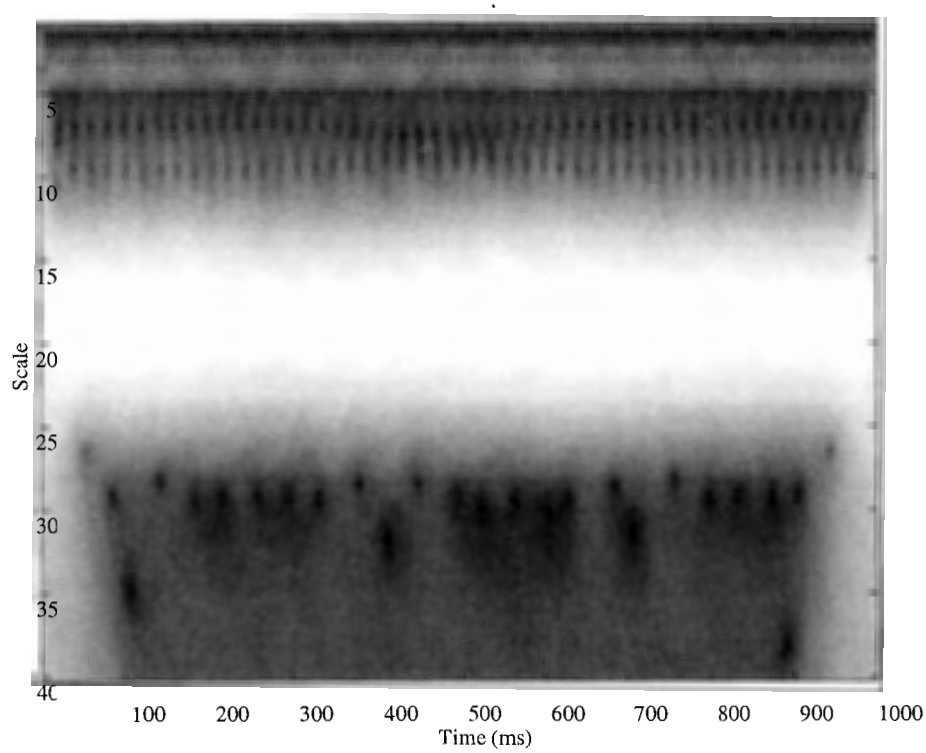

Figure 8.6: Wavelet transform of mains supply current waveform.

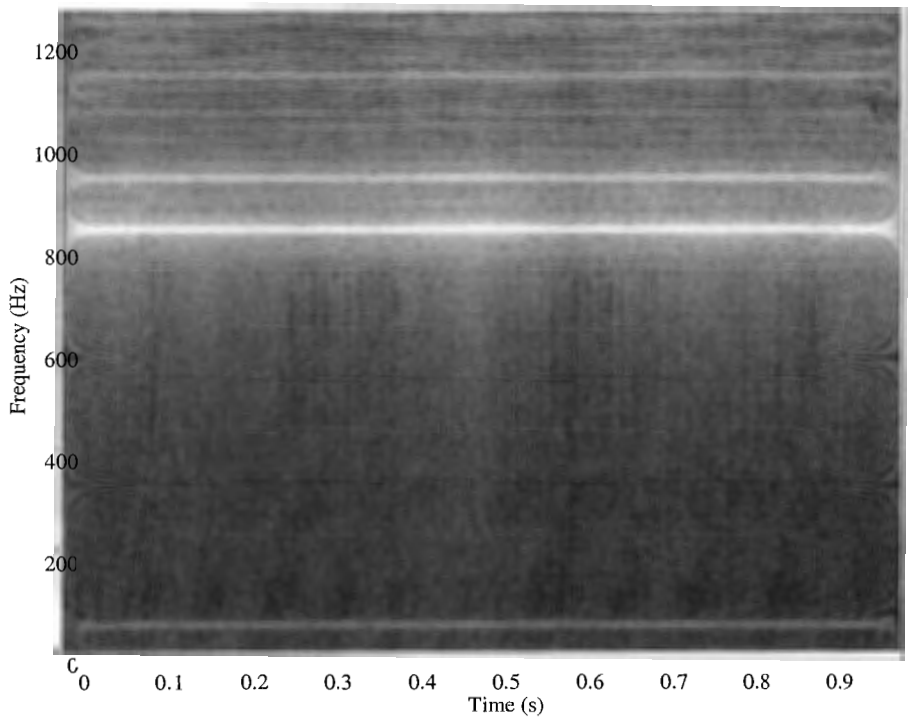

Figure 8.7: STFT of mains supply current waveform after 400Hz high-pass filtering.

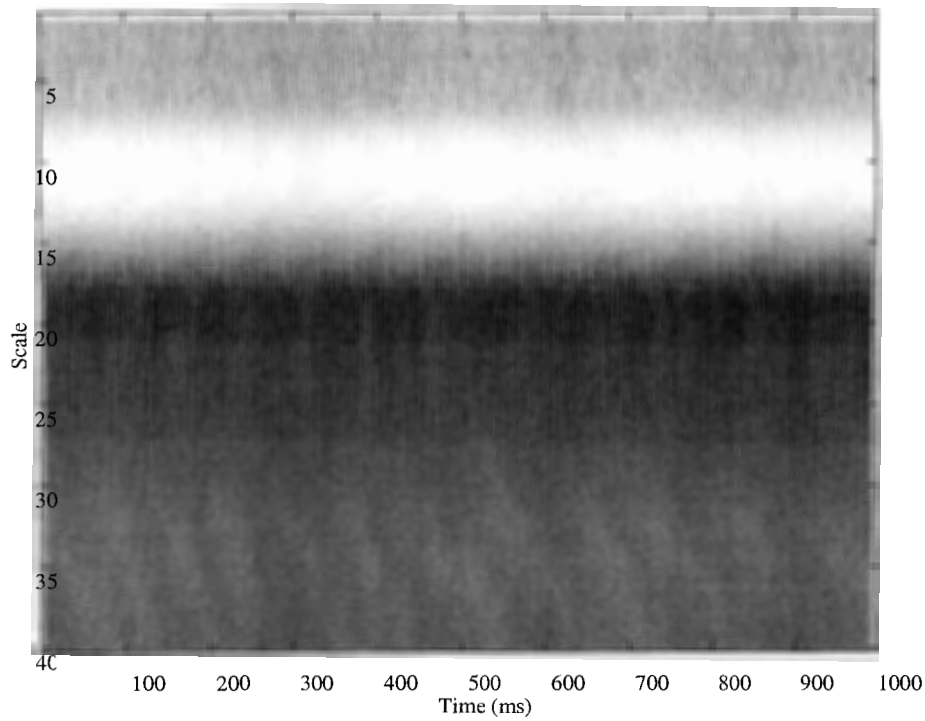

Figure 8.8: Wavelet transform of mains supply current waveform after 400Hz high-pass filtering.

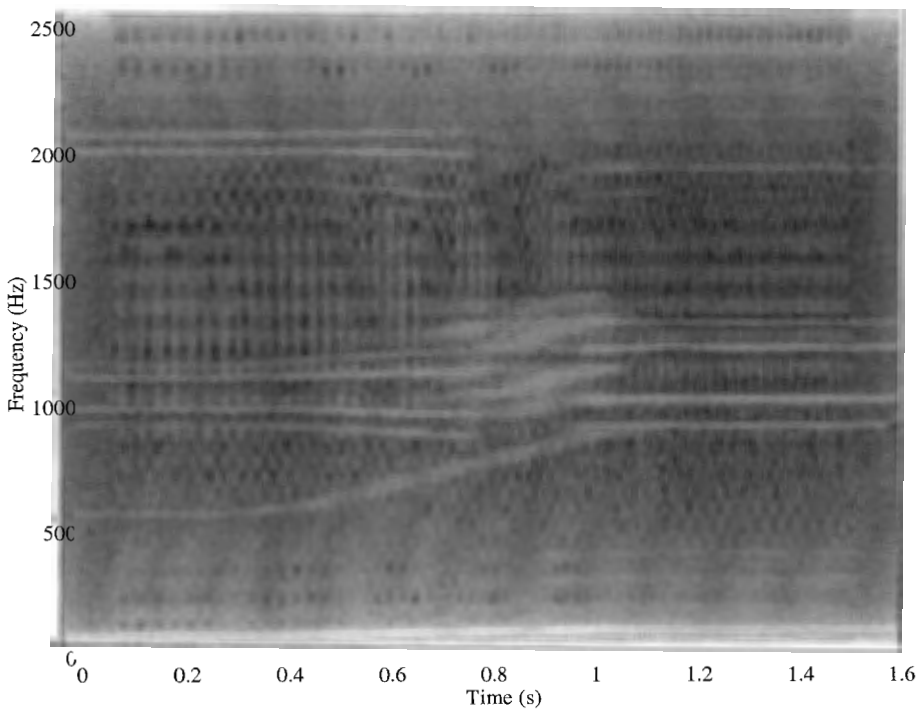

Figure 8.9: STFT of current waveform with drive frequency ramping from 30Hz to 50Hz.

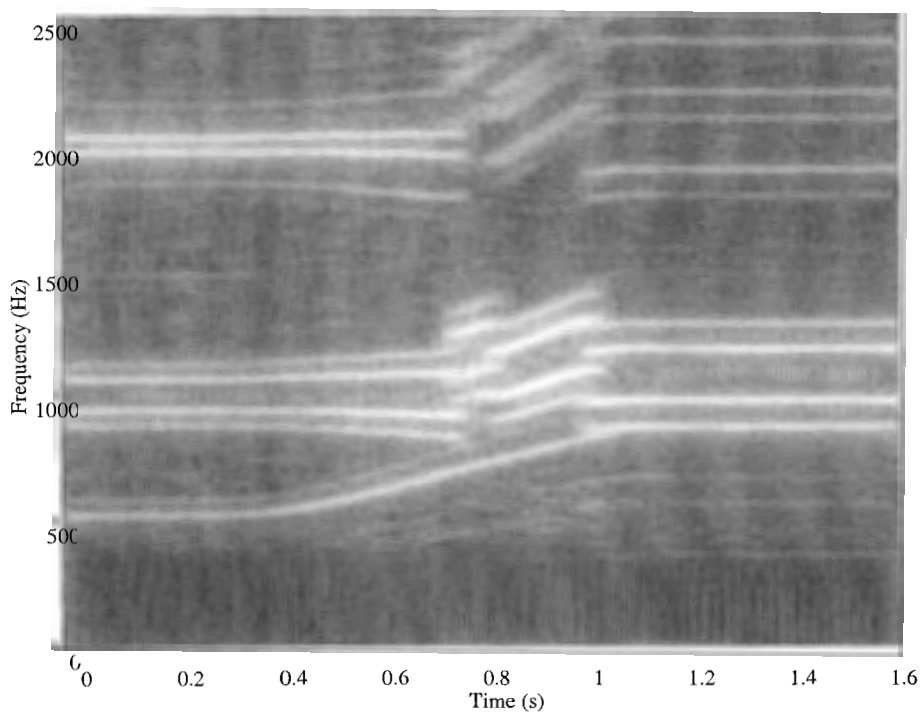

Figure 8.10: STFT of current waveform with drive frequency ramping from 30Hz to 50Hz, after 400Hz high-pass filtering, 512 point window.

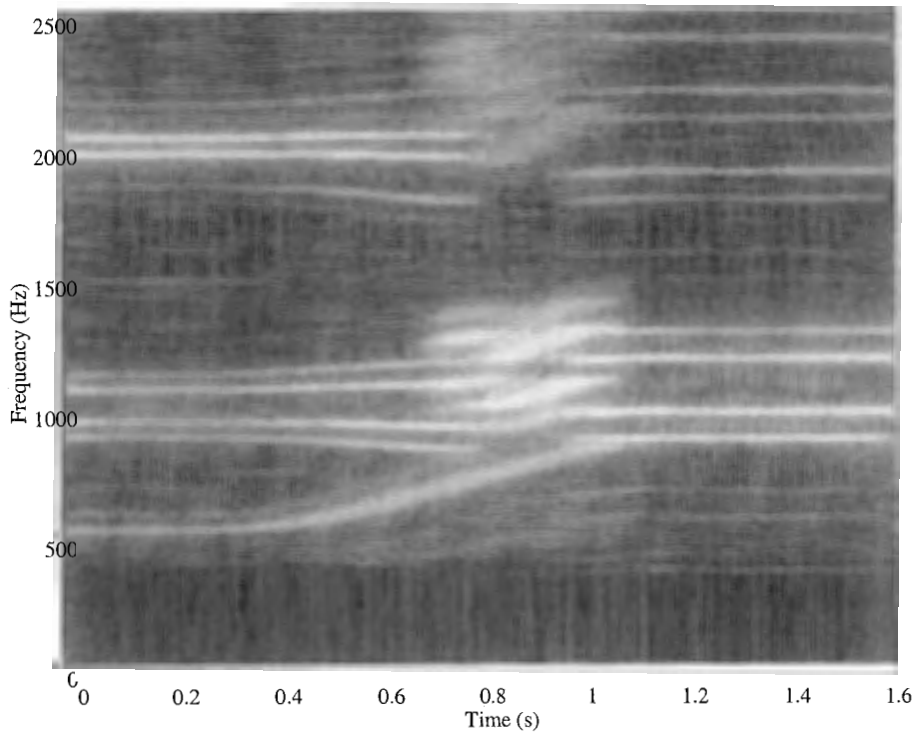

Figure 8.11: STFT of current waveform with drive frequency ramping from 30Hz to 50Hz, after 400Hz high-pass filtering, 1024 point window.

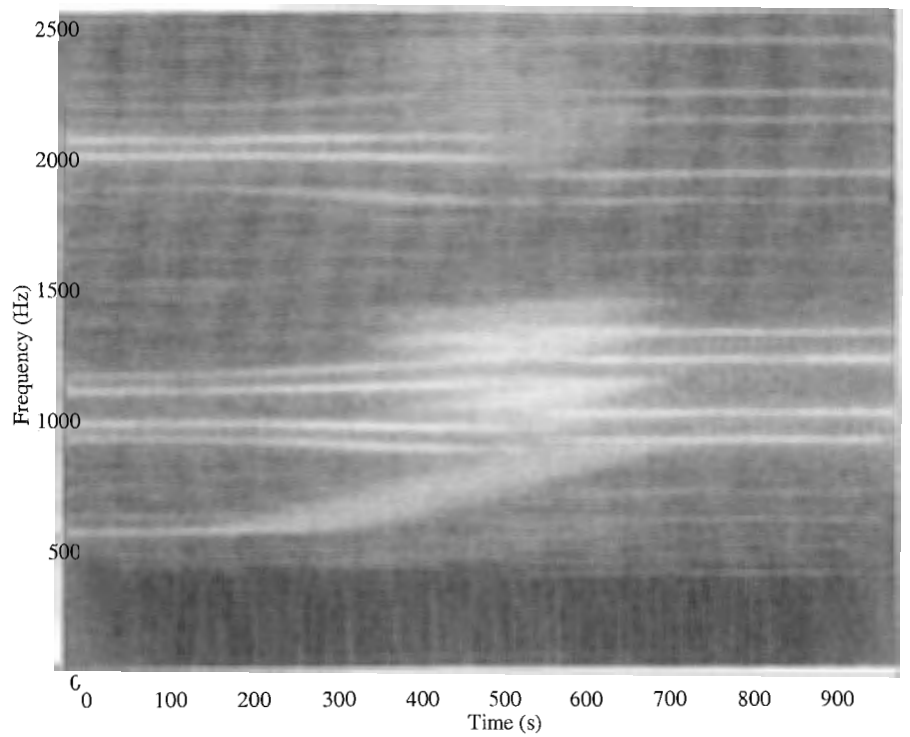

Figure 8.12: STFT of current waveform with drive frequency ramping from 30Hz to 50Hz, after 400Hz high-pass filtering, 2048 point window.

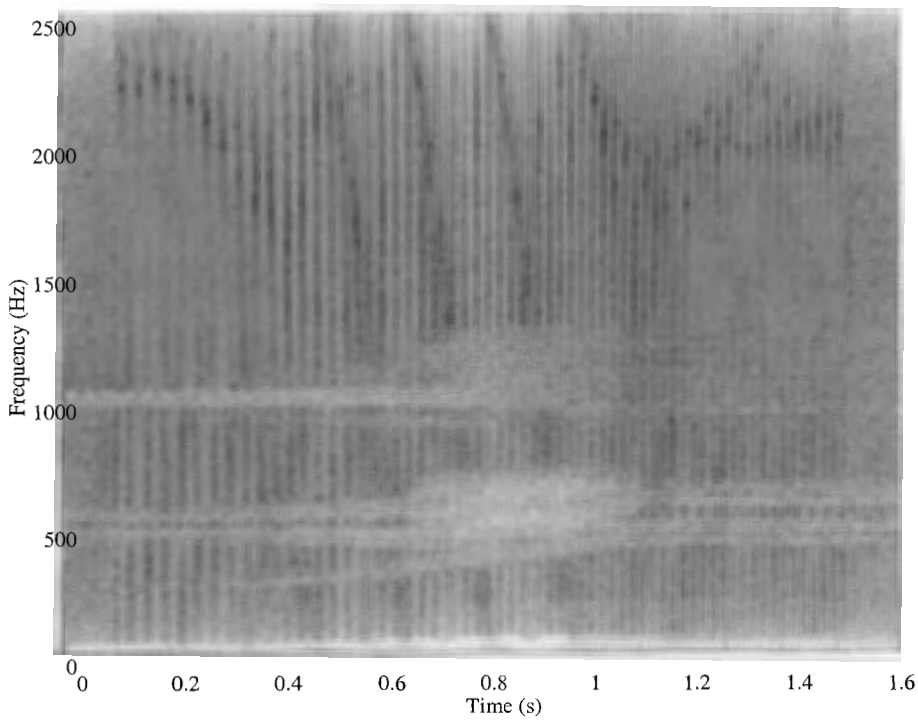

Figure 8.13: Wigner-Ville distribution of current waveform with drive frequency ramping from 30Hz to 50Hz.

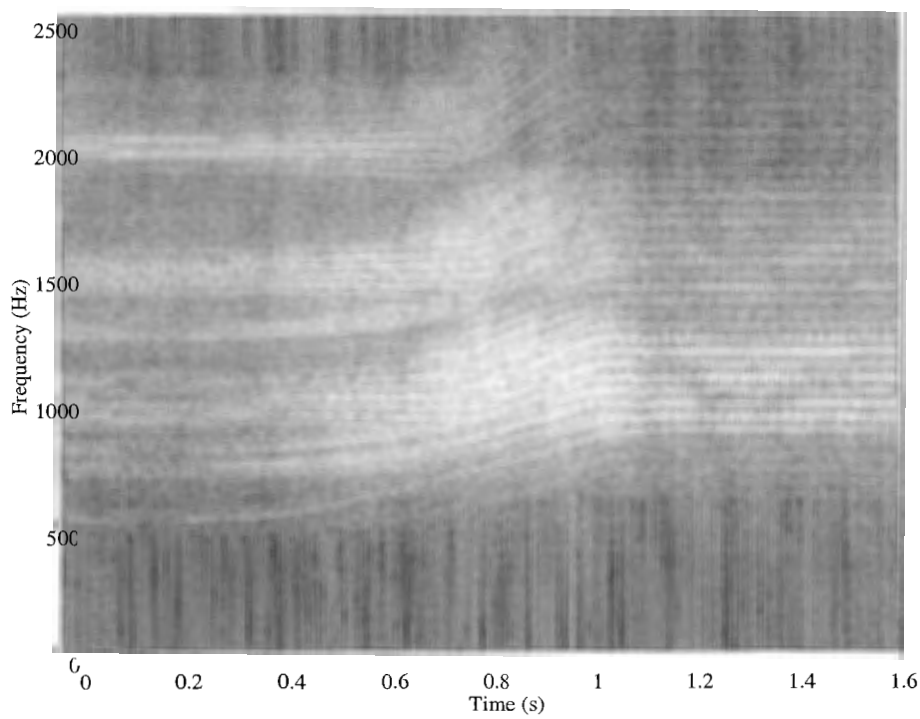

Figure 8.14: Wigner-Ville distribution of current waveform with drive frequency ramping from 30Hz to 50Hz, after 400Hz high-pass filtering.

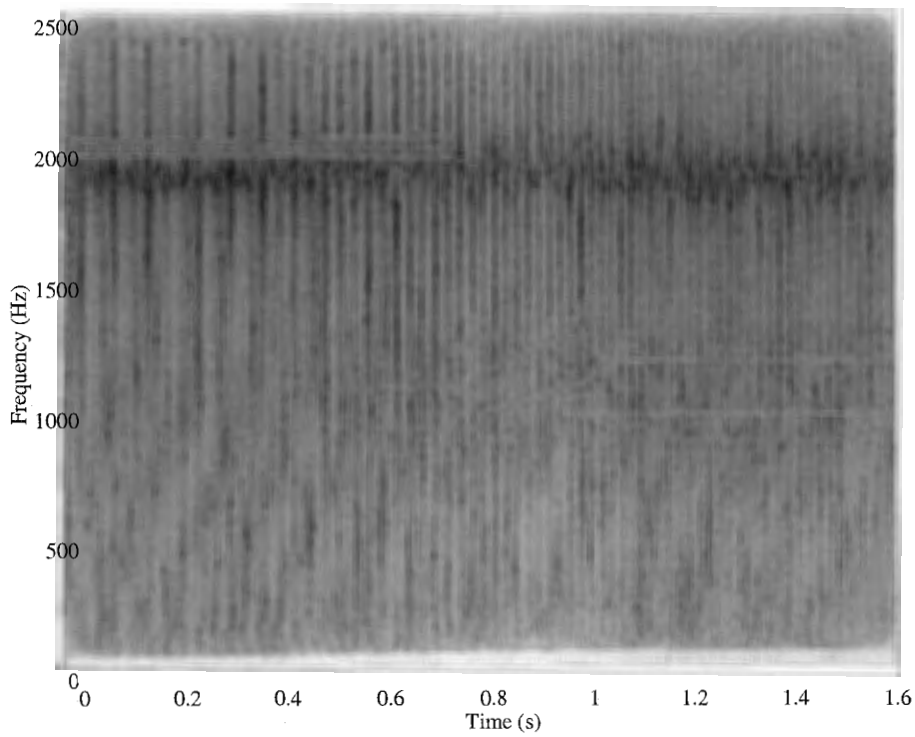

Figure 8.15: Choi-Williams distribution of current waveform with drive frequency ramping from 30Hz to 50Hz.

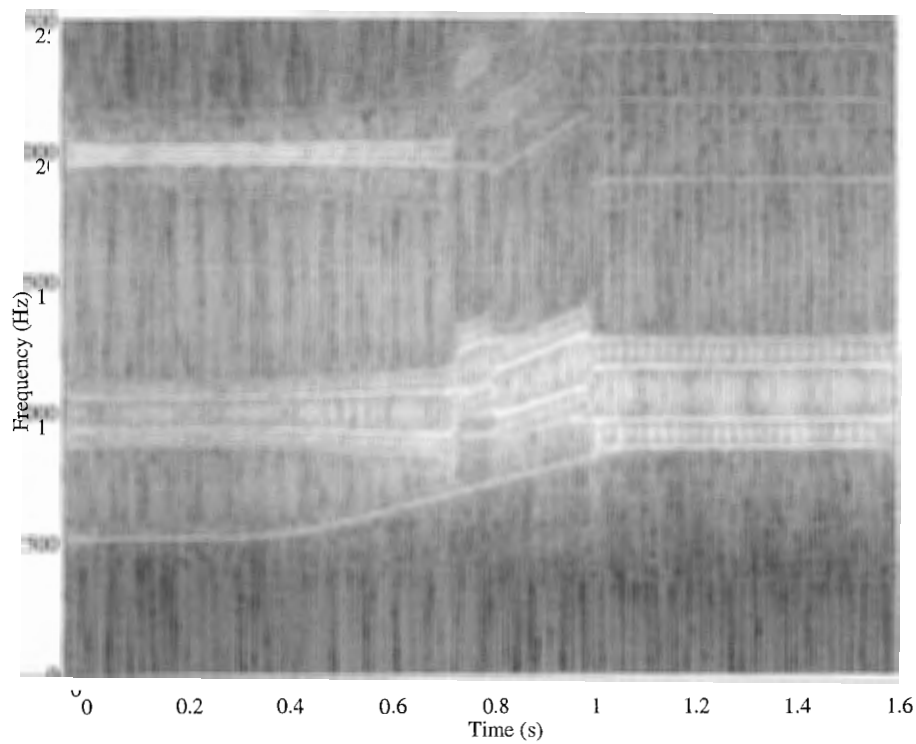

Figure 8.16: Choi-Williams distribution of current waveform with drive frequency ramping from 30Hz to 50Hz, after 400Hz high-pass filtering.

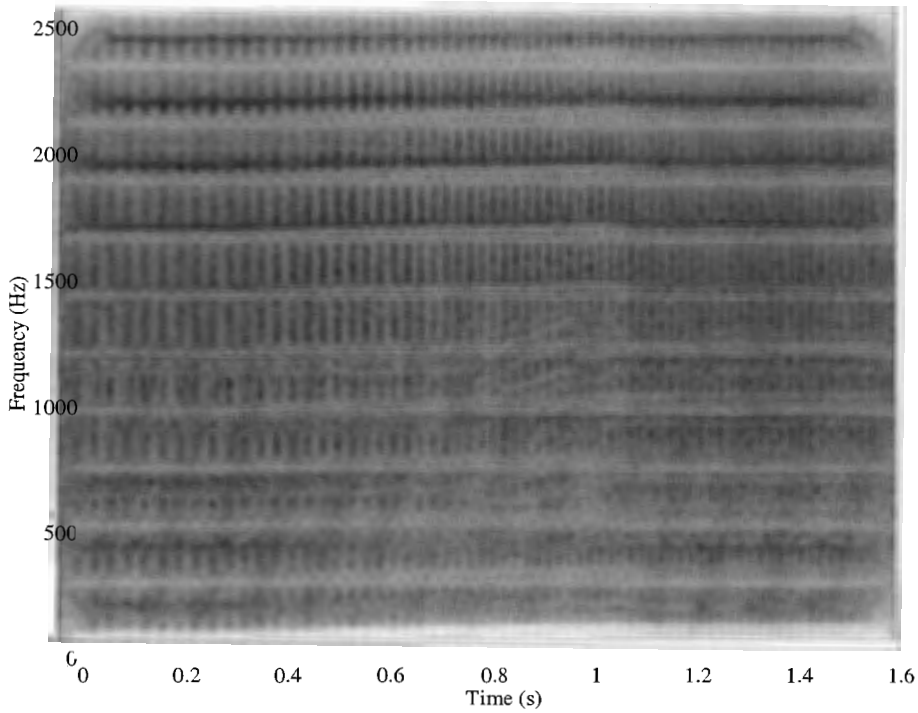

Figure 8.17: Zhao-Atlas-Marks distribution of current waveform with drive frequency ramping from 30Hz to 50Hz.

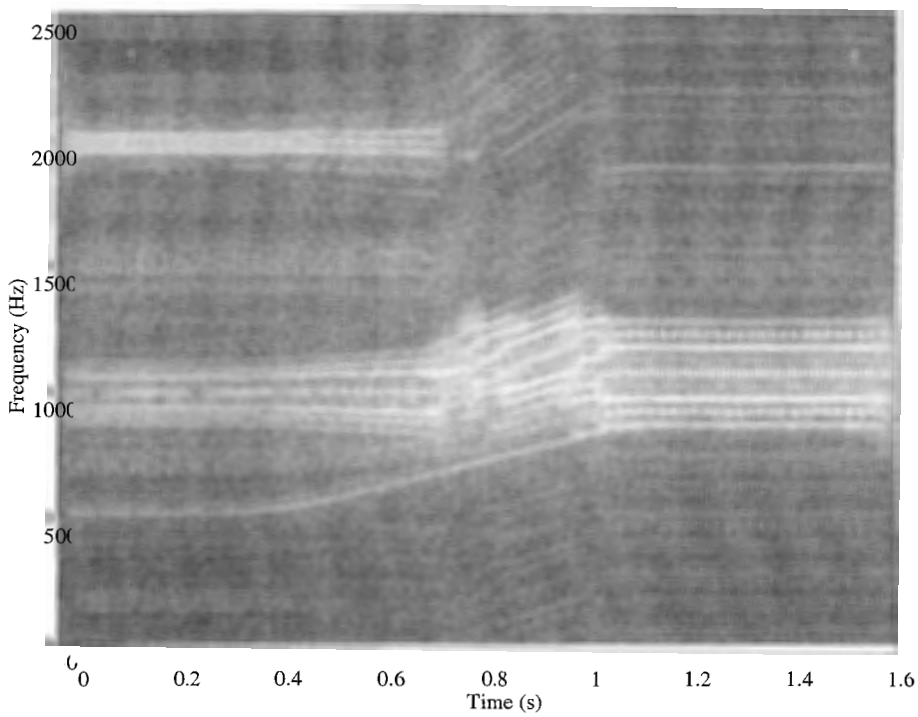

Figure 8.18: Zhao-Atlas-Marks distribution of current waveform with drive frequency ramping from 30Hz to 50Hz, after 400Hz high-pass filtering.

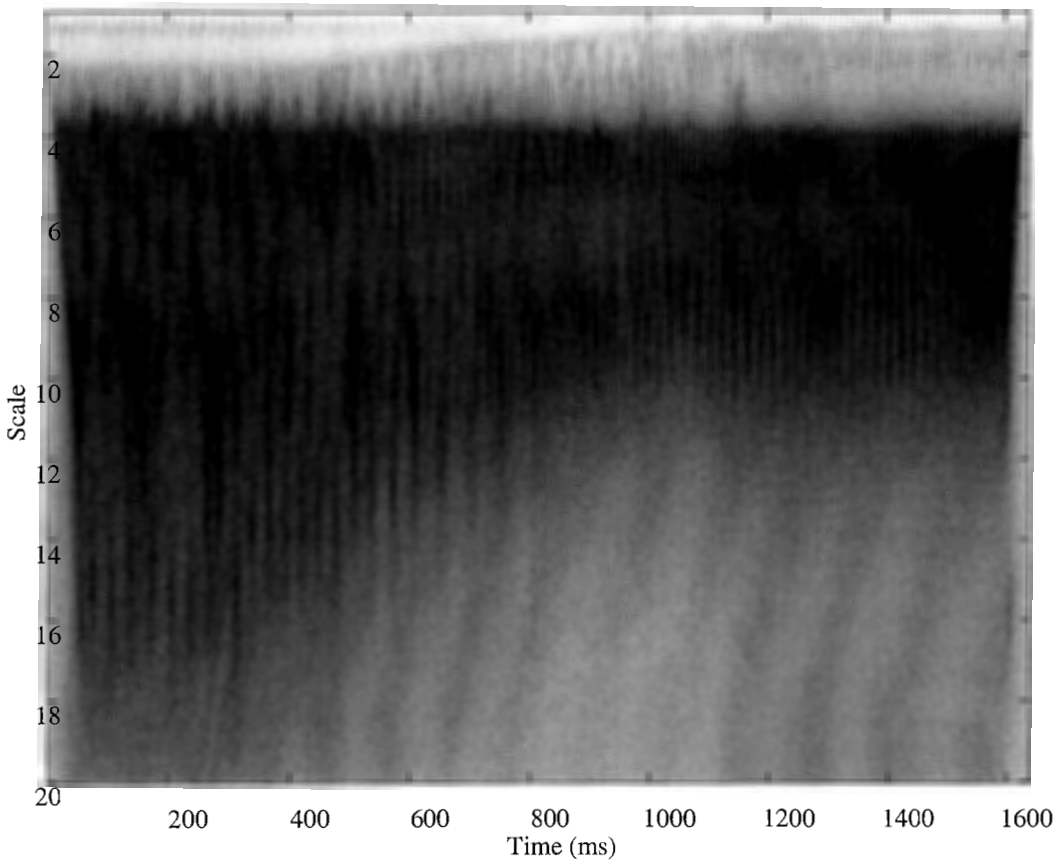

Figure 8.19: Wavelet transform of current waveform with drive frequency ramping from 30Hz to 50Hz.

CHAPTER 9

Summary and Recommendations for Future Work

9.1 Introduction

This thesis has examined a variety of topics related to the detection of broken rotor bars in squirrel cage induction motors, with particular reference to those motors controlled by variable speed drives. There has been significant research world-wide on the detection of broken rotor bars in mains supplied induction motors, but very little on motors controlled by variable speed drives. As the use of such drives becomes more widespread, this subject will gain in importance. This study examined some of the implications that variable speed drives have for the detection of rotor damage. In addition, a model was developed to allow the numerical simulation of induction motors with broken rotor bars, supplied by voltage source inverter drives.

This chapter summarises the important points encountered during the course of this study. A number of possible extensions and areas of improvement which could be further investigated are also outlined.

9.2 Summary of Work

Chapter 2 showed that broken rotor bars may be detected by the presence of twice slip-frequency sidebands in the stator current frequency spectrum, that is there are frequency components at $f_{bb} = f_1(1 \pm 2s)$, where f_1 is the supply frequency, and s is the per unit slip. The effects of window functions on the detection of these frequency components was examined in Chapter 3. Since the twice slip-frequency sidebands are so important for the detection of rotor damage, a statistical analysis of the variation in sideband amplitude due to slight variations in sampling and motor operation, was performed. One hundred records of the stator current were sampled with the motor operating in a steady state. The sideband amplitudes were calculated and their variation analysed and plotted. It was found that the standard deviation was about 1dB for an average value of about -36dB, whilst the amplitudes had a range of about 5dB. Thus for any particular frequency spectrum there may be an uncertainty in the sideband amplitudes of up to ±3dB. It is important to take this variation into account.

A parametric spectrum estimation technique, Prony's method, was also examined as a possible alternative to the Fourier transform. Parametric techniques model the signal using a limited number of frequency components, and require only a small number of data points in order to solve for the model parameters. The Prony method examined here uses a model order of 20, which required 200 data points to be sampled. In contrast, the Fourier transform required 32 768 data points in order to generate a spectrum with reasonable frequency resolution. Thus parametric techniques have the advantage that the signal being sampled need only be stationary for a very short time. However, the disadvantage is that they are not good at modelling signals with components that are close together in frequency, but of greatly different amplitude.

A frequency multiplying phase locked loop (PLL) can be used to ensure that the stator current waveform is synchronously sampled. This has the benefit of reducing the supply frequency peak to a single line in the frequency spectrum, eliminating the need for windowing, and allowing the broken rotor bar sidebands to be very well defined and easy to identify. It also has the major advantage that any change in the supply frequency is tracked and synchronous sampling maintained.

Chapter 4 developed a design for a PLL circuit, based on the 4046B integrated circuit, which generates a clock waveform at a constant multiple of the frequency of the signal being sampled. When used to control the sampling hardware, this circuit ensures that a signal is synchronously sampled. The circuit was designed for a centre frequency of 50Hz, and tuned to have a capture range of 45-55Hz, and a tracking range of 32-68Hz. This design makes it particularly suitable for mains supply operation.

The frequency tracking behaviour of the PLL sampling method naturally leads to application of the system to motors supplied by variable speed drives, in which the supply frequency can vary quite widely. It was found that the PLL circuit performance was sometimes unsatisfactory, depending on the drive used and the frequency variation that occurred. The main problem was found to be rapid jitter of the output frequency of the drive, which caused the PLL to lose lock. However, this problem could be overcome if the PLL sampling technique was integrated as part of the variable speed drive itself, as jitter-free control signals would be accessible.

The advent of the semiconductor switch has led to the development of the variable speed drive. Chapter 5 examined various pulse-width modulation strategies which are used by drives in order to produce the desired output voltage waveform. The strategies examined include natural-sampled, symmetric and asymmetric sampled, optimised, random, and space vector. The frequency spectra of these strategies have been examined, as has the implications that they have for condition monitoring.

It was found that pulse-width modulation strategies generally produce output harmonics at a number of discrete frequencies including the modulating frequency and harmonics, the carrier frequency and harmonics, and modulation products which combine the carrier and modulating frequencies. These frequency components are only a problem for condition monitoring if they mask any fault frequency components. Most of the components are quite high in the frequency range, but this is dependent on the parameters used to implement the pulse-width modulated waveform. They may mask the rotor slotting frequencies, which could be a problem for condition monitoring systems which depend on these to find the speed of the motor. The effect of drive harmonics could be completely disregarded if the drive and condition monitoring systems were integrated. The drive could then use an optimised pulse-width modulated technique to eliminate any frequency components that may mask fault frequency components.

This chapter also considered the effect of the drive frequency on the amplitudes of the twice slip-frequency sidebands. The amplitude of the upper sideband was found to decrease with increasing drive frequency, whilst that of the lower sideband increased. The average of the two appeared to remain about constant. Hence it may be better to consider using the average of the upper and lower sideband amplitudes as an indicator of rotor damage rather than either in isolation.

The effect of load level on the amplitude of the sidebands was also examined by varying the load at constant supply frequencies. It was found that the amplitude of the lower sideband increased with increasing load, whilst that of the upper sideband decreased. Again it is necessary to consider both sidebands to gain a better indication of damage.

Finally an interesting phenomenon, which was termed the reflected frequency, was noted when examining the spectra collected at different drive frequencies. The reflected frequency appeared at (100 - f_d)Hz, where f_d is the drive frequency, in the spectrum of the stator current. This component can mask the sideband frequencies, so it must be taken into account when examining the sideband amplitudes. The origin of the reflected frequency is unknown, though it is thought it could be a

product of the rectification of the mains to produce the DC link voltage. A drive output waveform was observed to contain a large ripple component and its spectrum contained the reflected frequency. However attempts to simulate this were unsuccessful.

The next chapter described the development of a mathematical model for the cage rotor induction motor, which takes into account the physical arrangement of the stator windings and rotor bars. The model incorporates torque and inertia into mechanical equations in order to allow full transient simulation. The motor model is based on magnetically coupled coils, and models the interaction of the stator and rotor magnetic fields as the rotor rotates by means of detailed descriptions of both stator and rotor coil geometry. It was modified in order to incorporate the effects of broken rotor bars.

A computer implementation of the model was used to simulate the operation of a laboratory motor, both with and without a broken rotor bar. Simulations for both mains and pulse-width modulated voltage operation were performed, and the resulting stator current spectrum analysed. The expected $(1\text{-}2s)f_1$ frequency component was observed to be present when a broken bar was simulated. In addition to this, the upper sideband $(1+2s)f_1$ was also observed due to the full transient nature of the model, which allowed the speed and torque to oscillate.

The amplitude of the sidebands was rather higher than those measured from the test motor. This was probably due to inter-bar currents in the test motor, which would tend to reduce the amplitude of the magnetic disturbance, and hence, the amplitude of the sidebands that were measured. Inter-bar currents were not accounted for in the model, which assumed that the bars were insulated from the iron core, whereas in practice they are not.

The next chapter examined some experimental results, both from a laboratory motor and an industrial case study. This demonstrated the utility of the PLL sampling circuit in an industrial situation, proving its use as a diagnostic tool.

The final chapter examined time-frequency and wavelet analysis of the stator current waveforms. It was found that these methods gave an overall picture of how the main frequency components of the waveform varied over time. However, the necessary resolution to distinguish the sidebands was lacking. The main use of these techniques would be to obtain the speed of the motor by tracking the rotor slotting frequency. Alternatively, they could be used to determine the times when the motor was operating at a constant speed, allowing other techniques to focus on this time.

9.3 Future Extensions

9.3.1 Implementation

This thesis has provided some background work on the detection of broken rotor bars in an induction motor supplied by a variable speed drive. This information could be used as the basis for implementing a condition monitoring system.

Modern variable speed drives are completely controlled by a digital computer, and all functions can be programmed. Since the system is already digital, it would be relatively simple to integrate another processing unit which would be dedicated to condition monitoring. Data could be obtained from the primary control computer to get the drive output frequency or even the actual switching times of the modulation control. In general, variable speed drives have current sensing transducers already installed to detect over-current faults. These could be utilised by a condition monitoring system to obtain the current waveform required to detect faults.

Since variable speed drives are increasingly part of an overall computerised plant control system, it seems obvious to use them for condition monitoring. Indeed, most drives already monitor internal quantities in order to detect some drive faults. It is a simple extension to provide full motor monitoring facilities. There are two options for implementing a condition monitoring system. One scenario would have the drive simply collecting raw data and sending it back through the communications link to a centralised processing facility for analysis. The other

would have a drive intelligent enough to analyse the data internally and advise the central control of any imminent faults. Both strategies are equally valid, though the first would certainly be cheaper to implement, and probably involve little more than reprogramming of the drive computer.

This type of condition monitoring system has several advantages over one which requires manual data collection. The first is that the motor can be continuously monitored in order to detect faults as they occur. The major advantage is that it does not require the data to be manually sampled, this increases the quality of the data, and decreases the costs. In fact, a fully automated system could be set up for remote condition monitoring.

It would seem to be relatively simple for a drive manufacturer to offer an integrated condition monitoring option for existing and new drive products.

9.3.2 Modelling of the Induction Motor with Broken Rotor Bars

The major improvement which could be made to the numerical modelling would be to include the effect of inter-bar currents. Heller and Hamata [47] modelled the core as a lattice of impedances between each bar. This is quite realistic to the extent that each lamination is insulated from the next and so could be modelled as a lumped impedance. However, there are too many laminations to model each individually so a number of them must be grouped as one equivalent lamination. Even so, including inter-bar currents in this way would increase the size of the matrices by a factor equal to the number of lumped impedances used to model the core laminations. As the time taken to run the simulations is proportional to the square of the size of the matrices, the computing time required rapidly becomes astronomical.

Another way to incorporate the effects of inter-bar currents may be to include the equation developed by Kerszenbaum and Landy [52], Equation (2.22). This would adjust them magnitude of the currents flowing in each bar, and should result in a more realistic simulation. It would not increase the computational complexity by much as it would only modify each bar current by a correction factor.

Another improvement to the model may be to include the effects of variation of inductance parameters with frequency. This would require the parameters, which are constants at the moment, to be modelled as varying with frequency.

9.3.3 Artificial Intelligence

The frequency spectrum of the stator current of an induction motor with a broken rotor bar contains a very large number of frequency components, especially when it is supplied by a variable speed drive. The process of determining which components are caused by what factors is a very difficult problem for most human experts. If a truly automatic condition monitoring system is to be built, then it is necessary for a computer to be able to successfully analyse the data collected. This is made easier if the condition monitoring system is integrated with a variable speed drive, as then more information is available to the algorithm.

Recently there has been some research reported which examines the feasibility of using neural networks [148-151], and expert systems [152] [153]. The future of condition monitoring systems certainly lies in this direction, as systems must become more automated. These methods will still need to be able to identify the origins of the various components of the frequency spectrum, hence there is still a need for basic research into the mechanisms causing each component to appear.

9.4 Concluding Remarks

This thesis has examined factors affecting the detection of broken rotor bars in induction motors supplied by variable speed drives. This area will become more important in time as the popularity of variable speed drives increases. The interest in the practical implementation of condition monitoring systems will also increase as companies try to further improve productivity by decreasing unscheduled outages. As the squirrel cage induction motor will continue to be the workhorse of industry for the foreseeable future, its continued operation will be vital to this process.

APPENDIX A

Laboratory Equipment

A.1 Induction Motors

The main motor used for laboratory experiments was manufactured by Pope Electric Motors Australia Pty. Ltd. This motor had two different rotors available for it, one was the original, whilst the other was damaged by milling through the junction between one rotor bar and an end-ring. The motor has the following specifications:

Rated output: 7.5kW.

Rated current: 14.1A.

Rated speed: 1420 rpm.

Moment of inertia: 0.040 kgm^2

415V, 50Hz, 3 phase, delta connected, 0.86 power factor, 4 pole.

Design details:

36 slot stator, concentric winding, three coils/group, 75 turns per coil.

32 rotor slots, cast aluminium cage.

Calculated values:

Stator resistance: 1.6Ω

Stator inductance: 0.346H

Rotor bar resistance: 52.43 μΩ

Rotor bar leakage reactance: 0.7746 μH

End ring segment resistance: 0.06972 μΩ

End ring segment leakage reactance: 0.003622 μH

A.2 Current Clamps

Two types of current clamp were used to sample the stator current waveform of induction motors.

A.2.1 Fluke Current Clamp

This is a Hall-effect, multimeter style clamp, made by Fluke Inc. It has an amplifier located in the handles, and it is all enclosed in a plastic case.

Model: 80i-1010

Current Range: 1-1000A DC, 1-700A AC

Frequency range: DC to 440Hz

Output: 1mV per amp

Uncertainty: 2-5% depending on current.

A.2.2 FCC Current Clamp

This is an RF type, fully shielded, wound transformer, manufactured by Fischer Custom Communications Inc.

Model: F-14-1

Serial No: 22

Frequency response: Flat from 10Hz - 400kHz. (with terminator)

A.3 Variable Speed Drives

The main variable speed drive that was used in the laboratory was a SAMI GS manufactured by ABB Strömberg Drives Oy, Finland.

Model: ACS501-020-3

Rated output 20kVA.

A.4 DC Loading Generator

The machine used in the laboratory as a DC generator to load the induction motor was manufactured by MacFarlane and was rated at:

Rated Output 10hp

Rated Speed 1500 rpm

Armature 240V 29A

Field 200V 1A

Serial number 13206

A.5 Data Acquisition System

The data acquisition system consisted of a 486 based PC, with a PCL-818 data acquisition card. A Keithley MetraByte SSH-4 simultaneous sample-and-hold board was used to hold up to four channels of data. Custom designed anti-aliasing filters were used.

APPENDIX B

Analytical Expressions for PWM Waveforms

B.1 Introduction

It is possible to analyse PWM waveforms to derive analytical expressions using a two-dimensional Fourier transform approach [83]. This results in analytical expressions for the time waveform as follows, for natural and regular sampled PWM. Space vector PWM can be analysed by considering a general switched waveform and decomposing it into patterns which have a symmetry property. The Fourier transforms of these can then be summed to get a spectrum of the original waveform [100]. In the following sections $J_n(x)$ is an *nth* order Bessel function of the first kind [154]. The waveform is assumed to be a line-to-line waveform of a three-phase system produced by the difference of two line-to-neutral waveforms. There are three possible output levels : $-E$, 0, and E. The carrier wave has an angular frequency of ω_c rad/s, and the modulating wave has an angular frequency

of ω_m, and an initial phase of ϕ. The frequency ratio is R = ω_c/ω_m, and M is the modulation depth, which is the ratio of the amplitudes of the carrier and modulating waves.

B.2 Natural Sampled PWM

A natural sampled PWM waveform, $PWM_{nat}(t)$, can be expressed as [85]:

$$PWM_{nat}(t) = EM\sin(\omega_m t+\phi) + \frac{2E}{\pi}\sum_{m=1}^{\infty}\sum_{\substack{n=\pm1\\ n\ odd}}^{\pm\infty}\frac{J_n(m\pi M)}{m}\sin\left[(m\omega_c+n\omega_m)t+n\phi\right] \tag{B.1}$$

B.3 Symmetrical Regular Sampled PWM

An analytical expression for a symmetrical regular sampled PWM waveform, $PWM_{srs}(t)$, is [87]:

$$\begin{aligned}
PWM_{srs}(t) = {} & \frac{4E}{\pi^2}\sum_{n=1}^{\infty}\frac{R}{n}\sin\left(\frac{n\pi}{3}\right)\left[\sum_{\substack{h=-\infty\\ h\neq -n}}^{\infty}\left[\frac{J_h\left(\frac{n}{R}M\frac{\pi}{2}\right)}{h+n}\sin\left\{(h+n)y^*\right\}\right.\right.\\
& \left.\times\left\{(-1)^{h+n+1}-1\right\}\sin\left\{\left(\frac{n}{R}+h\right)\frac{\pi}{2}\right\}\right]\\
& \left.+J_n\left(\frac{n}{R}M\frac{\pi}{2}\right)(\pi-2y^*)\sin\left\{\left(\frac{n}{R}+n\right)\frac{\pi}{2}\right\}+\frac{1}{n}\sin\left(\frac{n}{R}\pi\right)\sin(ny^*)\right]\\
& \times\cos\left(n\omega_m t+n\Phi-\frac{n}{R}\pi-n\frac{\pi}{3}+\frac{\pi}{2}\right)\\
& +\frac{4E}{\pi^2}\sum_{m=1}^{\infty}\sum_{\substack{n=\pm1\\ n\neq -mp}}^{\pm\infty}\frac{1}{m^*}\sin\left(\frac{n\pi}{3}\right)\left[\sum_{\substack{h=-\infty\\ h\neq -n}}^{\infty}\left[\frac{J_h\left(m^*M\frac{\pi}{2}\right)}{h+n}\sin\left\{(h+n)y^*\right\}\right.\right.\\
& \left.\left\{(-1)^{h+n+1}-1\right\}\sin\left\{(m^*+h)\frac{\pi}{2}\right\}\right]\\
& \left.+J_n\left(m^*M\frac{\pi}{2}\right)(\pi-2y^*)\sin\left\{(m^*+n)\frac{\pi}{2}\right\}+\frac{1}{n}\sin(m^*\pi)\sin(ny^*)\right]\\
& \times\cos\left\{(m\omega_c+n\omega_m)t+n\phi-\frac{n}{R}\pi-n\frac{\pi}{3}+\frac{\pi}{2}\right\}
\end{aligned} \tag{B.2}$$

where:

$$m^* = m + \frac{n}{R} \tag{B.3}$$

$$y^* = \begin{cases} \arccos\dfrac{1}{M}; & M > 1, \\ 0; & M \le 1. \end{cases} \tag{B.4}$$

$$\Phi = R\phi \tag{B.5}$$

B.4 Asymmetrical Regular Sampled PWM

An analytical expression for a symmetrical regular sampled PWM waveform, $PWM_{ars}(t)$, is [87]:

$$\begin{aligned} PWM_{ars}(t) = {} & \frac{4E}{\pi^2}\sum_{n=1}^{\infty}\frac{1}{n}\sin\left(\frac{n\pi}{3}\right)\left[\sum_{\substack{h=-\infty \\ h\neq -n}}^{\infty}\left[\frac{J_h\left(\frac{n}{R}M\frac{\pi}{2}\right)}{h+n}\sin\left\{(h+n)y^*\right\}\right.\right. \\ & \left.\times\left\{(-1)^{h+n+1}-1\right\}\sin\left\{h\frac{\pi}{2}\right\}\right] + J_n\left(\frac{n}{R}M\frac{\pi}{2}\right)(\pi-2y^*)\sin\left\{n\frac{\pi}{2}\right\} \\ & \left.+\frac{2}{n}\sin\left(\frac{n\pi}{2R}\right)\sin^2\left(n\frac{\pi}{2}\right)\sin(ny^*)\right] \\ & \times\cos\left(n\omega_m t + n\Phi - \frac{n\pi}{2R} - n\frac{\pi}{3} + \frac{\pi}{2}\right) \\ & + \frac{4E}{\pi^2}\sum_{m=1}^{\infty}\sum_{\substack{n=\pm 1 \\ n\neq -mp}}^{\pm\infty}\frac{1}{m^*}\sin\left(n\frac{\pi}{3}\right)\left[\sum_{\substack{h=-\infty \\ h\neq -n}}^{\infty}\left[\frac{J_h\left(m^*M\frac{\pi}{2}\right)}{h+n}\sin\left\{(h+n)y^*\right\}\right.\right. \\ & \left.\times\left\{(-1)^{h+n+1}-1\right\}\sin\left\{(m+h)\frac{\pi}{2}\right\}\right] \\ & + J_n\left(m^*M\frac{\pi}{2}\right)(\pi-2y^*)\sin\left\{(m+n)\frac{\pi}{2}\right\} \\ & \left.+\frac{1}{n}\sin(ny^*)\sin\left(\frac{n\pi}{2R}\right)\left\{\cos(m\pi)-\cos(n\pi)\right\}\right] \\ & \times\cos\left\{(m\omega_c + n\omega_m)t + n\phi - \frac{n\pi}{2R} - n\frac{\pi}{3} + \frac{\pi}{2}\right\} \end{aligned} \tag{B.6}$$

where the symbols are defined in the previous section.

B.5 Space Vector PWM

Boys and Handley [100] determined an approximate expression, $PWM_{sv}(t)$, for space vector PWM to be:

$$PWM_{sv}(t) = \sum_{i=1}^{15} P_i(t) \tag{B.7}$$

where:

$$P_1(t) = \sum_{p=0}^{\infty}\sum_{q=0}^{\infty} \frac{\pm 4}{\pi\left[2p \pm (2q+1)\frac{\omega_m}{\omega_c}\right]} J_{2q+1}\left\{\frac{\pi M}{2}\left(2p \pm (2q+1)\frac{\omega_m}{\omega_c}\right)\right\} \times \sin\left\{2p\omega_c t \pm (2q+1)(\omega_m t + \phi)\right\} \tag{B.8}$$

$$P_2(t) = \sum_{p=0}^{\infty}\sum_{q=0}^{\infty} \frac{\pm 2}{46.241\pi\left[2p \pm (2q+1)\frac{\omega_m}{\omega_c}\right]} \left\{\frac{\pi M}{2}\left(2p \pm (2q+1)\frac{\omega_m}{\omega_c}\right)\right\}^2 \times J_{2q+1}\left\{\frac{\pi M}{2}\left(2p \pm (2q+1)\frac{\omega_m}{\omega_c}\right)\right\} \sin\left\{2p\omega_c t \pm (2q+1)(\omega_m t + \phi)\right\} \tag{B.9}$$

$$P_3(t) = \sum_{p=0}^{\infty}\sum_{q=0}^{\infty}\sum_{r=1}^{\infty} \frac{\pm 1}{\pi\left[2p \pm (2q+1+6r)\frac{\omega_m}{\omega_c}\right]} \times \left[\frac{\pi M}{2}\left\{2p \pm (2q+1+6r)\frac{\omega_m}{\omega_c}\right\}\right]^2 \frac{(-1)^r}{8\pi\sqrt{3}(r+\frac{1}{3})(r-\frac{1}{3})} \times J_{2q+1}\left[\frac{\pi M}{2}\left\{2p \pm (2q+1+6r)\frac{\omega_m}{\omega_c}\right\}\right] \times \sin\left\{2p\omega_c t \pm (2q+1+6r)(\omega_m t + \phi)\right\} \tag{B.10}$$

$$P_4(t) = \sum_{p=0}^{\infty}\sum_{q=0}^{\infty}\sum_{r=1}^{\infty} \frac{\pm 1}{\pi\left[2p \pm (2q+1-6r)\frac{\omega_m}{\omega_c}\right]} \times \left[\frac{\pi M}{2}\left\{2p \pm (2q+1-6r)\frac{\omega_m}{\omega_c}\right\}\right]^2 \frac{(-1)^r}{8\pi\sqrt{3}(r+\frac{1}{3})(r-\frac{1}{3})} \times J_{2q+1}\left[\frac{\pi M}{2}\left\{2p \pm (2q+1-6r)\frac{\omega_m}{\omega_c}\right\}\right] \times \sin\left\{2p\omega_c t \pm (2q+1-6r)(\omega_m t + \phi)\right\} \tag{B.11}$$

$$P_5(t)=\sum_{p=0}^{\infty}\sum_{r=0}^{\infty}\frac{\pm(-1)^r M}{\pi\sqrt{3}(2r+\frac{2}{3})(2r+\frac{4}{3})}\ J_0\left\{\frac{\pi M}{2}\left(2p\pm 3(2r+1)\frac{\omega_m}{\omega_c}\right)\right\} \times\sin\left\{2p\omega_c t\pm 3(2r+1)(\omega_m t+\phi)\right\} \tag{B.12}$$

$$P_6(t)=\sum_{p=0}^{\infty}\sum_{q=0}^{\infty}\sum_{r=0}^{\infty}\frac{\pm(-1)^r M}{\pi\sqrt{3}(2r+\frac{2}{3})(2r+\frac{4}{3})} \times J_{2q}\left\{\frac{\pi M}{2}\left(2p\pm\left(3(2r+1)+2q\right)\frac{\omega_m}{\omega_c}\right)\right\} \times\sin\left\{2p\omega_c t\pm\left(3(2r+1)+2q\right)(\omega_m t+\phi)\right\} \tag{B.13}$$

$$P_7(t)=\sum_{p=0}^{\infty}\sum_{q=0}^{\infty}\sum_{r=0}^{\infty}\frac{\pm(-1)^r M}{\pi\sqrt{3}(2r+\frac{2}{3})(2r+\frac{4}{3})} \times J_{2q}\left\{\frac{\pi M}{2}\left(2p\pm\left(3(2r+1)-2q\right)\frac{\omega_m}{\omega_c}\right)\right\} \times\sin\left\{2p\omega_c t\pm\left(3(2r+1)-2q\right)(\omega_m t+\phi)\right\} \tag{B.14}$$

$$P_8(t)=\sum_{p=0}^{\infty}\sum_{q=0}^{\infty}\frac{-4}{\pi\left[(2p+1)\pm 2q\frac{\omega_m}{\omega_c}\right]}\ J_{2q}\left\{\frac{\pi M}{2}\left((2p+1)\pm 2q\frac{\omega_m}{\omega_c}\right)\right\} \times\sin\left\{(2p+1)\omega_c t\pm 2q(\omega_m t+\phi)\right\} \tag{B.15}$$

$$P_9(t)=\sum_{p=0}^{\infty}\frac{2}{46.241\pi(2p+1)}\left\{\frac{\pi M}{2}(2p+1)\right\}^2 \times J_0\left\{\frac{\pi M}{2}(2p+1)\right\}\sin\left\{(2p+1)\omega_c t\right\} \tag{B.16}$$

$$P_{10}(t)=\sum_{p=0}^{\infty}\sum_{q=0}^{\infty}\frac{2}{46.241\pi\left[(2p+1)\pm 2q\frac{\omega_m}{\omega_c}\right]}\left\{\frac{\pi M}{2}\left((2p+1)\pm 2q\frac{\omega_m}{\omega_c}\right)\right\}^2 \times J_{2q}\left\{\frac{\pi M}{2}\left((2p+1)\pm 2q\frac{\omega_m}{\omega_c}\right)\right\}\sin\left\{(2p+1)\omega_c t\pm 2q(\omega_m t+\phi)\right\} \tag{B.17}$$

$$P_{11}(t)=\sum_{p=0}^{\infty}\sum_{r=1}^{\infty}\frac{1}{\pi\left[(2p+1)\pm 6r\frac{\omega_m}{\omega_c}\right]}\frac{(-1)^r}{8\pi\sqrt{3}\left(r+\frac{1}{3}\right)\left(r-\frac{1}{3}\right)}$$
$$\times\left[\frac{\pi M}{2}\left\{(2p+1)\pm 6r\frac{\omega_m}{\omega_c}\right\}\right]^2 J_0\left[\frac{\pi M}{2}\left\{(2p+1)\pm 6r\frac{\omega_m}{\omega_c}\right\}\right] \quad \text{(B.18)}$$
$$\times\sin\left\{(2p+1)\omega_c t\pm 6r(\omega_m t+\phi)\right\}$$

$$P_{12}(t)=\sum_{p=0}^{\infty}\sum_{q=0}^{\infty}\sum_{r=1}^{\infty}\frac{1}{\pi\left[(2p+1)\pm(2q+6r)\frac{\omega_m}{\omega_c}\right]}\frac{(-1)^r}{8\pi\sqrt{3}\left(r+\frac{1}{3}\right)\left(r-\frac{1}{3}\right)}$$
$$\times\left[\frac{\pi M}{2}\left\{(2p+1)\pm(2q+6r)\frac{\omega_m}{\omega_c}\right\}\right]^2 \quad \text{(B.19)}$$
$$\times J_{2q}\left[\frac{\pi M}{2}\left\{(2p+1)\pm(2q+6r)\frac{\omega_m}{\omega_c}\right\}\right]$$
$$\times\sin\left\{(2p+1)\omega_c t\pm(2q+6r)(\omega_m t+\phi)\right\}$$

$$P_{13}(t)=\sum_{p=0}^{\infty}\sum_{q=0}^{\infty}\sum_{r=1}^{\infty}\frac{1}{\pi\left[(2p+1)\pm(2q-6r)\frac{\omega_m}{\omega_c}\right]}\frac{(-1)^r}{8\pi\sqrt{3}\left(r+\frac{1}{3}\right)\left(r-\frac{1}{3}\right)}$$
$$\times\left[\frac{\pi M}{2}\left\{(2p+1)\pm(2q-6r)\frac{\omega_m}{\omega_c}\right\}\right]^2 \quad \text{(B.20)}$$
$$\times J_{2q}\left[\frac{\pi M}{2}\left\{(2p+1)\pm(2q-6r)\frac{\omega_m}{\omega_c}\right\}\right]$$
$$\times\sin\left\{(2p+1)\omega_c t\pm(2q-6r)(\omega_m t+\phi)\right\}$$

$$P_{14}(t)=\sum_{p=0}^{\infty}\sum_{q=0}^{\infty}\sum_{r=0}^{\infty}\frac{(-1)^r M}{\pi\sqrt{3}\left(2r+\frac{2}{3}\right)\left(2r+\frac{4}{3}\right)}$$
$$\times\left[\frac{\pi M}{2}\left\{(2p+1)\pm\left((2q+1)-3(2r+1)\right)\frac{\omega_m}{\omega_c}\right\}\right]^2 \quad \text{(B.21)}$$
$$\times J_{2q+1}\left\{\frac{\pi M}{2}\left((2p+1)\pm\left((2q+1)-3(2r+1)\right)\frac{\omega_m}{\omega_c}\right)\right\}$$
$$\times\sin\left\{(2p+1)\omega_c t\pm\left((2q+1)-3(2r+1)\right)(\omega_m t+\phi)\right\}$$

$$
\begin{aligned}
P_{15}(t) = & \sum_{p=0}^{\infty}\sum_{q=0}^{\infty}\sum_{r=0}^{\infty} \frac{(-1)^r M}{\pi\sqrt{3}\left(2r+\frac{2}{3}\right)\left(2r+\frac{4}{3}\right)} \\
& \times \left[\frac{\pi M}{2}\left\{(2p+1)\pm\left((2q+1)+3(2r+1)\right)\frac{\omega_m}{\omega_c}\right\}\right]^2 \\
& \times J_{2q+1}\left\{\frac{\pi M}{2}\left((2p+1)\pm\left((2q+1)+3(2r+1)\right)\frac{\omega_m}{\omega_c}\right)\right\} \\
& \times \sin\left\{(2p+1)\omega_c t \pm \left((2q+1)+3(2r+1)\right)(\omega_m t+\phi)\right\}
\end{aligned}
\tag{B.22}
$$

[11] Natarajan R., "Failure identification of induction motors by sensing unbalanced stator currents", *IEEE Transactions on Energy Conversion,* Vol. 4, No. 4, pp585-590, December 1989.

[12] Binns K.J. and Dye M., "Identification of principal factors causing unbalanced magnetic pull in cage induction motors", *Proceedings of the IEE*, Vol. 120, No. 3, pp349-354, March 1973.

[13] Hargis C., Gaydon B.G., and Kamash K., "The detection of rotor defects in induction motors", *International Conference on Electrical Machines - Design and Applications*, IEE Conference Publication No. 213, pp213-220, London, 13-15 July 1982.

[14] Kliman G.B., "Spectral analysis of induction motor current to detect rotor faults with reduced false alarms", US Patent Number 5,049,815, 17 September 1991.

[15] Elder S., Watson J.F. and Thomson W.T., "Fault detection in induction motors as a result of transient analysis", IEE Publication No. 310, pp182-186, 1989.

[16] Tavner P.J., Armin K.K. and Hargis C., "An electrical technique for monitoring induction motor cages", *Proceedings of the Third International Conference on Electrical Machines and Drives*, IEE Publication No. 282, pp43-46, 16-18 November 1987.

[17] Keuck J.D., Criscoe J.C. and Burstein N.M., "Assesment of valve actuator motor rotor degradation by fourier analysis of current waveform", *IEEE Transactions on Energy Conversion*, Vol. 7, No. 3, pp460-469, September 1992.

[18] Thomson W.T. and Chalmers S.J., "On-line condition monitoring of electrical machines - research to applications", *Proceedings of the Vibration Analysis for Condition Monitoring - Techniques and User Experience Seminar*, British Institute of Non-Destructive Testing, pp73-87, 1984

[19] Hirvonen R., "On-line condition monitoring of defects in squirel cage motors", *Proceedings of the International Conference on Electrical Machines*, Vol. 2, pp267-272, Paris, France, 5-8 September 1994.

[20] Gaydon B.G. and Hopgood D.J., "Faltering pulse can reveal an ailing motor", *Electrical Review* Vol, 205, No. 14, pp37-38, 12 October 1979.

[21] Kliman G.B. and Koegl R.A., "Noninvasive detection of broken rotor bars in operating induction motors", *IEEE Transactions on Energy Conversion*, Vol. 3, No 4, pp873-879, December 1988.

[22] Elkasabgy N.M., Eastham A.R., and Dawson G.E., "The detection of broken bars in the cage rotor of an induction machine", *Conference*

Record of the IEEE Industry Applications Society Annual Meeting, Vol. 1, pp181-187, 1988.

[23] Steele M.E., Ashen R.A., and Knight L.G., "An electrical method for condition monitoring of motors", *International Conference on Electrical Machines - Design and Applications*, IEE Conference Publication No. 213, pp231-235, London, 13-15 July 1982.

[24] Kliman G.B. and Stein J., "Methods of motor current signature analysis", *Electric Machines and Power Systems*, Vol. 20, pp463-474, 1992.

[25] Watt P.A. and Langman R.A., "Condition monitoring of large induction motors", *IE Aust. Conference on Industrial Drives*, pp213-219, Rockhampton, Australia, 18-20 September1991

[26] Innes A.G., Watt P.A., and Langman R.A., "Condition monitoring of large induction motors", *Proceedings of the Australasian Instrumentation and Measurement Conference*, pp265-271, Auckland, New Zealand, 24-27 November 1992.

[27] Kryter R.C. and Haynes H.D., "Condition monitoring of machinery using motor current signature analysis", *Sound and Vibration*, pp14-21, September 1989.

[28] Thomson W.T., Leonard R.A., Milne A.J., and Penman J., "Failure identification of offshore induction motor systems using on-condition monitoring", *Proceedings of the Fourth National Reliability Conference*, 1983.

[29] Leonard R.A. and Thomson W.T., "Vibration and stray flux monitoring for unbalanced supply and inter-turn winding fault diagnosis in induction motors", *British Journal of NDT*, Vol. 28, pp211-215, July 1986.

[30] Cho K.R., Lang J.H. and Umans S.D., "Detection of broken rotor bars in induction motors using state and parameter estimation", *IEEE Transactions on Industry Applications*, Vol. 28 No. 3, pp702-709, May/June 1992.

[31] Firoozian R. and Lee C.C., "Condition monitoring of automatic control systems using parameter and systems identification: a numerical investigation", *Transactions of the Institute of Measurement and Control*, Vol. 16, No. 2, pp86-98, 1994.

[32] Du B., Capolino G.A. and Dessoude M., "A fast algorithm for a PC-based motor surveillant system", *Proceedings of the International Conference on Electrical Machines*, Vol. 2, pp273-277, Paris, France, 5-8 September 1994.

[33] Legowski S.F. and Trzynadlowski A.M., "Instantaneous stator power as a medium for the signature analysis of induction motors", *Conference*

Record of the 30th Industry Applications Society Annual Meeting, Vol.1, pp619-624, 8-12 October 1995.

[34] Thomson W.T. and Stewart I.D., "On-line current monitoring for fault diagnosis in inverter fed induction motors", *Proceedings of the Third International Conference on Power Electronics and Variable-Speed Drives*, IEE Conference Publication 291, pp432-435, 1988.

[35] Marques Cardoso A.J. and Sousa Saraiva E.S., "Condition monitoring of current source inverter-fed induction machines", *Proceedings of the 6th Conference on Power Electronics and Motion Control*, Vol. 3, pp744-748, Budapest, Hungary, 1990.

[36] Thian B.M., *Methods for Monitoring the Condition of Electrical Machines Fed from Variable Speed Drives*, PhD Thesis, University of Aberdeen, UK, 1991.

[37] Sethuraman S.K. and Saravanan M.G., "Pulse width modulated embedded control and on-line condition monitoring of induction motors", *Proceedings of the 29th Universities Power Engineering Conference*, Vol. 2, pp645-647, Galway, Ireland, 14-16 September 1994.

[38] Healy J.A., *Condition Monitoring at Associated Pulp and Paper Mills Wesley Vale, Tasmania*, M. Eng. Sc. Thesis, University of Tasmania, Australia, 1991.

[39] Penman J., Dey M.N., Tait A.J., and Bryan W.E., "Condition monitoring of electrical drives", *IEE Proceedings Part B*, Vol. 133, No. 3, pp142-148, May 1986.

[40] Krause P.C., Wasynczuk O. and Sudhoff S.D., *Analysis of Electrical Machinery*, IEEE Press, New York, 1995.

[41] Alger P.L., *Induction Machines: Their Behaviour and Uses 2nd ed.*, Gordon and Breach, Switzerland, 1995.

[42] Liwschitz-Garik M. and Whipple C.C., *Electric Machinery: Volume 2 AC Machines*, D. Van Nostrand Company Inc., New York, 1946.

[43] Chapman F.T., *A Study of the Induction Motor*, Chapman and Hall Ltd., London, 1930.

[44] Kostenko M. and Piotrovsky L., *Electrical Machines: Part Two*, Foreign Languages Publishing House, Moscow, 1962.

[45] Chochran P.L., *Polyphase Induction Motors: Analysis, Design, and Application*, Marcel Dekker Inc., New York, 1989.

[46] Yang S.J., *Low-noise Electrical Motors*, Clarendon Press, Oxford, 1981.

[47] Heller B. and Hamata V., *Harmonic Field Effects in Induction Machines*, Elsevier Scientific Publishing Company, Amsterdam, 1977.

[48] Cameron J.R., Thomson W.T., and Dow A.B., "Vibration and current monitoring for detecting airgap eccentricity in large induction motors", *IEE Proceedings Part B*, Vol. 133, No. 3, pp155-163, May 1986.

[49] Deleroi W., "Der stabbruch im Käfigläufer eines asynchronmotors, Teil 1: beschreibung mittels überlagerung eines störfeldes", *Archiv für Elektrotechnik*, Vol. 67, pp91-99, 1984.

[50] Deleroi W., "Squirrel cage motor with broken bar in the rotor - physical phenomena and their experimental assessment", *Proceedings of the International Conference on Electrical Machines*, Vol. 3, pp767-770, Budapest, Hungary, 1982.

[51] Christofides N., "Origins of load losses in induction motors with cast aluminium rotors", *Proceedings of the IEE*, Vol. 112, No. 12, pp2317-2332, December 1965.

[52] Kerszenbaum I. and Landy C.F., "The existence of large inter-bar currents in three phase squirrel cage motors with rotor-bar and/or end-ring faults", *IEEE Transactions on Power Apparatus and Systems*, Vol. 103, No. 7, pp1854-1862, July 1984.

[53] Walliser R.F. and Landy C.F., "Determination of interbar current effects in the detection of broken rotor bars in squirrel cage induction motors", *IEEE Transactions on Energy Conversion*, Vol. 9, No. 1, pp152-158, March 1994.

[54] Marple S.L., *Digital Spectral Analysis*, Prentice-Hall Inc., Englewood Cliffs New Jersey, 1987.

[55] Kay, S.M., Marple, S.L., "Spectrum analysis - A modern perspective", *Proceedings of the IEEE,* Vol. 69, No. 11, pp 1380-1419, November 1981.

[56] Gabel R.A. and Roberts R.A., *Signals and Linear Systems 3rd ed.*, John Wiley and Sons, New York, 1987.

[57] Stuart R.D., *An Introduction to Fourier Analysis*, Chapman and Hall, London, 1982.

[58] Shannon C.E. and Weaver W., *The Mathematical Theory of Communication*, University of Illinois Press, Urbana USA, 1971.

[59] Burrus C.S. and Parks T.W., *DFT/FFT and Convolution Algorithms*, John Wiley and Sons, New York, 1985.

[60] Press W.H., Teukolsky S.A., Vetterling W.T. and Flannery B.P., *Numerical Recipes in C: The Art of Scientific Computing 2nd ed.*, Cambridge University Press, Cambridge UK, 1992.

[61] Elliott D.F. and Rao K.R., *Fast Transforms: Algorithms, Analyses, Applications*, Academic Press, New York, 1982.

[62] Johnson L.W. and Riess R.D., *Numerical Analysis 2nd ed*, Addison Wesley, Reading Massachusetts, 1982.

[63] Oppenheim A.V. and Shafer R.W., *Digital Signal Processing*, Prentice-Hall Inc., Englewood Cliffs New Jersey, 1975.

[64] Rabiner L.R. and Gold B., *Theory and Application of Digital Signal Processing*, Prentice-Hall Inc., Englewood Cliffs New Jersey, 1975.

[65] Burrus C.S. and Eschenbacher P.W., "An in-place, in-order prime factor FFT algorithm", *IEEE Transactions on Acoustics, Speech and Signal Processing*, Vol. 29, No. 4, pp806-817, August 1981.

[66] Harris F.J., "On the use of windows for harmonic analysis with the discrete fourier transform", Proceedings of the IEEE, Vol. 66, No. 1, pp51-83, January 1978.

[67] Nuttall A.H., "Some windows with very good sidelobe behaviour", *IEEE Transactions on Acoustics, Speech and Signal Processing*, Vol. 29, No. 1, pp84-91, February 1981.

[68] Mitra S.K. and Kaiser J.F., *Handbook for Digital Signal Processing*, John Wiley and Sons, New York, 1993.

[69] Best R.E., *Phase-Locked Loops*, McGraw-Hill Inc., New York, 1984.

[70] Encinas J.B., *Phase Locked Loops*, Chapman and Hall, London, 1993.

[71] National Semiconductor Corporation, *CMOS Databook*, National Semiconductor Corporation, California, USA, 1981.

[72] Ferrero A. and Ottoboni R., "A low-cost frequency multiplier for synchronous sampling of periodic signals", *IEEE Transactions on Instrumentation and Measurement*, Vol. 41, No. 2, pp203-207, April 1992.

[73] Linehan D.J., Bunch S.L., and Lyster C.T., "Method and apparatus for generating motor current spectra to enhance motor system fault detection", US Patent Number 5,461,329, 24 October, 1995.

[74] Innes A.G., Langman R.A., and Mayhew G.R., "Condition monitoring of variable speed induction motor drives", *Proceedings of the International*

Conference on Electrical Machines in Australia, Vol. 1, pp158-163, Adelaide, Australia, 14-16 September 1993.

[75] Layos M. and Haritantis I., "Modelling of commercially available phase locked loop ICs", *International Journal of Electronics*, Vol. 75, No. 2, pp315-326, 1993.

[76] Private communication with control room staff of the Hydro Electric Commission of Tasmania, March 1996.

[77] Holtz J., "Pulsewidth modulation for electronic power conversion", *Proceedings of the IEEE*, Vol. 82, No. 8, pp1194-1214, August 1994.

[78] Klingshirn E.A. and Jordan H.E., "Polyphase induction motor performance and losses on nonsinusoidal voltage sources", *IEEE Transactions on Power Apparatus and Systems*, Vol. 87, No. 3, pp624-631, March 1968.

[79] Boys J.T. and Miles M.J., "Empirical thermal model for inverter-driven cage induction machines", *IEE Proceedings Part B: Electric Power Applications*, Vol. 141, No. 6, pp360-372, November 1994.

[80] Boldea I. and Nasar S.A., *Vector Control of AC Drives*, CRC Press, Boca Raton, USA, 1992.

[81] Mohan N., Undeland T.M. and Robbins W.P., *Power Electronics: Converters, Applications and Design*, John Wiley and Sons, New York, 1989.

[82] Shepherd W. and Hulley L.N., *Power Electronics and Motor Control*, Cambridge University Press, Cambridge, UK, 1987.

[83] Black H.S., *Modulation Theory*, Van Nostrand, New York, 1953.

[84] Bowes S.R., "New sinusoidal pulsewidth-modulated invertor", *Proceedings of the IEE*, Vol. 122, No. 11, pp1279-1285, November 1975.

[85] Bowes S.R. and Bird B.M., "Novel approach to the analysis and synthesis of modulation processes in power convertors", *Proceedings of the IEE*, Vol. 122, No. 5, pp507-513, May 1975.

[86] Bowes S.R. and Clements R.R., "Computer-aided design of PWM inverter systems", *IEE Proceedings Part B: Electric Power Applications*, Vol. 129, No. 1, pp1-17, January 1982.

[87] Franzó G., Mazzucchelli M., Puglisi L., and Sciutto G., "Analysis of PWM techniques using uniform sampling in variable-speed electrical drives with large speed range", *IEEE Transactions on Industry Applications*, Vol. 21, No. 4, pp966-974, July/August 1985.

[88] Zach F.C., Martinez R., Keplinger S., and Seiser A., "Dynamically optimal switching patterns for PWM inverter drives (for minimization of the torque and speed ripples)", *IEEE Transactions on Industry Applications*, Vol. 21, No.4, pp975-986, July/August 1985.

[89] Zach F.C. and Ertl H., "Efficiency optimal control for AC drives with PWM inverters", *IEEE Transactions on Industry Applications*, Vol. 21, No.4, pp987-1000, July/August 1985.

[90] Dewan S.B. and Straughen A., *Power Semiconductor Circuits*, John Wiley and Sons, New York, 1975.

[91] Bowes S.R. and Midoun A., "Suboptimal switching strategies for microprocessor-controlled PWM inverter drives", *IEE Proceedings Part B: Electric Power Applications*, Vol. 132, No. 3, pp133-148, May 1985.

[92] Houldsworth J.A. and Grant D.A., "The use of harmonic distortion to increase the output voltage of a three-phase PWM inverter", *IEEE Transactions on Industry Applications*, Vol. 20, No. 5, pp1224-1228, September/October 1984.

[93] Trzynadlowski A.M., Legowski S., and Kirlin R.L., "Random pulse-width modulation technique for voltage-controlled power inverters", *International Journal of Electronics*, Vol. 68, No. 6, pp 1027-1037, 1990.

[94] Chalmers B.J. ed, *Electric Motor Handbook*, Butterworths, London, 1988.

[95] Kirlin R.L., Kwok S., Legowski S., and Trzynadlowski A.M., "Power spectra of a PWM inverter with randomized pulse position", *IEEE Transactions on Power Electronics*, Vol. 9, No. 5, pp463-472, September 1994.

[96] Boys J.T., "Theoretical spectra for narrow-band random PWM waveforms", *IEE Proceedings Part B: Electric Power Applications*, Vol. 140, No. 6, pp393-400, November 1993.

[97] Habetler T.G. and Divan D.M., "Acoustic noise reduction in sinusoidal PWM drives using a randomly modulated carrier", *IEEE Transactions on Power Electronics*, Vol. 6, No. 3, pp356-363, July 1991.

[98] van der Broeck H.W., Skudley H., and Stanke G.V., "Analysis and realization of a pulsewidth modulator based on voltage space vectors", *IEEE Transactions on Industry Applications*, Vol. 24, No. 1, pp142-150, January/February 1988.

[99] Handley P.G. and Boys J.T., "Practical real-time PWM modulators: an assessment", *IEE Proceedings Part B: Electric Power Applications*, Vol. 139, No. 2, pp96-102, March 1992.

[100] Boys J.T. and Handley P.G., "Harmonic analysis of space vector modulated waveforms", *IEE Proceedings Part B: Electric Power Applications*, Vol. 137, No. 4, pp197-204, July 1990.

[101] Deng X. and Ritchie E., "Detection of broken rotor bars in induction motor rotors by investigating the flux linkages of the stator winding", *Proceedings of the International Conference on Electrical Machines in Australia*, Vol. 1, pp164-169, Adelaide, Australia, 14-16 September 1993.

[102] Chari M.V.K., and Silvester P.P., *Finite Element Problems in Electrical and Magnetic Field Problems*, John Wiley and Sons, New York, 1980.

[103] Salon S., Palma R., and Hwang C.C., "Dynamic modeling of an induction motor connected to an adjustable speed drive", *IEEE Transactions on Magnetics*, Vol. 25, No. 4, pp3061-3063, July 1989.

[104] Salon S., Burow D., Slavik C., Bushman R., and DeBortoli M., "Comparison of pulsating torques in induction motors by analytic and finite element methods", *Proceedings of the International Conference on Electrical Machines*, Vol 3 pp732-737, Paris, France, 5-8 September 1994.

[105] Williamson S. and Smith A.C., "Steady-state analysis of 3-phase cage motors with rotor-bar and end-ring faults", *IEE Proceedings Part B, Electrical Power Applications*, Vol. 129, No. 3, pp 93-100, May 1982.

[106] Muller G.H. and Landy C.F., "Finite element analysis of field distribution of squirrel cage induction motors having broken rotor bars and interbar currents", *Proceedings of the International Conference on Electrical Machines*, Vol. 2, pp577-581, Paris, France, 5-8 September 1994.

[107] O'Kelly D. and Simmons S., *Introduction to Generalized Electrical Machine Theory*, McGraw-Hill, London, 1968.

[108] Krause P.C., "Method of multiple reference frames applied to the analysis of symmetrical induction machinery", *IEEE Transactions on Power Apparatus and Systems*, Vol. 87, No. 1, pp218-227, January 1968.

[109] Barton T.H. and Doxey B.C., "The operation of three-phase induction motors with unsymmetrical impedance in the stator circuit", *Proceedings of the IEE Part A: Power Engineering*, Vol. 102, No. 1, pp71-79, February 1955.

[110] Vas P. and Vas J., "Transient and steady-state operation of induction motors with rotor asymmetries", *Archiv für Elektrotechnik*, Vol. 59, pp55-60, 1977.

[111] Vas P., "Steady state and transient performance of induction motors with rotor asymmetry", *IEEE Transactions on Power Apparatus and Systems*, Vol. 101, No. 9, pp3246-3251, September 1982.

[112] Vas P., Filippetti F., Franceschini G. and Tassoni C., "Transient modelling oriented to diagnostics of induction machines with rotor asymmetries", *Proceedings of the International Conference on Electrical Machines*, Vol. 2, pp62-67, Paris, France, 5-8 September 1994.

[113] Lipowski J.S. and Duggal B.R., "Monitoring faults in the rotor of a squirrel-cage induction motor throught the analysis of harmonic content of stator currents", *Proceedings of the International Power Engineering Conference*, pp484-490, Singapore, 18-19 March 1993.

[114] Ritchie E., Deng X. and Jokinen T., "Dynamic model of three-phase squirrel cage induction motors with rotor faults", *Proceedings of the International Conference on Electrical Machines*, Vol. 2, pp348-352, Paris, France, 5-8 September 1994.

[115] Fudeh H.R. and Ong C.M., "Modeling and analysis of induction machines containing space harmonics part I: modeling and transformation", IEEE Transactions on Power Apparatus and Systems, Vol. 102, No.8, pp2608-2615, August 1983.

[116] Fudeh H.R. and Ong C.M., "Modeling and analysis of induction machines containing space harmonics part II: analysis of asynchronous and synchronous actions", IEEE Transactions on Power Apparatus and Systems, Vol. 102, No.8, pp2616-2620, August 1983.

[117] Fudeh H.R. and Ong C.M., "Modeling and analysis of induction machines containing space harmonics part III: three-phase cage rotor induction machines", IEEE Transactions on Power Apparatus and Systems, Vol. 102, No.8, pp2621-2628, August 1983.

[118] Toliyat H.A., Lipo T.A., and White J.C., "Analysis of a concentrated winding induction motor for adjustable speed drive applications part 1 (motor analysis)", *IEEE Transactions on Energy Conversion*, Vol. 6, No. 4, pp679-683, December 1991.

[119] Toliyat H.A., *Analysis of Concentrated Winding Induction and Reluctance Machines for Adjustable Speed Drive Applications*, PhD Thesis, University of Wisconsin-Madison, USA, 1991.

[120] Toliyat H.A. and Lipo T.A., "Transient analysis of cage induction machines under stator, rotor bar and end ring faults", *IEEE Transactions on Energy Conversion*, Vol. 10, No. 2, pp241-247, June 1995.

[121] Luo X., Liao Y., Toliyat H.A., El-Antably A. and Lipo T.A., "Multiple coupled circuit modeling of induction machines", *IEEE Transactions on Industry Applications*, Vol. 31, No. 2, pp311-317, March/April 1995.

[122] Stewart D.E. and Leyk Z., *Meschach: Matrix Computations in C*, Proceedings of the Centre for Mathematics and its Applications, Volume 32, The Australian National University, Canberra, Australia, 1994.

[123] Newland D.E., "Wavelet analysis of vibration, part 1: Theory", *Transactions of the ASME: Journal of Vibration and Acoustics*, Vol. 116, pp409-416, October 1994.

[124] Newland D.E., "Wavelet analysis of vibration, part 1: Wavelet maps", *Transactions of the ASME: Journal of Vibration and Acoustics*, Vol. 116, pp417-425, October 1994.

[125] Tansel I. N., Mekdeci C., Rodriguez O., and Uragun B., "Monitoring drill conditions with wavelet based encoding and neural networks", *International Journal of Machine Tools and Manufacture*, Vol. 33, No. 4, pp559-575, 1993.

[126] Forrester D., "Time-frequency analysis in machine fault detection", in *Time-frequency Signal Analysis - Methods and Applications* (Boashash B. ed.), Longman Cheshire, Melbourne, Australia, 1992.

[127] Loughlin P., Atlas L., Bernard G., and Pitton J., "Application of time-frequency analysis to the monitoring of machining processes", *Life Extension of Aging Machinery and Structures, Proceedings of the 49th Society of Machinery Failure Prevention Technology Conference* (Pusey H.C. ed.), Vibration Institute, Illinois, USA, April 1995.

[128] Williams W.J., "Bearing monitoring using reduced interference distributions", *Life Extension of Aging Machinery and Structures, Proceedings of the 49th Society of Machinery Failure Prevention Technology Conference* (Pusey H.C. ed.), Vibration Institute, Illinois, USA, April 1995.

[129] McFadden P.D., "Application of the wavelet transform to early detection of gear failure by vibration analysis", *Proceedings of the Condition Monitoring '94 Conference* (Jones M.H. ed.), pp172-183, Swansea, UK, 1994.

[130] Salvatore L. and Stasi S., "Monitoring of inverter drives in time-frequency domain", *Proceedings of the International Conference on Electrical Machines*, Vol. 2, pp73-78, Paris, France, 5-8 September 1994.

[131] Burnett R., Watson J.F., and Elder S., "The detection and location of rotor faults within three phase induction motors", *Proceedings of the*

International Conference on Electrical Machines, Vol. 2, pp288-293, Paris, France, 5-8 September 1994.

[132] Burnett R. and Watson J.F., "The current analysis program - a software tool for rotor fault detection in three phase induction motors", *Electrical Machines and Drives*, IEE Conference Publication No. 412, pp156-160, 11-13 September 1995.

[133] Gabor D., "Theory of communication", *The Journal of the IEE Part III: Radio and Communication Engineering*, Vol. 93, No. 26, November 1946.

[134] Speiser J.M., Whitehouse H.J. and Allen J.C., "Wideband time-frequency distributions", in *Time-frequency Signal Analysis - Methods and Applications* (Boashash B. ed.), Longman Cheshire, Melbourne, Australia, 1992.

[135] Choi H. and Williams W.J., "Improved time-frequency representation of multicomponent signals using exponential kernels", *IEEE Transactions on Acoustics, Speech, and Signal Processing*, Vol. 37, No.6, pp862-871, June 1989.

[136] Williams W.J. and Jeong J., "Reduced interference time-frequency distributions", in *Time-frequency Signal Analysis - Methods and Applications* (Boashash B. ed.), Longman Cheshire, Melbourne, Australia, 1992.

[137] Zhao Y., Atlas L.E., and Marks II R.J., "The use of cone-shaped kernels for generalized time-frequency representations of nonstationary signals", *IEEE Transactions on Acoustics, Speech, and Signal Processing*, Vol. 38, No.7, pp1084-1091, July 1990.

[138] Cohen L., "Introduction: A primer on time-frequency analysis", in *Time-frequency Signal Analysis - Methods and Applications* (Boashash B. ed.), Longman Cheshire, Melbourne, Australia, 1992.

[139] Atlas L.E., Loughlin P.J., and Pitton J.W., "Signal analysis with cone kernel time-frequency distributions and their application to speech", in *Time-frequency Signal Analysis - Methods and Applications* (Boashash B. ed.), Longman Cheshire, Melbourne, Australia, 1992.

[140] Rioul O. and Vetterli M., "Wavelets and signal processing", *IEEE Signal Processing Magazine*, Vol. 8, No. 4, pp14-38, October 1991.

[141] Graps A., "An introduction to wavelets", *IEEE Computational Science and Engineering*, Summer, pp50-61, 1995.

[142] Daubechies I., *Ten Lectures on Wavelets*, CBMS-NSF Series in Applied Mathematics, SIAM, Philadelphia, Pennsylvania, 1992.

[143] Grossman A., Kronland-Martinet R., Morlet J., "Reading and understanding continuous wavelet transforms," in *Wavelets: Frequency Methods and Phase Space, 2nd ed.* (Combes J.M., Grossman A., Tchamitchian Ph., Eds.), pp. 2-20, New York: Springer-Verlag, 1989/1990.

[144] Morlet J., Arens G., Fourgeau E., and Giard D., "Wave propogation and sampling theory", *Geophysics*, Vol. 47, No. 2, pp203-236, February 1982.

[145] Heneghan C., Khanna S.M., Flock Å, Ulfendahl M., Brundin L., and Teich M.C., "Investigating the nonlinear dynamics of cellular motion in the inner ear using the short-time fourier and continuous wavelet transforms", *IEEE Transactions on Signal Processing*, Vol. 42, No. 12, pp3335-3352, December 1994.

[146] Boashash B., Boles P., Reilly A., Frazer G., and Hatton B., *TFSA Time-Frequency Analysis Toolbox*, Signal Processing Research Centre, Queensland Univeristy of Technology, Brisbane, Australia, 1994.

[147] The Mathworks Inc., *MATLAB Reference Guide*, The Mathworks Inc., Natick Ma., USA, 1992.

[148] Filippetti F., Franceschini G., and Tassoni C., "Neural networks aided on-line diagnostics of induction motor rotor faults", *IEEE Transactions on Industry Applications*, Vol. 31, No. 4, pp892-899, July/August 1995.

[149] Penman J. and Yin C.M., "Feasability of using unsupervised learning, artificial neural networks for the condition monitoring of electrical machines", *IEE Proceedings - Electric Power Applications*, Vol. 141, No. 6, pp317-322, November 1994.

[150] Filippetti F., FranceschiniG., Tassoni C., Meo S., and Ometto A., "Neural network aided on-line diagnostics of induction machine stator faults", *Proceedings of the 30th Universities Power Engineering Conference*, Vol. 1, pp148-151, London, UK, 5-7 September 1995.

[151] Penman J., Stavrou A., Yin C.M., Jiang H., and Hatzipantelis E., "Machine diagnostics with ANNs: possibilities and problems", *Proceedings of the International Conference on Electrical Machines*, Vol. 2, pp363-368, Paris, France, 5-8 September 1994.

[152] Protopapas C.A., Kaminaris S.D., Machias A.V., and Papadias B.C., "An expert system for fault repairing and maintenance of electric machines", *IEEE Transactions on Energy Conversion*, Vol. 5, No. 1, pp79-83. March 1990.

[153] Gentile G., Rotondale N., Tursini M., Franceschini G., and Tassoni C., "An approach to knowledge-base representation in electric drive fault

diagnosis", *Proceedings of the International Conference on Electrical Machines*, Vol. 2, pp358-362, Paris, France, 5-8 September 1994.

[154] Watson G.N., *Theory of Bessel Functions*, Cambridge University Press, Cambridge, UK, 1922.